Christian Lackner

Prestressed reinforced soil – Concept, investigations and recommendations

Dissertation

Eingereicht an der Fakultät für Bauingenieurwissenschaften
der Technischen Universität Graz

Begutachter:

Em.Univ.-Prof. Dipl.-Ing. Dr.techn. Stephan Semprich
Institut für Bodenmechanik und Grundbau
Technische Universität Graz

Prof. Dr. Dennes T. Bergado
School of Engineering and Technology
Asian Institute of Technology

Univ.-Prof. Dipl.-Ing. Dr.techn. Roman Marte
Institut für Bodenmechanik und Grundbau
Technische Universität Graz

Graz, September 2012

Acknowledgements

This dissertation would not have been possible without the consistent support and advice of Em.Univ.-Prof. Dipl.-Ing. Dr.techn. Stephan Semprich. I cordially thank Prof. Semprich for sharing his knowledge and ideas about geotechnical engineering and related areas. I am thankful to Prof. Semprich for providing the resources and the academic environment essential for creating this thesis. I am very grateful for being given the opportunity to attend various conferences to present my research to an international academic society and for supporting me during my research exchange at the Asian Institute of Technology.

I feel fortunate to have worked with Prof. Dr. Dennes T. Bergado of the Asian Institute of Technology (AIT) and I am gratefull for reviewing this thesis. Furthermore, I cordially thank Prof. Bergado for inviting me to the AIT as a fellow researcher. The fruitful time for research and learning inspired my academic and personal life.

I am grateful to Univ.-Prof. Dipl.-Ing. Dr.techn. Roman Marte, Head of the Institute of Soil Mechanics and Foundation Engineering at Graz University of Technology. I appreciate your reviewing of this thesis. I cordially thank you for all the exciting academic and personal discussions and conversations.

A special thanks to all my colleagues at the Institute of Soil Mechanics and Foundation Engineering for many fruitful discussions, research related or otherwise. In particular I would like to thank Franz Tschuchnigg, Gregor Supp Bert Schädlich, Gerhard Steger, Ali Nasekhian, Ikhya and Indra Hamdhan.

I thank my master students, Simone Feiertag, Ševal Brkić, Michael Burgstaller, Mario Dijak and Michael Havinga for being honestly fascinated by my topic.

The financial support by the Österreichische Gesellschaft für Geomechanik (ÖGG) is gratefully acknowledged. I am grateful for the support of Hüsker Synthetics GmbH, Gescher and IBH Herold VBI GmbH, Weimar.

Last but not least, I would like to thank Lisa, my family and friends for their understanding, patience and support during the past four years.

I wish to pay special tribute to my father and want to dedicate this thesis to him who supported me with his endless energy and kindness.

Graz, September 2012 Christian Lackner

Kurzfassung

Vorgespannte Bewehrte Erde – Konzept, Untersuchungen und Empfehlungen

In dieser Arbeit wird das Konzept der Vorgespannten Bewehrten Erde (PRS_i) zur Verbesserung des Last-Verformungsverhaltens von Strukturen aus Bewehrter Erde vorgestellt. Ergebnisse aus experimentellen und numerischen Untersuchungen des mit Geogittern bewehrten, innovativen Bauverfahrens für granularen Boden werden präsentiert.

Bei den experimentellen Untersuchungen handelt es sich um großmaßstäbliche Laborversuche. Mehr als 60 weggesteuerte, statische Last-Verformungsversuche wurden durchgeführt um das Verhalten bewehrter Erdstrukturen zu untersuchen. Die Ergebnisse zeigen eine beträchtliche Verbesserung des Last-Verformungsverhaltens der Bewehrten Erdkörper im Fall einer Vorspannung nach dem Konzept der PRS_i. Mehr als 80 zyklische Last-Verformungsversuche wurden in Weimar, Deutschland durchgeführt um das Konzept der PRS_i unter zyklischer Belastung zu validieren. Ein bewehrtes Bodenelement wurde unter biaxialen, vertikalen und horizontalen Lastzuständen untersucht. Die makroskopischen Ergebnisse zeigen, dass sich Verformungen unter zyklischer Last reduzieren, wenn das Konzept der PRS_i angewandt wird. Neben der Untersuchung zum makroskopischen Last-Verformungsverhalten der bewehrten Erdkörper und Bodenelemente wurden mit Hilfe der PIV Methode mesoskopische Analysen durchgeführt, um einen Einblick in den Lastabtragungs- und Interaktionsmechanismus zwischen Geogitter und Boden zu erlangen.

Des Weiteren wurden numerische Simulationen, basierend auf der Finiten (FEM) und Diskreten Element Methode (DEM) genutzt um die makro- und mesoskopischen Laborergebnisse zu errechnen und zu validieren. Eine geometrisch detaillierte DEM Modellierung von Bodenkörner und Geogitterstrukturen wurde durchgeführt. Die innovative Methode des Computer Aided Design (CAD) für clumps (diskrete Bodenpartikel) und Geogitterstrukturen gewährleisten eine detaillierte mesoskopische Modellierung der Boden-Geogitter Interaktion. Die Ergebnisse der diskreten numerischen Berechnung validieren die experimentellen Ergebnisse und verbessern das grundlegende Verständnis des mechanischen Verhaltens von Vorgespannter Bewehrter Erde.

Praktische Bemessungs- und Einbauempfehlungen schließen diese Arbeit ab, welche die Grundlagen für die Vorgespannte Bewehrte Erde liefert.

Abstract

Prestressed reinforced soil – Concept, investigations and recommendations

In this thesis the concept of prestressed reinforced soil (PRS_i) to improve the load displacement behaviour of reinforced soil structures is introduced. Results of numerical and experimental investigations on the innovative construction method for granular soil structures reinforced by geogrids are presented.

The experimental investigations are based on large scale laboratory tests. More than 60 path-controlled static load displacement tests have been conducted to investigate the behaviour of reinforced soil structures. The results show a considerable improvement of the load displacement behaviour of the soil structures reinforced by utilizing the concept of prestressed reinforced soil (PRS_i). More than 80 cyclic load displacement tests have been utilized in Weimar, Germany to validate the concept of PRS_i under cyclic loading conditions. A reinforced soil element has been investigated under biaxial vertical and horizontal cyclic load conditions. The macroscopic results of the research show that displacements occurring under cyclic loading reduce conspicuously when installing a geogrid by utilizing the concept of PRS_i.

Besides investigating the macroscopic load displacement behaviour of the reinforced soil structures and the reinforced soil elements, a detailed mesoscopic analysis using the Particle Image Velocimetry (PIV) method has been performed to gain a detailed insight in the load transfer- and soil geogrid interaction mechanism.

In addition, numerical simulations based on the Finite (FEM) and Discrete Element Method (DEM) are utilized to calculate and validate the macro- and mesoscopic experimental test results. A detailed geometrical DEM modelling of soil particles and geogrid structures has been performed. The innovative method of Computer Aided Design (CAD) for clumps (discrete soil particles) and geogrid structures ensure a detailed mesoscopic modelling of the soil geogrid interaction. The results of the discrete numerical analysis validate the experimental results and further improve the fundamental understanding of the mechanical behaviour of prestressed reinforced soil.

Practical design and construction recommendations complete this thesis which presents the fundamentals of prestressed reinforced soil.

Table of contents

List of symbols and abbreviations

1 Reinforced soil structures, review on open issues, methodology and outline of the thesis 1

1.1 Introduction 1

1.2 Literature review: reinforced soil structures 1

1.2.1 General principle 1

1.2.2 Soil geogrid interaction 3

1.2.3 Design concepts 6

1.2.4 Construction recommendations 6

1.3 Case Study: reinforced soil structure B114, Austria 7

1.3.1 Geotechnical project information 7

1.3.2 Soil geogrid interaction 8

1.3.3 Design concepts 8

1.3.4 Construction recommendations 9

1.4 Open issues 10

1.5 Methodology and outline of the thesis 10

2 Introduction to the concept of prestressed reinforced soil (PRS_i) by geogrids 13

2.1 Introduction 13

2.2 Literature review: prestressed reinforced soil 13

2.2.1 General information 13

2.2.2 Prestressing the reinforced soil structure 13

2.2.3 Prestressing the reinforcement in the soil structure 14

2.3 Prestressed reinforced soil (PRS_i) using geogrids 14

2.3.1 Prestressing as a result of compaction (PRS_c) 18

2.3.2 Permanently prestressed reinforced soil (PRS_p) 19

2.3.3 Temporarily prestressed reinforced soil (PRS_t) 21

2.4 Summary and conclusions 22

3 Experimental investigations on prestressed reinforced soil (PRS_i) by geogrids 24

3.1 Introduction 24

3.2 Literature review: experimental investigations on prestressed reinforced soil (PRS_i) by geogrids 24

3.2.1 Static load displacement experiments 24

3.2.2 Cyclic load displacement experiments 25

3.3 Static load displacement experiments on prestressed reinforced soil (PRS_i) by geogrids 26

3.3.1 Overview on the experimental investigations 26

3.3.2 Experimental setup and testing equipment 28

3.3.3 Experimental materials 29

3.3.4 Experimental procedure 39

3.3.5 Experimental results and discussion 40

3.4 Cyclic load displacement experiments on prestressed reinforced soil (PRS_i) by geogrids 50

3.4.1 Overview on the experimental model 50

3.4.2 Experimental setup and testing equipment 52

3.4.3 Experimental materials 53

3.4.4 Experimental procedure 55

3.4.5 Experimental results and discussion 60

3.5 Summary and conclusions 71

4 Numerical investigations on prestressed reinforced soil (PRS_i) by geogrids 73

4.1 Introduction 73

4.2 Literature review: numerical investigations on prestressed reinforced soil (PRS_i) by geogrids 73

4.2.1 Finite Element Method (FEM) investigations 74

4.2.2 Discrete Element Method (DEM) investigations 74

4.3 Multiscale Finite Element and Discrete Element modelling 75

4.4 Finite Element Method (FEM) investigations on prestressed reinforced soil (PRS_i) by geogrids 78

4.4.1 Overview on the numerical model 78

4.4.2 Numerical setup and calculation process 78

4.4.3 Numerical material parameters 79

4.4.4 Numerical procedure 80

4.4.5 Numerical results and discussion 81

4.5 Discrete Element Method (FEM) investigations on prestressed reinforced soil (PRS_i) by geogrids 86

4.5.1 Overview on the numerical model 87

4.5.2 Numerical setup and calculation process 87

4.5.3 Numerical material parameters 88

4.5.4 Numerical procedure 95

4.5.5 Numerical results and discussion 97

4.6 Summary and conclusions 106

5 Design and construction recommendations on PRS_i by geogrids 110

5.1 Introduction 110

5.2 Design recommendations on prestressed reinforced soil 110

5.2.1 Design recommendations for prestressed reinforced soil foundations 111

5.2.2 Design recommendations for prestressed reinforced soil slopes 124

5.3 Construction recommendations on prestressed reinforced soil 129

5.3.1 Construction recommendations for prestressing the geogrid by compaction (PRS_c) 132

5.3.2 Construction recommendations for prestressing the geogrid with the shovel of an excavator ($PRS_{p,t}$) 133

5.3.3 Construction recommendations for prestressing the geogrid with a trench (PRS_p) 135

5.3.4 Construction recommendations for prestressing the geogrid with tensioning equipment ($PRS_{p,t}$) 138

5.4 Summary and conclusions 140

6 Conclusions and further research 142

7 Literature 149

Appendix 162

List of symbols and abbreviations

Small letters

a	[m]	length of cube representing deformation boundaries
$a_{grid,x,y}$	[mm]	geogrid aperture size, x, y direction
c	[kN/m²]	cohesion
c_a	[kN/m²]	adhesion of soil
c_m	[N/m^2]	cohesion of embankment soil
c^*_m	[-]	non-dimensional cohesion of embankment soil ($c_m/\gamma_t H$)
d_{50}	[mm]	soil grain diameter with respect to 50 % mass of grains
d_{100}	[mm]	soil grain diameter with respect to 100 % mass of grains
d	[m]	depth
d	[m]	thickness of reinforced zone
d_{foot}	[mm]	footing embedment depth
d_{grain}	[mm]	soil grain diameter
$d_{grid,l}$	[mm]	thickness of geogrid longitudinal member
$d_{grid,t}$	[mm]	thickness of geogrid transverse member
$d_{grid,j}$	[mm]	thickness of geogrid junction
d_h	[m]	horizontal distance of experimental device
d_{test}	[m]	testing distance to facing
d_v	[m]	vertical distance of experimental device
f	[Hz]	frequency
h	[m]	vertical spacing between the reinforcement layers
h_{layer}	[m]	height of soil layer
id_{grain}	[mm]	multiple of grain diameter
k_f	[m/s]	permeability
k_n	[N/m]	soil grain contact normal stiffness
k_s	[N/m]	soil grain contact shear stiffness
$l_{geogrid}$	[m]	length of geogrid specimen
l_{test}	[m]	length of testing specimen
m	[-]	power index, controlling stress dependency of stiffness
m_{stage}	[-]	total multiplier for stage construction (0.0 - 1.0)
n	[-]	porosity
n	[-]	number of friction planes between geogrid and soil
n_{exp}	[-]	experimental porosity
n_{max}	[-]	maximum porosity
n_{min}	[-]	minimum porosity
$n_{\_bond}$	[N]	contact bond normal force
p	[kN/m²]	bearing capacity, pressure

$pb_{\_kn}$	[Pa/m]	parallel bond normal stiffness
$pb_{\_ks}$	[Pa/m]	parallel bond shear stiffness
$pb_{\_nstrenght}$	[Pa]	parallel bond normal strength
$pb_{\_radius}$	[-]	radius multiplier
$pb_{\_sstrength}$	[Pa/m]	parallel bond shear strength
p_c	[kN/m²]	compaction pressure
p_{grain}	[-]	flatness ratio
p_{hf}	[kN/m²]	pressure hard facing
$p_{hf,UR}$	[kN/m²]	pressure hard facing of unreinforced soil
$p_{hf,PRSi}$	[kN/m²]	pressure hard facing of prestressed reinforced soil
p_{LP}	[kN/m²]	pressure load plate
p_{ref}	[kN/m²]	reference pressure
p_{sf}	[kN/m²]	pressure soft facing
q_{grain}	[-]	elongation ratio
$q_{u(R)}$	[kN/m²]	ultimate bearing capacity for footing on reinforced soil
$q_{u(UR)}$	[kN/m²]	ultimate bearing capacity for footing on unreinforced soil
q_b	[kN/m²]	ultimate bearing capacity of underlaying unreinforced soil settlement
r_T	[-]	dimensionless factor according to Chen (2007)
s_h	[mm]	horizontal displacement
s_{max}	[mm]	maximum displacement (stroke)
$s_{\_bond}$	[N]	contact bond shear force
s_{shear}	[m]	shear displacement
s_{tot}	[mm]	total displacement
s_v	[mm]	vertical displacement
$s_{v,failure}$	[mm]	vertical displacement at failure
t	[mm]	distance between the reinforcement
t	[s]	time
u	[m]	top layer spacing
v_c	[m/s]	compaction velocity
v_{test}	[m/s]	testing velocity
v_{train}	[m/s]	train velocity
$w_{geogrid}$	[m]	width of geogrid specimen
w	[%]	water content
x	[m]	x-coordinate of centre of slip circle
x_c	[m]	x-coordinate of centre of critical slip circle
y	[m]	y-coordinate of centre of slip circle
y_c	[m]	y-coordinate of centre of critical slip circle
y^*_c	[-]	non-dimensional y-coordinate of centre of slip circle (y_c/H)
z	[m]	depth

Capital letters

A	[m²]	cross section of the specimen
A	[m]	maximum grain elongation
A_{grain}	[m²]	projected grain area
AH_{test}	[°]	testing air moisture content
B	[m]	middle grain elongation
B	[m]	width of load plate
BCR_{hf}	[-]	bearing capacity ratio hard facing
BCR_{sf}	[-]	bearing capacity ratio soft facing
C	[m]	minimum grain elongation
C_c	[-]	curvature coefficient
C_u	[-]	uniformity coefficient
D	[-]	packing density
D	[m]	depth of limiting tangent
D^*	[-]	non-dimensional depth of limiting tangent (D/H)
D_f	[m]	embedment depth of footing
D_P	[m]	indentation depth
E_{50}	[MN/m²]	Young`s modulus of elasticity corresponding to 50 % of the maximum shear strength
E_{oed}	[MN/m²]	actual soil stiffness for primary oedometer loading
E_{ur}	[MN/m²]	soil stiffness for un- and reloading at actual stress
E_s	[MN/m²]	soil stiffness
EA	[kN/m]	tensile stiffness of geogrid
F_c	[N]	compaction force
$F_{contact}$	[N]	contact force
F_{max}	[N]	maximum Force
FS	[-]	factor of safety
F_{spread}	[kN/m]	spreading force
$F_{tensile,max}$	[kN/m]	maximum tensile force in geogrid
H	[m]	height
K	[-]	earth pressure coefficient
K_0	[-]	initial earth pressure coefficient
K_S	[-]	punching shear coefficient
L	[m]	length
L_A	[m]	anchorage length of reinforcement
M_o	[kNm]	overturning moment
M_1	[kg]	total mass 1
M_2	[kg]	total mass 2
M_R	[kNm]	resisting moment
N	[-]	number of load steps
N	[-]	number of reinforcement layers
N_{max}	[-]	maximum number of load steps

N_p	[-]	number of reinforcement layers located in the punching shear failure zone
R	[-]	ratio between prestress strain and residual strain
R_{inter}	[-]	interaction coefficient between soil and structure (geogrid)
RK	[-]	roundness coefficient
S	[kN/m²]	surcharge
SI	[%]	shape index
S_u	[kN/m^2]	undrained shear strength of foundation soil
S^*_u	[-]	non-dimensional undrained shear strength of foundation soil ($S_u/\gamma_t H$)
T_a	[kN/m]	allowable tensile force of geosynthetic
T_m	[kN/m]	mobilised tensile force in geosynthetic
T^*_m	[-]	non-dimensional mobilised force in geosynthetic ($T_m/\gamma_t H$)
T_p	[kN/m]	prestressing force in geosynthetic
T^*_p	[-]	non-dimensional prestressing force in geosynthetic ($T_p/\gamma_t H$)
T_i	[kN/m]	tensile force in the i_{th} layer
$T_{prs,p}$	[kN/m]	tensile force due to permanent prestressing
$T_{sum,i}$	[kN/m]	total tensile force
T_{test}	[°]	testing temperature
U_{grain}	[m]	projected grain contour
W	[m]	width

Greek letters

β	[°]	slope angle, angle of repose
δ_s	[°]	angle of interaction
Δq_T	[kN/m²]	increased bearing capacity due to tensile force of reinforcement
$\Delta q_{T,prs,p}$	[kN/m²]	increased bearing capacity due to permanent prestressing
$\Delta q_{T,prs,t}$	[kN/m²]	increased bearing capacity due to temporary prestressing
$\Delta\sigma_{h,prs,t}$	[kN/m²]	horizontal stress due to residual strain
$\Delta\sigma_{v,prs,t}$	[kN/m²]	vertical stress due to residual strain
ε_{creep}	[%]	creep strain of geogrid
ε_{PRSi}	[%]	prestress strain of geogrid
$\varepsilon_{tensile}$	[%]	tensile strain of geogrid
$\varepsilon_{tensile,\ max}$	[%]	maximum tensile strain of geogrid
γ_t	[g/cm³]	unit weight of soil in reinforced zone
γ_s	[g/cm³]	grain unit weight

μ	[-]	friction coefficient, microscopic roughness
ν	[-]	poisson ratio
ψ	[°]	dilatancy angle
κ	[-]	factor to determine thickness of shear band
λ	[-]	averaging coefficient for frictional stress in embankment
ρ_{grid}	[g/m²]	mass per unit area
σ	[kN/m²]	total stress
σ_c	[kN/m²]	cyclic stress
σ_h	[kN/m²]	horizontal stress
σ_n	[kN/m²]	normal stress
σ_v	[kN/m²]	vertical stress
σ_z	[kN/m²]	static stress in z direction
$\sigma_{zd,sleeper}$	[kN/m²]	dynamic, cylic stress under sleeper
$\sigma_{zd,z}$	[kN/m²]	dynamic, cylic stress in z direction
τ	[kN/m²]	shear stress
τ_{spread}	[kN/m²]	spreading stress
φ	[°]	effective friction angle
φ_{peak}	[°]	effective peak friction angle

Abbreviations

CAD	Computer Aided Design
DEM	Discrete Element Method
FEM	Finite Element Method
MV	mean value
PET	Polyethyleneterephthalate
PP	Polypropylene
PRS_c	Prestressed Reinforced Soil by compaction
PRS_i	Prestressed Reinforced Soil
PRS_p	Permanently Prestressed Reinforced Soil
PRS_t	Temporarily Prestressed Reinforced Soil
PIV	Particle Image Velocimetry
RE	reinforced
ROI	region of interest
UR	unreinforced
∅	diameter of experimental device

1 Reinforced soil structures, review on open issues, methodology and outline of the thesis

1.1 Introduction

Reinforced soil structures are nowadays utilized for a lot of civil engineering applications, especially for fast and economical geotechnical engineering solutions. Without the use of these geosynthetic reinforcement materials, in most cases geogrids, many construction projects all around the world would not have succeeded outstandingly.

Meanwhile, several design standards and recommendations for the European regions (British Standard BS 8006-1 (BSI) 2010, Deutsche Gesellschaft für Geotechnik (DGGT) EBGEO 2010) but also for the USA are available (National Highway Institute, USA (NHI) 2008). International technical journals and handbooks for soil improvement respectively the designing with geosynthetics and books related to different applications of geosynthetics (Brandl 1987, Bergado et al 1996, Koerner 1998) have been published in the last decades.

1.2 Literature review: reinforced soil structures

1.2.1 General principle

The general principle of reinforcing soil structures is concisely described in BSI (2010) *"...Soil has an inherently low tensile strength but a high compressive strength which is only limited by the ability of the soil to resist applied shear stresses. An objective of incorporating soil reinforcement is to absorb tensile loads, or shear stresses, thereby reducing the loads that might otherwise cause the soil to fail in shear or by excessive deformation. ..."*

Different projects of research on reinforced soil structures have been conducted in the past. A large number of research results gained from large scale laboratory and in situ field tests are nowadays available to the scientific society. The first geosynthetic reinforced soil structures were constructed in France (Leflaive 1988, Leclercq et al. 1990). Leflaive (1988) and Leclercq et al. (1990) e.g. reported on the long-term durability observed for a polyester geosynthetic

reinforced soil structure. In the German region, Bauer (1989), investigated the bearing capacity of a two layered geosynthetic reinforced soil structure by utilizing laboratory model tests. Nimmesgern (1998) inserted a large scale biaxial testing device to investigate the stress-strain behaviour of a multi-layer reinforced sand body. Bussert (2006) performed model and large scale in situ tests to consecutively develop a design concept based on the energy theorem for reinforced soil structures.

The NHI (2008),USA, provides a detailed overview of case histories with respect to geometry, reinforcement type, backfill material and wall facing. Twenty geosynthetic wall case histories are presented. These case histories cover a variety of wall heights, surcharge conditions, foundation conditions, facing types and batter, reinforcement types and stiffness and reinforcement spacing. Most of the reinforced soil structures performed well for the last twenty years with low tensile reinforcement strains and minimum deflections (NHI 2008).

The following conclusions can be drawn from these investigations: The overall stress-strain behaviour is improved by reinforcing the soil structures with geosynthetics which can be verified by researches done decades ago (Ingold 1982). The measured tensile strains $\varepsilon_{tensile}$ of the investigated granular reinforced soil bodies differ between 0.2 to 2.0 %. The maximum tensile strains $\varepsilon_{tensile,max}$ and therefore the maximum tensile force $F_{tensile,max}$ distribution in the reinforcement of a soil structure have been observed by several researchers (Lee 2000, Allen and Bathurst 2002). A trapezoidal envelope is proposed for the geosynthetic wall case studies. In this envelope the ratio of the maximum reinforcement load T_{max} in a layer divided by the maximum reinforcement load for all layers T is plotted against the depth z of the layer plus surcharge height S normalized by the total wall height H plus the average surcharge height H $((z+S)/(H+S))$.

Furthermore it can be stated that most of the different reinforcement materials exhibit time dependent behaviour over their operational time ($\varepsilon_{creep} \sim 0.2$ %). Geosynthetics made out of linear polyester (PET) react least due to time respectively creeping mechanisms. Creeping effects estimated in the laboratory correlate to the in situ field measurements although stress relaxation effects in the reinforcement may also occur in a reinforced soil structure (Müller-Rochholz 2004, NHI 2008).

Laboratory testing and measurement techniques are continuously improving. Different kinds of testing devices have been developed to especially investigate the soil reinforcement interaction.

Numerical studies on reinforced soil structures have also been performed in the last years. In particular Finite Element Method (FEM) simulations have not only

been utilized to back calculate but also to design construction projects and make it possible to describe the macroscopic load displacement behaviour of the reinforced soil structure very well. To understand the mesoscopic load transfer mechanisms occurring in reinforced soil structures during loading, researchers started to utilize numerical mesoscopic Discrete Element Methods (DEM) simulations.

1.2.2 Soil geogrid interaction

In this chapter the macroscopic and mesoscopic soil geogrid reinforcement interaction is described. Some researchers (Ingold 1982, Ruiken 2009) investigated the continuous compounded material "reinforced soil" by conducting large scale biaxial and triaxial tests. Different concepts such as the anisotropic cohesion concept or the enhanced confining pressure concept worked out at the Laboratoire Central des Pont et Chaussees and the New South Wales Institute of Technology have been developed to describe this homogeneous reinforced material (Ingold 1982).

In addition the author of this thesis strictly differs between the reinforcement material and the surrounding granular soil, macro- and mesoscopically, and describes both discrete materials and their interaction separately.

The soil geogrid interaction is of paramount importance for the design and the performance of reinforced soil structures. The interaction behaviour depends on the geometry and mechanical properties of the reinforcement and the surrounding soil. Therefore, different types of laboratory tests but also theoretical work has been developed in order to improve the understanding of the discrete soil geosynthetic interaction (Dyer 1985, Aydogmus 2006, Liu et al. 2008, Palmeira 2009).

Palmeira (2009) presents the state of the art with regard to the fundamental understanding of macroscopic soil reinforcement interaction. Different failure mechanisms occurring in specific zones lead to different interactions between the backfill material and the reinforcement. First, the classical shear interaction mechanism between reinforcement and surrounding soil within a reinforced soil structure is characterized. The interaction behaviour is divided into interfriction and interlocking (passive resistance) effects (NHI 2008). If the soil reinforcement interaction is too low the reinforced soil structure will fail. Classical tests such as direct shear tests (Jewell 1981, Bergado et al. 1993) are carried out to determine an interaction respectively interface shear strength coefficient R_{inter}.

If the soil reinforcement interaction is strong enough, a second failure might occur. The reinforcement is going to be strained until its maximum tensile force T_{max}. A tensile strength failure occurs in the geosynthetic reinforcement and the reinforced structure fails. Tensile strength tests are conducted to estimate the short time tensile strength of the geosynthetic. The long time design tensile strength depends on the lifetime of the structure because of the creeping effects of the polymer material, the installation procedure and the compaction process, the surrounding soil properties and the forces acting on the soil structure.

Another third failure mode describes a situation where shearing takes place in a specific angle to the reinforcement. Direct shear tests where the reinforcement is inclined to the shear plane are utilized to investigate this failure mode. In another failure, the reinforcement might be pulled-out. In this case classical pull-out tests (Bergado et al. 1992 and 1994) are applicable to investigate the soil reinforcement interaction behaviour. It is well known that all these tests have limitations due to the actual conditions in a reinforced soil structure (Palmeira 2009).

The fairly complex soil reinforcement interaction becomes even more extensive in the case of investigating the mesoscopic granular soil and the discrete geogrid interaction.

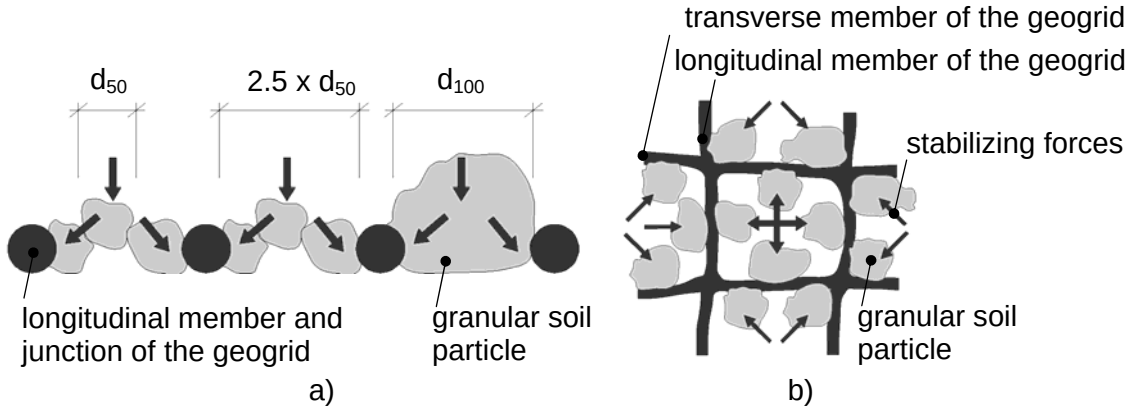

Fig. 1: Granular soil particle geogrid interaction: a) ideal particle size with respect to the gaps between the longitudinal and transverse members and junctions (cross section) b) grid structure stabilizing the granular particles (top view) (modified figure according to Izvolt & Kardos 2010).

The assumption that soil particles are fixed in between the gaps of the transverse members of the geogrid while the reinforcement itself moves is certainly unrealistic. It is a matter of fact that, the relative size of the soil particle with respect to the transverse member thickness of the geogrid will influence the interaction which has been investigated in a series of pullout tests (Palmeira et al. 1989). The higher the ratio of the transverse member thickness of the geogrid

versus soil particle diameter is, the better is the geogrid reinforcement soil interaction behaviour.
Another important aspect of the interaction between soil and geogrid is the effect of the opening size, respectively the distance between the transverse members of the geogrid. The discrete interaction between the transverse members of the grid and the surrounding soil has been investigated by photo-elastic studies for three decades (Dyer 1985). The results show that by reducing the distance between the transverse members discrete non-uniformities in the distribution of bearing loads among transverse members might occur. This non-uniform load distribution is the result of the highly discrete behaviour between granular soil and grid-reinforcement (Dyer 1985).

The ideal interaction between granular soil particles and discrete reinforcement evolves in the case of installing a geogrid with a mesh size from 2.5 (Izvolt & Kardos 2010) to 3.5 (Sarsby 1985) the diameter d_{50} of the granular particle. The diameter d_{100} of the granular particle should not be bigger than the gaps between the longitudinal and transverse members of the reinforcement (Figure 1).

A series of large scale direct shear tests to investigate the soil and the polyethylenterephthalat (PET) geogrid reinforcement interaction behaviour were conducted by Liu et al. (2008). The investigations show that the interface shear strength coefficient R_{inter} between soil and geogrid is generally smaller than the soil to soil shear strength. In addition, Liu et al. (2008) state that the soil geogrid interface value is usually higher than the value resulting out of soil geotextile interaction. The interface shear strength coefficient R_{inter} for granular soil geogrid interaction ranges between 0.89 and 1.01.

Large scale direct shear tests have been utilized at the Institute of Soil Mechanics and Foundation Engineering, Graz University of Technology performed with gravel and a PET geogrid and have shown that the interface shear strength coefficient R_{inter} can also reach values above 1.0 (Chapter 3).

The skin, respectively surface friction of the geogrid reinforcement material and the granular soil particles, further influence the granular soil reinforcement interaction. The higher the skin or surface friction of both materials, the better is the interaction behaviour and finally the overall behaviour of reinforced soil structure.

Finally it has to be stated that some geosynthetics used as reinforcing materials such as geogrids additionally add complex problems due to their time and strain rate dependent behaviour. Still, the soil reinforcement interaction behaviour is an unsolved scientific problem (Palmeira 2009).

1.2.3 Design concepts

Researchers have put a lot of effort in inventing or even advancing different design concepts for reinforced soil structures. In principle there are three main design methods available (Koerner 1998).

Design by costs and availability was performed in the early days and is nowadays no longer state of the art. When dealing with public agencies it is common to design by specification. Therefore defined mechanical properties are predefined listed for geosynthetics in association with application categories (NHI 2008).

Design by function is the state of the art design practise for international construction projects with soil reinforcement. According to this concept a factor of safety is calculated by dividing the tested properties of the reinforcement material by the required properties. In case of soil reinforcing the tested tensile strength of the geogrid is divided by a calculated required tensile force in the geogrid layer (Sarsby 2007).

The scientific society is quite aware of the conservative design results by using such concepts. For that reason researchers developed innovative design concepts to take the reinforced soil structures deformations into account (Bathurst et al. 2005, Bussert 2006, NHI 2008). Bussert (2006) e.g. utilizes the energy theorem to analyse not only the ultimate limit state but also the serviceability limit state of a geosynthetic reinforced soil structure. The NHI (2008) proposes the K-stiffness method developed by Bathurst et al. (2005) when designing geosynthetic reinforced soil structures.

1.2.4 Construction recommendations

Only a few scientists have researched on construction recommendations for reinforced soil structures (NHI 2008). The lack of knowledge in that field of research is partly filled by the National Highway Institute, US (NHI). The NHI (2008) notes 14 bits of advice relating to the installation procedures of reinforcement materials. They mark out the preparation and excavation of the designed grade, the cutting, rolling, overlapping and covering of the geogrid reinforcement liners and the installation of the dumping material depending on its thickness and dumping direction. The construction process of reinforced soil structures is still an open issue due to the lack of research.

1.3 Case Study: reinforced soil structure B114, Austria

This chapter presents a case study in Austria. The previously described concepts and recommendations on reinforced soil structures (chapter 1.2) were compared and validated during the design and construction process of the project highway B114 from Trieben to Sunk.

As pointed out in chapter 1.1, without the use of geosynthetic reinforcement, in most cases geogrids, many road construction projects around the world would not have succeeded outstandingly. An impressive example for a geogrid reinforced soil structure used to build up a highway in a geological complex surrounding is the B114 highway in Austria from Trieben to Sunk. Up to 35 m high and 70 degrees sloped geogrid reinforced embankments over a distance of 3.5 km have been constructed to connect two existing highways in upper Styria, Austria (Lackner 2008, Alexiev et al. 2010, Hippacher et al. 2009).

1.3.1 Geotechnical project information

The B114 highway is an important connection between motorway A9 in Upper and the highway S36 in Lower Styria, Austria. On average 2000 vehicles pass the road per day, out of nine percent being trucks. It was permitted to obstruct traffic flow during the construction of the new highway from 2006 till 2008. Therefore, the new road has been built on the opposite side of the steep valley. The average building costs were calculated with 21 Million Euros (Lackner 2008).

The 3.5 km long highway has been divided into seven geotechnical zones. The geologically most endangered area has been defined as zone 3. Geologically, this zone is composed out of coarse grain dominated slope debris which is interrupted by aquiferous fine grain dominated slope debris. The constructive design of the geosynthetic reinforced embankment and the stabilising procedures have already been published in the last years (Lackner 2008, Alexiev et al. 2010, Hippacher et al. 2009).

Shotcrete and 12 m long IBO anchors have been utilized to cover the successive excavation due to the massive footing of the geogrid reinforced embankment. A reinforced concrete plate has been constructed as a massive footing of the embankment. To prevent a slip failure of the footing two 16 m long GEWI anchors have been installed into the solid rock mass. The construction sequence of the green faced geosynthetic reinforced embankment has been performed state of the art and is described in Hippacher et al. (2009), Lackner (2008) and Alexiev et al. (2010).

1.3.2 Soil geogrid interaction

The soil geogrid interaction behaviour has been of high importance for this project. In order to ensure an ideal interaction (Sarsby 1985, Rüegger & Hufenus 2003, Izvolt & Kardos 2010) between the coarse grained (d_{grain} = 32 - 63 mm) backfill material and the geogrid reinforcement a specially tuned geogrid has been produced. A linear polyester (PET) woven geogrid with an opening size of 70 mm has been installed to ensure an interaction coefficient $\alpha \geq 0.9$, tested in the large scale direct shear box. The positive interlocking effects between the flexible and coarsely meshed geogrid reinforcement and the coarse grained backfill material have been visible on the building site.

1.3.3 Design concepts

As pointed out in chapter 1.2.3, design by function is the state of the art design concept. This main function in case of designing the reinforced soil structure for the project B114 was reinforcing.

According to the concept of design by function, the factor of safety is calculated by dividing the allowable tested tensile strength properties after ÖNORM EN ISO 10319 (2008) of the material with the required tensile forces in the reinforcement calculated for the ultimate limit state. The required properties have been computed and validated by two different methods. Conventional external and internal ultimate limit state analyses have been performed with analytical slope stability software (GGU Stability V.10) and the K-stiffness method proposed by the NHI (2008). These results have then been compared (Table 1) to those results gained from numerical finite element analysis (Lackner 2008).

Table 1: Results of the different calculation methods

Caculation method	Factor of safety *FS*	Force geogrid T_{max}
Bishop	1.84	19 [kN/m]
Janbu	1.78	18 [kN/m]
K-stiffness	1.94	11 [kN/m]
FEM	1.72	15 [kN/m]

The numerical simulations present the factor of safety by performing a φ - c reduction. The friction angle φ and the cohesion c are reduced until the soil body collapses. Forces in geogrids and anchors and the deformation of the embankment during the construction process are calculated. Therefore the computed factor of safety has been investigated regarding the numerical mesh dependency (Lackner 2008).

Three-dimensional effects have also been implemented in the two-dimensional model. By comparing the maximum expanse of the excavation in three dimensions, just before failure, with the maximum percentage of the excavation in two dimensions, a two dimensional pre-relaxation factor (m_{stage}) has been evaluated. The analytically calculated factors of safety and those from the numerical φ - c reduction correlate well. The failure mechanism has been comparable.

Still it has to be stated that the numerical simulation itself detects the more critical failure mechanism, which results in a slightly lower factor of safety (Lackner 2008).

The results of the numerical design methods have been validated by the measured displacements in situ on the building site. Inclinometers, GPS and surface measuring points have been utilized to monitor the building site before, during and after the construction process (Feiertag 2009).

The results of measurement and computation show sound agreement. Nevertheless it has to be stated that there are limitations. The performed conventional analyses deliver factors of safety without taking into account the deformation behaviour of the reinforced soil structure. In case of utilizing macroscopic numerical simulations such as the presented Finite Element Method the discrete geogrid and granular soil interaction behaviour cannot be simulated in detail.

1.3.4 Construction recommendations

The construction process of reinforced soil structures is generally important and influences the overall load displacement behaviour of the structure (NHI 2008, Rüegger & Hufenus 2003). To obtain the ideal interaction between geogrid reinforcement and granular backfill material, the conscientious installation of the geogrid and the intensive but also homogenous compaction of the backfill layers are of high importance.

By installing the geogrid reinforcement on the backfill layer it has been categorical important to strain the geogrid immediately. Every single wrinkle in the reinforcement can cause local deformations in the case of loading the structure. The importance of this effect will to be shown in the next chapters.

As only few researchers focus on construction recommendations there are still a lot of open issues to be clarified.

1.4 Open issues

As already pointed out in the previous chapters there is still a urgency to improve the fundamental understanding of reinforced soil structures. The requirements to geogrid reinforced soil structures are increasing rapidly. As opposed to conventional road construction methods, reinforced soil structures sometimes do not behave strongly and stiffly enough. Developing and validating a system to easily increase the bearing capacity of the geogrid reinforced soil structures and to improve their deformation behaviour is of course an important research task.

Working out a concept for optimal construction methods of reinforced soil structures and scientifically validating this concept by macroscopic experimental and numerical investigations is therefore a valid research topic and the objective of this thesis.

In order to successfully work out that practical task a fundamental mesoscopic understanding of the soil geogrid interaction behaviour has to be gained by utilizing mesoscopic experimental and numerical investigations.

It is of importance to work out practical and mechanically sound design methods and construction recommendations to finally construct improved reinforced soil structures on the building sites.

1.5 Methodology and outline of the thesis

The flowchart of Figure 1 describes the general methodology of this thesis. The objective of the thesis is verbalized on top of the flow chart. It is pointed out that a detailed literature review is important to work out practical and innovative concepts.

In chapter 2 the innovative concept of prestressed reinforced soil (PRS_i) is introduced. A literature review on PRS_i will point out the need for further research on that topic (Tatsuoka et al. 1997, Shinoda et al. 2002, Lovisa et al. 2009).

Experimental investigation methods to validate the concept of PRS_i are presented in chapter 3. Large scale static, path-controlled load displacement tests have been utilized to investigate the macroscopic load displacement behaviour of different reinforced soil structures.

By using photogrammetric methods (PIV), the mesoscopic soil geogrid interaction can be investigated in detail. Experimental results based on cyclic

load displacement (LD) tests are presented in this chapter to further validate the concept of PRS_i macroscopically and to gain a detailed mesoscopic insight in the bonded soil structure by using PIV analysis.

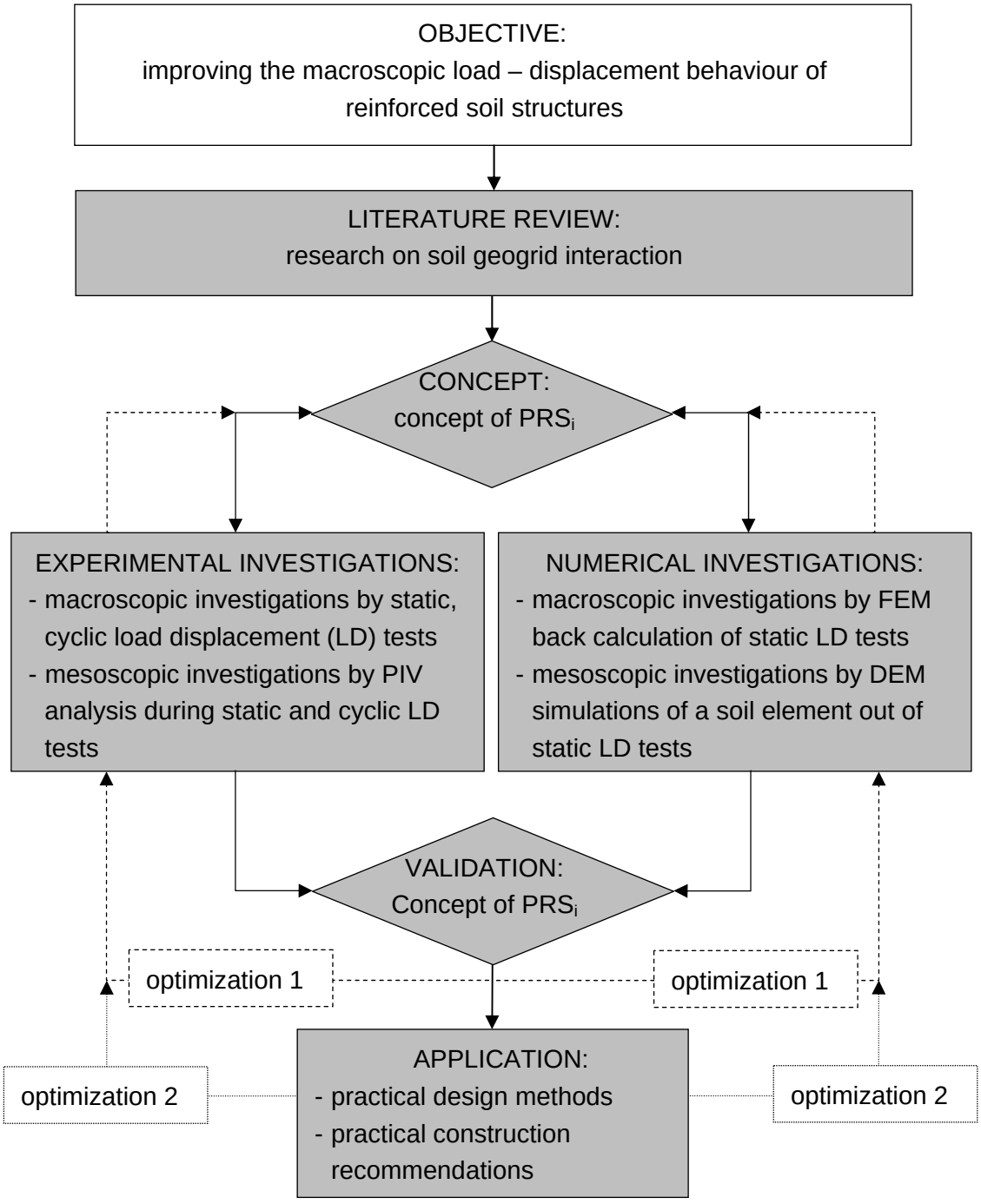

Fig. 2: Flow chart: methodology of the thesis.

In chapter 4 results from numerical investigations on PRS_i are presented to macroscopically validate the concept described in chapter 2. Finite Element simulations (FEM) have been utilized to research on the load displacement behaviour of the large scale static load experiment described in chapter 3 and to further validate the force distribution in the geogrid reinforcement.

Mesoscopic Discrete Element Method (DEM) analyses have been performed to analyse the soil geogrid interaction behaviour. The results are compared with the mesoscopic PIV analysis results shown in chapter 3.

In chapter 5 analytical building site design methods for reinforced soil foundations and reinforced soil walls are presented and practical construction recommendations for different kinds of applications for PRS_i are described. The design methods presented have been developed from existing concepts (Sharma et al. 2009, Lawson et al. 2008). The construction recommendations given have been established under technical, economical and practical issues.

In chapter 6 the most important research results on prestressed reinforced soil structures are highlighted. Conclusions out of the macroscopic and mesoscopic experimental and numerical results are drawn to finally summarize the concept, design and construction recommendations of PRS_i.

The closing outlook presents visions and recommendations of the author for further research activities in the field of prestressed reinforced soil structures.

2 Introduction to the concept of prestressed reinforced soil (PRS_i) by geogrids

2.1 Introduction

As pointed out in Chapter 1, requirements to reinforced soil structures have been increasing constantly. In contrast to conventional road construction methods reinforced soil structures sometimes do not behave robust respectively stiff enough. Developing concepts to easily increase the bearing capacity of the geogrid reinforced soil structure and coevally improve its stiffness is therefore an important research task and the aim of this thesis.

The concepts introduced in this Chapter have already had some requirements from the start. Of course the major objective has been to improve the macroscopic load displacement behaviour of the geogrid reinforced soil structure. Nevertheless, a further important demand has been the artless, simple and cost effective construction and implementation of the innovative concepts on the building site.

2.2 Literature review: prestressed reinforced soil

2.2.1 General information

Sparse relevant research work has been done and may be mentioned later after reviewing literature referring to concepts of prestressed geogrid reinforced soil structures (Tatsuoka et al. 1997, Shinoda et al. 2002, Lovisa et al. 2009, Lawson & Yee 2008).

2.2.2 Prestressing the reinforced soil structure

The Japanese system of preloaded and prestressed reinforced soil structures (Tatsuoka et al. 1996a, 1996b, Uchimura et al. 1996 Tatsuoka et al. 1997, Shinoda et al. 2002) was developed in 1997. According to this method the geosynthetic reinforced soil structure itself is preloaded, respectively prestressed perpendicular to the horizontal reinforcement layers. Prestressed anchors and

huge concrete plates are installed and mobilized to apply preloading forces into the geosynthetic reinforced soil structure, basically bridge abutments.

2.2.3 Prestressing the reinforcement in the soil structure

Lovisa et al. (2009) conducted laboratory physical model tests and finite element analyses to study the behaviour of a prestressed geotextile reinforced sand bed supporting a loaded circular footing. The results of the experimental and numerical investigations show that the implementation of prestress into the geotextile reinforcement significantly improves the settlement response and load-bearing capacity of geosynthetic reinforced soil (Shukla & Chandra 1994).

Lawson & Yee (2008) deal with reinforced soil structures, in detail segmental block reinforced soil walls with constrained reinforced fill zones. In order to constrain the reinforced fill zone, the geogrid reinforcement has been connected to low capacity anchors which are drilled and fixed into a rigid quartzite fixed zone. The innovative concept of constraining the geosynthetic reinforced fill zone results in saving a considerable amount of geosynthetic reinforcement material.

2.3 Prestressed reinforced soil (PRS_i) using geogrids

The concept of an innovative system called prestressed reinforced soil (PRS_i) developed at Graz University of Technology to increase the bearing capacity of the geogrid reinforced soil structure and additionally improve its load-displacement behaviour is presented later in this Chapter.

Prestressing the geogrid reinforcement in its axial direction is the main idea of the concept of PRS_i. By investigating the tensile material properties of most of the geogrids available on the market, it is visible that their tensile load strain behaviour is highly nonlinear. Especially when installing a geogrid on the building site, the tensile stiffness of the geogrid reinforcement is quite low until the tensile strains in the reinforcement increases during the compaction process. During compaction the geogrid is strained and tensile forces in the reinforcement are activated. The strain ratio of the geosynthetic reinforcement is still unknown and as a result the tensile stiffness of the reinforcement material cannot be defined.

To point out the nonlinearity of the geosynthetic reinforcement and to visualize the different load activation phases in the geosynthetic, the tensile load strain

behaviour of the reinforcement material has been investigated by conducting 20 modified tensile tests after ÖNORM EN ISO 10319.

The modifications to the tensile tests relating to ÖNORM EN ISO 10319 result in a reduction of the testing velocity to a value v_{test} = 0.5 mm/s and an initial, non prestressed start of the load deformation measurement. In principle the code recommends a prestrain ratio $\varepsilon_{prestrain}$ = 1 % in the geogrid reinforcement material just before starting the tensile tests.

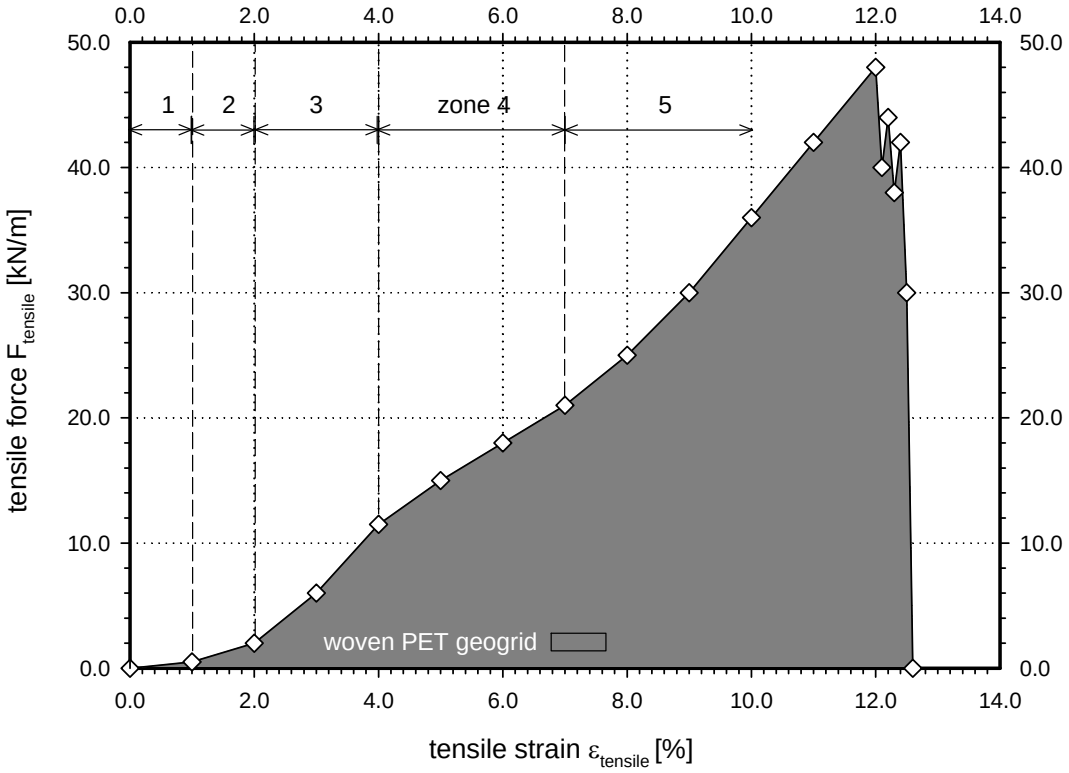

Fig. 3: Typical tensile load-strain distribution of a woven PET geogrid reinforcement material during a modified tensile test according to ÖNORM EN ISO 10319.

In order to monitor the geogrid under realistic building site conditions no initial prestress has been applied to the reinforcement material. Figure 3 shows the load strain distribution of a typical reinforcement material. A biaxial woven linear polyester geogrid described in Chapter 3 has been investigated in detail. As a matter of course, the preparations of the geogrid reinforcement and the testing conditions comply with ÖNORM EN ISO 10319.

The geogrid tests specimen reinforcement material has been prepared with a length $l_{geogrid}$ = 0.2 m and a width $w_{geogrid}$ = 0.2 m. In a specially designed installation device the geogrid has been fixed into clamps with a distance l_{test} =

0.1 m. To ensure reproducible results the clamps have been screwed continuously with a dynamometric key until a defined moment of a torque has been reached.

The results have been produced under constant laboratory conditions. The testing temperature T_{test} ranged between 23.3 and 24.1 °C and the relative air moisture AH_{test} has been measured during the testing period from 37.6 to 39.5 %.

The plotted tensile load strain behaviour (Fig. 3) is highly nonlinear, especially under initial non-prestrained conditions (Fig. 3, zone 1 = building site effect). This nonlinearity results from the initial undulated shape of the geogrid reinforcement just after installation.

The installed geosynthetics show particularly these effects at the building site. In zone 2, the longitudinal members of the reinforcement material are strained primarily. The single fibres in the longitudinal members of the geogrid arrange themselves by translation and rotation until a compact, homogeneous string is formed (longitudinal member hardening effect).

In case of tensioning the compact longitudinal string (zone 3), the maximum tensile stiffness properties *EA* can be reached. These tested properties are closely related to the material properties (material property effect).

By further tensioning the reinforcement, a constriction of the geogrid can be observed. This effect leads to a slow activation of the transverse members of the reinforcement material which finally results in a slight decrease of the tensile stiffness properties (zone 4 = constriction effect and transverse member hardening effect). The effect of constriction generally does not occur at the building site. In most of the road construction projects reinforced soil structures with extreme elongations in the third dimensions are built.

After the activation of the transverse members of the geogrid the tested tensile strain properties *EA* of the reinforcement again correlate with the mechanical material properties (zone 5).

As already mentioned in Chapter 1, the time dependent behaviour of most of the geogrid reinforcement materials available on the market is a matter of fact (NHI 2008). Depending on their raw materials geogrids tend to time dependent behaviour. One limitation of the presented prestressing concepts PRS_i could be that creeping strains, occurring over time release the initial prestress of the geogrid. If the prestress in the geogrid decreases, the tensile stiffness *EA* of the geogrids decreases according to Figure 3.

The reinforcement material has to be tested with respect to creep effects, to ensure the positive effects of the concepts of prestressed reinforced soil. The

creeping strains ε_{creep} of the tested PET woven biaxial geogrid are low according to Müller-Rochholz (2004). Müller-Rochholz (2004) has tested the creep behaviour of the PET yarns of the geogrid reinforcement for 10^4 h. In the potential prestress strain range ε_{PRSi} between 0 to 4 % the strains relating to creep ε_{creep} vary between 0.1 and 0.4 % after 120 years.

Detailed information about the material properties of the woven PET geogrid is given in Chapter 3.

Another important influence on the concept of PRS_i is the interaction between geogrid reinforcement and the granular soil particles.

As described in Chapter 1, the geogrid interacts with its surrounding soil particles by interfriction and interlocking effects. Figure 4 shows the interaction behavior in detail with respect to the concept of PRS_i.

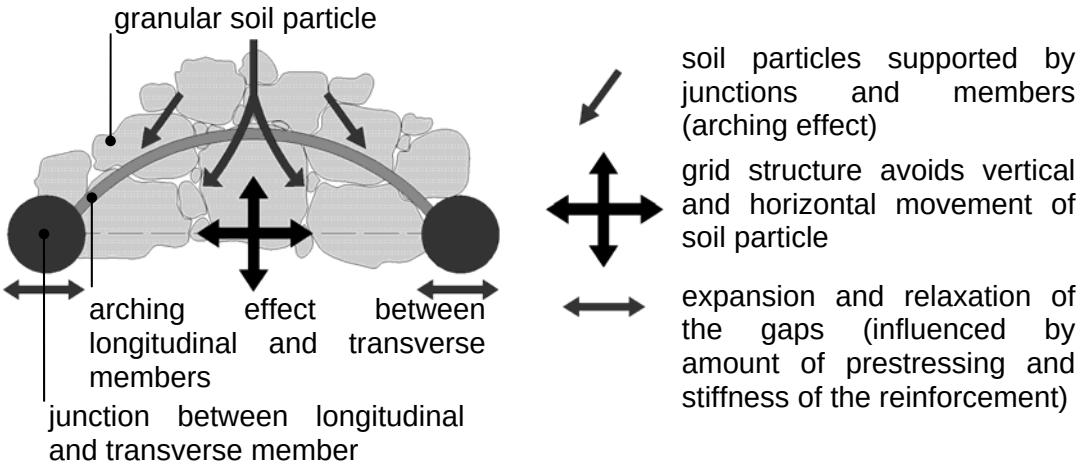

Fig. 4: Interaction behaviour of the granular soil particles and the geogrid reinforcement: a) load transfer from soil particles to transverse and longitudinal members and junctions by arching effect b) caption for the load transfer mechanism (modified figure according to Izvolt & Kardos 2010).

Loads acting on a reinforced soil structure are transferred by arching effects from the granular soil particles to the transverse and longitudinal members and junctions of the discrete geogrid reinforcement. The arching effect is thereby highly influenced by the capability of the expansion respectively relaxation of the gaps between the members of the reinforcement. The stiffer the members and junctions behave the higher the bearing capacity of the arch between the members of the geogrid.

In addition the soil reinforcement interaction improves if the geogrid reinforcement is able to fit in and arrange itself properly around the soil particles to avert voids in the soil structure. In other words, the installation of very stiff geogrids may lead to negative interaction effects.

As already described in Chapter 1.2.2, the tensile stiffness of the geosynthetic material increases due to an applied prestress to the geogrid reinforcement. Pressure forces may be transferred into the granular soil structure by temporarily prestressing the members of the discrete geogrid reinforcement.

The following three different methods have been developed to prestress the geogrid reinforcement in a reinforced soil structure:

- Prestressed reinforced soil by compaction: PRS_c
- Permanently prestressed reinforced soil: PRS_p
- Temporarily prestressed reinforced soil: PRS_t

The three different methods of prestressed reinforced soil (PRS_i) are presented in detail subsequently.

2.3.1 Prestressing as a result of compaction (PRS_c)

Prestressing in the geogrid due to compaction of the overfilled granular soil layer (PRS_c) can be achieved by using spreading stresses τ_{spread} acting between soil and the geogrid reinforcement (Lackner et al. 2012).

Rendulic (1938) already showed the horizontal and vertical earth pressure distribution on the surface of an embankment with a horizontal base in the late thirties of the last century.

During compaction of a dumping strip, loads affect the reinforced soil layer as described by Rendulic (1938). Compaction leads to a lateral spreading of the loosely dumped compaction strip. As a result lateral stresses develop on the base of the dumped soil and thereby the axial forces in the geogrid reinforcement layer increase (Lackner & Semprich 2009 and 2010).

At the bottom of the soil layer where the geogrid reinforcement is usually installed, spreading stresses τ_{spread} reach their maximum. A local maximum tensile force T_{max} in the geogrid develops due to interaction effects between soil

and the geogrid reinforcement. Thereafter, the tensile stiffness *EA* of the reinforcement increases as explained in Chapter 2.3.

As a result of increasing the tensile stiffness of the geogrid, the load displacement behaviour of the reinforced soil structure is improved.

Figure 5 schematically shows the behaviour of the prestressing as a result of compaction.

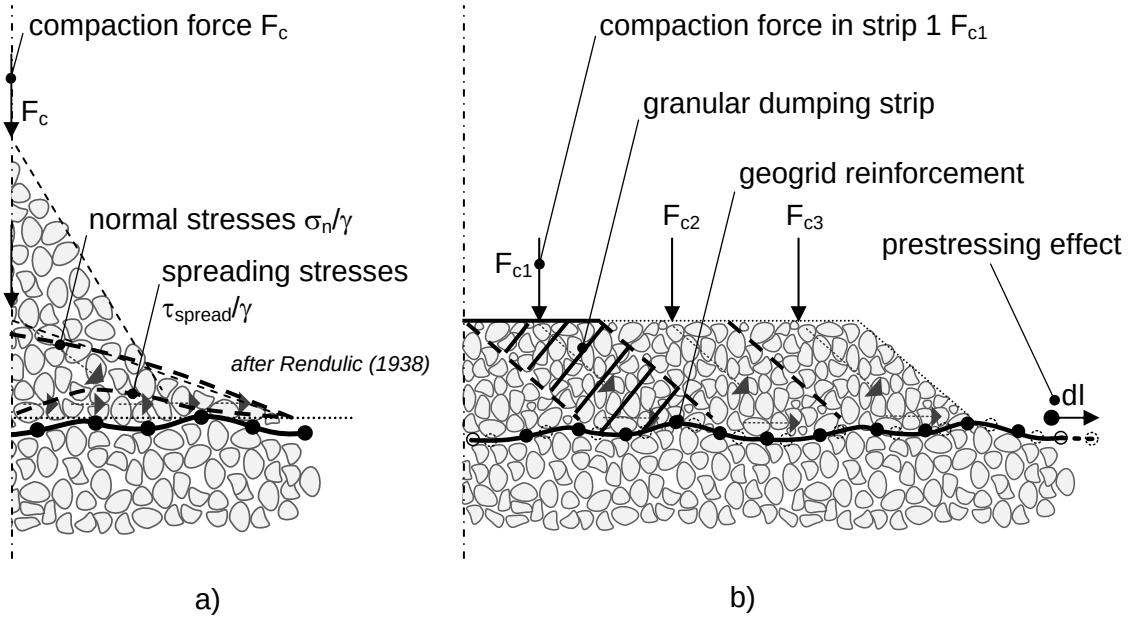

Fig. 5: Prestressed reinforced soil by compaction (PRS_c): a) concept to constitute spreading stresses τ_{spread} during compaction b) compaction advice to prestress the geogrid (after Lackner & Semprich 2009).

Figure 5a) shows the concept to develop lateral spreading stresses τ_{spread} during compaction into the geogrid reinforcement. A possible schematic compaction recommendation is given as a sketch in Figure 5b).

2.3.2 Permanently prestressed reinforced soil (PRS_p)

The concept of permanently prestressed reinforced soil (PRS_p) is applied if the geogrid reinforcement is prestressed just before dumping the backfill material (Lackner et al. 2012). The geogrid reinforcement is fixed permanently right after the prestressing procedure. Of course permanent prestressing the geogrid (PRS_p) can be applied by various methods. During the experimental investigations (Chapter 3) the axial prestressing in the horizontal geogrid layer has been applied by hydraulic jacks.

Tensioning the reinforcement on the side in axial, mostly horizontal direction is applicable with the shovel of an excavator which also leads to a defined strain ε_{PRSi} in the geogrid (Detert et al. 2004).

The principal mechanical behaviour of the concept has already been explained in Chapter 2.3. The positive effect by prestressing permanently occurs due to the nonlinear load strain behaviour of e.g. PET geogrids. The maximum tensile stiffness of some materials occurs at axial strains ε_{axial} = 1 – 3 %. By increasing the geogrids tensile stiffness, the overall system behaviour improves consequentially.

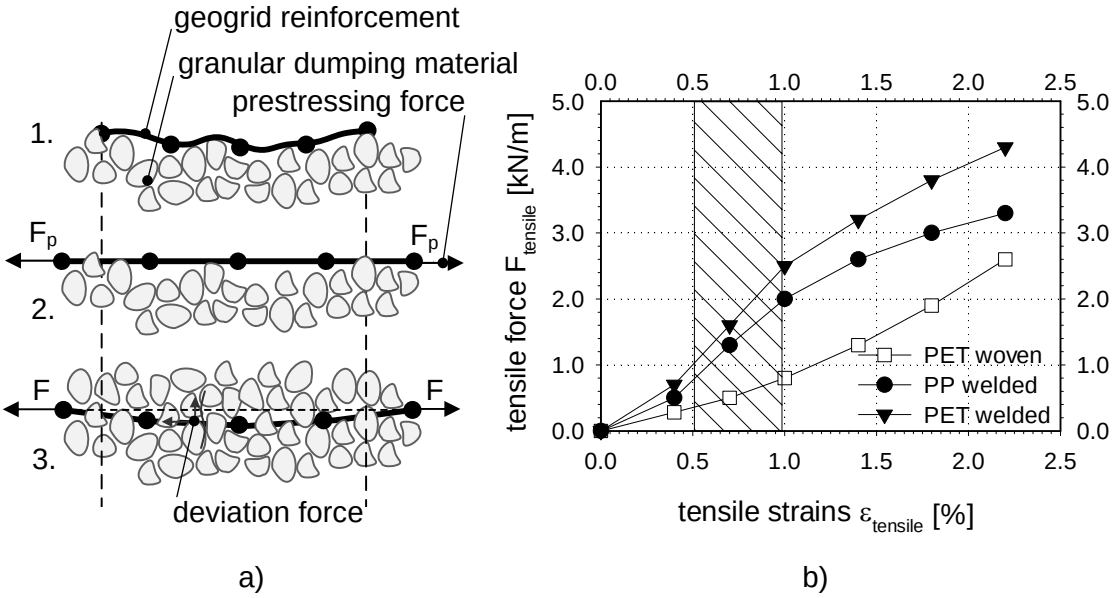

Fig. 6: Permanently prestressed reinforced soil (PRS_p): a) concept to prestress the reinforcement permanently b) non linear tensile load-strain curve to estimate the correct amount of prestressing.

An additional positive effect on the load displacement behaviour occurs by prestressing the reinforcement permanently. Higher tension in the geogrid leads to higher deviation forces in the vertical direction (Fig. 6) and a bigger bedding support supplied by the reinforcement. Figure 6a) shows the concept to prestress the reinforcement permanently. The geogrid is placed on the granular soil (step 1) prestressed with a predefined force F_p (step 2) and dumped with the next layer of granular backfill material. In Figure 6b) the principal mechanical behaviour (Chapter 2.3) is exemplarily given for three different kinds of geogrids currently available on the market. The graph (Fig. 6b) shows the tensile load-strain behaviour of two welded (PP and PET) and one woven (PET) geogrid. It is important to evaluate the actual strains in the geogrid to estimate the correct tensile stiffness *EA* of the reinforcement material.

2.3.3 Temporarily prestressed reinforced soil (PRS_t)

Especially when building up geogrid reinforced soil structures with coarse grained granular backfill materials such as gravelly materials, temporarily prestressed reinforced soil (PRS_t) is well applicable (Lackner et al. 2012). By prestressing the geogrid reinforcement right before dumping the backfill material its mesh expands and the dumped granular soil particles can easily access the gaps of the polymer longitudinal and transverse members of the geogrid during the compaction process (Fig. 7).

As already pointed out in Chapter 1, the relation between mesh size of the geogrid and the grain size of the backfill material is of utmost importance.

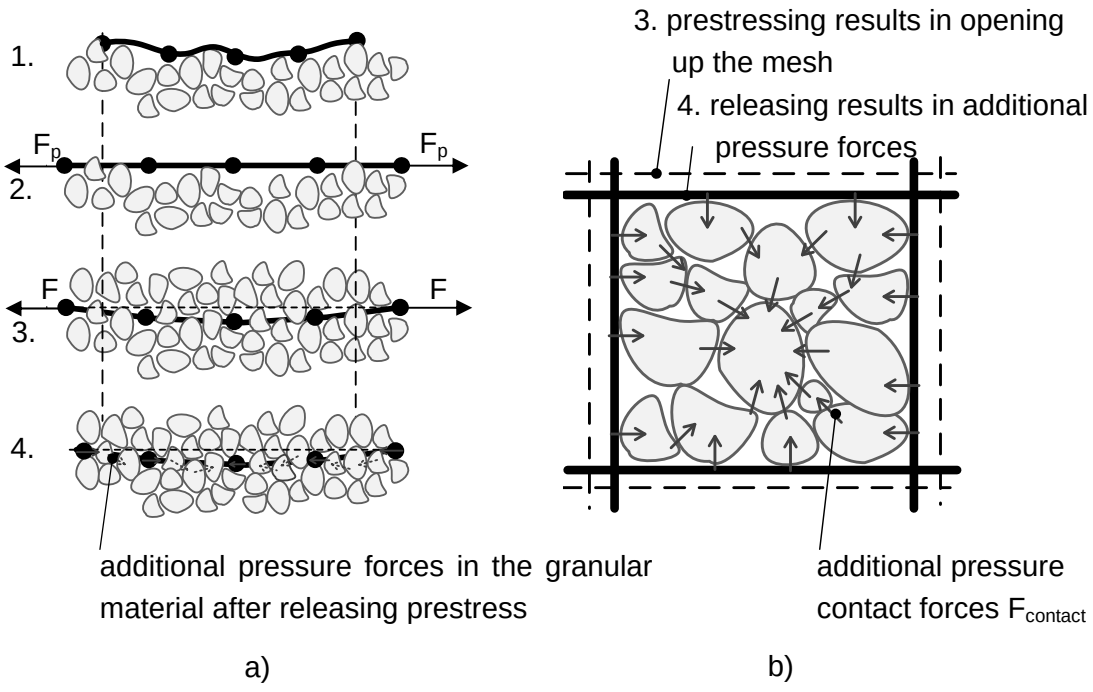

Fig. 7: Temporarily prestressed reinforced soil (PRS_t): a) concept to prestress the reinforcement temporarily b) prestressed and released mesh of a geogrid to apply additional pressure forces $F_{contact}$ to the granular soil.

Figure 7a) shows the concept of prestressing the geogrid reinforcement temporarily. After appropriate compaction of the granular soil layer, the applied temporary prestressing in the reinforcement is released and by soil geogrid interfriction and interlocking effects additional pressure forces $F_{contact}$ act on the granular particles (Figure 7b). In Figure 7b) the expansion of the mesh of the geogrid reinforcement by prestressing the reinforcement is shown.

These higher inner pressure forces $F_{contact}$ stabilize the granular soil body and thereby increase the bearing capacity of the reinforced soil structure. The additional increase of the tensile stiffness *EA* of the geogrid due to prestressing the reinforcement finally improves the general load displacement behaviour of the reinforced soil structure.

2.4 Summary and conclusions

In this Chapter concepts of prestressed reinforced soil (PRS_i) to increase the bearing capacity of the geogrid reinforced granular soil structures and to improve their load displacement behaviour have been introduced.

The Chapter has started with a literature review on reinforced soil structures where prestressing is applied. Most of the findings from the literature review have shown positive effects in the case of prestressing the reinforcement material or the reinforced soil structures themselves.

However, the need for further research on that scientific topic has been pointed out by several researchers (Tatsuoka et al. 1997, Shinoda et al. 2002, Lovisa et al. 2009, Lawson & Yee 2008). It is a major task to develop new innovative concepts to practically prestress the reinforcement, cost effectively but also scientifically sound

Moreover, detailed knowledge about the load strain behaviour of the geogrid reinforcement material to estimate the accurate tensile stiffness properties *EA* of the geosynthetic has been gained by conducting special modified tensile load tests. The test results have shown 5 zones with different load strain behaviour. To obtain the highest tensile stiffness *EA* of the reinforcement it is important to prestress the geogrid. By prestressing the geogrid and thereby increasing its tensile stiffness *EA*, the overall load displacement behaviour of the reinforced soil structure improves. The stiffer and stronger the members and junctions behave the higher the bearing capacity of the arch acting between the members of the discrete geogrid reinforcement material. Coevally, the soil reinforcement interaction improves when the geogrid reinforcement is able to fit in and arrange itself properly around the soil particles. Thereby voids in the soil structure are averted. The installation of very stiff geogrids may lead to negative interaction effects.
In order to prestress the geogrid reinforcement in the soil structure three innovative concepts have been presented and described in detail in this Chapter.

- Prestressed reinforced soil by compaction: PRS_c

- Permanent prestressed reinforced soil: PRS_p

- Temporary prestressed reinforced soil: PRS_t

These three concepts will be experimentally (Chapter 3) and numerically (Chapter 4) investigated to validate their macroscopic effects on the load displacement behaviour of the reinforced granular soil structures.

Additionally, the mesoscopic interaction between the discrete soil grains and the discontinuous geogrid reinforcement will be investigated to further improve the fundamental understanding of the mesoscopic soil reinforcement interaction process.

3 Experimental investigations on prestressed reinforced soil structures (PRS_i) by geogrids

3.1 Introduction

Experimental investigation methods to validate the concept of PRS_i (Chapter 2) are presented in this third Chapter. Static, path-controlled load displacement tests have been conducted to investigate the macroscopic load displacement behaviour of soil structures reinforced according to different concepts (Chapter 3.3). By performing Particle Image Velocimetry analysis (PIV), the mesoscopic soil geogrid interaction has been investigated in detail. Additional macroscopic experimental results based on cyclic, biaxial tests are presented to further investigate the concepts of PRS_i (Chapter 3.4). Again photogrammetrical (PIV) analyses have been utilized to gain a detailed mesoscopic insight into the geogrid reinforced soil element under cyclic loading conditions.

3.2 Literature review: experimental investigations on prestressed reinforced soil structures (PRS_i) by geogrids

3.2.1 Static load displacement experiments

Experimental investigations, especially physical model tests have been conducted in the past. The results have shown that the installation of one or more geosynthetic layers to support a shallow granular soil foundation, is effective to reduce settlements and to increase the load bearing capacity (Guido et al. 1985, 1986, Khing et al. 1993, Omar et al. 1993, Yetimoglu et al. 1994, Ismail & Raymond 1995, Adams & Collin 1997, Adams 2000, Shin & Das 2000, Sitharam & Sireesh 2004, Patra et al. 2005).

Lovisa et al. (2009) conducted laboratory physical model tests to study the behaviour of a prestressed reinforced sand bed supporting a loaded circular footing. The addition of prestress to the geotextile reinforcement results in significant improvement to the settlement response and the load bearing capacity of the foundation. The load bearing capacity at a settlement s = 5 mm in the case of performing prestressed geotextile tests approximately doubles in comparison

to the geotextile reinforced sand test without applied prestress. The amount of prestress is equal to ε_{PRSi} = 2 % of the allowable tensile strength of the geotextile. The beneficial effects of the prestressed geotextile configuration have been evident for greater footing depths.

Based on the obtained test results the following conclusions can be drawn (Lovisa et al. 2009): The addition of prestress to the geotextile reinforcement material significantly improves the overall settlement response and bearing capacity of the reinforced soil foundation. The beneficial effects of the geotextile reinforcement without applying any kind of prestress are insignificant beyond a footing embedment depth d_{foot} = 50 mm for low displacements. However, the additional prestress ε_{PRSi} applied to the geotextile reinforcement improves the settlement response s and bearing capacity for all footing depths (Lovisa et al. 2009).

To achieve the positive effects of prestressing the geosynthetic under field conditions, the geosynthetic reinforcement material should be prestressed following the laboratory method in principle and anchored in trenches surrounding the area to be reinforced before covering it with granular fill. Lovisa et al. (2009) state that the prestressing process may not be artless to simulate under field conditions. A useful method shall be developed, especially in the case of utilizing a high prestress level (ε_{PRSi} > 4 %) in the geosynthetic. However, Lovisa et al. (2009) expect that suitable practical methods of prestressing the geosynthetic under in situ field conditions will be developed in the near future.

3.2.2 Cyclic load displacement experiments

Tatsuoka et al. (1997) proposed an innovative construction method for reinforced soil structures named “Preloaded and Prestressed Reinforced Soil” method (PLPS). As opposed to Adams (1997) and Ketchart & Wu (1997) the applied preload is not removed after the construction process (Uchimura et al. 1997). A tensile prestress to tie rods fixed on bottom and top reaction concrete plates is applied by utilizing hydraulic jacks to preload the soil structure perpendicular to the horizontal geosynthetic reinforcement layers. After the construction of a geosynthetic reinforced soil structure utilizing the concept of PLPS, the bonded soil structure behaves stable and stiff against vertical static and cyclic loading (Shinoda et al. 2002). The advantages of the innovative method PLPS have been confirmed by performing small scale model tests in the laboratory (Shinoda et al. 1999) and by conducting a full scale prototype test of a reinforced soil pier for a railway bridge (Uchimura et al. 2003).

The following conclusion can be drawn from the performed research work. A significant improvement of the transient and long time performance of the geosynthetics reinforced soil pier can be seen. There is also a decrease of

deformations in horizontal and vertical directions, in comparison to a conventionally geosynthetic reinforced soil bridge abutment. It can therefore be stated that the system of PLPS is efficient against static and cyclic loads by traffic in a long term. The improved performance of the reinforced soil pier occurs due to the stiff and elastic behaviour of the backfill material achieved by the described preloading and prestressing procedure. The back calculated in situ stiffness of the geosynthetic reinforced soil structure correlates with the stiffness values predicted by laboratory stress strain tests on the backfill material. With a decrease of stiffness of the tie rods the prestress against residual compression reduces.

3.3 Static load displacement experiments on prestressed reinforced soil structures (PRS_i) by geogrids

This Chapter deals with results of 60 static, path-controlled large scale laboratory load displacement tests utilized to investigate the behaviour of 10 different reinforced soil structures. Therefore adaptable experimental testing equipment has been developed and has been fabricated with regard to homogeneous laboratory conditions.

3.3.1 Overview on the experimental investigations

The main objective of the performed experimental investigations is the validation of the static load displacement behaviour of soil structures unreinforced, conventionally reinforced and reinforced by the concept of PRS_i presented in Chapter 2 (Fig. 8).

Large scale physical model tests have been conducted in order to investigate the soil structure macroscopically. The large scale granular soil structures have been built up under laboratory conditions and represent a one meter strip of a geogrid reinforced soil structure with 3 reinforcement layers.

The embankment has been constructed as a hybrid structure. One end of the 2 m long and 1 m wide reinforced soil body is supported by a vertical wall acting as an abutment for the reinforcement (hard facing wall). The other end of the 0.45 m high structure represents a soft facing slope. Besides investigating the reinforced soil structure macroscopically, the mesoscopic soil geogrid interaction is analyzed by utilizing the PIV method (Fig. 8).

During the validation process macroscopic and mesoscopic results interact. It has to be verified that results from both investigation methods, macroscopic and mesoscopic research activities finally correlate.

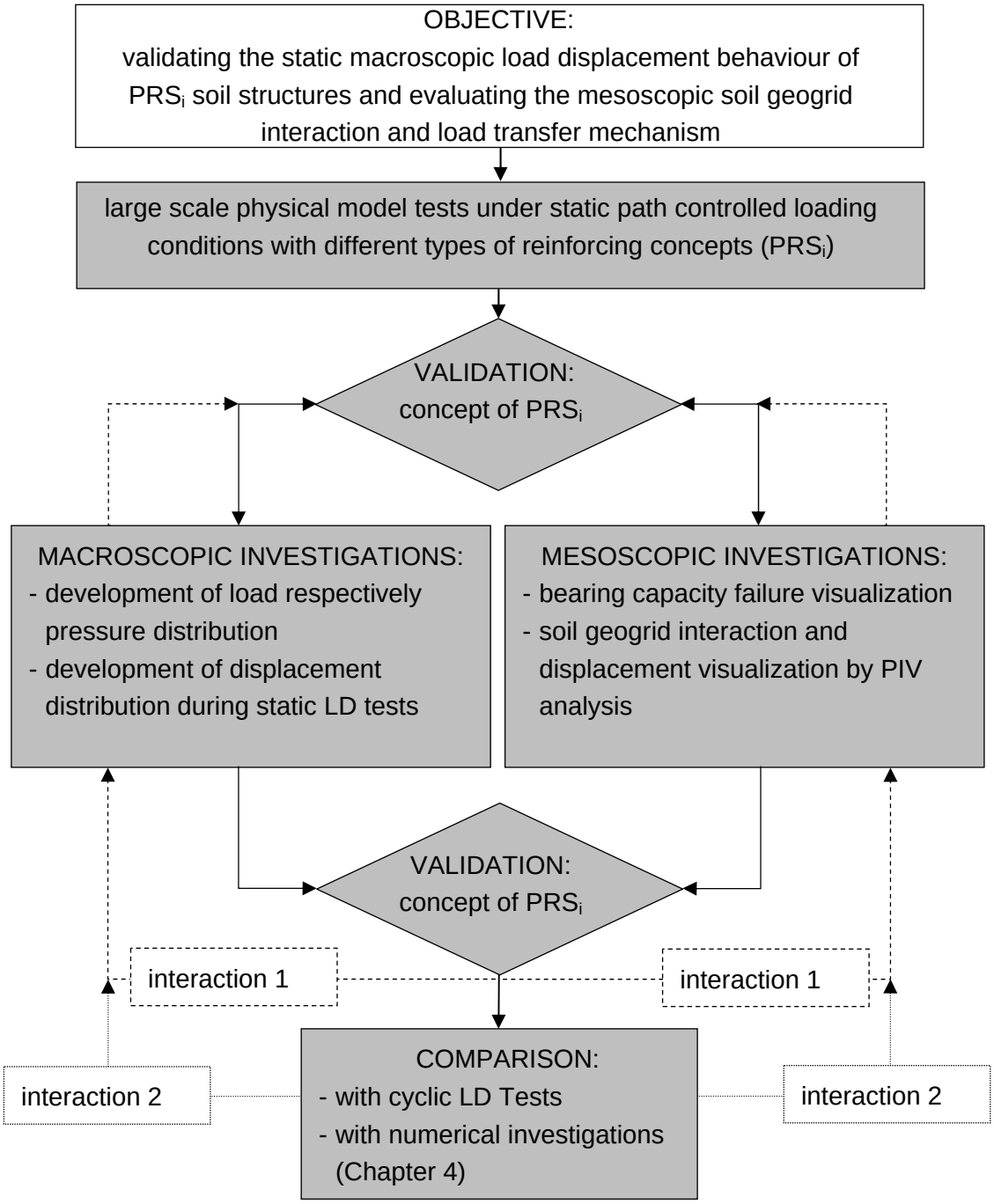

Fig. 8: Flow chart: overview on the experimental investigations.

In addition, results gained from the static large scale laboratory experimental investigations naturally interact with the produced results from conducted cyclic laboratory biaxial tests (Chapter 3.4) and the conclusion drawn after numerical investigations (Chapter 4).

3.3.2 Experimental setup and testing equipment

A 3 m long, 1m wide and 1m high experimental box (Fig. 9) surrounded by a mobile steel frame has been fabricated to investigate the behaviour of granular soil structures reinforced by different concepts described in Chapter 2.

Those geogrid reinforced soil structures are built up by three compaction layers, with a height of h_{layer} = 0.15 m each, of granular soil and polymer geogrids. Every layer consists of dumping strips. Each strip is 0.4 m long and is compacted path controlled with a compaction speed v_c = 2 mm/min until a vertical compaction force F_c = 40 kN respectively a compaction pressure p_c = 100 kN/m² is applied (Brkic 2011).

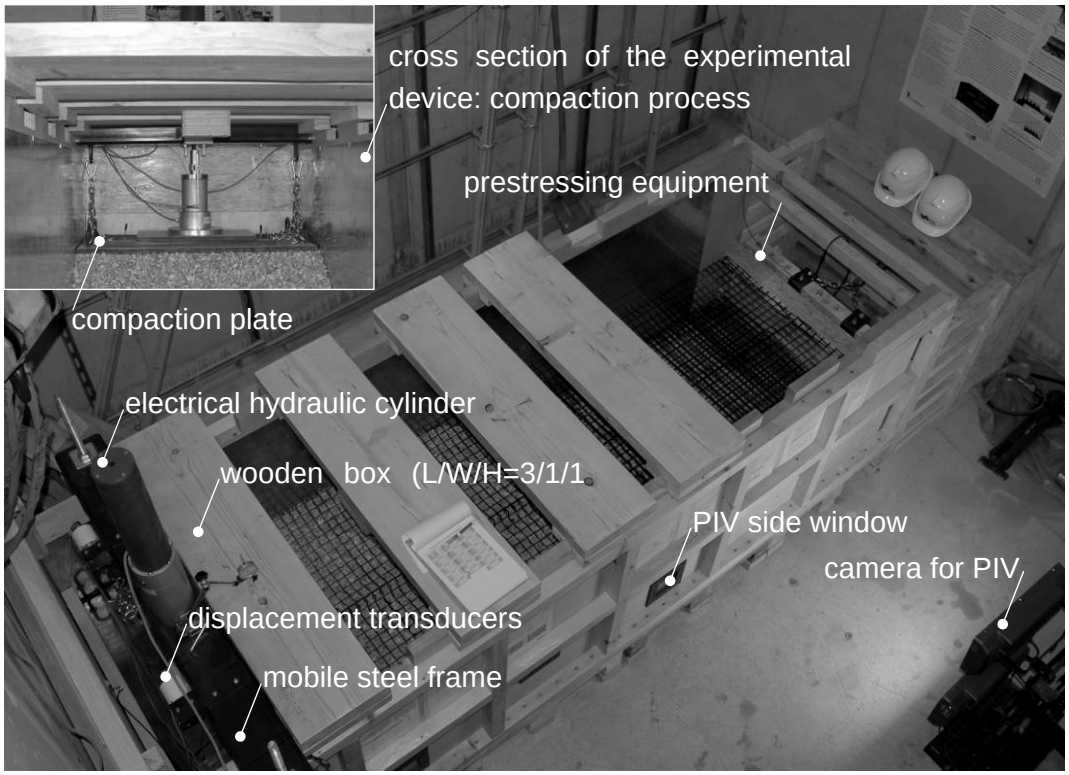

Fig. 9: Experimental testing device: wooden box (*L/W/H* = 3/1/1 m) surrounded by a mobile steel frame with an electrical hydraulic cylinder.

Therefore an automatically computer controlled electrical hydraulic cylinder with a maximum pressure force F_{max} = 50 kN and a maximum stroke s_{max} = 0.1 m is installed. Three computer connected displacement transducers are fixed on the mobile steel beam to measure deformations during the path controlled compaction and testing procedure. The hydraulic jack`s load F_c is measured by a full bridge load cell installed between the cylinder and the compaction respectively load plate. The prestressing axial to the reinforcement (ε_{PRSi} = 2.5 %)

is applied constantly over the 1 m wide geogrid by a manually handled hydraulic jack.

3.3.3 Experimental materials

The experimentally used backfill material for the bonded soil structures is a washed rounded, coarse gravel 8/16 mm, C_u = 1.43 typically for the subsoil conditions in Graz, Austria called "Murschotter". Figure 10 shows the grain size distribution of the granular material described consecutively.

The unit weight (γ_s = 26.4 kN/m³) of the gravel and the natural water content (w = 0.21 %) of the granular soil has been tested.

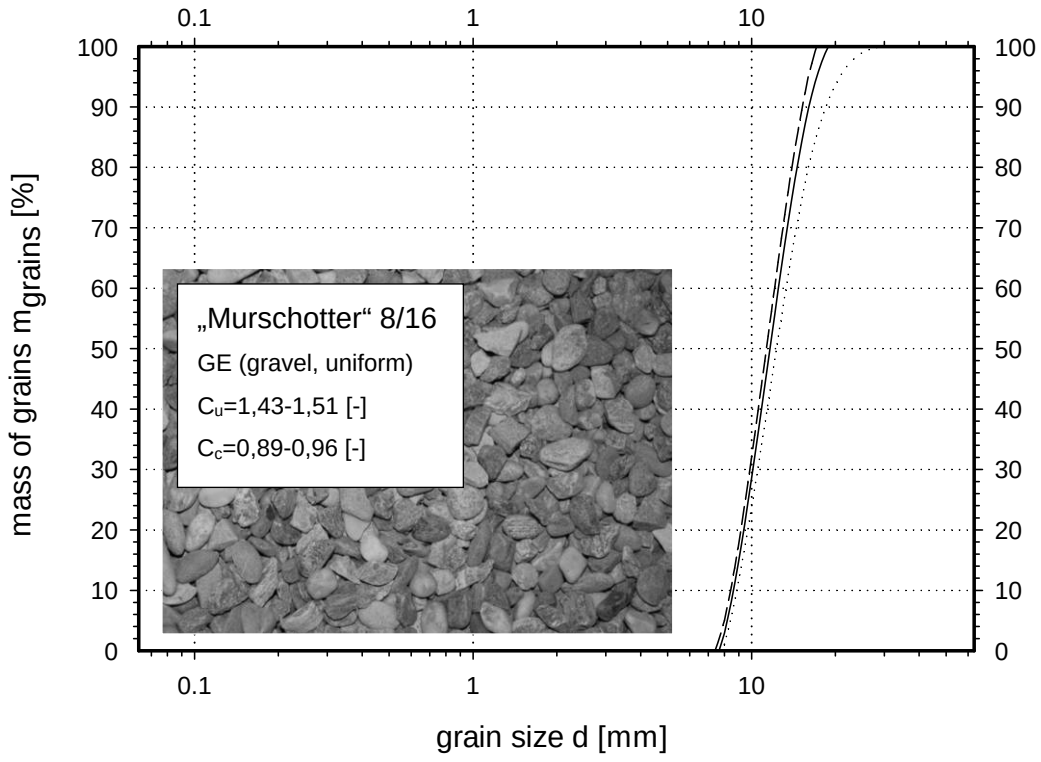

Fig. 10: Experimental backfill material: "Murschotter" rounded gravel 8/16 mm.

A maximum porosity of n_{max} = 43.1 % and a minimum porosity n_{min} = 39.0 % have been investigated by laboratory studies. Large scale direct shear tests have been utilized to estimate the shear parameters of the granular material. A peak friction angle φ_{peak} = 40.1 - 46.0 ° is determined. The hydraulic conductivity (k_f = 1-2e^{-1} m/s) of the highly permeable granular soil is estimated by the grain size distribution with respect to the equations provided by Hazen (1893) and Beyer (1964).

The stiffness parameter E_s = 40 MPa according to a stress level of (σ = 100 kN/m²) is determined by performing large scale oedometer tests ($\varnothing/H$ = 0.3/0.1 m) with a prototype oedometer (Wieser 2011) device (Tab. 2).

Tab. 2: Soil parameters for the granular backfill material

Property	Symbol	Value	Unit
unit weight	γ_s	26.4	[kN/m³]
shape index	SI	29	[%]
coefficient of uniformity	C_u	1.43 – 1.51	[-]
coefficient of curvature	C_c	0.89 – 0.96	[-]
max. porosity	n_{max}	43.1	[%]
min. porosity	n_{min}	39.0	[%]
experimental porosity	n_{exp}	39.0 – 41.0	[%]
water content	w	0.21	[%]
peak friction angle	φ_{peak}	40.1 – 46.0	[°]
permeability Hazen (1893), Beyer (1964)	k_f	1e-1 - 2e-1	[m/s]
stiffness parameter (σ = 10 / 100 kN/m²)	E_s	10 / 40	[MN/m²]

In order to describe the discrete properties of the backfill material properly, detailed research relating to the shape of the gravelly soil particles has been performed to later on numerically investigate the mesosopic soil reinforcement interaction by utilizing simulations based on the Discrete Element Method (Chapter 4).

150 particles have been randomly selected to perform a detailed geometrical experimental study. Apart from visual classification (von Soos & Bohac 2002) relating to the shape of the grains every particle has been measured with a digital sliding calliper in A (maximum elongation) B (middle elongation) and C (minimum elongation) direction.

The shape index SI = 29 % of the granular soil particles has been calculated after the Austrian Standard ÖNORM EN 933-4 (2008). Thereby M_2 defines the total mass of 150 randomly selected granular soil particles. Particles with an A/C ratio bigger than three ($A/C > 3$) are weighted and their mass M_1 is recorded.

$$SI = \frac{M_2}{M_1} \cdot 100 \tag{1}$$

To evaluate the roundness of the granular particles, the roundness coefficient RK according to Cox (1927) has been calculated. Photos of the granular particles have been taken in order to computer aided measure. The projected area A_{grain} and the projected contour U_{grain} from the pictures have been measured.

The roundness coefficient is calculated according to Equation 2.

$$RK = \frac{4 \cdot \pi \cdot A_{grain}}{U_{grain}^{\ 2}} \tag{2}$$

Additionally, a flatness ratio p_{grain} and an elongation ratio q_{grain} have been calculated according to Aschenbrenner (1956) to finally evaluate the shape of the granular soil particles.

elongation ratio q_{grain}:

$$q_{grain} = \frac{B}{A} \tag{3}$$

flatness ratio p_{grain}:

$$p_{grain} = \frac{C}{B} \tag{4}$$

Most of the grains have been analyzed as spheres and discs. The sphericity and roundness of the grains with respect to a sphere (sphericity = roundness = 1.0) have also been investigated by using the tables provided by Krumbein & Sloss (1963). Further on Rittenhouse (1943) provides a fast method to describe the shape properties of the particles. The results of the analysis are summarized in 4 categories (Chapter 4.2) and are presented in Table 3.

Tab. 3: Results of the mesoscopical grain shape analyse.

Shape	Fraction [%]	von Soos & Bohac	Cox RK	Krumbein & Sloss	Rittenhouse
1	43	semispherical subrounded	0.75-1.0	sphericity 0.7 roundness 0.9	subrounded subangular
2	29	flat subrounded	0.68-1.0	sphericity 0.5 roundness 0.9	subrounded subangular
3	5	semispherical subrounded	0.71-1.0	sphericity 0.7 roundness 0.9	subrounded subangular
4	23	spherical rounded	0.81-1.0	sphericity 0.9 roundness 0.9	subrounded

In order to correlate the shape of the grain with their mineralogical components petro graphical investigations have been carried out. The Mohs hardness and the reaction with hydrochloric acid which is dropped on all particles has been estimated to assign a mineralogical fraction to each type of shape. 35 % of quartzite, 30 % of granite and roughly 20 % of carbonate have been assigned.

The rest of the mineralogical fraction has been evaluated as weathered granite. It can be stated that no correlation between grain shape and mineralogical components have been observed during the investigation of the 150 analyzed discrete gravelly grains.

An opto-electronic instrument, a prototype called “petroscope” (Lee et al. 2005, 2007) has been employed to additionally investigate the shape of the granular particles automatically. The prototype was constructed by Lee et al. (2005, 2007), using entirely generic components. Two JAI CV-M33 cameras, a Stocker Yale laser diode with uniform line projection optics and a matt black plastic conveyor belt driven by a frequency inverter are shown in Fig. 11a).

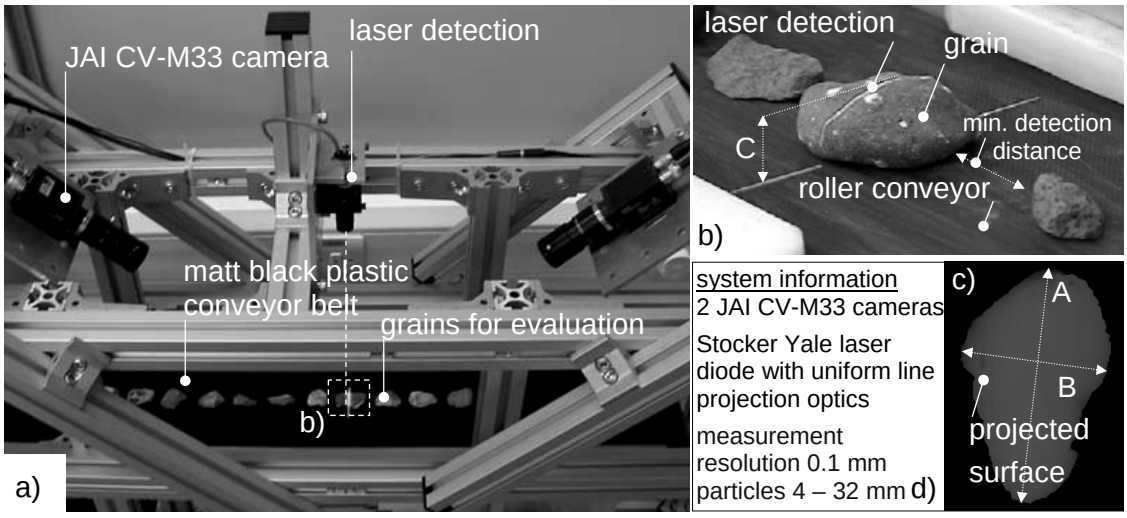

Fig. 11: Opto-electronic instrument “petroscope”: a) overview of the system components (according to Lee et al. 2005, 2007) b) detailed photo of the granular soil particles during detection c) visualisation of the projected surface detected by the laser diode d) system information.

Figure 11b) shows the granular soil particles during their laser detection in detail. The conveyor belt moves the granular particles under the laser diode constantly forward, in one predefined direction. A dual camera laser triangulation system is installed to allow sufficient surface coverage. A complete model of the upper hemisphere of the granular particle is thereby provided. The projected surface of the upper hemisphere of the particle is shown in Figure 11c). The elongations of the grains in *A*, *B* and *C* direction are detected automatically by the petroscope equipment. In Figure 11d) detailed information about the system and its components is given.

To evaluate the performance of the petroscope prototype 150 particles, the ones already investigated are detected and analyzed by the presented equipment. The fundamental mathematical morphology approach to calculate and evaluate the shape of the grains is presented by Lee et al. (2005, 2007). The results analyzed

with the petroscope and the ones gained from manual computing and measuring with an electrical sliding calliper are compared. As explained in Lee et al. (2005, 2007) user defined information about the gravelly material can be evaluated by the petroscope. The petroscope calculates the shape index *SI* of the 150 particles by utilizing the mathematical morphology approach provided by Lee et al. (2005, 2007). The *SI* value amounts to 34 % and correlates with the value (*SI* = 29 %) manually evaluated in the laboratory and calculated by Equation (1).

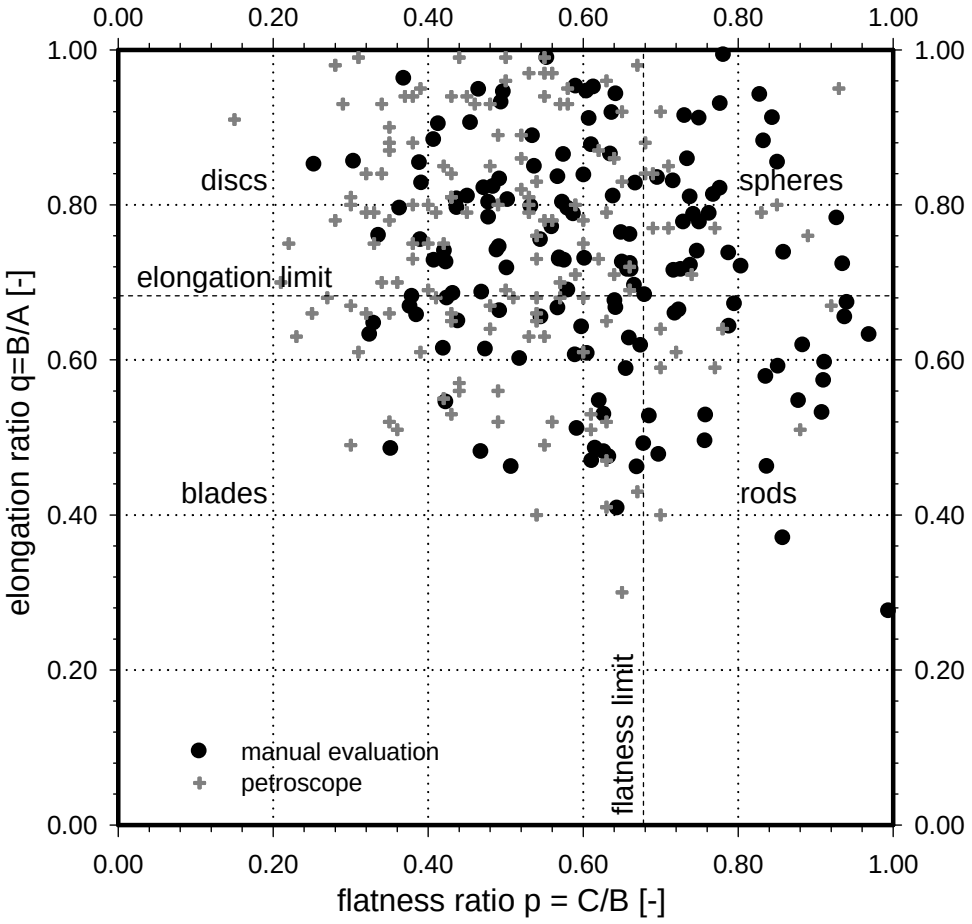

Fig. 12: Evaluation of grain shape: elongation *q* and flatness ratio *p* according to Aschenbrenner (1956), linear regressions including the 95 % confidence band, correlation and comparison between manual and automatic evaluation.

Additionally, the elongation q_{grain} and flatness ratio p_{grain} according to Aschenbrenner (1956) respectively regarding the Equations (3) and (4) are calculated by the petroscope equipment automatically. The results of the manual evaluation and the results gained from the automatic calculation of the petroscope (Lee et al. 2005, 2007) are presented in Figure 12. The results show a sound agreement. The linear regressions, including the 95 % confidence band of the manual evaluation and the calculation performed by petroscope prototype correlate precisely. It can finally be stated that investigations with the petroscope

prototype show sound agreement regarding to the mesoscopic investigations performed manually.

To reinforce the soil structures which are investigated in the laboratory, geometrical and mechanical biaxial geogrids woven out of linear polyester (PET) are used. The thickness of the longitudinal member of the geogrid $d_{grid,l}$ amounts to 1.4 mm. The thickness of the transverse members $d_{grid,t}$ = 1.17 mm and the thickness at the junctions $d_{grid,j}$ = 1.75 are given in Table 4.

The axial aperture sizes of the reinforcement amount to $a_{grid,x,y}$ = 20.0 mm in longitudinal and 20.0 mm in transverse direction. The tensile strength T_{max} and stiffness properties EA have been investigated in detail (Chapter 2) in the strain range ε_{PRSi} between 0 % and 2.5 %. This is due to the prestressing of the reinforcement. To activate the maximum tensile stiffness of the geogrid the reinforcement is prestressed up to 2.5 % (Chapter 2). The interaction coefficient between granular soil and geogrid reinforcement material has been determined by carrying out large scale direct shear tests (Tab. 4). The tested interaction coefficient R_{inter} varies between a value of 0.88 and 1.19. The results of the tensile load and the ones gained from direct shear tests are presented in detail later.

Tab. 4: Material parameters for woven, biaxial, PET geogrid

Property	Symbol	Value	Unit
mass per unit area	ρ_{grid}	250	[g/m²]
thickness l/t/j	$d_{grid,l,t,j}$	1.40/1.17/1.75	[mm]
aperture size x	$a_{grid,x,}$	20.0	[mm]
aperture size y	$a_{grid,y}$	20.0	[mm]
max. tensile strength	T_{max}	50.0/50.0	[kN/m]
tensile stiffness	EA	450-700	[kN/m]
interaction coefficient	R_{inter}	0.88-1.19*	[-]

The detailed results of the tensile load tests already described in Chapter 2, with the above presented geogrids are shown in Figure 13b). As already mentioned the tensile load tests have been modified according to Chapter 2. Load strain tests with a velocity v_{test} = 0.5 mm/sec have been conducted on newly fabricated, unused geogrids but also geogrid reinforcement materials used during the experimental investigations (Chapter 3.3.3) have been tested. The tensile forces $F_{tensile}$ of both woven linear polyester reinforcement material distribute nonlinear versus the occurring strain ratio $\varepsilon_{tensile}$ in the reinforcement materials. The load strain behaviour of the used and unused geogrid correlates closely. Both graphs develop similarly until a tensile force of 35 kN/m is activated in the longitudinal and transverse members of the geogrid reinforcement material.

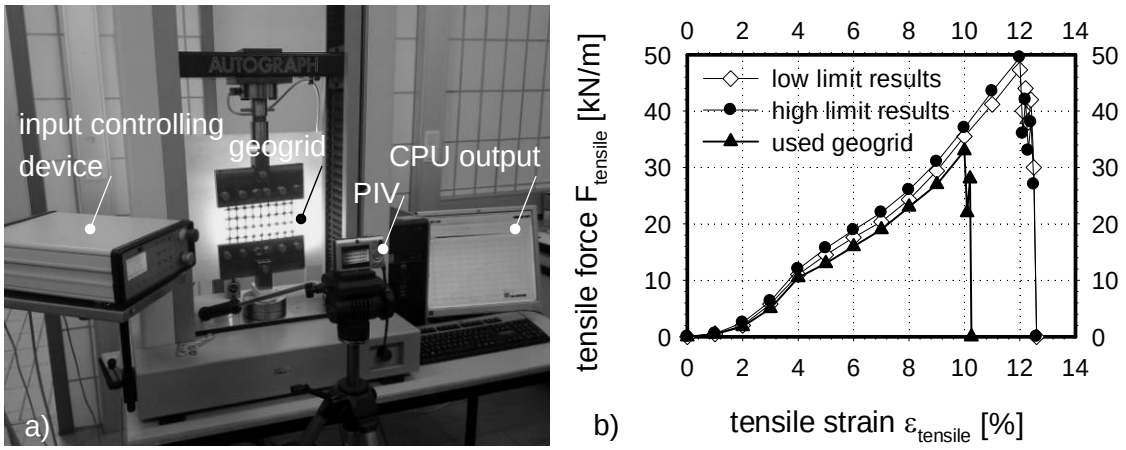

Fig. 13: Tensile load-strain tests: a) experimental testing device including input and controlling device, geogrid fixed in clamps, PIV setting and the CPU output b) low and high limit results from tests.

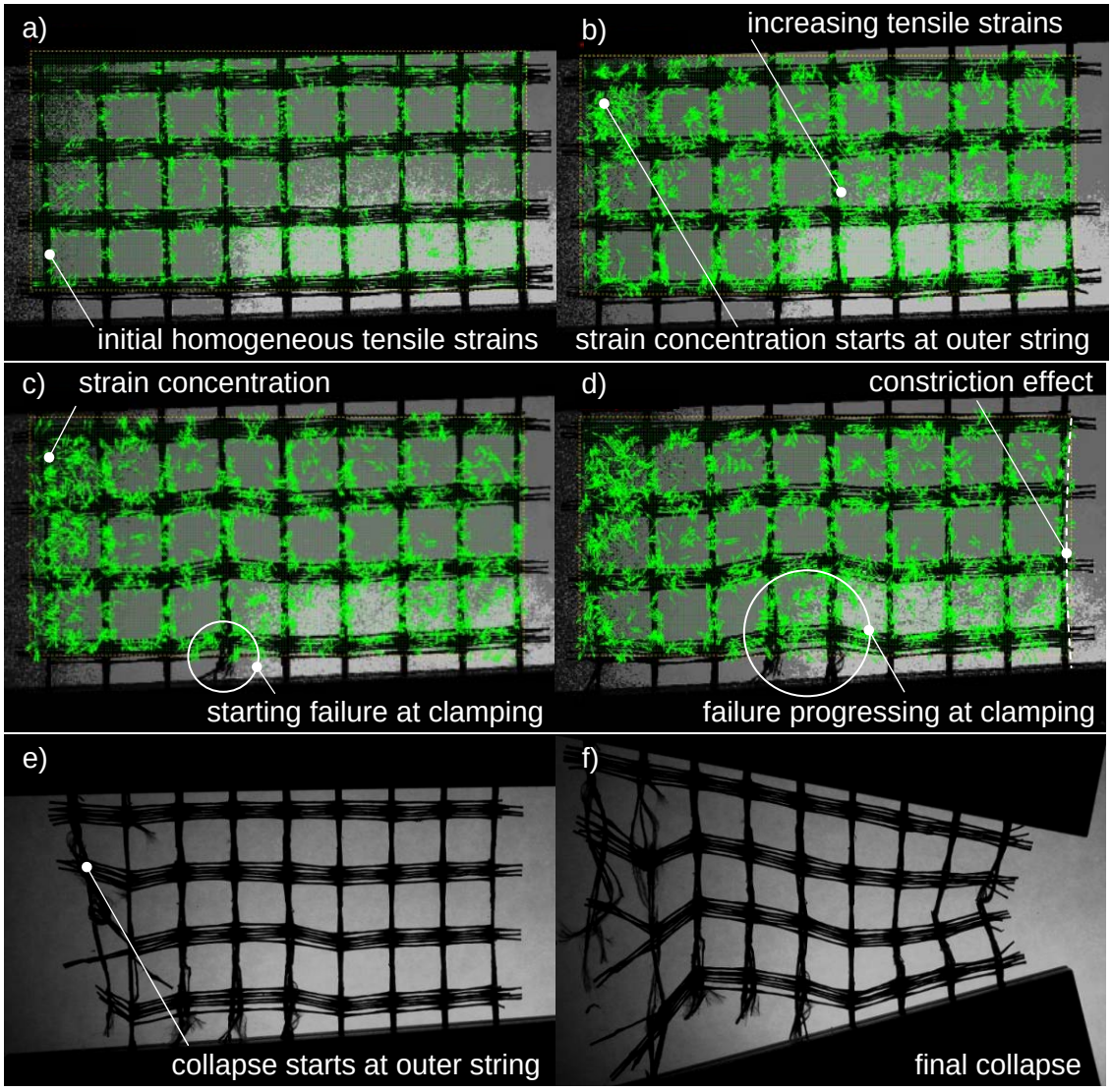

Fig. 14: PIV analysis: load-strain distribution along geogrid reinforcement from the start of the testing procedure until the final collapse.

The linear polyester geogrids used fail at tensile strains $\varepsilon_{tensile}$ around 10 % with a maximum tensile force $F_{tensile,max}$ = 40 kN/m. The unused geosynthetics finally rupture at tensile strains $\varepsilon_{tensile}$ varying around 2.5 %. The maximum tensile force amounts to $F_{tensile,max}$ = 50 kN/m.

Figure 13a shows the tensile load strain experimental setup, including the input controlling device, the PIV camera and the CPU output equipment.

During the tensile tests photos have been taken every 30 seconds in order to investigate the strain distribution in the reinforcement in detail until the reinforcement finally collapses (Fig. 14). Immediately after the start of the tests a homogeneous tensile strain distribution along the geogrid reinforcement is observed (Fig. 14a). The initial tensile strains increase with respect to the increasing tensile testing load (Fig. 14b). After stress concentrations along the clamping some failure is visible (Fig. 14c), d).

Starting with the failure of one single string, that progresses at an outer longitudinal member of the geogrid reinforcement (Fig. 14e) and f) the reinforcement finally collapses.

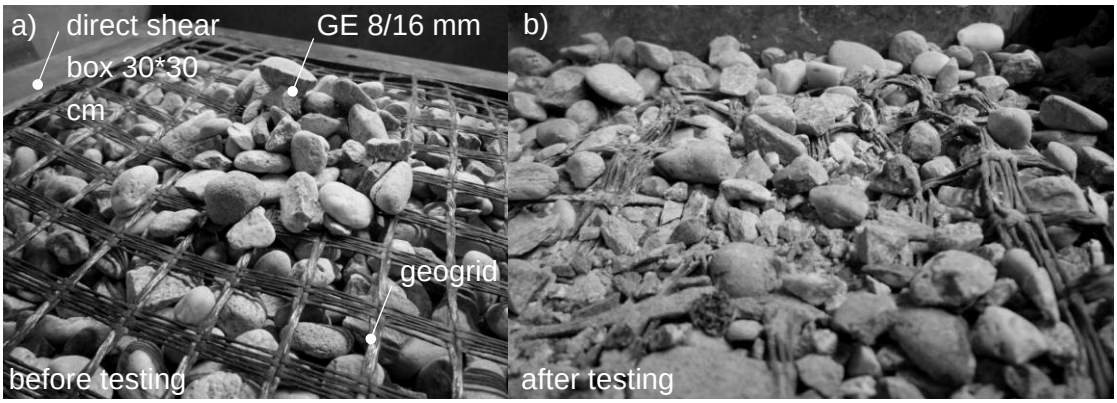

Fig. 15: Direct shear test: photo of the shear plane before and after the testing procedure including granular material and geogrid.

In order to estimate the soil geogrid interaction coefficient α properly large scale direct shear tests ($L/W/H$ = 0.3/0.3/0.2 m) have been conducted with unreinforced and reinforced soil test specimens. With respect to the stress conditions during the experimental investigations the testing stress levels have been adapted. Normal stresses σ_n = 100, 200 and 350 kN/m² have been applied to the unmodified direct shear tests. The “low stress” direct shear tests have been conducted with normal stresses σ_n ranging from 10 to 20 and 40 kN/m².

Figure 15 shows the direct shear experimental device including the granular material and the geogrid reinforcement before and after the shear test. The photos show the intense interlocking between the soil particles and the discrete geogrid.

After conducting the unmodified direct shear tests, breakage of some particles has been observed. The occurring abrasion of the geogrid during the loading and shear phase is visible on the taken and presented photos (Fig. 15).

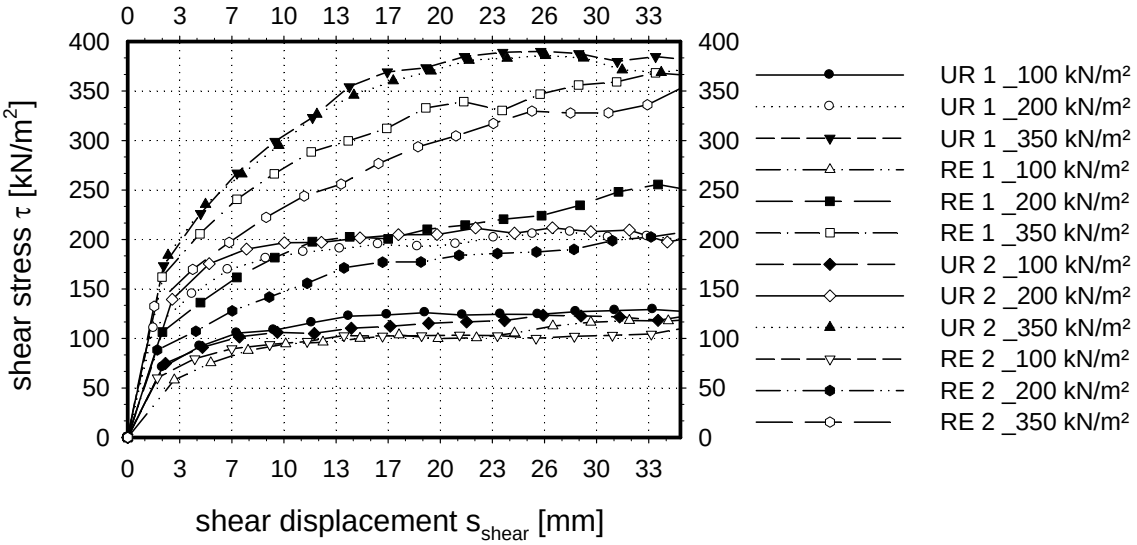

Fig. 16: Direct shear test: shear stresses τ versus shear displacement s_{shear} resulting from the unmodified direct shear test (σ_{normal} = 100, 200, 350 kN/m²).

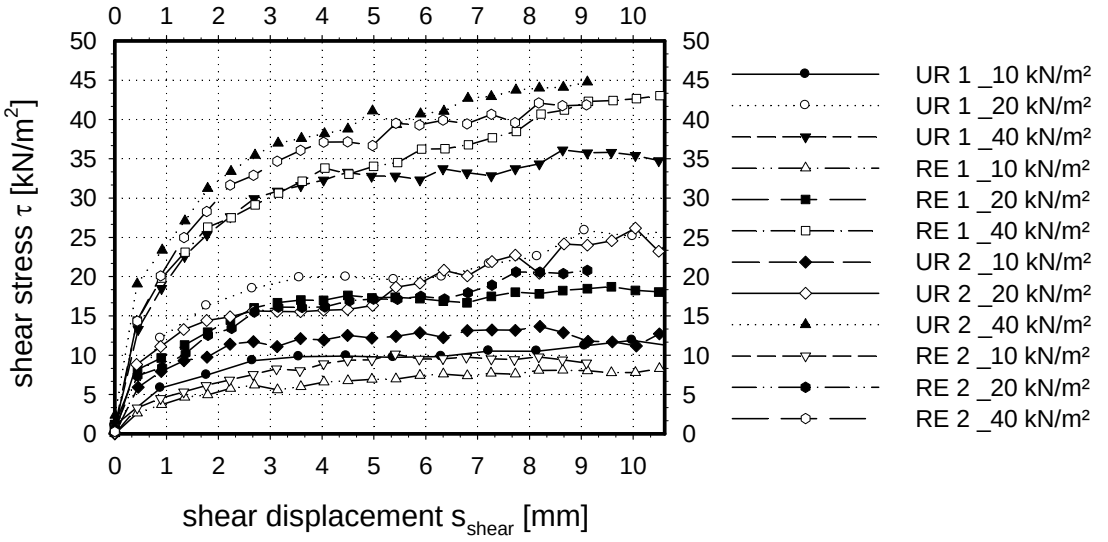

Fig. 17: Direct shear test: shear stresses τ versus shear displacement s_{shear} resulting from the "low stress" direct shear test (σ_{normal} = 10, 20, 40 kN/m²).

Figure 16 and 17 show the shear stress τ versus the shear displacement s_{shear} of the unreinforced soil body (UR) and the reinforced soil element (RE). Results of two unreinforced and two reinforced tests are shown in the graphs (Fig. 16 and 17). The evaluated shear parameters of the unreinforced and reinforced soil specimen are summarized in Table 5 and 6. Friction and dilatancy angle (Fig. 18)

of the unreinforced and reinforced soil elements are analyzed and the calculated mean values (MV) are given in the Tables 5 and 6. The unreinforced tests generally show slightly higher shear stresses τ than the reinforced ones. The interaction coefficient R_{inter} is calculated with a value below 1.

Tab. 5 Shear parameters of unreinforced test specimen: dilatancy angle ψ, friction angle φ, mean values (MV) of friction and dilatancy.

	MV ψ [°]	UR 1 φ [°]	UR 2 φ [°]	MV φ [°]	MV $\varphi+\psi$ [°]
low stresses	5.6	40.3	42.0	41.2	46.8
usual stresses	3.3	42.0	42.0	42.0	45.3

Tab. 6 Shear parameters of reinforced test specimen: dilatancy angle ψ, friction angle φ, mean values (MV) of friction and dilatancy.

	MV ψ [°]	RE 1 φ [°]	RE 2 φ [°]	MV φ [°]	MV $\varphi+\psi$ [°]
low stresses	4.1	38.6	39.9	39.3	43.4
usual stresses	3.3	41.5	40.6	41.1	44.4

It may happen that the interaction improves by reinforcing the soil element. Especially in the case of conducting “low stress” direct shear tests an increase of the shear stresses τ by reinforcing with a geogrid can be observed (Fig. 17, UR 1_40 and RE 1_40).

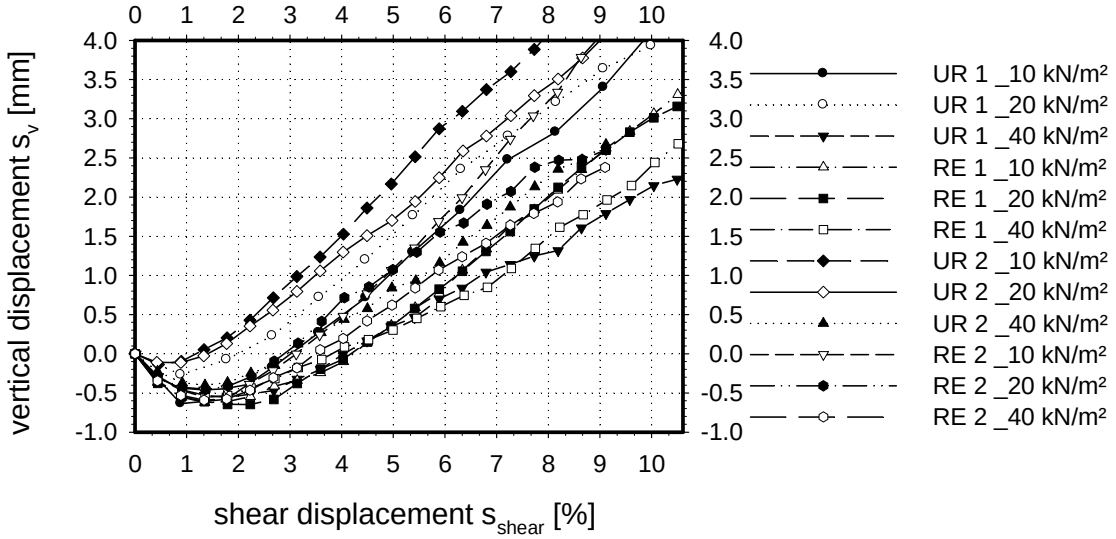

Fig. 18: Direct shear test: vertical displacements of the load plate s_v versus horizontal shear displacements s_{shear} resulting from the “low stress” direct shear test (σ_{normal}=10, 20, 40 kN/m²).

The reinforced tests, with a normal stress level σ_{normal} = 40 kN/m² result in higher shear stresses τ than the unreinforced tests. This results in a soil geogrid interaction coefficient R_{inter} slightly higher than 1. This is due to confining

respectively interlocking effects between the discrete geogrid and the granular soil particles directly in between the shear zone (Kawamura et al. 2000).

3.3.4 Experimental procedure

In order to install reproducible reinforced soil structures a detailed experimental procedure has been worked out.

In a first step, a 0.02 m thick layer of gravel as described in Chapter 3.3.3 is dumped on the bottom of the experimental device. On top of the gravely layer the geogrid (Chapter 3.3.3) is installed. In a next step, one strip after the other *L/W/H* = 0.4/1.0/0.15 m is dumped and afterwards compacted path controlled (v_c = 2 mm/min) with a constant amount of compaction pressure p_c = 100 kN/m² to produce a homogeneous soil structure.

After installing the first compaction layer, respectively 4 compaction strips, the second geogrid reinforcement layer is installed. The same procedure is repeated till three layers of reinforced granular soil are installed if the soil structure is reinforced by the concepts of PRS_c. Permanent prestressing of the geogrid in the PRS_p structure is applied by a hydraulic jack just before the upper compaction layer is dumped. The reinforcement is tensioned. A prestessing strain ε_{PRSi} = 2.5 % is applied. The geogrid is permanently fixed just after its installation. In the case of applying temporary prestress to the geogrid reinforcement the prestrain in the geosynthetic ε_{PRSi} = 2.5 % is slowly released right after the compaction of each layer of the PRS_t soil structure.

After the artificial installation of the reinforced soil structures has been completed six load displacement tests (LDT) at different locations are carried out. A circular load plate with a diameter B = 0.24 m is dropped path controlled with a testing speed v_{test} = 5 mm/min until vertical displacements s = 0.035 m are reached.

Tab. 7 Overview of the experimental procedure

Experiment	Dumping strip	Prestressing	Release
Unreinforced (UR)	x		
Reinforced (RE)			
Prestressed by compaction (PRS_c)	x	x	
Prestressed permanently (PRS_p)	x	x	
Prestressed temporarily (PRS_t)	x	x	x

Table 7 summarizes the experimental procedures. The columns of the table are marked with an x when prestressing has been applied to the reinforcement. In case of utilizing the concept of PRS_t, the prestress in the geogrid is released. The

soil structure is constructed by dumping the material in single dumping strips. In case of conventional reinforcing (RE) a whole compaction layer without separate compaction strips is installed.

3.3.5 Experimental results and discussion

In this Chapter the results of 10 different experiments at the top layer of the soil structure are shown.

In order to validate the static load displacement behaviour of the reinforced soil structure, Figure 19 and 20 show the testing pressure p_{hf} near the hard and p_{sf} near the soft facing, versus settlements s normalized by the width B of the load plate respectively normalized by the distance between the reinforcement layers t. The results are plotted for tests conducted on unreinforced soil structures (UR) on conventionally reinforced ones (RE) and on soil structures reinforced by the concept of PRS_i. The load displacement tests have been carried out with a distance d_{test} = 0.2 m to the hard and with the same distance to the soft facing (Fig. 20).

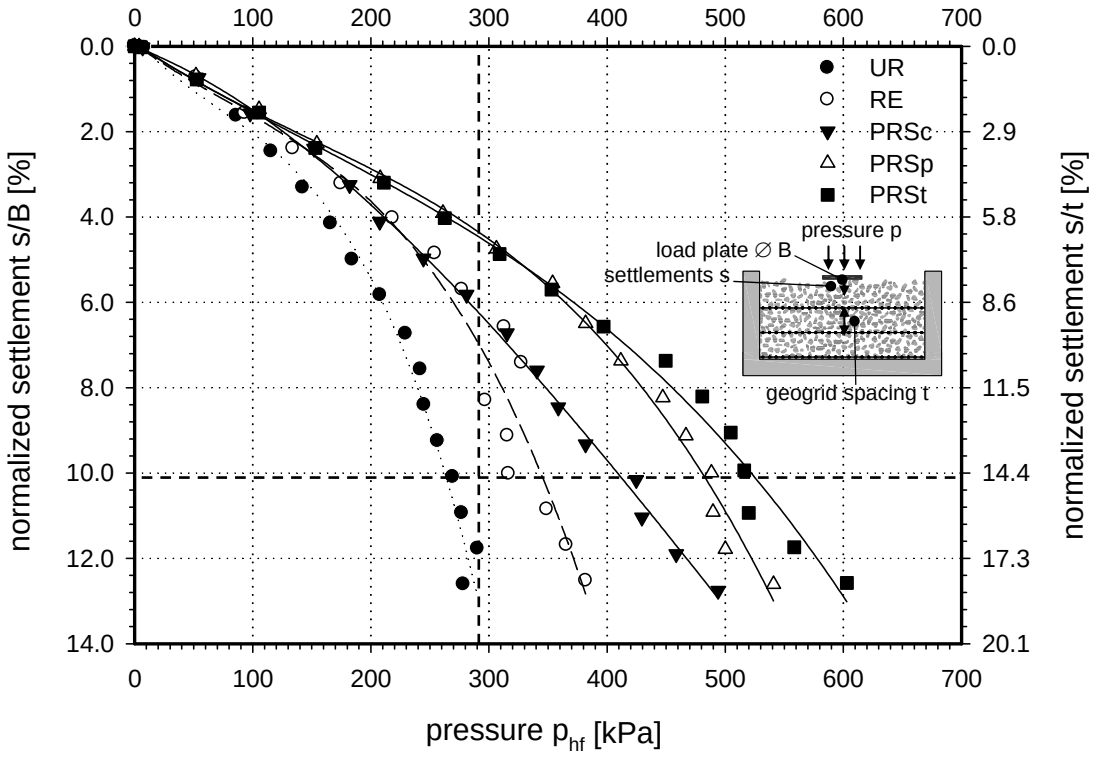

Fig. 19: Testing pressure p_{hf} near the hard facing versus settlement s normalized by the load plate's width B respectively normalized by the distance between the reinforcement layers t.

The graphs (Fig. 19, 20) show an increase of the bearing capacity respectively of the pressures p close to the hard and to the soft facing when reinforcing (RE) the

soil structure. Coevally the settlement *s* decreases with regard to the same pressure *p* in case of reinforcing the soil structure conventionally. When using the concepts of PRS_i, described in Chapter 2, the pressures further increase whereas the plate settlements decrease. The graphs of the reinforced (RE) and prestressed reinforced concept by compaction (PRS_p) show a closely related behaviour (Fig. 20). This is due to the soft facing. In case of the compaction of the reinforced granular soil layer close to the soft facing, the geogrid is able to move sidewards and as a result a prestress is activated in the geosynthetic reinforcement due to an automatic compaction.

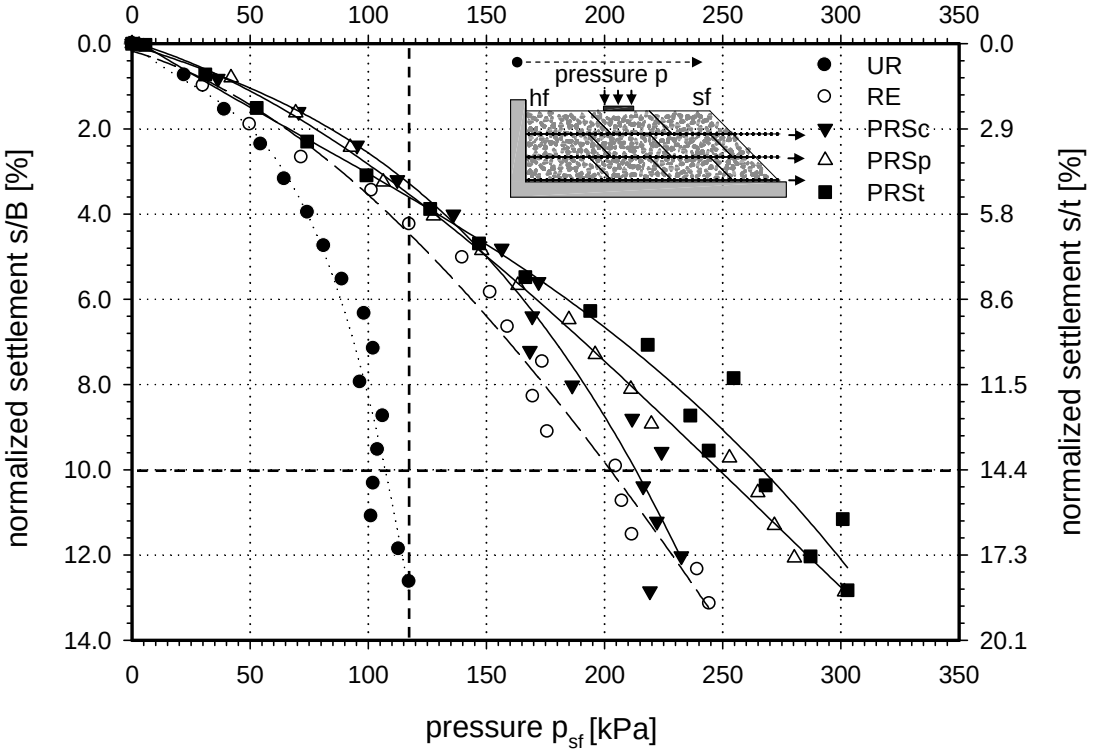

Fig. 20: Testing pressure p_{sf} near the soft facing versus settlement *s* normalized by the load plate's width *B* respectively normalized by the distance between the reinforcement layers *t*.

Figure 21a) shows the maximum load plate pressure p_{LP} with respect to the load displacement test on different reinforced soil structures versus the horizontal distances of the experimental device d_h. It is apparent that the maximum pressures p_{LP} occur close to the hard facing (d_h = 0 m), no matter whether they are measured during a load displacement test of an unreinforced (UR), reinforced (RE) or prestressed reinforced soil structure (PRS_i).

The load plate pressures p_{LP} decrease with the distance from the hard facing and reach minimum values by testing the soil structures load displacement behaviour close to the soft facing (d_h = 1.2 m). Besides investigating the load plate pressures along the horizontal distance of the experimental device, the pressure distribution

has been evaluated with respect to the vertical distance of the experimental device d_v (Fig. 21b). The results assign higher load plate pressures in the middle of the experimental device (d_v = 0.3 m) in the case of testing a reinforced (RE) respectively prestressed reinforced (PRS_i) soil structure.

The geogrid placed at the bottom of the experimental device (d_v = 0.02 m) does not have a big influence on the results of the load deformation tests (Fig. 21b). The pressures p_{LP} on the bottom layer of the experimental device are lower than the pressures p_{LP} measured at a vertical distance of 0.3 m. The results of the load displacement test show a homogenous pressure distribution along the vertical distance d_v of the experimental device (Fig. 21b) when testing an unreinforced soil structure.

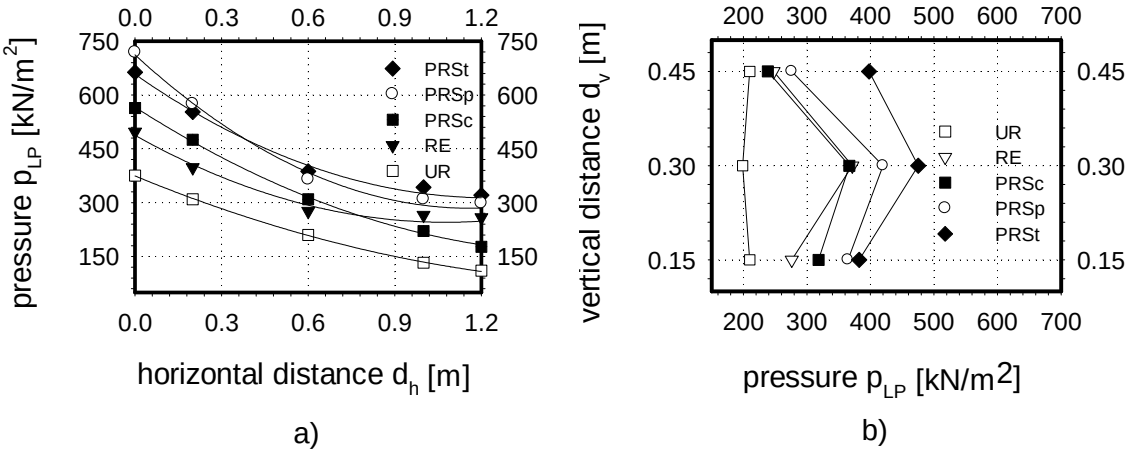

Fig. 21: a) Load plate pressure p_{LP} versus horizontal distances of the experimental device d_h. b) Load plate pressure p_{LP} versus vertical distances of the experimental device d_v.

To evaluate the theoretical increase of the bearing capacity of the different reinforced soil structures, their bearing capacity ratios BCR_{hf} and BCR_{sf} are calculated by equation 5.

The bearing capacity ratio BCR_{hf} is defined as

$$BCR_{hf} = p_{hf,PRSi}/p_{hf,UR} \tag{5}$$

whereas, $p_{hf,PRS}$ and $p_{hf,UR}$ are the pressures tested during the experimental investigations close to the hard facing.

Fig. 22 and 23 show the BCR_{hf} and BCR_{sf} values for the hard and the soft facing versus the settlements s normalized by the width B of the load plate and normalized by the distance between the reinforcement layers t. The values are plotted with respect to conventionally reinforced (RE) soil structures and for the soil structures reinforced with the concept of PRS_i.

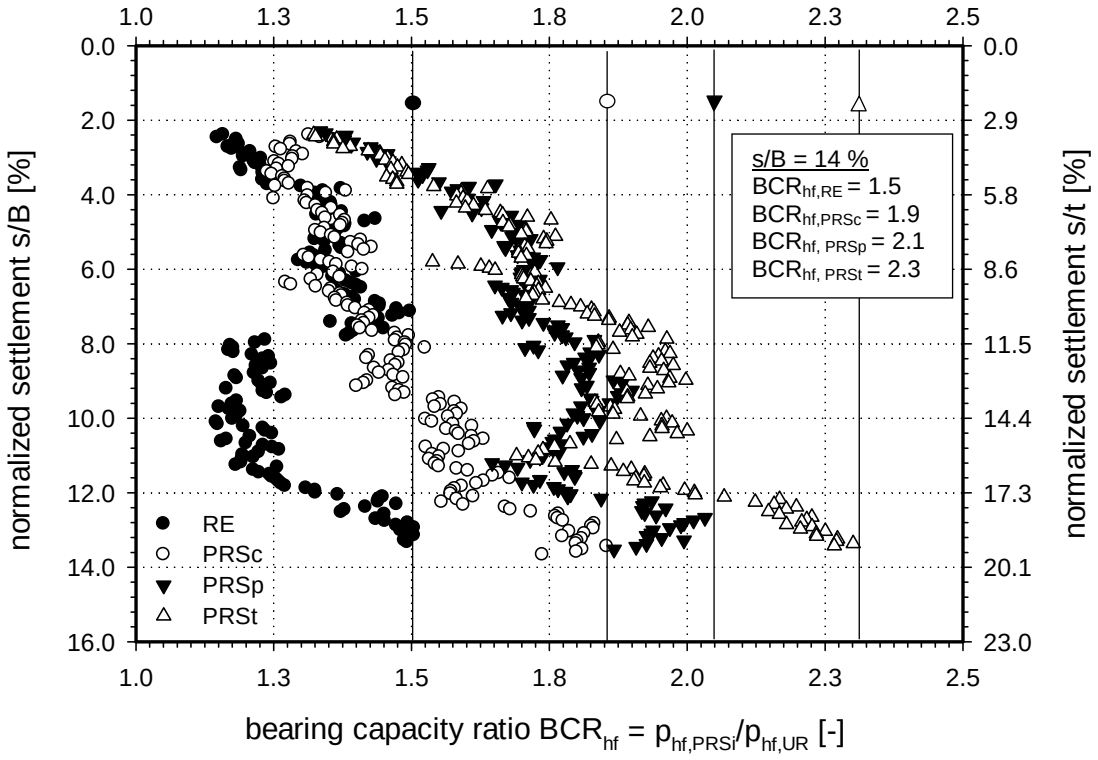

Fig. 22: BCR_{hf} values for the hard facing versus settlement s normalized by the load plate's width B respectively normalized by the distance between the reinforcement layers t.

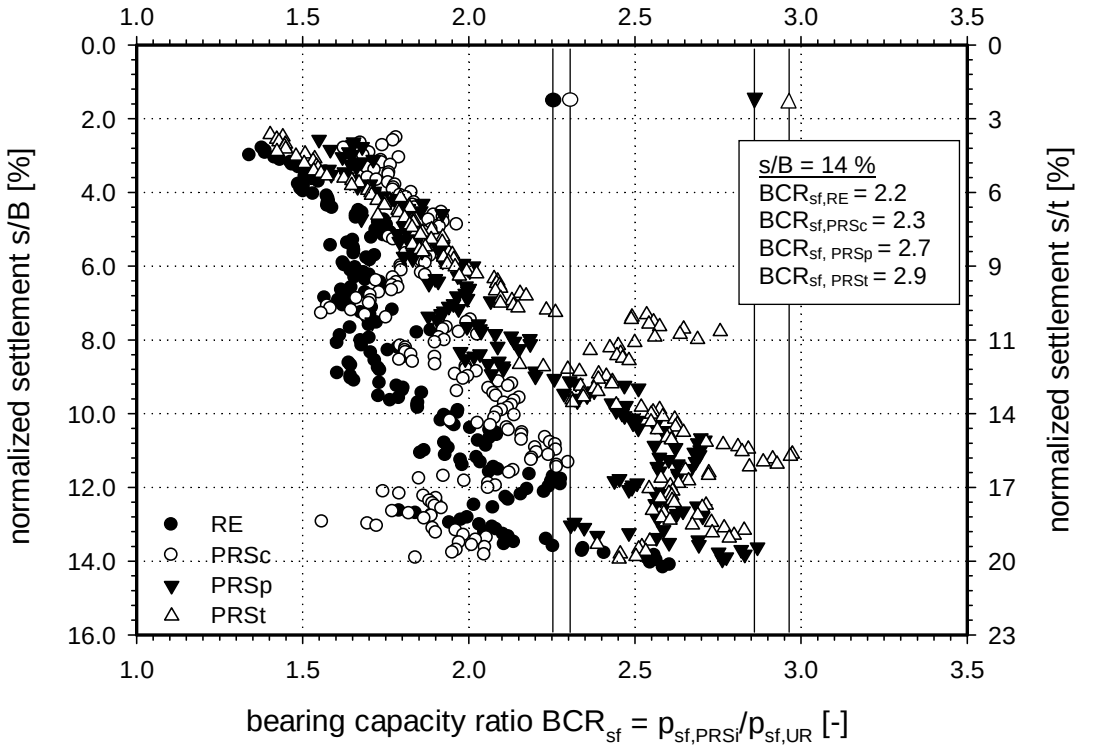

Fig. 23: BCR_{sf} values for the soft facing versus settlement s normalized by the load plate's width B respectively normalized by the distance between the reinforcement layers t.

The calculated and plotted results (Fig. 22 and 23) show an improvement of the load displacement behaviour of the soil structure by installing the geogrid reinforcement (RE).

The maximum BCR_{hf} differs between 1.5 for a conventional reinforcement (RE) and increases up to 1.9 when using the concepts of PRS_c. The ratio reaches its maximum at a value of 2.1 and 2.3 by utilizing the concept of PRS_p and PRS_t (Fig. 22).

Figure 23 shows the maximum bearing capacities BCR_{sf} at the soft facing. The bearing capacity amounts to 2.2 for conventionally reinforcing the soil structure (RE) and 2.3 in the case of utilizing the concepts of PRS_c. The highest bearing capacity values are 2.7 and 2.9 when employing the concept of PRS_p and PRS_t.

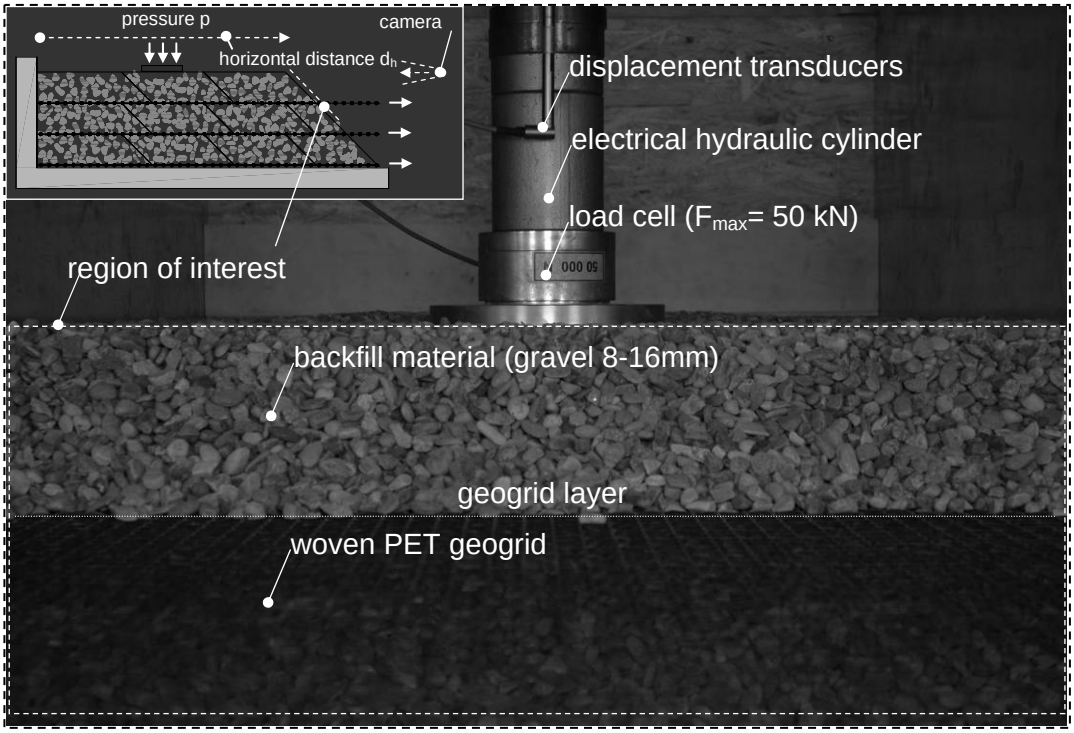

Fig. 24: PIV photo sequentially taken during the load plate tests including the analyzed region of interest.

It can be stated that in the case of installing the same backfill- and reinforcement materials, by applying the same compaction pressures and by constructing equally, the load displacement behaviour of the soil structure can be even more than doubled e.g. when using the concept of PRS_t. These results verify the concept described in Chapter 2.

Interlocking effects between the discrete geogrid reinforcement and the granular backfill material stabilize the structure. Besides keeping the granular gravelly particles in their initial place, additional pressure forces resulting out of the

temporary prestressing act on the discrete soil body. These additional forces finally improve the macroscopic load displacement behaviour of the temporary prestressed reinforced soil structure PRS_t.

The mesoscopic behaviour of the granular material and the reinforcement is investigated by utilizing the Particle Image Velocimetry (PIV) method (Raffel et al. 2007). During the load displacement testing process the displacement of the granular soil particles and the geogrid is analyzed from sequentially taken photos. A digital camera is installed in front of the soft facing of the reinforced soil structure.

Figure 24 gives an overview of the picture taken by a 6.1 Million megapixels digital camera including the analyzed region of interest (ROI).

The analyzed results from photos taken before, after and between the load tests are shown in Figures 25 and 26. The horizontal s_h and vertical displacement s_v of the granular soil particles visualize a local bearing capacity failure under the load plate in the case of testing a conventional reinforced (RE) and a soil structure reinforced by the concepts of PRS_c.

While testing the reinforced soil structure and by prestressing the geogrid either permanently (PRS_p) or temporarily (PRS_t) the same mechanism but fewer local displacements are visible.

The permanently prestressed geogrid is pulled back (“pulling back” effect) while settling the load plate. The mobilization of the geogrid thereby leads to an activation of a homogeneous support which results in a reduction of the local failure mechanism. In fact, about 80 % of the analyzed ROI gets activated by the geogrid to provide a higher bearing resistance of the reinforced structure. Constant and lower displacements all around the analyzed PIV picture visualize this mobilization. In the case of testing the temporary prestressed reinforced soil structure PRS_t, vertical but also horizontal displacements decrease because of the intense activation of the geogrid reinforcement.

The more activation the geogrid obtains respectively mobilizes the higher is its additional bearing capacity effect. Thereby the concept of PRS_t leads to a general decrease of the local bearing capacity failure mechanism.

It has to be stated that the photos taken from the front of the experimental devise have their limitations. The load displacement test is performed 20 cm behind the edge of the slope. Three dimensional effects consecutively influence the results of the PIV analysis insignificantly. Nevertheless a quantitative validation has been reached by using the PIV method.

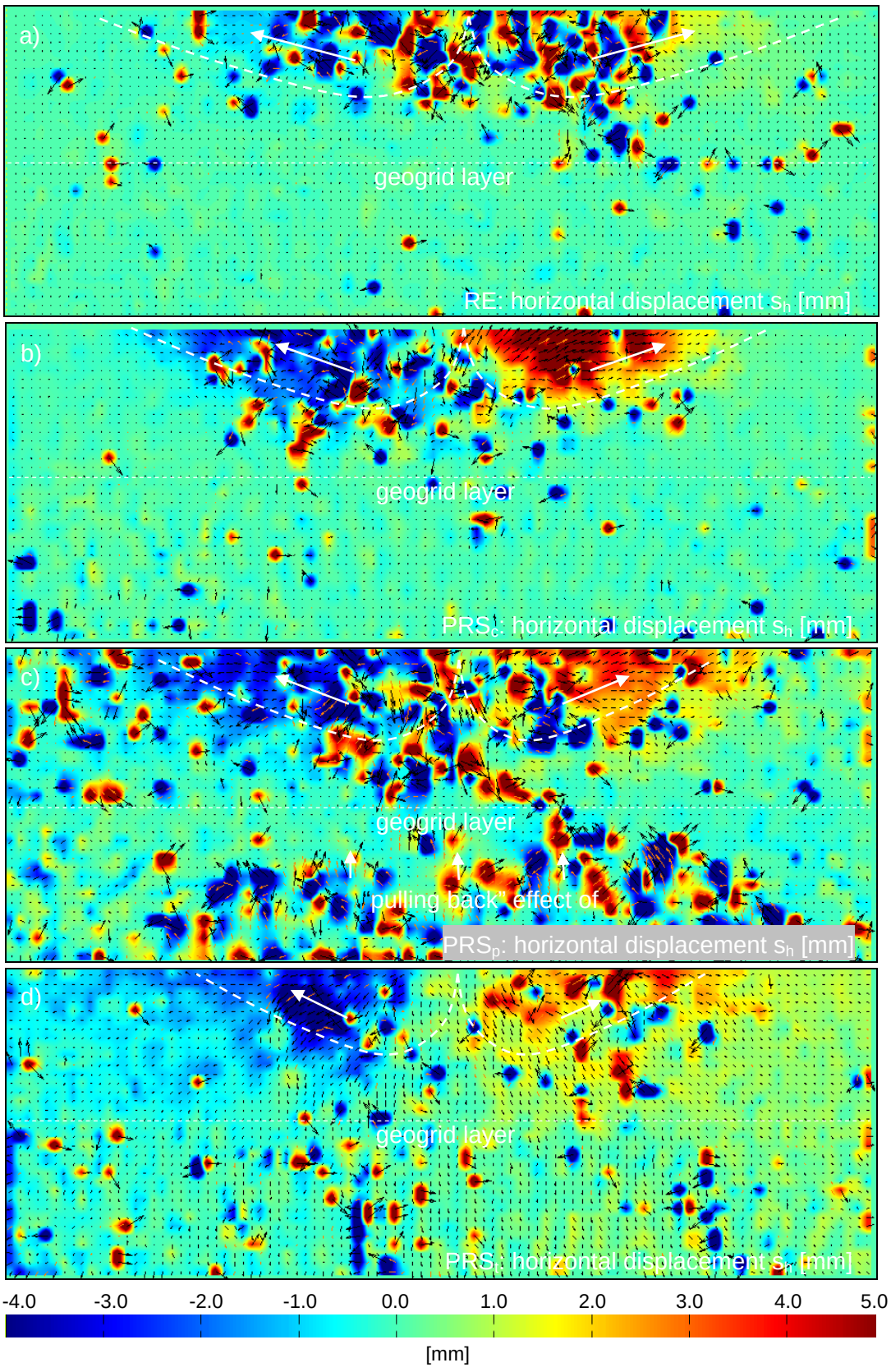

Fig. 25: Horizontal displacement s_h during load displacement test out of PIV: a) reinforced (RE) b) prestressed reinforced soil as a result of compaction (PRS_c) c) permanent prestressed reinforced soil (PRS_p) d) temporary prestressed reinforced soil (PRS_t).

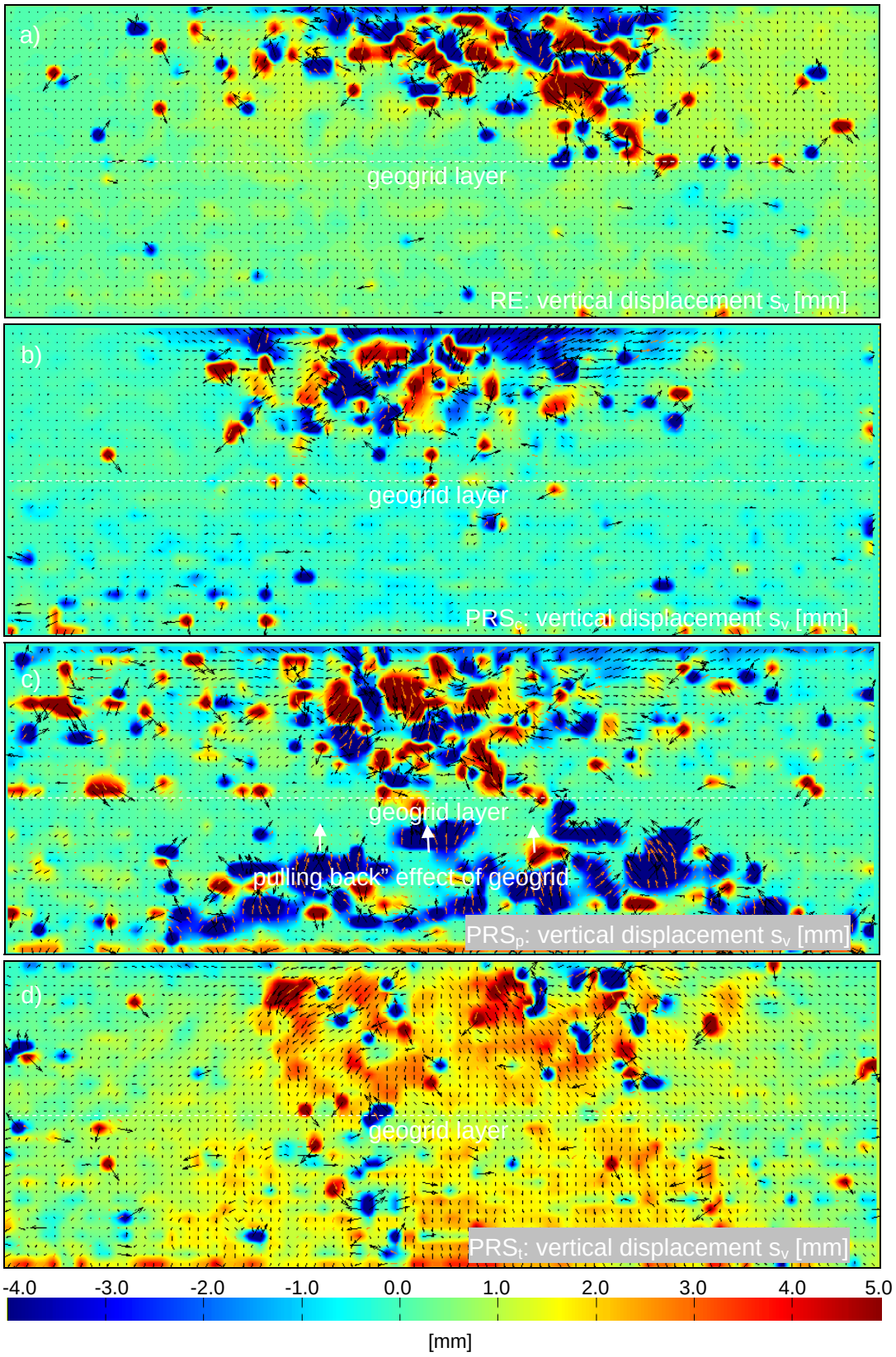

Fig. 26: Vertical displacement s_v during load displacement test out of PIV: a) reinforced (RE) b) prestressed reinforced soil as a result of compaction (PRS_c) c) permanent prestressed reinforced soil (PRS_p) d) temporary prestressed reinforced soil (PRS_t).

The mesoscopic soil geogrid interaction has additionally been observed during the compaction of the dumping strip 23 (2 = second layer, 3 = third strip).

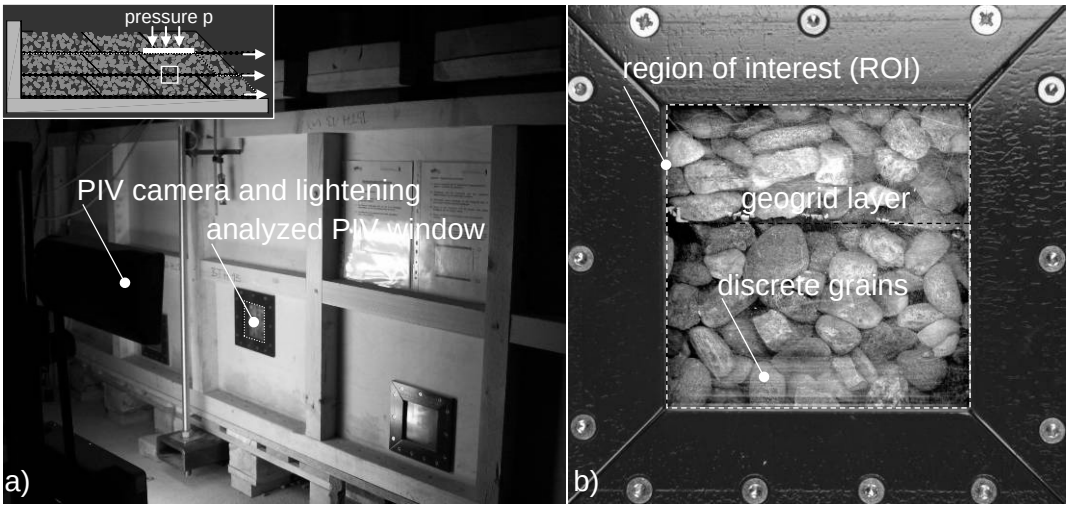

Fig. 27: a) Experimental device including the PIV camera and the analyzed side window. b) PIV photo sequentially taken during the load plate tests including the analyzed region of interest.

Figure 27a) gives an overview of the experimental device including the PIV camera and lightening. The position of the side window is visualized in the photo and the analyzed side window relating to the dumping strip is marked with a white frame (Fig. 27a).

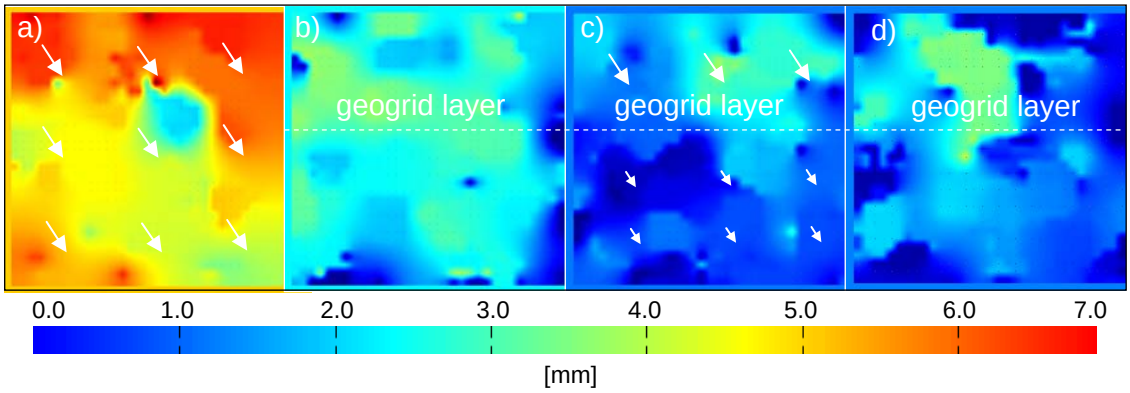

Fig. 28: Total displacement during compaction of the third dumping strip in the second layer taken from PIV window: a) reinforced (RE) b) prestressed reinforced soil as a result of compaction (PRS_c) c) permanent prestressed reinforced soil (PRS_p) d) temporary prestressed reinforced soil (PRS_t).

One sample photo and its analyzed region of interest (ROI) are shown in Figure 27b). The geogrid layer and the discrete soil particles surrounding the reinforcement are presented.

In order to quantitatively evaluate the displacements of the geogrid reinforcement and the soil particles, Figure 28 presents the total displacements during compaction of the dumping strip 23. High and homogeneous displacements occur in case of compaction of the unreinforced soil structures (Fig. 28a). The conventional reinforcing (RE) with the geogrid material results in lower displacements above and below the geogrid reinforcement layer. When utilizing the concept of PRS_i the theoretical additional bedding support (Chapter 2) provided by the prestressed reinforcement is verified. There is a further decrease in overall displacements. Additionally, a rapid reduction of the total displacements below the geogrid reinforcement layer is registered (Fig. 28c), d).

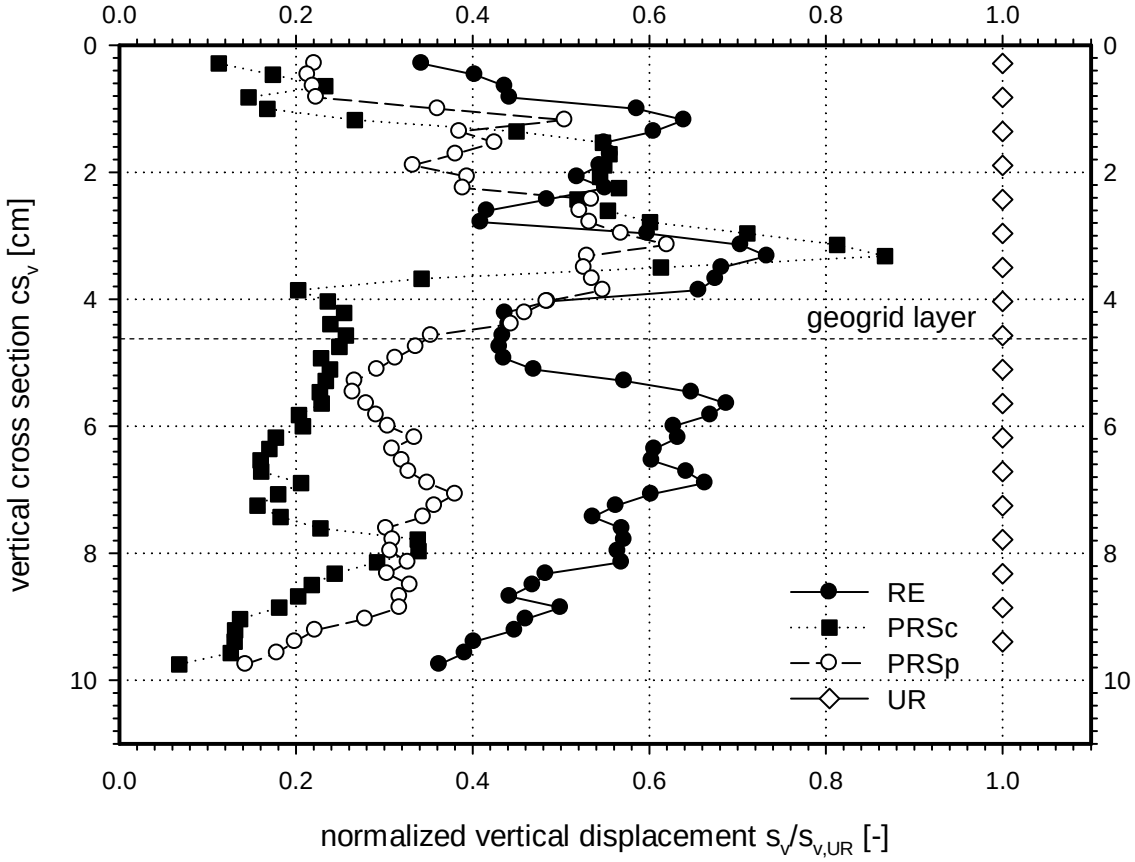

Fig. 29: Normalized vertical displacements $s_v/s_{v,UR}$ out of PIV analysing a vertical cross section in the middle of the PIV window.

The normalized vertical displacements $s_v/s_{v,UR}$ result from PIV analyses of a vertical cross section in the middle of the PIV side window (Fig. 27b) and are plotted in Figure 29. The graph confirms the findings written above. In the case of reinforcing the soil structure conventionally (RE), the settlements decrease homogeneously along the cross section. The curves PRS_c and PRS_p generally show lower settlements. Apparently, the settlements decrease suddenly below the polymer geogrid. The additional bedding support provided by the prestressed and thereby stiffer geogrid (Chapter 2.3) explains this effect.

It may be concluded that the results of the described static load displacement tests verify the positive effects illustrated in Chapter 2. The macroscopic and mesoscopic results interact positively. Both investigations show the same positive improvement regarding to the bearing capacity when utilizing the concept of PRS_i. It can finally be stated that the macroscopically evaluated displacements and the mesoscopic analyzed displacement distribution show and thereby verify the positive effects on the soil structures reinforced by the concept of PRS_i described in Chapter 2.

3.4 Cyclic load displacement experiments on prestressed reinforced soil (PRS_i) by geogrids

In this Chapter experimental test results produced at IBH Herold VBI in Weimar, Germany are presented to further validate the cyclic load displacement behaviour of PRS_i structures. Biaxial cyclic load displacement tests have been conducted to investigate the macroscopic load displacement behaviour of soil structures reinforced by the concept of prestressed reinforced soil (PRS_i) described in Chapter 2.

The cyclic interaction behaviour of granular gravely sand with three different kinds of polymer geogrid reinforcements has additionally been investigated mesoscopically by analysing the deformation of the granular soil particles by the utilized PIV method.

3.4.1 Overview on the experimental model

The validation of the cyclic load displacement behaviour of soil structures reinforced by the concept of PRS_i presented in Chapter 2 is the main objective of the utilized cyclic experimental investigations (Fig. 30).

Biaxial cyclic load displacement tests have been conducted in order to investigate the geosynthetic reinforced soil structure macroscopically. The biaxial testing device ($L/W/H$ = 0.25/0.25/0.25) represents a soil element of a geosynthetic reinforced soil structure. By applying different static and cyclic loading conditions, different positions of the soil element in the structure are simulated.

Besides investigating the cyclic performance of the different reinforced soil structure macroscopically, the mesoscopical soil geogrid interaction has been analyzed by utilizing the PIV method.

Figure 30 provides an overview of the cyclic experimental investigations closely related to the static load displacement test in Chapter 3.3.1.

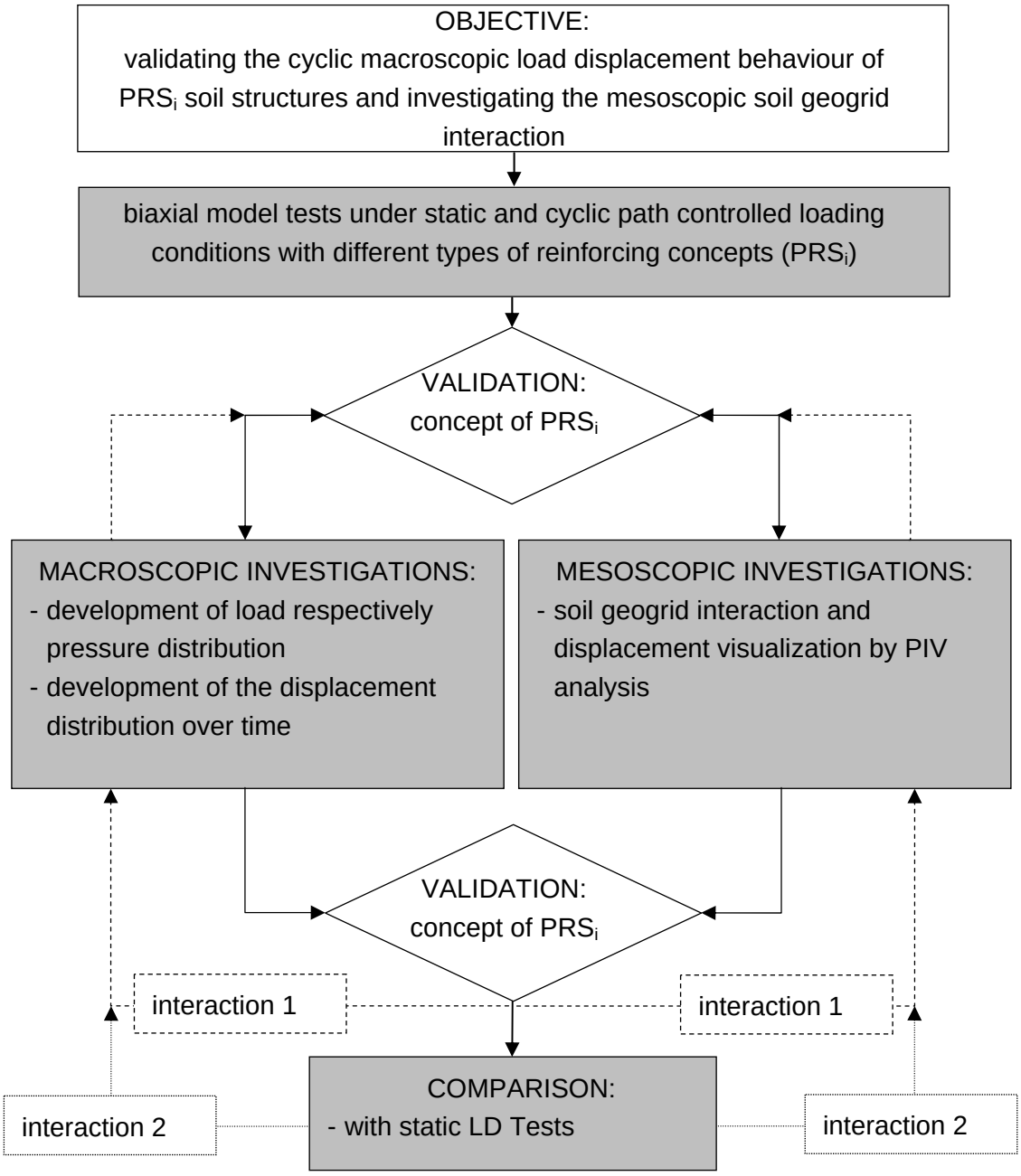

Fig. 30: Flow chart: overview on the experimental investigations.

The objective of the experimental investigations is defined at the beginning of the flow chart (Fig. 30). To validate the concepts of PRS_i under cyclic loading conditions biaxial model tests are conducted.

There is an interaction of the macro- and mesoscopic results during the validation process (Fig. 30). It has to be verified that the results gained from both investigation methods, macroscopic and mesoscopic research, finally correlate.

Results gained from the static large scale laboratory experimental investigations naturally interact by comparison with the results measured during of the static load displacement tests presented in Chapter 3.3.

3.4.2 Experimental setup and testing equipment

In order to investigate the time depending load displacement behaviour of a static and cyclic loaded and geosynthetic reinforced soil structure in the laboratory, a (prestressed) reinforced soil element is theoretically taken out of a typical geogrid reinforced soil wall (Fig. 31).

The described soil element is installed into a horizontally and vertically cyclically loaded biaxial element test and tested under homogeneous laboratory conditions. The enhanced experimental testing device (Fig. 32) is a 0.25 m long, 0.25 m wide and 0.25 m high steel box, described in detail by Burgstaller (2011). The steel box surrounds a reinforced soil element installed porosity controlled in two layers of gravely sand, 12.5 cm each (h_{layer} = 0.125 m), divided by one layer of a polymer geogrid.

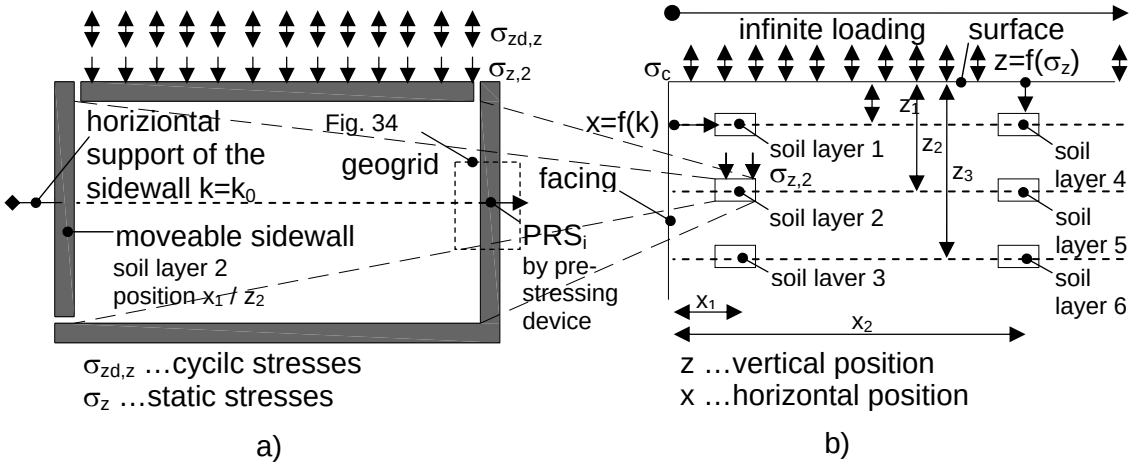

Fig. 31: Schematic sketch: a) Biaxial static and cyclic loaded soil element out of soil layer 2 reinforced with a geosynthetic b) typical geogrid reinforced soil wall including the positions of the biaxial loaded soil element (modified with respect to Burgstaller 2011).

To measure the macroscopic experimental test results such as vertical and horizontal loads and displacements over a period of time full bridge load cells and inductive displacement transducers have been installed on the vertical top wall and the moveable horizontal side wall of the experimental device. Further more, laser controlled displacement transducers are installed to separately monitor and validate the measured displacements.

To investigate the mesoscopic cyclic load displacement behaviour and the geogrid soil interaction, a 10.1 megapixel digital camera has been installed in front of the side window (L/H = 0.07/0.1 m) of the experimental device. A computer controlled photo sequence has been taken during one cyclic stage to analyse the soil and geogrid displacements with the help of the PIV (Raffel et al. 2007) method.

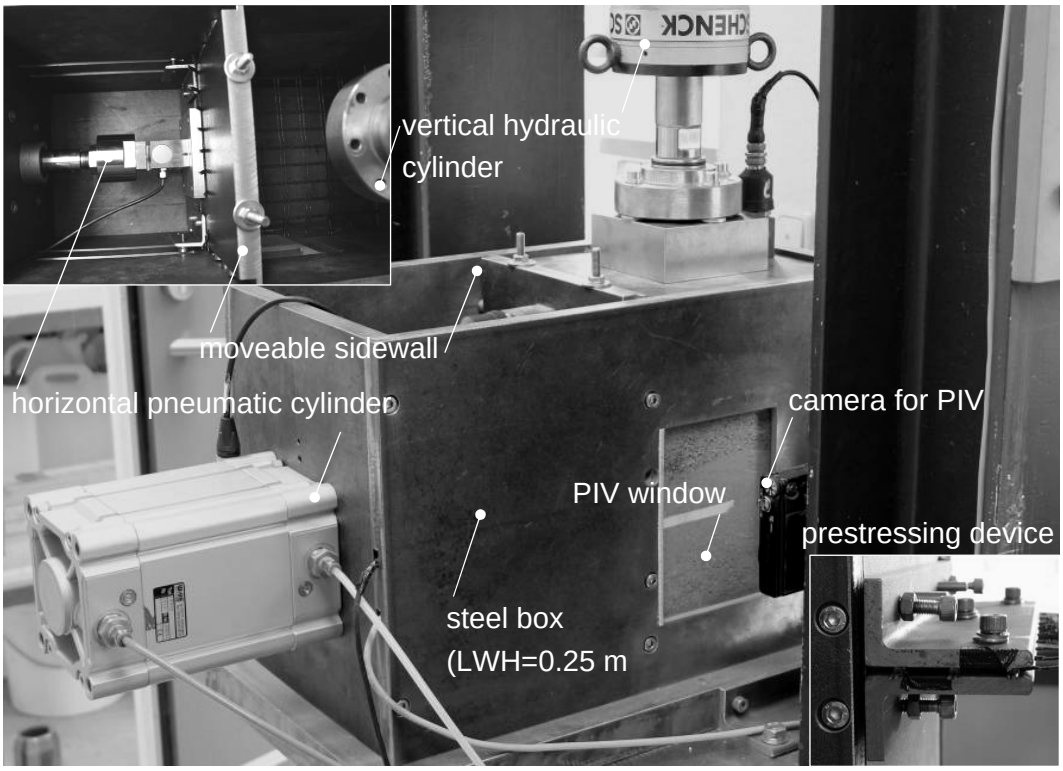

Fig. 32: Experimental testing device: steel box (L/W/H=0,25 m) surrounded by a vertical hydraulic and a horizontal pneumatic cylinder.

3.4.3 Experimental materials

The reinforced soil elements in the biaxial testing device are backfilled with a washed gravely sand with a diameter d_{grain} = 0.2 to 20 mm (Burgstaller 2011). The unit weight (γ_s = 26.4 kN/m³) of the gravelly sand and the natural water content (w = 0.23 %) of the granular material have been tested. A maximum porosity of n_{max} = 42.8 % and a minimum porosity n_{min} = 31.1 % have been evaluated by laboratory studies. During the experimental investigations a constant porosity n_{exp} = 35 % has to be guaranteed in order to gain reproducible results.

Figure 33 shows the grain size distribution of the artificially mixed granular material (Sa gr) and a photo taken of the gravelly sand described later. The coefficient of uniformity C_u = 2.8 to 2.9 and the coefficient of curvature C_c = 0.8

to 0.9 has been calculated from the scatter of the grain mass vs. grain diameter curve.

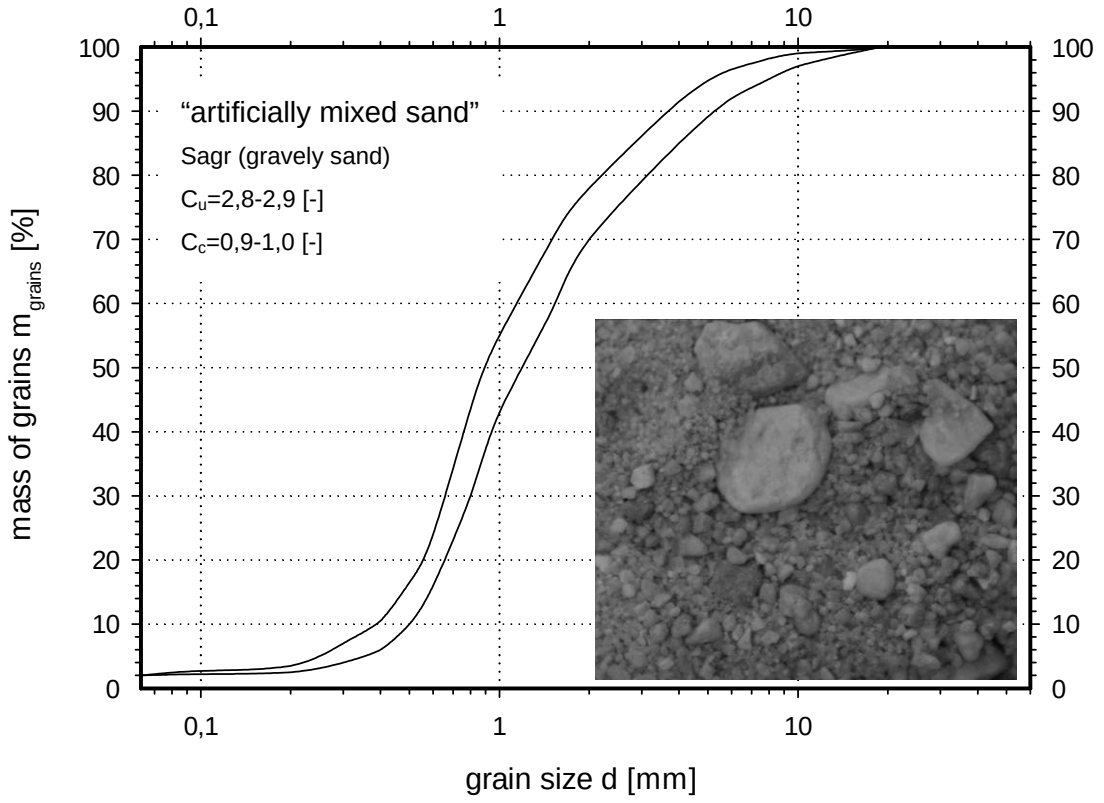

Fig. 33: Experimental backfill material: "artificially mixed sand".

Direct shear tests have been carried out to estimate the shear parameters of the gravely sand backfill material.

Tab. 8 Soil parameters for granular backfill material.

Property	Symbol	Value	Unit
unit weight	γ_s	26.4	[kN/m³]
coefficient of uniformity	C_u	2.8-2.9	[-]
coefficient of curvature	C_c	0.9-1.0	[-]
max. porosity	n_{max}	42.8	[%]
min. porosity	n_{min}	31.1	[%]
experimental porosity	n_{exp}	35.0	[%]
water content	w	0.23	[%]
peak friction angle	φ_{peak}	29.0-34.0	[°]
stiffness parameter (σ_{static} = 50-100 kN/m²)	E_s	40	[MN/m²]

A peak friction angle of φ_{peak} = 34.0° is determined. The stiffness parameters of the soil are investigated by performing oedometer tests. The stiffness parameter

E_s = 39.6 MPa is determined in the stress range of σ_{static} = 50-100 kN/m² (Table 8).

In order to reinforce the soil elements, three different geometrical and mechanical biaxial geogrids are used. One reinforcement material is a woven linear polyester (PET) geogrid (Chapter 3.3.3) and the other two geogrids are welded out of PET and polypropylene (Tab. 9).

The aperture sizes $a_{grid,x,y}$ of the welded geogrids amount to 32.0 mm in longitudinal and 32.0 mm in transverse direction. The tensile strength T_{max} and stiffness EA properties are investigated in detail in the strain range prestressing ε_{PRSi} = 0 % to 2.25 % to achieve the maximum stiffness of the geogrid.

Tab. 9 Material parameters for welded, biaxial, PP/PET geogrid.

Property	Symbol	Value	Unit
mass per unit area	ρ_s	250	[g/m²]
aperture size x	$a_{grid,x,}$	32.0	[mm]
aperture size y	$a_{grid,y}$	32.0	[mm]
max. tensile strength	T_{max}	40.0/40.0	[kN/m]
tensile stiffness PP/PET	EA	720-900/860-1150	[kN/m]

3.4.4 Experimental procedure

The installation of the gravely sand is described later in Chapter 3.4.3. The backfill material is dumped into the experimental device and compacted soil layer by layer mass and porosity controlled (n_{test} = 0.35) to ensure a constant packing density D = 0.75.

After the installation of the first soil layer h_{layer} = 0.125 m the geogrid (L/W = 0.6/0.25 m) is fixed on the moveable sidewall like being anchored on the facing in situ. Depending on the experiment the geogrid is prestressed with a predefined amount of strains ε_{PRSi} = 0.75, 1.5, 2.25 % on the opposite side of the moveable sidewall (Fig. 31) by utilizing the constructed prestressing apparatus.

In a next step the second soil layer h_{layer} = 0.125 m is dumped into the experimental device and compacted to achieve a constant and homogeneous packing density of the tested specimen.

After the installation of the measurement equipment mentioned in 3.4.2, the camera for the PIV analysis is installed. Finally a multistage static and cyclic loading is applied by the vertical hydraulic and horizontal pneumatic cylinder to test the soil element reinforced differently.

Tab. 10 Overview of the experimental procedure.

Test	Load situation 1	Load situation 2	Prestrain [%]
UR	x	x	
RE	woven PET/welded PP	woven PET/welded PET	
PRSp	woven PET/welded PP	woven PET/welded PET	0.75/1.5/2.25
PRSt	woven PET/welded PP	woven PET/welded PET	0.75/1.5/2.25

An overview of the experimental procedure is given in Table 10. In order to evaluate the performance of the soil structure reinforced by the concepts of PRS_i, described in Chapter 2, unreinforced (UR) and conventionally reinforced (RE) biaxial cyclic loading tests are conducted additionally. The amount of prestress in the geogrid reinforcement in the case of utilizing the concept of PRS_i is summarized in Table 10. The reinforcement is prestrained between ε_{PRSi} = 0.75 and 2.25 %.

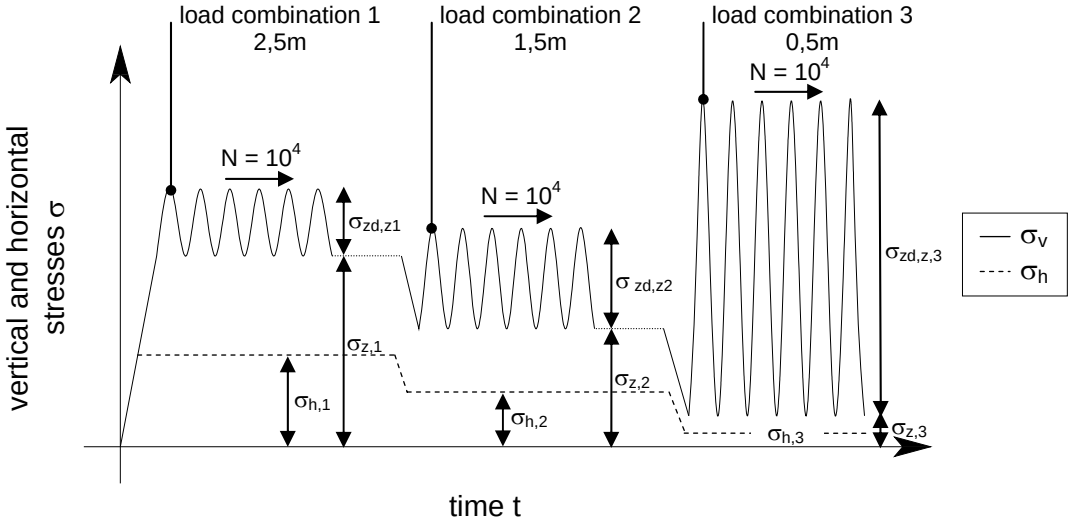

Fig. 34: Schematic sketch of load situation 1: vertical and horizontal stresses σ_v and σ_h plotted over time t for load combination 1, 2 and 3 (according to Burgstaller 2011).

All tests have been conducted with two loading situations. In the first loading situation the horizontal pneumatic cylinder supports the movable horizontal sidewall permanently with a constant pressure σ_h equal to a recalculated initial earth pressure distribution ($K = K_0 \sim 0.55$).

The vertical hydraulic cylinder loads the soil element with multistage static and cyclic pressures σ_v with respect to three predefined load combinations with a frequency f = 5 Hz recommended by Gotschol (2002). Figure 34 shows the schematic sketch of load situation 1. Vertical and horizontal stresses σ_v and σ_h are plotted over time t for load combination 1, 2 and 3.

In the first load combination, horizontal and vertical pressures σ_v and σ_h are applied. They represent the stress distribution in a soil element situated in the road bed in a depth z = 2.5 m under the sleeper of a railway. Those static and cyclic, respectively dynamic pressures σ_z and $\sigma_{z,d}$, last 10^4 load cycles N, respectively 2000 seconds.

Lower static but higher dynamic stresses representing the pressures in a depth z = 1.5 m under the sleeper of a railway act on the vertical load plate in case of testing the reinforced soil element during load combination 2 (Fig. 34).

There is a further of static stresses 0.5 m under the sleeper of a railway. On the contrary, acting dynamic loads increase in case of simulating a soil element closer to the surface (Fig. 34).

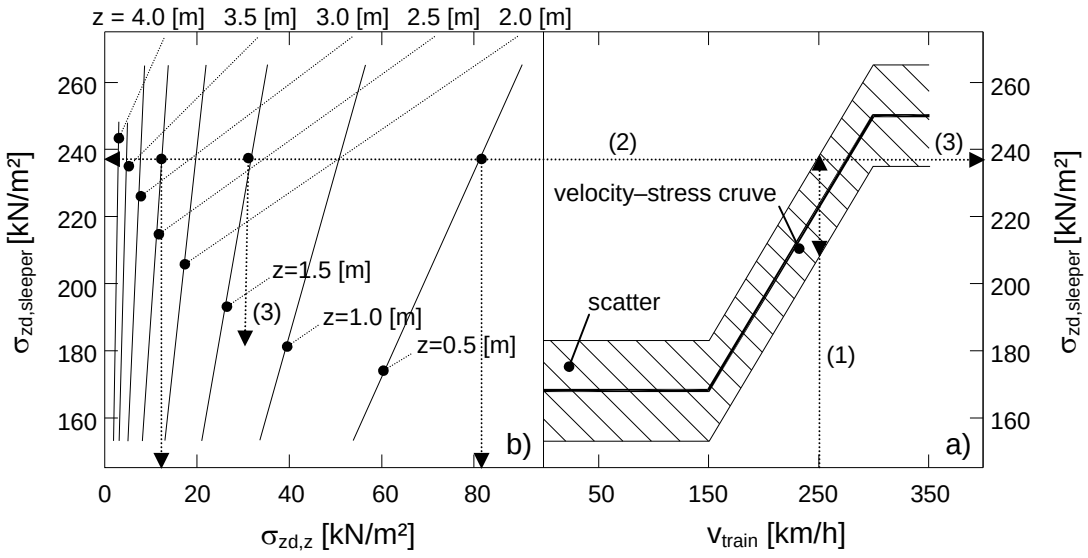

Fig. 35: Nomogram to estimate the static and cyclic load distribution in the ballast structure under a sleeper loaded by a train (200 kN load per axle) with a speed v_{train} of 250 km/h (according to Gotschol 2002): a) velocity v_{train} stress $\sigma_{zd,z}$ curve including scatter b) dynamic load $\sigma_{zd,z}$ in a certain depth z.

Figure 35 shows a nomogram to estimate the cyclic load distribution in the ballast structure under a sleeper. The Figure provides the investigated relation between the velocity v_{train} of a train (200 kN load per axle) and the dynamic stresses $\sigma_{zd,z}$ in a certain depth z in a ballast structure under the sleeper. The stress distribution generally correlates with the analytical assumption provided by Fröhlich (1934).

To estimated the dynamic stresses $\sigma_{zd,z}$ in the road bed in a certain depth z the nomogram in Figure 35 is utilized as followed. First an optional velocity v_{train} of a train is fixed. The arbitrarily fixed experimental velocity v_{train} of a train amounts

250 km/h. A vertical line (1) is drawn until the maximum scatter value of the stress velocity curve is reached. In a second step, a horizontal line (2) is plotted and the dynamic stresses occurring in a specific depth (z = 0.5, 1.5 and 2.5 m) are evaluated.

Figures 36a) and b) show the calculated stress distribution σ_v and σ_h over depth z with respect to the research results provided by Gotschol (2002).

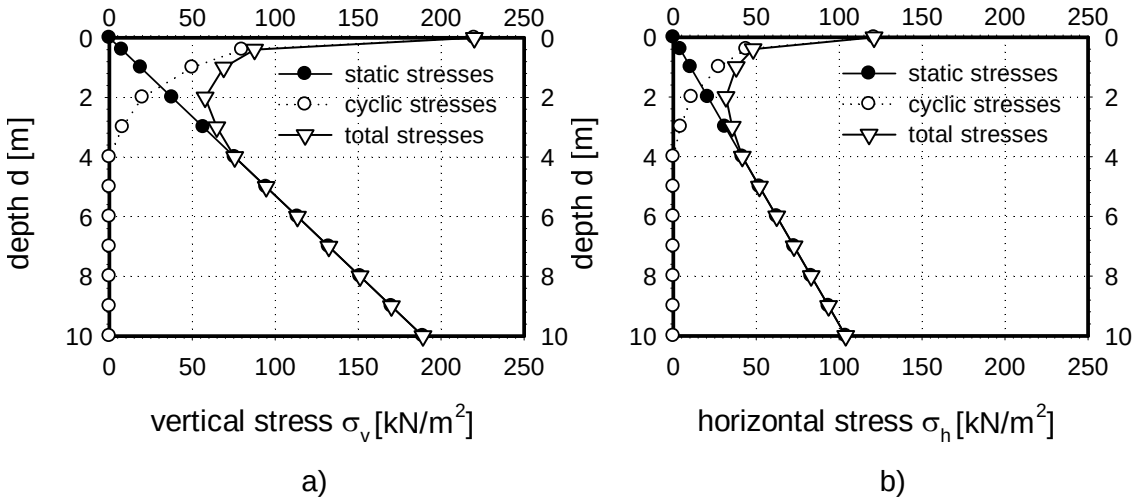

Fig. 36: Load distribution under the bar loaded by a train with a speed of 250 km/h (Gotschol 2002): a) vertical stresses σ_v versus depth d b) horizontal stresses σ_h versus depth d.

Table 9 provides the evaluated static and cyclic stresses σ_z and $\sigma_{zd,z}$ for the different load combinations.

Tab. 9 Load situation 1

Load situation 1 (Frequency = 5 Hz)	Vertical stresses [kN/m²]	Load cycles [-]	Variation of K_0
Load combination 1 (2.5 m under bar)	σ_z = 47.5 $\sigma_{zd,z}$ = 12.5	10^4	1.0
Load combination 2 (1.5 m under bar)	σ_z = 27.0 $\sigma_{zd,z}$ = 25.0	10^4	1.0
Load combination 3 (0.5 m under bar)	σ_z = 9.5 $\sigma_{zd,z}$ = 82.0	10^4	1.0

Figure 37 shows the schematic sketch of the stress time distribution occurring during load situation 2. During all load combinations 1, 2 and 3 static and cyclic respectively dynamic pressures σ_z and $\sigma_{zd,z}$ are kept constant. The horizontal support σ_h of the sidewall has been varied to investigate the influence of the horizontal position x of the soil element in the reinforced soil wall (Fig. 31). The

horizontal cylinder supports the side wall with the theoretically occurring horizontal stresses in situ. The horizontal support of the soil element changes with its distance *x* due to the facing in situ. The closer the soil element is situated to the facing of the geogrid reinforced soil wall, the smaller the soil element is supported horizontally.

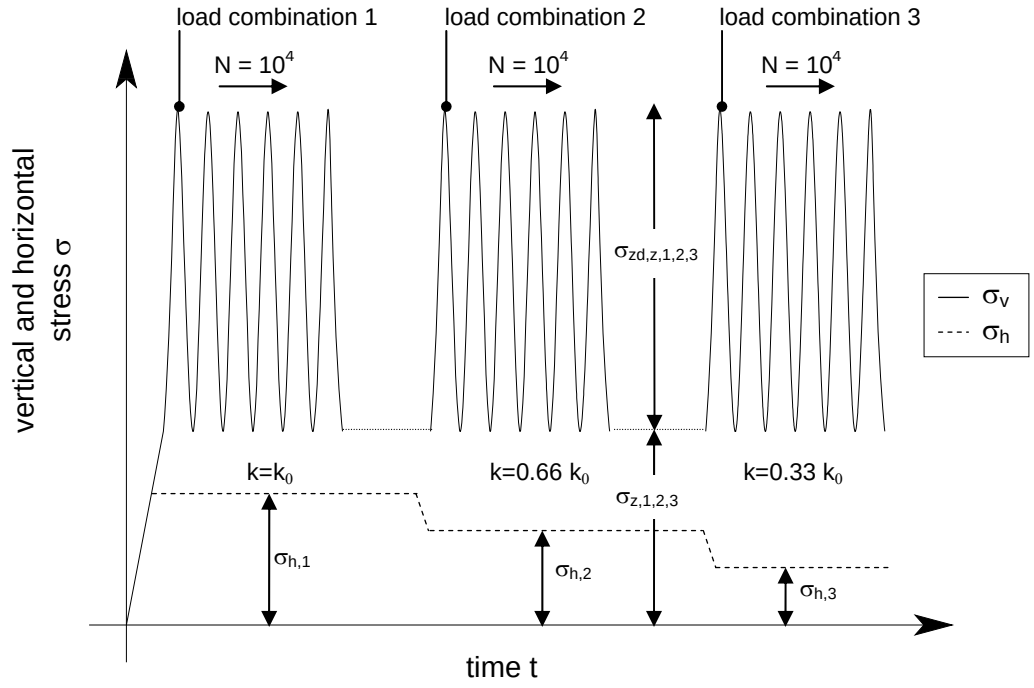

Fig. 37: Schematic sketch of load situation 2: vertical and horizontal stresses σ_v and σ_h plotted over time *t* for load combination 1, 2 and 3 (according to Burgstaller 2011).

Additionally the stiffness of the facing installed in front of the geogrid reinforced soil wall is investigated. The harder the wall facing behaves in situ the higher is the bedding support σ_h provided by the horizontal pneumatic cylinder fixed on the moveable sidewall of the experimental device. A hard and stiff facing such as a concrete panned is simulated by high horizontal support. A flexible soft wall facing such as a planted facing is represented by supporting the horizontal sidewall lowly. Therefore the horizontal support given by the pneumatic cylinder has been varied to a pressure σ_h equal to the horizontal stress distribution along the moveable horizontal wall and has been calculated with an earth pressure coefficient ranging from $K = K_0$ (hard facing), $K = 0.66 * K_0$ to $K = 0.33 * K_0$ (soft facing) (Table 10).

Conducting the tests according to loading situation 2 the vertical hydraulic cylinder compresses the test specimen with a static load of σ_z = 54.4 kN/m² and a cyclic pressure $\sigma_{zd,z}$ of 96.0 kN/m² (Table 10).

Both loading situations have been investigated with a constant frequency f = 5 Hz and a maximum number of load cycles $N_{max} = 10^4$.

Tab. 10 Load situation 2

Load situation 2 (Frequency = 5 Hz)	Vertical stresses [kN/m²]	Load cycles [-]	Variation of K_0
Load combination 1 (artificial load)	σ_z = 54.4 $\sigma_{zd,z}$ = 96.0	10^4	1.0
Load combination 2 (artificial load)	σ_z = 54.4 $\sigma_{zd,z}$ = 96.0	10^4	0.66
Load combination 3 (artificial load)	σ_z = 54.4 $\sigma_{zd,z}$ = 96.0	10^4	0.33

The findings of the cyclic biaxial tests with a doubled frequency f = 10 Hz do not show relevant influences on the time-displacement results presented subsequently in Chapter 3.4.5 (Burgstaller 2011).

3.4.5 Experimental results and discussion

This Chapter considers the mesoscopic and macroscopic experimental results of the cyclic biaxial element tests.

Macroscopic results are presented consecutively for the third load combination (0.5 m under the sleeper of a railway) measured during load situation 1 (Chapter 3.4.4). The time-displacement behaviour of the vertical loaded plate and the horizontal loaded side wall has been monitored. Results with respect to two different types of geogrids are compared.

The load displacement behaviour of the soil structures reinforced by different concepts (Chapter 2) has been validated. Figure 38 shows the settlements s_v normalized by the unreinforced failure settlements $s_{v,failure}$ versus time t for the woven PET geogrid. In case of testing the unreinforced soil element the structure fails after 600 seconds.

It can be stated that the vertical displacements s_v decrease by conventionally installing a geogrid. The normalized settlements measured at the top wall differ with respect to the interaction of 0 respectively 1 between the granular soil structure and the geogrid reinforcement. An interaction of 0 is applied to the reinforcing by adding no additional fixation at the end of the soil element. The geogrid may slide freely between the two soil layers which results in the ability of the reinforcement to move towards the vertical sidewall during loading (Fig. 40). In case of fixing the reinforcement at the end of the soil element the interaction is simulated as 1. The geogrid cannot slip respectively move

horizontally between the two soil layers so that an ideal interaction between soil and geogrid is assured. The fixity of the reinforcement results in a decrease in settlements s_v versus time t (Fig. 38).

By further prestressing the geogrid PRS_t and by releasing the prestress after compaction of the soil layer an ongoing decrease in settlement can be observed. The maximum effect in reducing vertical and horizontal displacements (Fig. 32) is reached by prestressing the geogrid permanently PRS_p. The settlements can be reduced to 20 % of the unreinforced settlements.

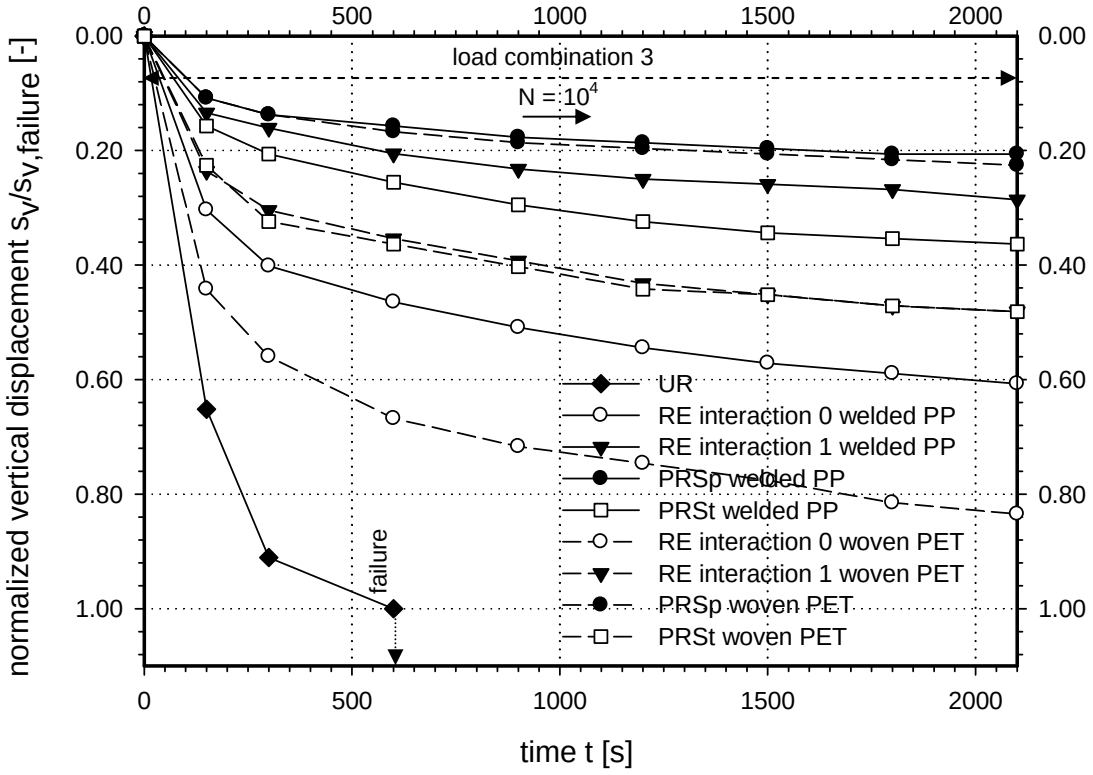

Fig. 38: Normalized vertical settlement $s_v/s_{v,failure}$ versus time t for the woven PET and the welded PP geogrid reinforcement: load situation 1, load combination 3.

As opposed to the results of the experiment presented in Chapter 3.3.5 the concept of temporarily prestressing (PRS_t) is not as effective. Interlocking effects between geogrid and gravely sand cannot be activated as intensely because of the grain size distribution of the backfill material. By releasing the prestressing in the geogrid the reinforcement slides back without, respectively with little interaction, in the case of reinforcing the sandy backfill material.

The interaction and thereby the additionally activated pressure forces in the soil structure increase with the same reinforcement material in combination with the coarse grained gravel (“Murschotter” 8/16 mm) described in Chapter 3.3.3.

Interfriction is activated while the geogrid is being pulled back but additional interlocking effects do not occur. Therefore additional pressure forces cannot be activated due to the granular soil particles by interlocking effects (Chapter 2).

Figure 38 is drawn to compare the results of installing different kinds of geogrids used for the experiments. The graph shows the normalized settlements s_v versus time t for a welded PP geogrid. The overall settlements s_v are smaller compared to the results gained from the tested soil elements reinforced with woven PET geogrids. This is due to the high stiffness property EA of the PP geogrid.

Figure 39 presents the normalized horizontal displacements s_h versus time t for both types of geogrids. After 600 seconds the horizontal moveable sidewall collapses in case of testing the unreinforced soil element (UR). After conventionally reinforcing the soil element (RE), equilibrium can be reached till the maximum number of load steps N=10^4.

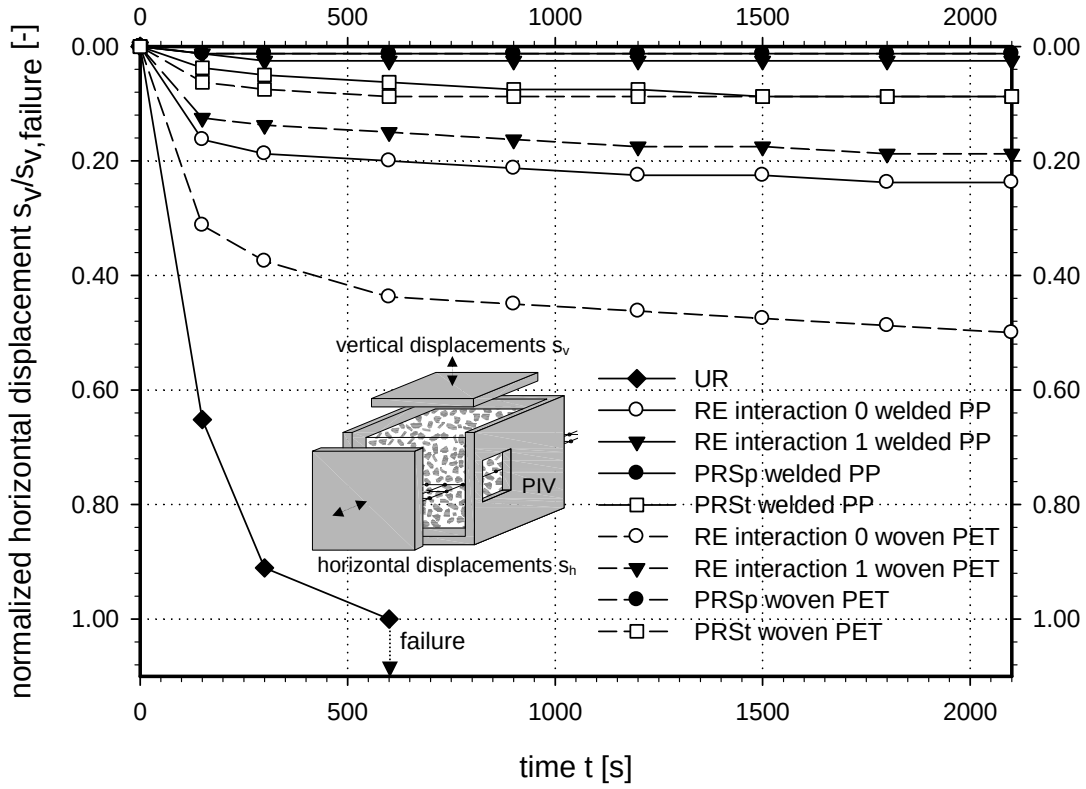

Fig. 39: Normalized horizontal displacement $s_h/s_{h,failure}$ versus time t for the woven PET and the welded PP geogrid reinforcement: load situation 1, load combination 3.

The normalized horizontal displacement s_h measured at the moveable side wall of the experimental device decrease in the case of conventionally (RE) reinforcing the soil element with an interaction of 1.

The horizontal displacements of the moveable sidewall again decrease in case of utilizing the concept of PRS_i. Rather small displacements are observed in case of prestressing the geogrid permanently. It therefore can be stated that the concept of PRS_p highly improves the vertical and horizontal displacement behaviour of the soil element versus time *t*.

It can further be stated that the welded PP geogrid performs better with respect to the woven PET reinforcement relating to the horizontal and vertical wall deformations. The welded PP reinforcement offers a higher tensile stiffness EA itself. The higher the stiffness of the reinforcement the stiffer the soil element generally behaves.

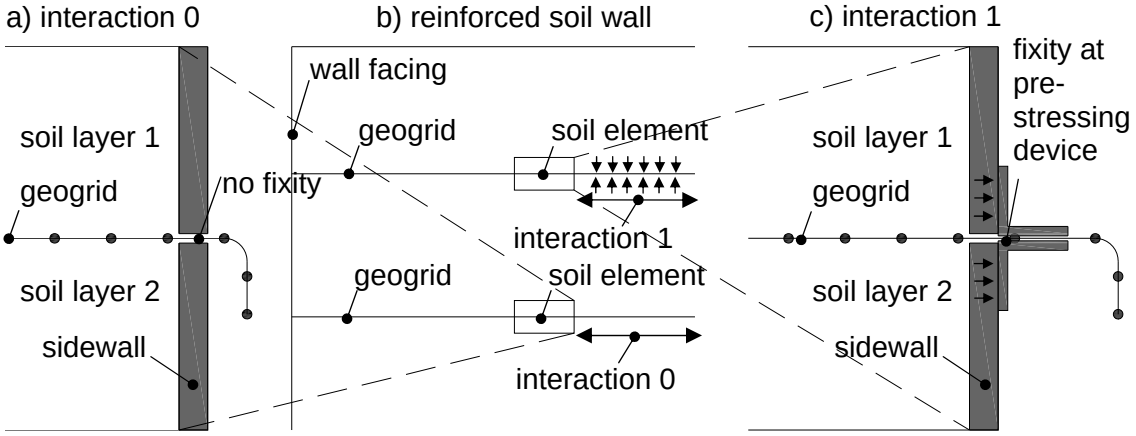

Fig. 40: Schematic sketch of interaction: a) end of the biaxial static and cyclic loaded soil element without fixity of the geogrid (interaction 0) b) typical geogrid reinforced soil wall including the positions of the biaxial loaded soil element c) end of the biaxial static and cyclic loaded soil element with fixity of the geogrid (interaction 1) (modified according to Burgstaller 2011).

In order to evaluate the influence of the horizontal position of the soil element, or the stiffness of the facing, the soil element has been loaded under loading situation 2 (Chapter 3.4.4).

A vertical artificial constant pressure σ_v is applied during all load cycles N=10^4. The support σ_h provided by the horizontal pneumatic cylinder fixed on the moveable sidewall varies after 2000 seconds (N = 10^4). In the first load combination the sidewall is supported with a horizontal pressure σ_h recalculated with an earth pressure coefficient $K = K_0$. After 2000 seconds the horizontal support decreases with regard to an earth pressure coefficient of $K = 0.66 * K_0$. In the last load steps (loading combination 3) the horizontal supports σ_h further decreases according to an earth pressure coefficient $K = 0.33 * K_0$.

During load situation 2 the soil element is reinforced with the PET woven geogrid described in Chapter 3.3.3. A welded PET geogrid described in Chapter 3.4.3 is additionally installed to investigate the performance of different reinforcement types.

As pointed out in Chapter 3.4.4 the reinforced soil element is biaxially loaded with artificially fixed static and cyclic vertical stresses σ_v. The horizontal stresses during the three load combinations change as described in Chapter 3.4.4.

Figure 41 shows the settlements s_v normalized by the unreinforced failure settlements $s_{v,failure}$ versus time t for the woven PET geogrid. Load combination 1, 2 and 3 ($N = 10^4$) are additionally shown in Figure 41.

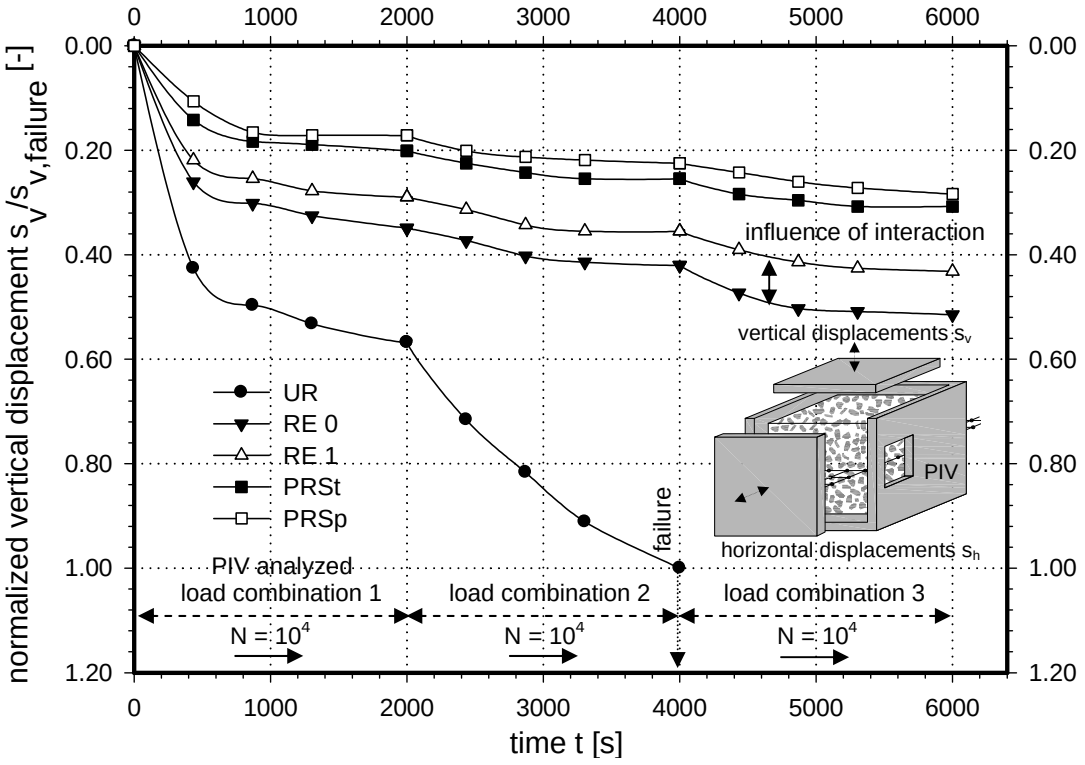

Fig. 41: Normalized vertical displacement $s_v/s_{v,failure}$ versus time t for the woven PET geogrid reinforcement: load situation 2, load combination 1, 2 and 3.

In case of testing the unreinforced soil element the structure fails just after starting the third load combination (Fig. 41, failure 4000 seconds).

After the installation of the woven PET geogrid reinforcement the soil structure is able to resist the cyclic loading during load combination 3. The influence of the interaction between reinforcement and soil is shown in Figure 41. The better the interaction (interaction 1), the lower the settlements s_v normalized by the unreinforced failure settlements $s_{v,failure}$ over time t. The reinforced settlements

vary between 40 % and 50 % of the unreinforced settlements. There is a further decrease of settlements after utilizing the concept of PRS_i. Permanent prestressing to the reinforcement PRS_p show the best settlement behaviour over time *t*. The measured settlements after 4000 seconds reach about 20 % of the unreinforced vertical displacements just before failure.

During loading situation 2 the horizontal displacements s_h of the moveable sidewall have been measured. Figure 42 shows the normalized horizontal settlements $s_h/s_{h,failure}$ versus time t for the woven PET geogrid reinforcement during load combination 1, 2 and 3. The unreinforced soil structure collapses after 4000 seconds which results in a large and sudden horizontal movement of the moveable wall.

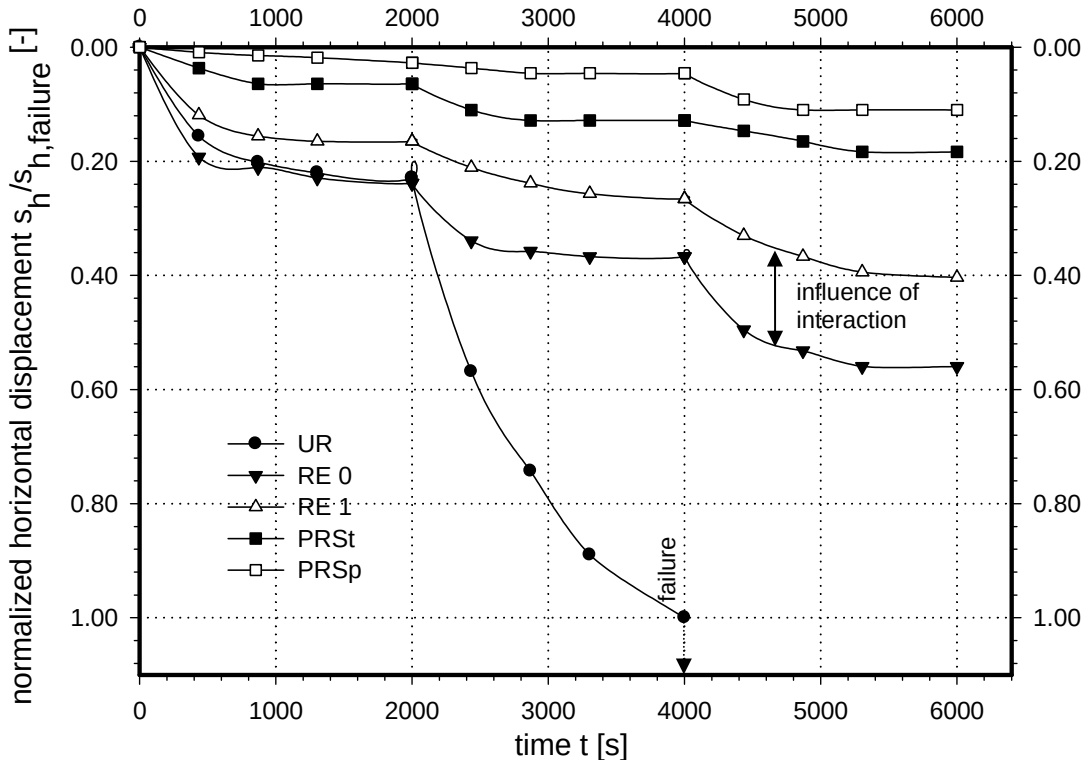

Fig. 42: Normalized horizontal displacement $s_h/s_{h,failure}$ versus time *t* for the woven PET geogrid reinforcement: load situation 2, load combination 1, 2 and 3.

The influence of the reinforcement on the horizontal displacement s_h of the sidewall over time *t* is shown in Figure 42. After 4000 seconds the sidewall deforms less than 40 % of the unreinforced sidewall deformation. It is shown that the interaction between geogrid and surrounding soil is of high importance regarding the displacement behaviour of the reinforced soil structure.

The normalized horizontal displacements $s_h/s_{h,failure}$ decrease in the case of utilizing the concept of PRS_i. Just before failure the wall moves horizontally 80

to 90 % lower than the moveable sidewall deforms if testing the unreinforced soil element.

Figure 43 represents the settlements s_v normalized by the unreinforced failure settlements $s_{v,failure}$ versus time t for the welded PET geogrid. Figure 43 additionally shows the load combinations 1, 2 and 3 (N = 10^4). After 4000 seconds the vertical displacements s_v of the reinforced soil element reach 60 % of the unreinforced settlements s_v. The soil reinforcement interaction (RE 0 – RE 1) highly influences the vertical displacement behaviour over time t. The settlements measured while testing the reinforced soil element with high interaction (RE 1) amount to 20 % of the settlements resulting from reinforced soil tests with low (RE 0) interaction.

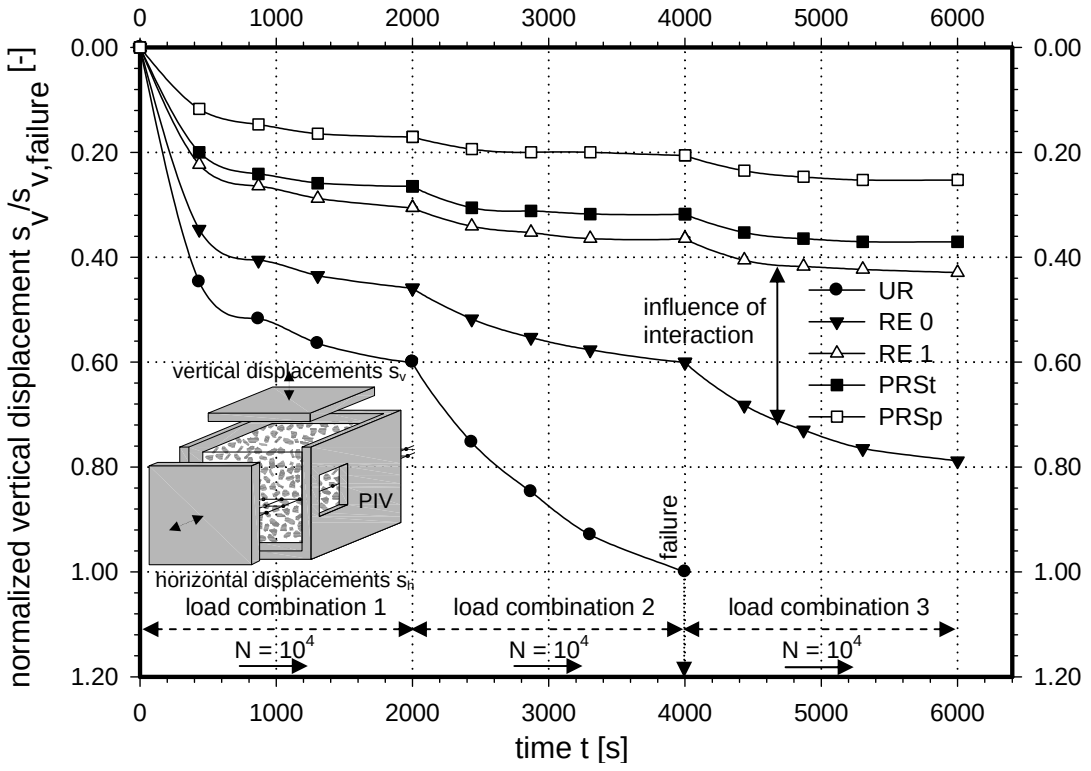

Fig. 43: Normalized vertical displacement $s_v/s_{v,failure}$ versus time t for the welded PET geogrid reinforcement: load situation 2, load combination 1, 2 and 3.

The reinforcement generally performs worse than the PET woven geogrid (Fig. 41). This is due to the low interaction behaviour between geogrid and soil. Tests results from soil elements reinforced with the concept of PRS_t confirm this statement. The settlements reach values up to 35 % of unreinforced settlements. Tests with the PET woven geogrid used as reinforcement for the concept of PRS_t (Fig. 41) show values about 25 % of the unreinforced settlements. The concept of PRS_p once again shows the best performance.

Figure 44 shows the normalized horizontal settlements $s_h/s_{h,failure}$ versus time t for the welded PET geogrid reinforcement during load combination 1, 2 and 3. The woven PET geogrid (Fig. 42) performs slightly better. Vertical but also horizontal displacements during all loading combinations are by trend lower than in the case of conducting cyclic load tests with the woven PET geogrid reinforcement.

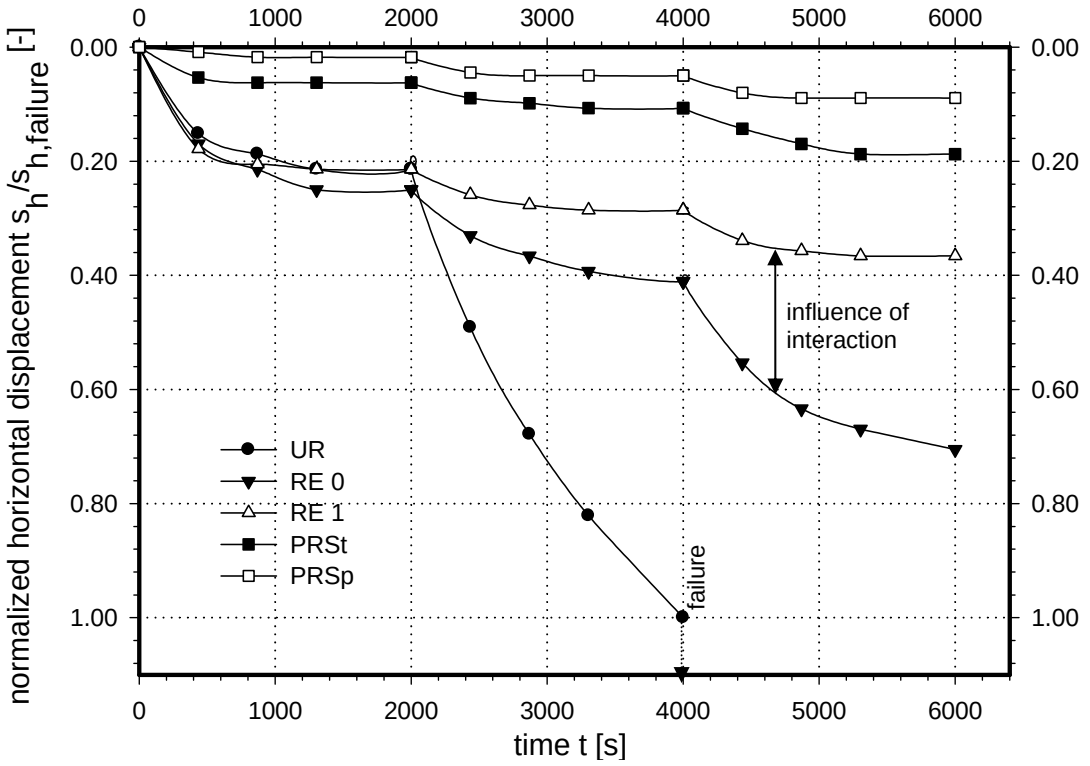

Fig. 44: Normalized horizontal displacement $s_h/_{h,failure}$ versus time t for the welded PET geogrid reinforcement: load situation 2, load combination 1, 2 and 3.

Further, the mesoscopic behaviour of the gravely sand and the reinforcement is investigated by using the Particle Image Velocimetry (PIV) method (Raffel et al 2007). High resulted photos (10.1 Mio megapixels) are taken before, during and after each cyclic stage (load combination 1, 2 and 3). The photos are analyzed and the displacements of the granular soil particles and the geogrid are visualized.

The mesoscopic results of the second load situation, load combination 1 (Fig. 41) are shown in Figure 45a), b) and Figure 46a), b). The shadings of the vertical settlement s_v and the horizontal displacement shadings s_h are presented for the different reinforcing concepts described in Chapter 2.

The horizontal s_h and vertical displacements s_v reach their maximum among the investigated area in the case of evaluating the shading plots of the unreinforced

soil element (Fig. 45a) and b). The horizontal support ($\sigma_h = f(K_0)$ Table 10) provided by the moveable sidewall is not sufficient enough. Some failure progresses along a visible shear zone. The shading plots mesoscopically evaluate the macroscopic collapse of the soil element presented in Figure 41 and 42.

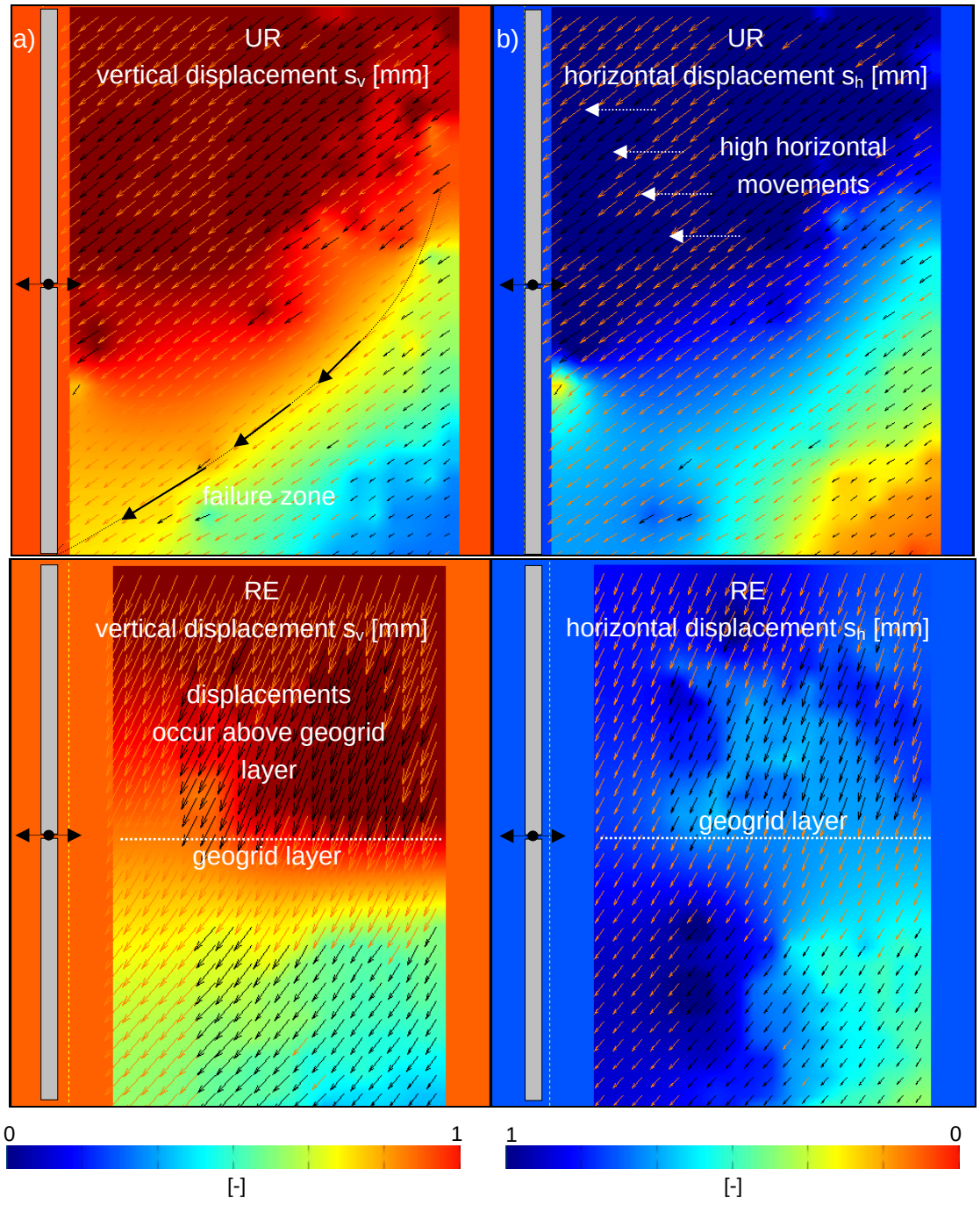

Fig. 45: Normalized displacement shadings for unreinforced (UR) and conventionally reinforced (RE) soil element out of PIV: a) vertical displacements s_v b) horizontal displacements s_h.

Displacements decrease in the case of testing a reinforced soil element. No mesoscopic collapse can be evaluated. The reinforcement provides the missing horizontal support and the soil element finally reaches equilibrium.

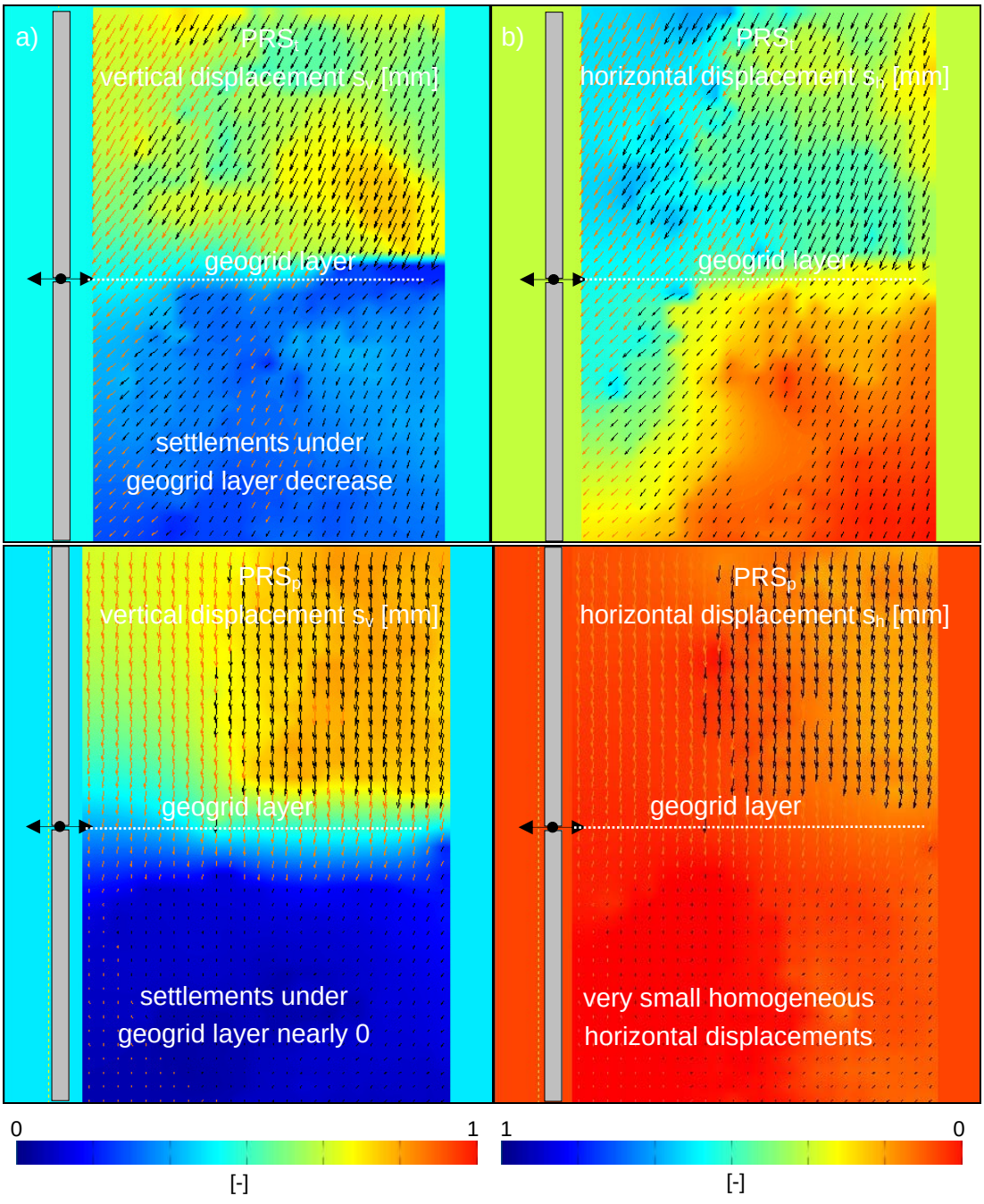

Fig. 46: Normalized displacement shadings for temporarily and permanently prestressed reinforced soil element out of PIV: a) vertical displacements s_v b) horizontal displacements s_h.

When utilizing the concept of PRS_i the shading plots show a further decrease of the horizontal and vertical displacements s_h and s_v (Fig. 46a), b). Vertical and horizontal displacements are higher above the geogrid layer than below the

reinforcement. This effect is described in Chapter 4.4. The reinforcement provides an additional bedding support to the soil element by a discrete interaction between the granular particles and geogrid reinforcement as described in Chapter 2.

This bedding support further increases by prestressing the geogrid, either temporarily PRS_t or permanently PRS_p. In the case of utilizing the innovative concept of PRS_p the displacements below the geogrid are nearly zero. The first soil layer and the prestressed geogrid resist the cyclic loading without transferring the experimentally applied stresses into the second soil layer.

This behaviour is shown in detail in Figure 47. The vertical displacements s_v normalized by the unreinforced displacements $s_v/s_{v,failure}$ have been analyzed over a vertical section (7 cm) of the PIV window. High displacements occur above the geogrid layer. Below the reinforcement layer the settlements once again (Chapter 4.4) decrease rapidly.

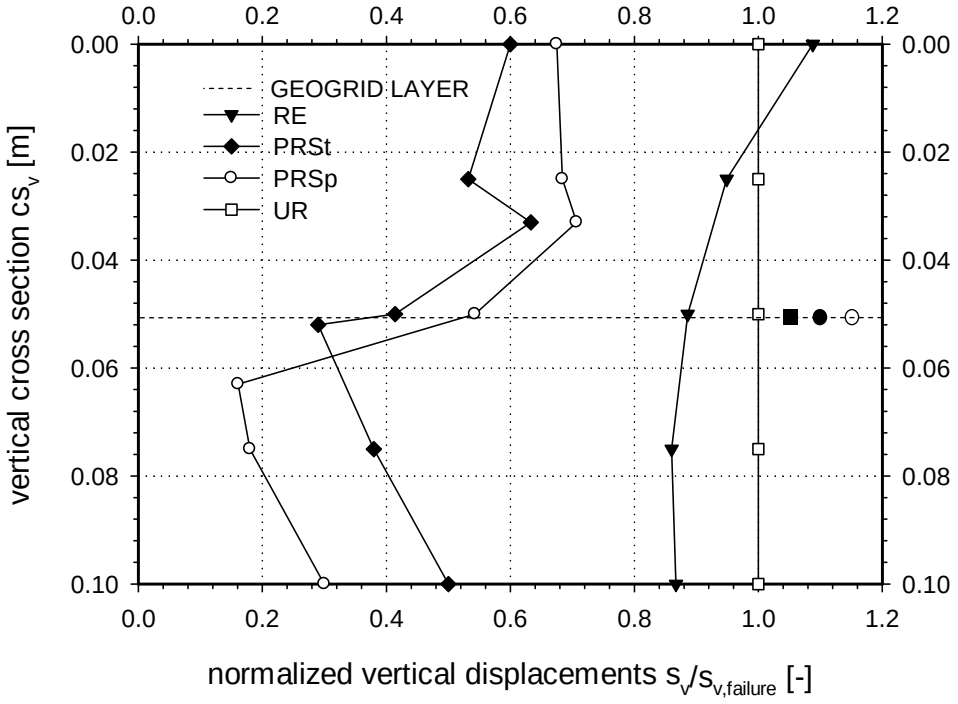

Fig. 47: Normalized vertical displacements $s_v/s_{v,failure}$ out of PIV analyzing a vertical cross section in the middle of the PIV window.

Normalized vertical displacements s_v decrease to a value of 85 % of the unreinforced (UR) settlements by conventionally reinforcing (RE) the soil element (Fig. 47). When prestressing the reinforcement temporarily, settlements reach a value of 50 % with respect to the unreinforced soil element. 20 to 30 % of the unreinforced settlements can be recalculated of the vertical cross section when reinforcing the soil element with the concept of PRS_p.

It can finally be stated that the positive effects of the concept of PRS_i (Chapter 2) are verified macroscopically and mesoscopically under cyclic loading conditions.

3.5 Summary and conclusions

In this Chapter the concept of prestressed reinforced soil (PRS_i) to improve the load displacement behaviour of reinforced soil structures has been validated by large scale experimental test results produced at the Institute of Soil Mechanics and Foundation Engineering at Graz University of Technology, Austria. More than 60 path-controlled static load displacement tests have been performed. The overall results have shown an improvement of the macroscopic load displacement behaviour of the structure by installing the geogrid reinforcement. By prestressing the geogrid reinforcement PRS_i a further increase in strength and stiffness of the reinforced structure can be observed. The static test results have shown that the macroscopic maximum bearing capacity can be more than doubled by prestressing the geogrid reinforcement temporarily (PRS_t).

These macroscopic effects have been investigated mesoscopically by performing PIV analyses. It can be visualized photogrammetrically and thereby stated that by prestressing the geogrid, an additional bedding support is activated. The positive effects of the concept of PRS_i result in a general decrease of the local bearing capacity failure mechanism. Furthermore, it can be stated that the visualised displacements below the geogrid reinforcement layer decrease rapidly.

In addition, the test results of 87 cyclic load displacement tests in Weimar, Germany, to validate the concept of PRS_i under cyclic loading conditions have been presented. A soil element taken out of a reinforced soil structure is used to investigate the behaviour of the reinforced soil structure under specific biaxial load and horizontal support conditions. The macroscopic research has shown that displacements can be reduced by conventionally installing a geogrid. By further prestressing the geogrid PRS_t and releasing the prestress after compaction the soil layer settlements decrease further. The maximum effect in reducing vertical and horizontal displacements is reached by prestressing the geogrid permanently PRS_p. The settlements occurring under cyclic loading could have been decreased up to 20 % of the unreinforced displacements (normalized vertical displacements $s_v / s_{v,failure} = 0.2$).

After conducting mesosopic investigations, it can be stated that high displacements are visualized above the reinforcement layer. Below the geogrid layer the settlements occurring under cyclic loading decrease rapidly.

Furthermore, it can be stated that the reinforcement stiffness is of high importance in relation to the reinforced soil structures load displacement behaviour. The stiffer the geogrid behaves the better the general behaviour of the reinforced soil structure. The better is the geogrid soil interaction the better the overall load displacement behaviour. According to this fact temporary prestressed reinforced soil PRS_t should be applied in combination with coarse grained material such as the gravel described in Chapter 3.3.3.

In conclusion it can be stated, that the system of PRS_i has been experimentally, statically and cyclically, validated. By using the same materials, soil and reinforcement, and by prestressing the geogrid reinforcement with the concept the load displacement behaviour of reinforced soil structures can be increased properly.

4 Numerical investigations on prestressed reinforced soil (PRS_i) by geogrids

4.1 Introduction

Numerical investigations are presented in Chapter 4. First, the concept of PRS_i, presented in Chapter 2, is generally validated. Second, results of the experimental investigations (Chapter 3.3) are evaluated in detail. Multiscale modelling is utilized to investigate the macroscopic load displacement behaviour of the reinforced soil structures. Additionally, the mesoscopic soil geogrid interaction behaviour and the load transfer mechanism of the geogrid reinforced granular soil structures are investigated. Multiscale modelling (Chapter 4.3) combines macroscopic Finite Element modelling (FEM) and mesoscopic Discrete Element modelling (DEM).

4.2 Literature review: numerical investigations on prestressed reinforced soil (PRS_i) by geogrids

Galvanetto & Aliabadi (2010) provide the fundamental computational approaches regarding multiscale modelling in solid mechanics. The basic hypothesis states that a material, macroscopically assumed as homogeneous consists micro- respectively mesoscopically, of distinguishable components. In case of computationally modelling soil macroscopically a continuously homogenous soil element is assumed. This is true for continuum mechanics approaches such as Finite Element modelling. In the case of investigating the continuously assumed soil element in a mesoscopic scale, discrete soil particles can be visualized. The mesoscopic discrete behaviour is nowadays computed by Discrete Element modelling approaches. Cundall & Strack already presented a discrete numerical model for granular assemblies in 1979.

It has to be stated that both computational approaches have their limitations. As previously pointed out in the case of conducting fast and effective macroscopic finite element modelling, the mesoscopic discrete soil particle interaction is totally neglected. By utilizing highly sophisticated mesoscopic discrete element analysis, computational time due to the state of the art, CPUs is a restricting factor. This results in simulating small numerical models in a mesoscopic scale.

Later (Chapter 4.3 and 4.4) macroscopic finite element modelling and mesoscopic discrete modelling are presented to investigate the concepts presented in Chapter 2 fast, effectively and detailed by utilizing a simple multiscale approach.

4.2.1 Finite Element Method (FEM) investigations

Lovisa et al. (2009) performed Finite Element Method simulations to investigate the effect of a prestressed geotextile, installed in a sand bed supporting a circular footing. In order to validate the results gained from conducted experiments (Chapter 3.2.1) Lovisa et al. (2009) utilized radial symmetrical Finite Element modelling. A Finite Element analysis has been carried out using an axis-symmetric numerical model. The mesh boundaries are based on the tank dimensions used for the physical model test (Lovisa et al. 2009). A preliminary Finite Element analysis has demonstrated that the boundary distances do not influence the results. Stresses and deformations have been developed well within the boundaries. The settlement of the rigid footing is simulated using prescribed displacements. The prestress in the geotextile has been applied by activating a prestress force at the end node of the geosynthetic reinforcement material. The numerical results have shown a sound agreement with the ones obtained from physical model tests (Lovisa et al. 2009).

4.2.2 Discrete Element Method (DEM) investigations

As there is little literature available regarding prestressed reinforced soil concepts (Chapter 2) hardly any relevant mesoscopic numerical simulations for PRS_i are available in the respective international journals. Still, the discrete soil geogrid interaction has been investigated by several researchers in the last years (Konietzky et al. 2004, Bauer et al. 2006, Konietzky 2006, McDowel et al. 2006, Zhang et al. 2007, Bhandari & Han 2010, Tutumluer et al. 2009, Stahl. & Konietzky 2011).

Three dimensional discrete element simulations have been utilized to model numerical triaxial tests on soil elements reinforced with one to three layers of a geometrically detailed modelled geogrid. Konietzky et al. (2004) and Konietzky (2006) conclude that the performed DEM simulations of triaxial reinforced soil element tests have given a valuable insight into the soil geogrid interaction mechanism.

Discrete element method (DEM) simulations have been used to model the interaction between ballast material and a geogrid by simulating pull-out tests

and comparing their results with experimental data by McDowel et al. (2006). The DEM simulations predict precisely the peak mobilised resistance and the displacement necessary to mobilise a peak pull-out force. In addition, the effect of the ratio of the geogrid aperture size to ballast particle diameter on the pull-out resistance has been investigated. McDowel et al. (2006) found that a value of 1.4 is the ideal ratio between the opening size of the geogrid and the diameter of the grain.

Zhang et al. (2007) performed discrete simulations of pullout tests to investigate the effect of compaction of the reinforced soil body on the pullout force during the tests. The results of the discrete modelling have correlated with the tests results gained from laboratory studies.

Bhandari & Han (2010) have utilized two dimensional Discrete Element modelling to investigate the soil geotextile interaction under a cyclic vertical load. The DEM results show that the geotextile prevents the particles from vertical movement. At the same time the geotextile anticipates the horizontal movement of the granular, spherical particles. This is due to the lower frictional resistance of the soil particles, rolling and sliding on the surface of the geotextile. Bhandari & Han (2010) state that the benefit of the geotextile in minimizing the vertical deformation depends on the vertical position of the geotextile.

Tutumluer et al. (2009) conducted a detailed discrete element study on direct shear tests including two different shapes (angular and triangular) of discrete geogrids. Out of the utilized numerical simulations but also as a result of conducted direct shear tests in the laboratory, Tutumluer et al. (2009) found out that the soil geogrid interaction coefficients α becomes higher than 1.0 in case of reinforcing the soil element in the shear box. This is due to the interlocking effects between the discrete particles and the gaps of the geogrid reinforcement. Tutumluer et al. (2009) concludes that both geogrid geometries have provided significant stiffening effects.

4.3 Multiscale Finite Element and Discrete Element modelling

The multiscale Finite and Discrete Element modelling combines investigations on the macroscopic load displacement behaviour of the presented experiment (Chapter 3.3) and the validation of the results from the mesoscopic soil geogrid interaction analysis with the Particle Image Velocimetry method (Chapter 3.3). The investigation process regarding the performed multiscale modelling is consecutively described in the presented flow chart (Figure 48). Fast and effective two dimensional (2D) Finite Element simulations are utilized to back

analyse the experimental procedure and thereafter to compare the experimental macroscopic results with the one generated by the numerical analysis. Those simulations are also conducted to further evaluate the stress and deformation behaviour of the geogrid reinforced soil structure and to investigate occurring tensile forces in the reinforcement in detail.

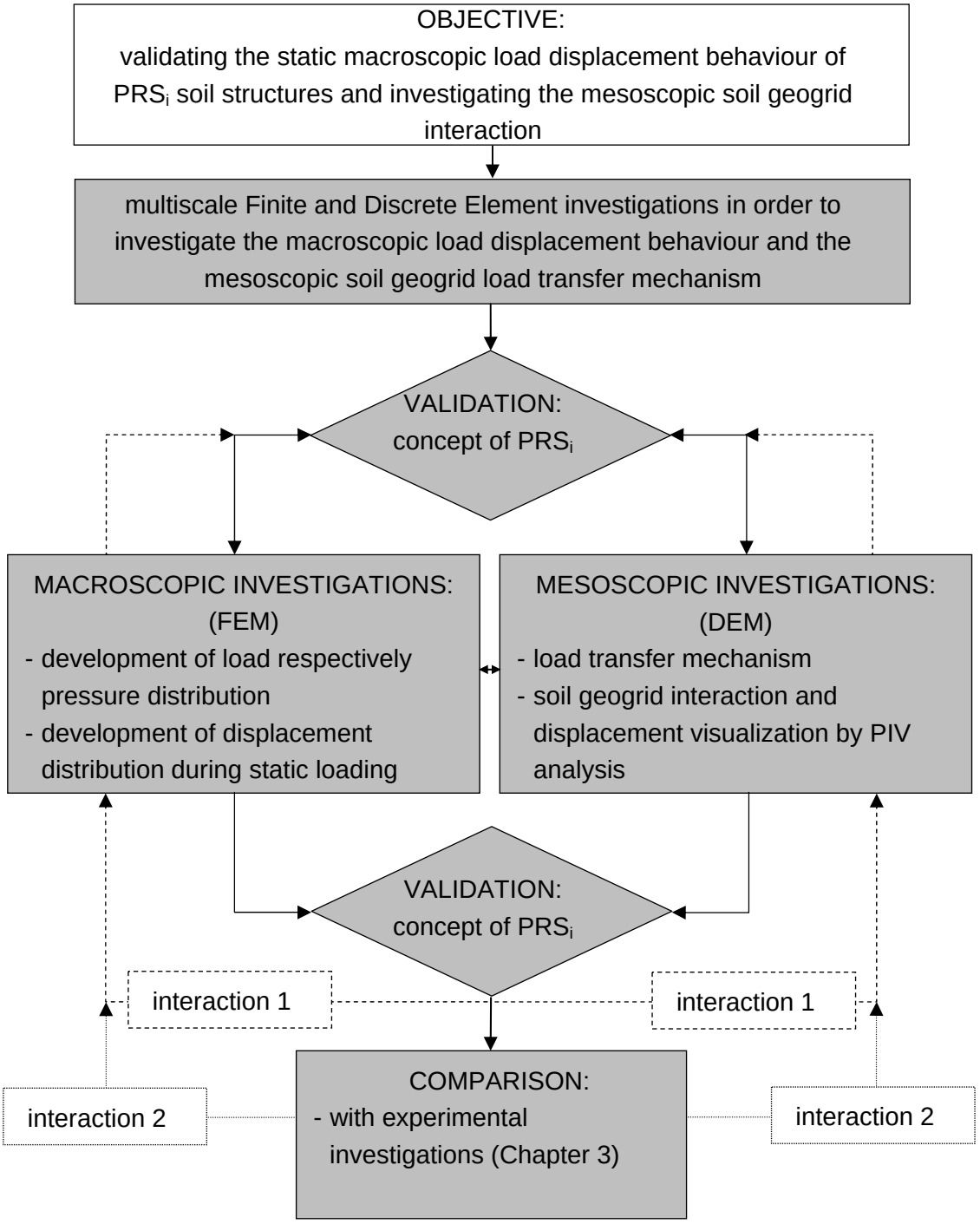

Fig.48: Flow chart: overview on the numerical multiscale Finite and Discrete Element investigations.

The Finite Element simulation is additionally performed to calculate the macroscopic stress and deformation boundaries as an input value for the mesoscopic Discrete Element model (Figure 49 a). The calculated stresses and deformations evaluated from the Finite Element simulation in a predefined plane are utilized to define the mesoscopic boundary conditions for the DEM model (Figure 49 b). The deformation boundaries resulting from the Finite Element simulation are validated by the conducted plane strain PIV analysis (Chapter 3.3) in the laboratory (Figure 49 c).

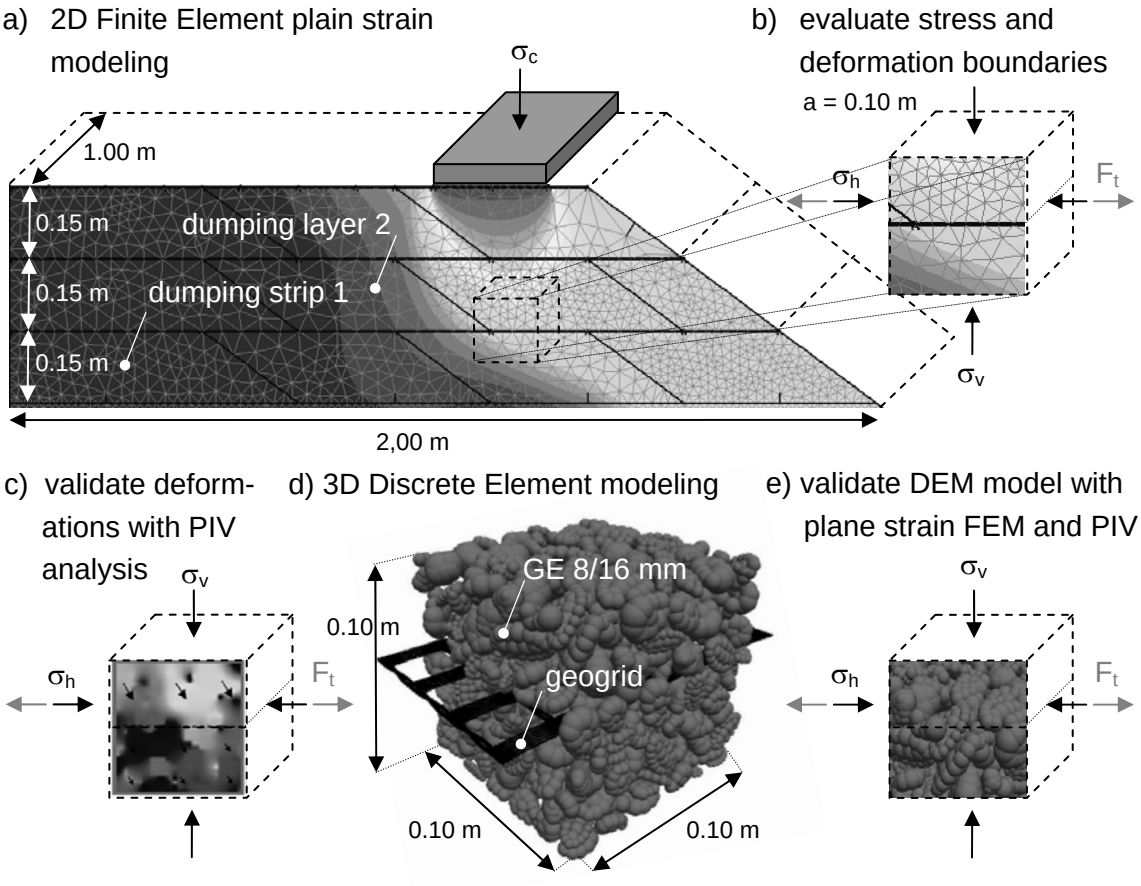

Fig. 49: Schematic sketch of multiscale Finite and Discrete Element modelling: a) 2D Finite Element model under plane strain conditions b) evaluation of the stress and deformation boundaries out of FEM model c) validation of the results by PIV comparison. d) 3D Discrete Element modelling e) validation of DEM model with plane strain PIV analysis and FEM model.

A three dimensional (3D) Discrete Element model with boundary conditions evaluated, from macroscopic Finite Element simulations is finally constituted (Figure 49 d). Deformations of the geogrid and the granular soil particles are visualized on a predefined plane to compare the results with the ones calculated by utilizing Finite Element simulations and by conducting PIV analyses (Figure 49 e). To gain a detailed insight in the discrete soil geogrid interaction process,

the soil element is investigated in three dimensions, regarding the load transfer mechanism of the reinforced soil element. The effect of prestressing the geogrid reinforcement in between the numerical discrete soil grains will additionally be evaluated mesoscopically.

4.4 Finite Element Method (FEM) investigations on prestressed reinforced soil (PRS_i) by geogrids

In this Chapter, investigations on prestressed reinforced soil utilizing Finite Element Method modelling are presented. As pointed out in Chapter 4.3, the two dimensional (2D) Finite Element model is employed to evaluate the macroscopic load displacement behaviour of the reinforced soil structure. The results are compared with the experimental investigations described in Chapter 3.3. Furthermore, the plain strain simulation is performed to calculate the macroscopic stress and deformation boundaries as an input value for the mesoscopic Discrete Element model (Chapter 4.5).

4.4.1 Overview on the numerical model

A two dimensional plane strain Finite Element model has been employed in order to analyse the experimental investigations presented in Chapter 3.3. For this analysis a two dimensional Finite Element Code provided by Plaxis (Version 2010.01) has been employed (Brinkgreve et al. 2010).

4.4.2 Numerical setup and calculation process

Brinkgreve et al. (2010) provide the principals on Finite Element Modelling with the Plaxis Code. The basic geometry of the numerical model is presented in Figure 50.

The boundaries of the numerical model are set by applying horizontal and vertical fixities on the hard facing sidewall and the bottom of the experimental device. Interface elements are utilized to model the interaction between the experimental device and the backfill material. In addition, interface elements are implemented to model the macroscopic soil geogrid interaction behaviour.

The numerical model of the backfill material consists of three dumping layers and 11 dumping strips. Each dumping strip is compacted with a compaction plate and loaded with a compaction force F_c. To finally test the backfill material,

vertical displacements s_v = 3.5 cm are prescribed on the load plate. In the case of utilizing PRS_i, the geogrid reinforcement is prestressed with ε_{PRSi} = 2.5 % by prescribed displacements.

The reinforcement is modelled with linear elastic geogrid elements implemented in the two dimensional Finite Element Code provided by Plaxis (Version 2010.01). A 15 noded element calculation has been performed.

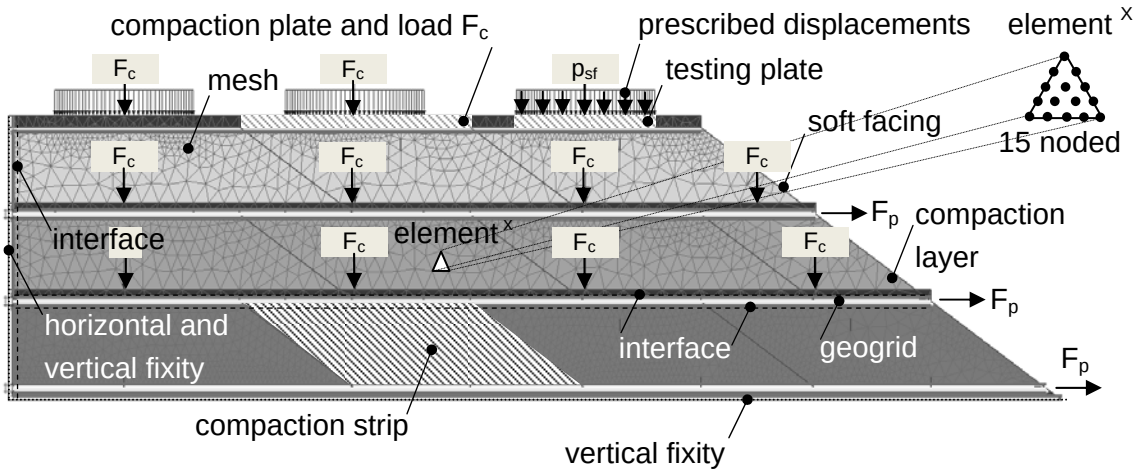

Fig. 50: Schematic sketch of the overview on Finite Element model: boundary fixities and interfaces, compaction strip and layer, geogrid and interfaces, compaction and testing plates, prescribed displacements for testing and prestressing the geogrid.

4.4.3 Numerical material parameters

The numerical input parameters for the granular backfill material called "Murschotter" (Chapter 3.3.3) are given in Table 11. Taking into account the increase of stiffness over depth of the granular soil material, the hardening soil model (Benz 2007) provided by Plaxis has been utilized. The increase of stiffness during the compaction process is accounted for a model that includes stress depending stiffness.

The numerical material parameters have been estimated experimentally. The results of the experiments are presented in Chapter 3.3.3. Marked properties and their values (*), given in Table 11, represent recommended data from literature (Brinkgreve et al. 2010).

A linear elastic soil model is implemented in Plaxis to model structure elements such as geogrids. The numerical stiffness and strength parameters to describe the stress-strain behaviour of the reinforcement material are given in Table 12.

Tab. 11 FEM soil parameters for granular backfill material

Properties	Symbol	Value	Unit
unit weight	γ_s	26.4	[kN/m³]
experimental porosity	n_{exp}	39.0 – 41.0	[%]
peak friction angle	φ_{peak}	40	[°]
dilatancy angle	Ψ	6	[°]
stiffness parameter 50 % (σ_{ref} = 10 kN/m²)	E_{50}	10	[MN/m²]
stiffness parameter (oedometer loading)	E_{oed}	30	[MN/m²]
stiffness parameter (un/reloading)	E_{ur}	30	[MN/m²]
soil wall interaction (stainless steel)	R_{inter}	0.33	[-]
Poisson ratio*	ν*	0.2*	[-]
stiffness distribution*	m*	0.5*	[-]
horizontal earth pressure coefficient	K_0	1-sinφ	[-]

The soil reinforcement interaction is numerically simulated with interface elements generated between the nodes of the soil cluster and the geogrid structure. The interaction coefficient is given in Table 12.

Tab. 12 FEM material parameters for woven, biaxial, PET geogrid

Property	Symbol	Value	Unit
tensile stiffness ($RE,PRS_c/PRS_{p.t}$)	EA	50/400	[kN/m]
tensile strength	F_{max}	50	[kN/m]
soil geogrid interaction	R_{inter}	0.8	[-]

The presented numerical parameters have been evaluated by conducting tensile strength tests and direct shear tests with and without installing a geogrid in between the shear zone. The results are presented in Chapter 3.3.3.

4.4.4 Numerical procedure

The numerical Finite Element model is generated according to the experimental procedure described in Chapter 3.3.4. Every single strip and layer (h_{layer} = 0.15 m) is dumped and compacted regarding to the experimental procedure presented in Table 7 (Chapter 3.3.4).

The first construction stage includes the generation of a dumping strip by performing a plastic analysis in plane strain. Not only this strip but also the next ones are compacted by activating a compaction plate loaded with the compaction force measured in the laboratory (F_c = 40 kN). In the case of reinforcing the soil structure a geogrid is installed after each compaction layer (h_{layer} = 0.15 m). In

the case of utilizing the concept of PRS_i, the geogrid reinforcement is prestressed. For this purpose, prescribed displacements are activated on the nodes ending at the soft facing. After the soil structure has been dumped and compacted, the maximum pressures p_{sf} of the unreinforced and geogrid reinforced soil structures are investigated. In order to do this prescribed vertical displacements (s_v = 3.5 cm) are applied on the top of the load plate.

4.4.5 Numerical results and discussion

In this Chapter the numerical results of the Finite Element Method simulation are presented.

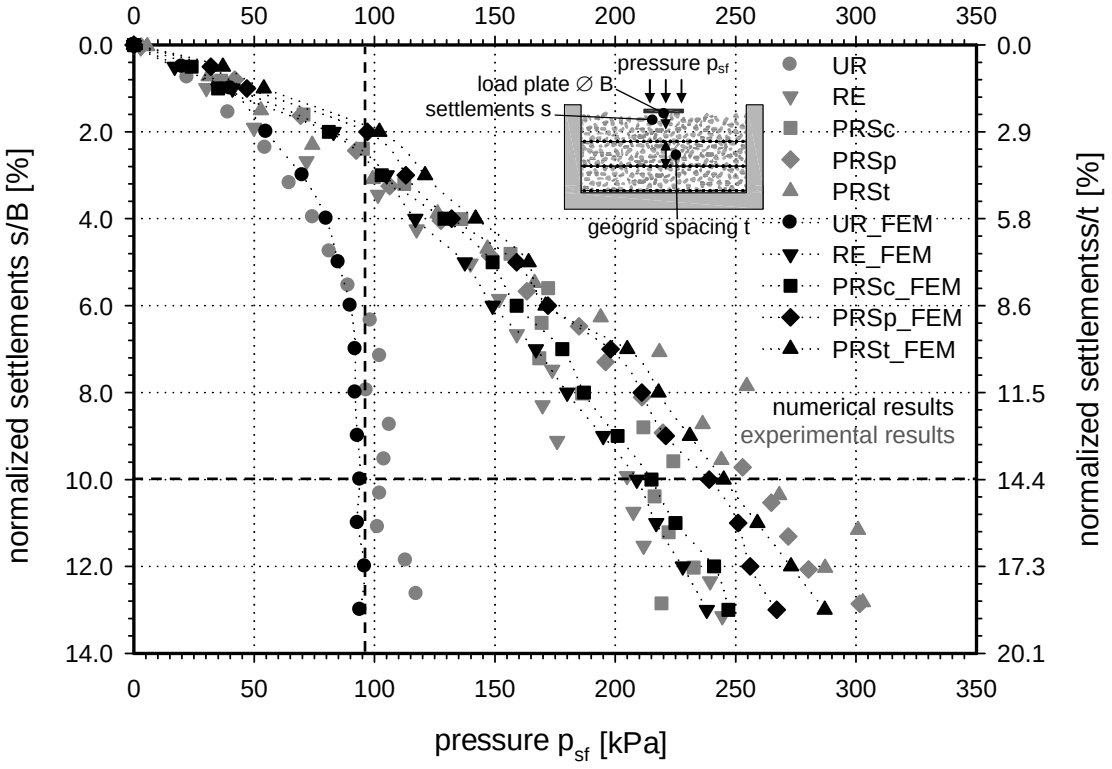

Fig. 51: Testing pressure p_{sf} near the soft facing versus settlements s normalized by the width B of the load plate respectively normalized by the distance between the reinforcement layers t.

The macroscopic load displacement results are shown in Figure 51 and are compared to the ones of the experimental investigations presented in Chapter 3.3.5. Figure 51 shows the testing pressure p_{sf} near the soft facing versus the settlements s normalized by the width B of the load plate respectively normalized by the distance between the reinforcement layers t. The macroscopic results of experimental (grey) and numerical (black) FEM investigations generally show a sound agreement. The experimental and numerical results correlate well in case of comparing the unreinforced (UR), reinforced (RE) and PRS_c curves. The

Finite Element Method analysis fits well in between the laboratory results. When comparing the numerical results it is apparent that the FE analysis slightly underestimates the experimentally measured pressures p_{sf}. In the case of increasing the tensile stiffness EA of the geogrid or the interface coefficient R_{inter}, between the reinforcement and the surrounding soil, the experimental results can numerically be fitted.

It has to be stated that the modelling of the experimental procedure accurately according to Chapter 3.3.4 is of high importance to produce reliable results.

Next, the macroscopic displacement characteristic of the soil structure is investigated in detail. During the compaction (F_{comp} = 40 kN) of the third dumping strip of the second dumping layer (layer 2, strip 3) a mesoscopic PIV analysis has been performed (Chapter 3.3.5). The PIV analysis (Fig. 52c) shows a homogeneous movement of the unreinforced soil body in the downwards vertical and the right horizontal direction (Chapter 3.3.5). The total amount of 5 mm of vertical and horizontal displacements has been analyzed by utilizing the PIV method.

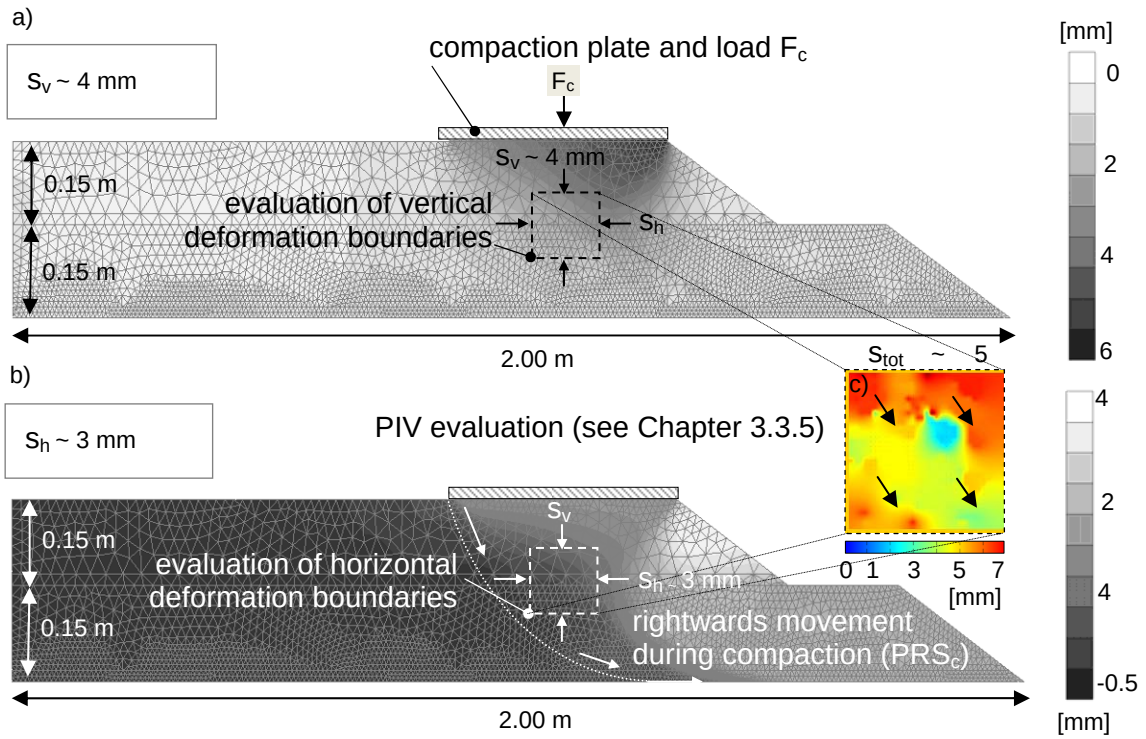

Fig. 52: Macroscopic results from evaluation of the deformation boundaries during compaction (F_{comp} = 40 kN) of the unreinforced (UR) compaction strip 2, 3 (layer 2, strip 3) a) shading plot of the vertical deformations s_v b) shading plot of the horizontal deformations s_h c) PIV Evaluation according to Chapter 3.3.5.

The macroscopic results from the FEM back analysis are presented in Figure 52a) and b). The vertical displacements s_v are evaluated in the investigated area (Fig. 52a) - dashed square). The soil body deforms on average 4 mm in the vertical direction. The higher displacements (4.5 mm) are visible in the upper right corner of the investigated region. Displacements decrease (3 mm) with respect to the depth of the unreinforced soil structure.

Horizontal displacements s_h are also evaluated in the investigated area (Fig. 52b) - dashed square). The soil body moves 3 mm in the horizontal direction. The highest horizontal movements are observed on the surface of the slope and amount to 4 mm. During compaction, the soil body moves right towards the soft facing (Fig. 52b). This is due to the dumping and compaction procedure of the soil structure and verifies the concept of PRS_c (Chapter 2).

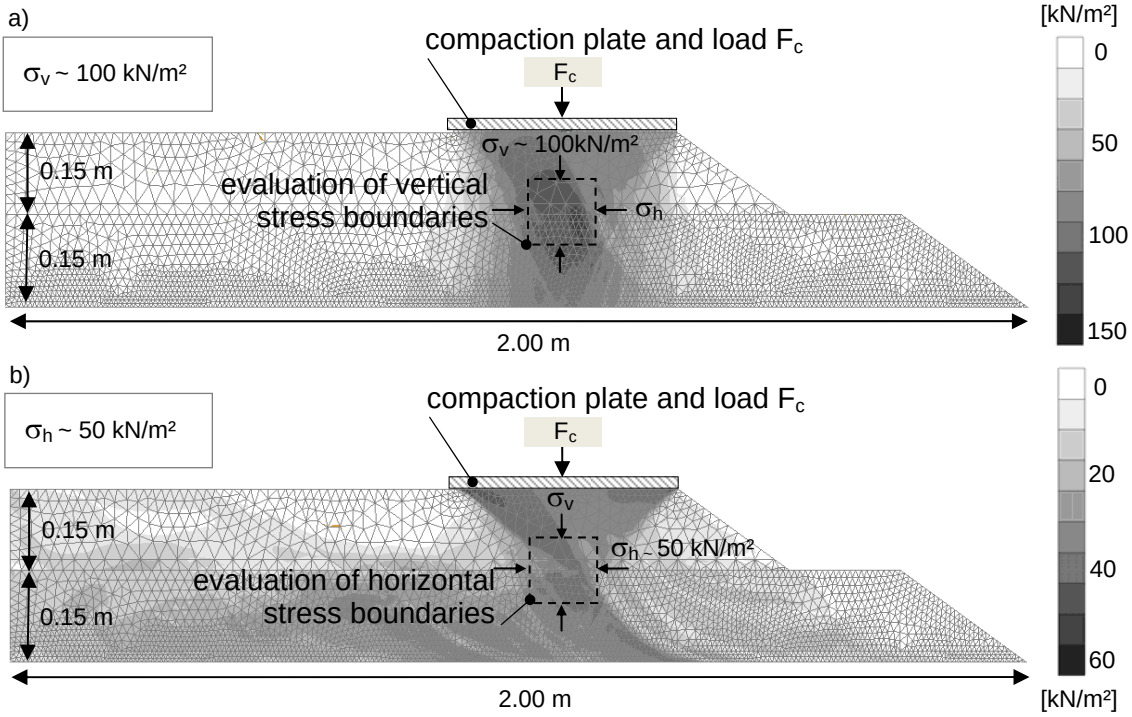

Fig. 53: Macroscopic results from evaluation of the stress boundaries during compaction (F_c = 40 kN) of the unreinforced (UR) compaction strip 2, 3 (layer 2, strip 3): a) shading plot of the vertical stresses σ_v b) shading plot of the horizontal stresses σ_h – input boundary for mesoscopic DEM analysis.

The horizontal and vertical displacements are added to calculate the total amount of displacements. The total displacements in the investigated region (Fig. 52a) and b) - dashed square) are 5 mm (Fig. 52c). The results show a sound agreement with the measured ones during the experimental investigations (Chapter 3.3.5). This is also true for the reinforced and prestressed reinforced soil structures.

Next, the deformation boundaries of the FEM simulation are validated according to Figure 49b) and c) the stress boundaries for the DEM simulation are evaluated. Figure 53a) and b) show the macroscopic results of the FEM stress analysis. The vertical stresses σ_v are evaluated in the investigated area (Fig. 53a) - dashed square). On average the vertical stresses level σ_v amounts to 100 kN/m². High local stresses naturally occur close to the edges of the compaction plate.

Tab. 13 Macroscopic results of evaluation of the stress boundaries during compaction (F_c = 40 kN) of the reinforced (RE) and prestressed reinforced (PRS_i) compaction strip 2, 3 (layer 2, strip 3): a) shading plot of the vertical stresses σ_v – input boundary for mesoscopic DEM analysis

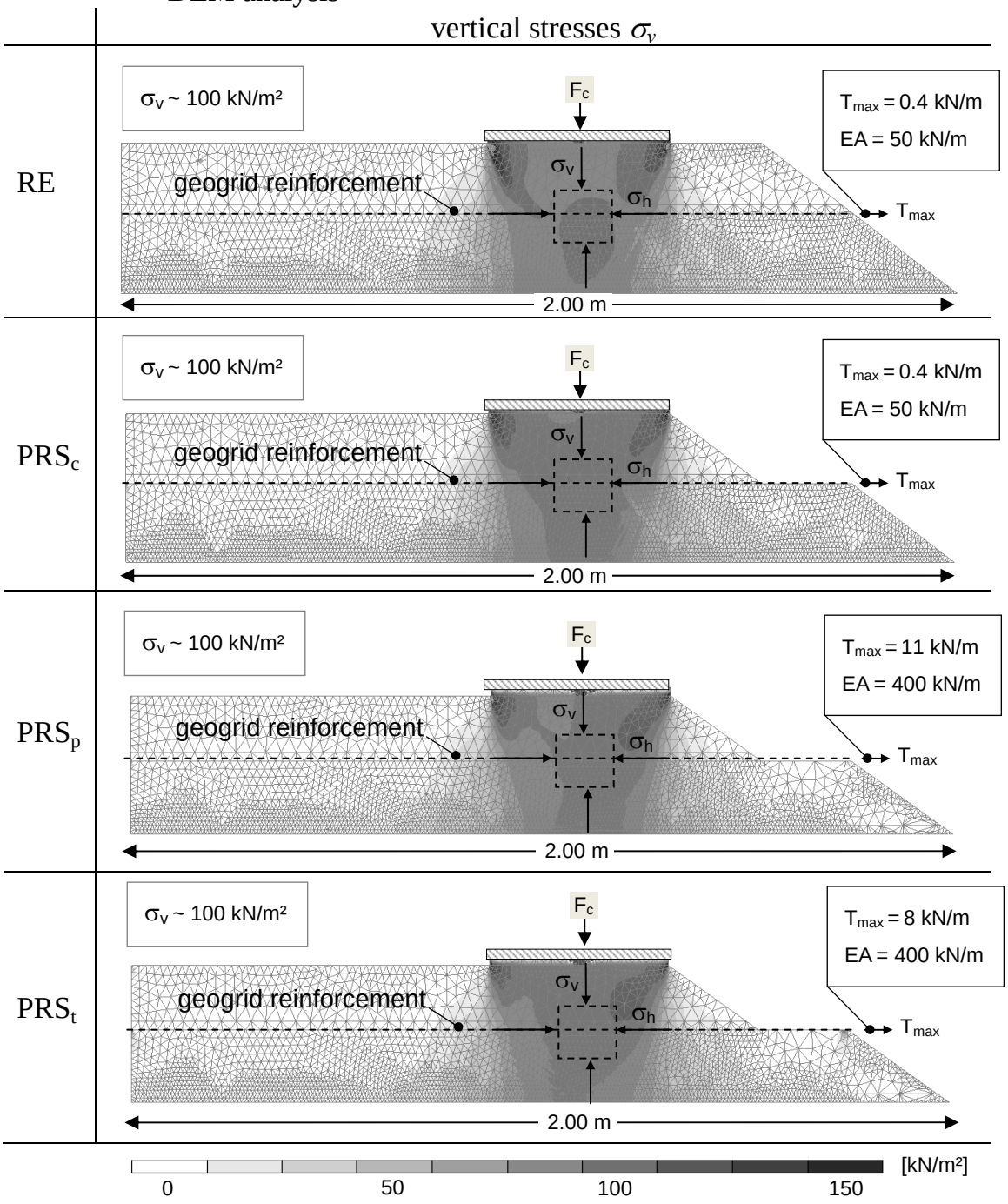

Tab. 14 Macroscopic results of evaluation of the stress boundaries during compaction (F_c = 40 kN) of the reinforced (RE) and prestressed reinforced (PRS_i) compaction strip 2, 3 (layer 2, strip 3): shading plot of the horizontal stresses σ_h – input boundary for mesoscopic DEM analysis

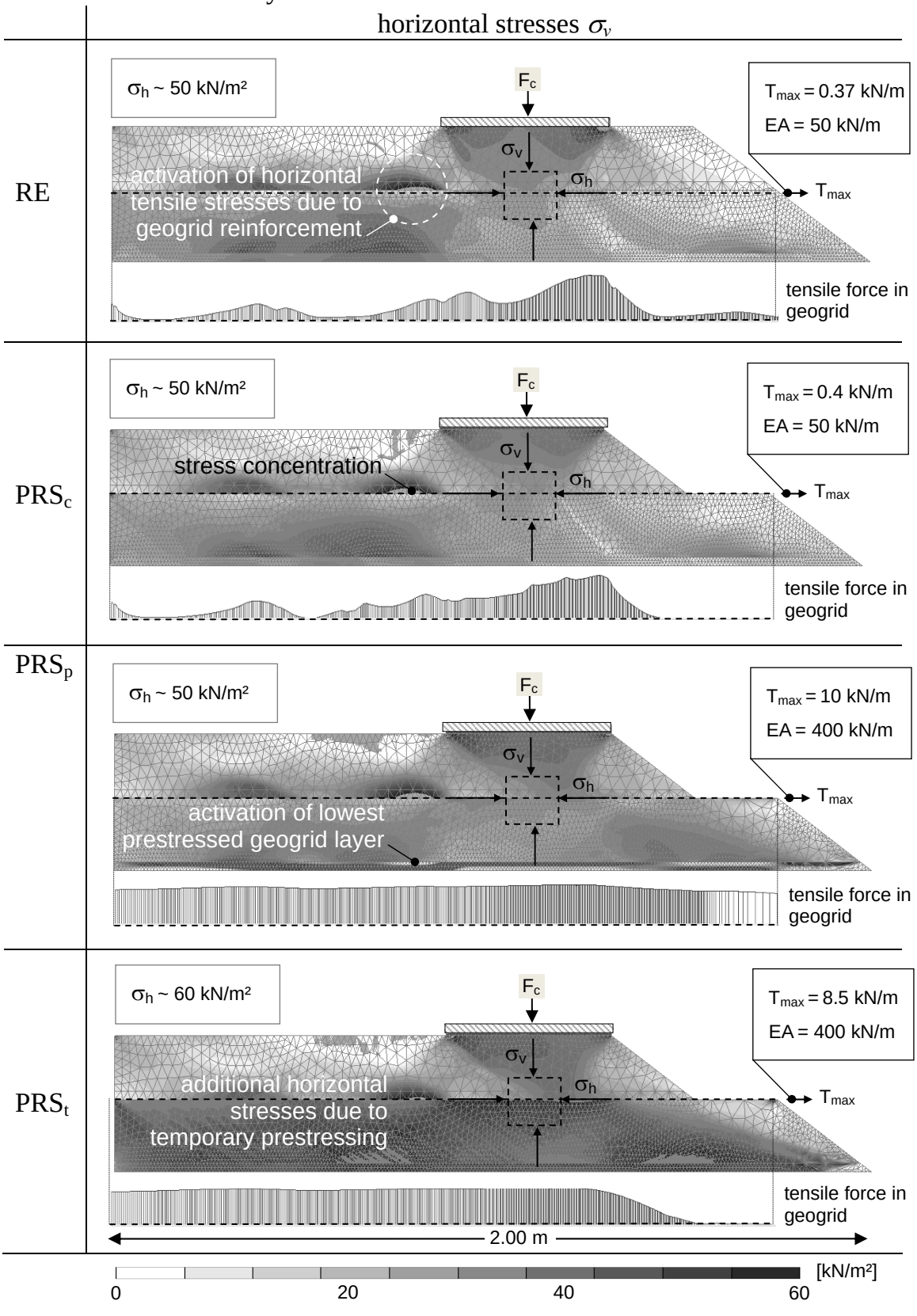

The horizontal stresses σ_h are shown in Figure 53b). The shading plots visualize the high (dark) and low (light) horizontal stress σ_h concentrations. The average horizontal stresses in the investigated area (Fig. 53b) - dashed square) amount to 50 kN/m² during the compaction (F_c = 40 kN).

The evaluated vertical and horizontal stresses are used as input boundaries for the mesoscopic DEM analysis. The input values for the stress boundaries are given in Table 13 and 14.

Table 13 additionally presents the tensile forces T_{max} occurring in the geogrid during compaction. The lowest tensile forces T_{max} (0.37 kN/m) occur during compaction of the reinforced soil structure (RE). Similar tensile forces T_{max} are calculated when compacting a reinforced soil structure utilizing the concept of PRS_c. The highest tensile forces in the reinforcement act while prestressing the geogrid permanently (PRS_p). With regard to 2.5 % prestrain ε_{PRS} and a tensile stiffness EA = 400 kN/m, the geogrid obtains 10 kN/m tensile force T_{max}. The tensile force T_{max} in the reinforcement decreases of in case of releasing the prestress (PRS_t). The tensile force T_{max} amounts to 8.5 kN/m.

Table 14 additionally shows the tensile force distribution of the geogrid reinforcement during the compaction of the third dumping strip of soil layer two. The tensile forces T_{max} reach their maximum right under the compaction plate. In the case of releasing the geogrid the tensile force in the reinforcement is zero close to the soft facing and increases with regard to the distance to the hard facing to its maximum.

It can finally be stated that the results from numerical FEM analysis show a sound agreement with the experimental investigations (Chapter 3.3.5). The performed macroscopic, numerical FEM investigations verify the concept of PRS_i.

4.5 Discrete Element Method (FEM) investigations on prestressed reinforced soil (PRS_i) by geogrids

In this Chapter, investigations on prestressed reinforced soil utilizing Discrete Element Method modelling are presented. As already pointed out in Chapter 4.3 a three dimensional (3D) Discrete Element model is constituted to evaluate displacements and contact forces between discrete particles in the reinforced soil structure. A cube with a side length a = 0.1 m represents a soil element. This element is numerically simulated.

4.5.1 Overview on the numerical model

A three dimensional Discrete Element model has been utilized to investigate the mesoscopic load transfer and soil geogrid interaction mechanism. The three dimensional Discrete Element Method code, "Particle Flow Code (PFC^{3D})" provided by Itasca (Version 4.00-191 64-bit), has been employed (Itsaca Consulting Group 2005). A cubical model (a = 0.1 m) with geometrically detailed modelled grains and geogrid has been set up. The granular soil particles and the discrete geogrid reinforcement have been modelled "Computer Aided Designed" (CAD) (Chapter 4.5.3). The granular soil particles have been mesoscopically investigated in detail (Chapter 3.3.3) and generated as clumps in PFC^{3D} (Itsaca Consulting Group 2005).

4.5.2 Numerical setup and calculation process

The Itsaca Consulting Group (2005) provides the fundamental principles on Discrete Element Modelling with the Particle Flow Code in three dimensions (PFC^{3D}). Fundamentals have been prepared by Halsegger (2004), Zöhrer (2006) and Lenzi (2009).

The basic geometry information of the numerical model is presented in Figure 54. The three dimensional model (Figure 54a) is generated by utilizing CAD designed clumps, representing the granular soil particles and a CAD designed discrete geogrid reinforcement.

Figure 54b) represents the x-y plan view of the model. The longitudinal and transverse members of the geogrid and the shape of clump 1 are schematically shown. Additionally the applied stress boundaries σ_v and σ_h according to Chapter 4.4.5 are presented. The tensile force F_t of the geogrid reinforcement is additionally shown in Figure 54b).

Figure 54c) shows the x-z side view of the numerical model. An additional prestress is applied to the longitudinal members of the discrete geogrid in case of utilizing the concept of PRS_i.

The fixed boundaries of the model are shown in Figure 54d). The boundary conditions are numerically modelled by so called wall elements (Itsaca Consulting Group 2005). The input values for the boundary conditions have been calculated by utilizing the FEM model presented in Chapter 4.4.5. The calculated stresses have been applied by programming servo controlled walls. Thereafter, velocities are applied on the wall. The velocities result in a movement of the walls. Due to the contact forces between the particles, the walls obtain stresses

depending on the movement of the wall. The walls stop, when the stresses have reached the calculated input value according to the FEM analysis.

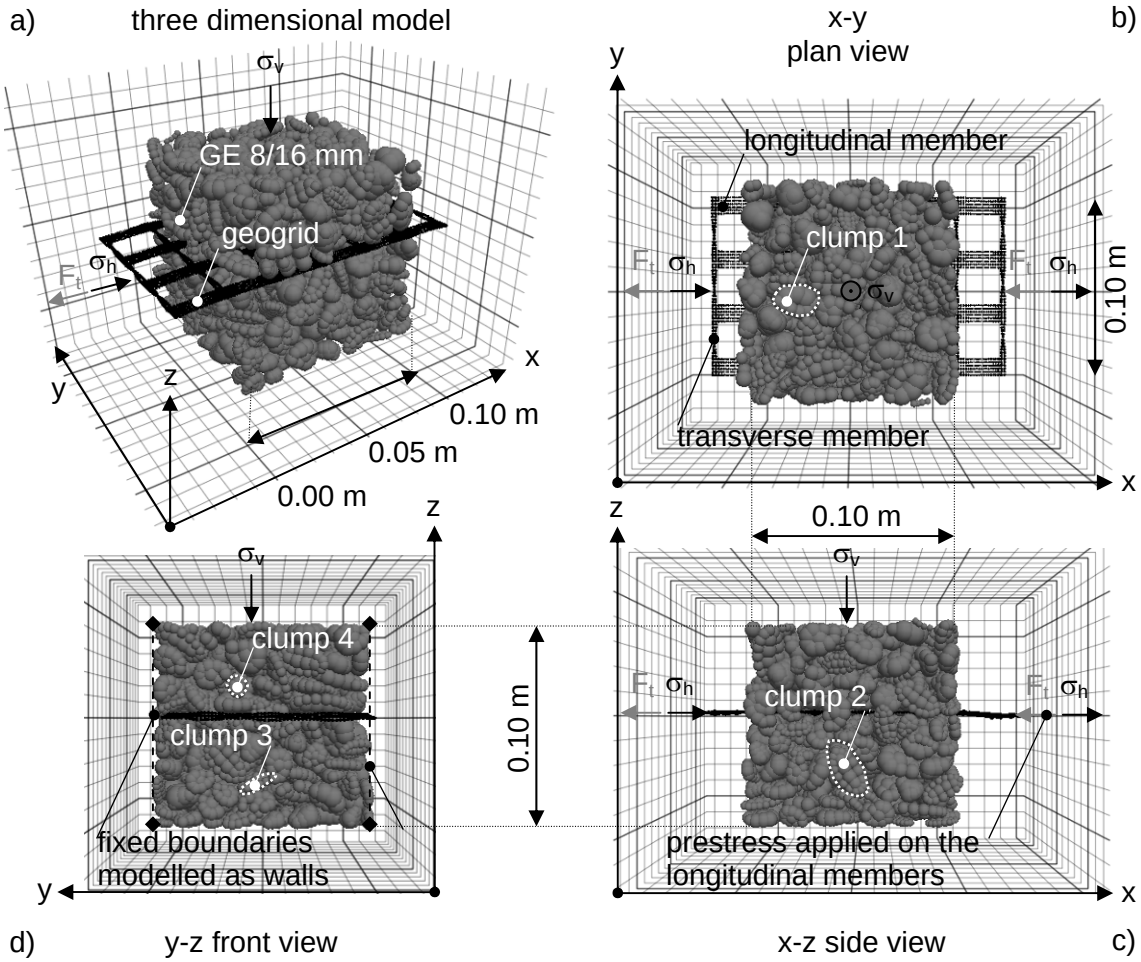

Fig. 54: Schematic sketch of the overview on the Discrete Element model: a) three dimensional model including boundary fixities b) x-y plan view c) x-z side view d) y-z front view.

4.5.3 Numerical material parameters

The mesoscopic investigated gravelly material (Chapter 3.3.3) has been numerically modelled in detail. The shape of the grains has been modelled by so called clumps (Itsaca Consulting Group, 2005). These clumps have been implemented in the numerical model as described in Figure 55.

The surface of a predefined grain has been modelled by utilizing the software Blender (Version 2.4). Blender (Version 2.4) is an open source software for 3D creation. The shape of the grain is first visualized by implementing 3 photos of the grain with different perspectives into the software Blender. Thereafter the command `Background Image` is executed. One photo is taken with a plan

view perspective from the top of the granular soil particle and is afterwards imported into Blender. Two more photos are taken from the front and back side of the grain and are imported in the software.

The surface of one clump is then modelled by generating a mesh representing the surface of the grain (Fig. 55b). Thereafter, the command `subsurface` has to be executed. The generated mesh is refined until the virtual and real surfaces correlate well. The surface of the clump is modelled accurately. Every point of the generated mesh is able to be moved separately. Once the surface is generated the volume inside the surface is filled with spheres. To add spheres into the surface the command `Add - Mesh - UV-Sphere` has to be employed.

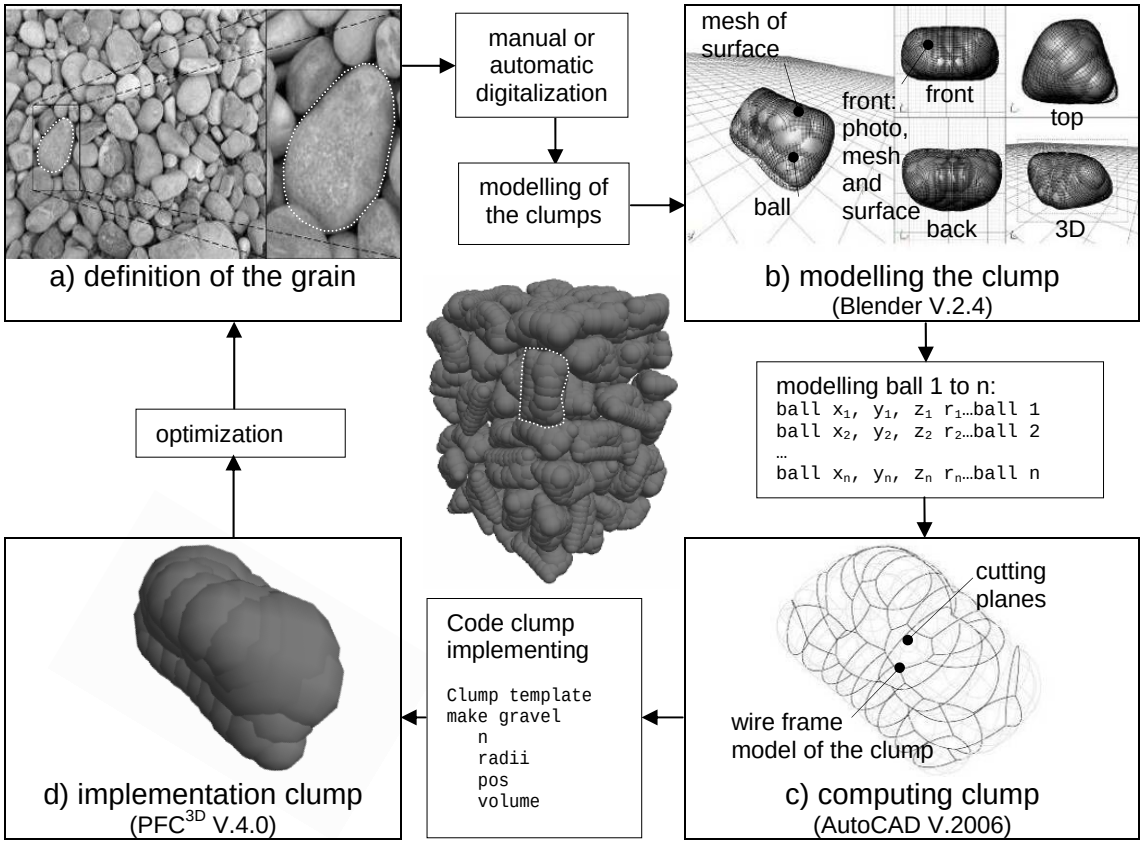

Fig. 55: Schematic sketch of a generation, digitalisation and implementation process of a discrete clump: a) definition of the grain b) modelling of the clumps surface and filling with spheres c) computing the clumps volume d) implementation of the clump in the DEM model code.

Only spheres may be added to the generated volume. This is due to the limitations of PFC^{3D}. The software merely generates spherical particles (Itsaca Consulting Group 2005).

Finally, the clump is generated. In order to implement the generated clump into the PFC^{3D} code, the position (x, y, z) and the radius of each sphere has to be

defined. Additionally, the volume of the generated clump has to be analyzed. Thereafter the generated spheres are implemented in AutoCAD (Version 2006). The spheres are merged together by performing the `union` command in AutoCad. The `massprop` command is conducted and the volume of the generated clump is calculated automatically.

Finally, the clump is implemented into the Discrete Element Method software by creating an ASCI file. The PFC^{3D} command to model the high resulted clump 1 (Figure 56) is exemplarily given. The clump consists of 30 single spheres. Their radii and positions have to be set. Finally, the calculated volume has to be inputted.

```
clump template make RK1_HQ 30 &

radii
0.8075 0.835 0.809 0.8485 0.985 0.867 0.8425 0.85 0.8435 0.9040      &
0.8415 0.9635 0.8415 1.0025 1.004 0.837 0.921 0.771 0.8965 0.827     &
0.633 0.6195 0.5365 0.407 0.374 0.402 0.3845 0.622 0.847 0.9155

pos
(1.336,0.086,-0.268)   (1.191,0.446,-0.251)   (1.281,-0.229,-0.264)  &
(1.012,0.666,-0.282)   (0.780,0.081,-0.140)   (0.891,0.777,-0.282)   &
(1.060,-0.442,-0.277)  (0.683,0.884,-0.300)   (0.870,-0.561,-0.272)  &
(0.488,0.822,-0.277)   (0.612,-0.634,-0.272)  (0.148,0.694,-0.224)   &
(0.331,-0.640,-0.255)  (0.162,0.061,-0.139)   (-0.002,0.575,-0.159)  &
(0.072,-0.614,-0.266)  (-0.244,0.538,-0.118)  (-0.306,-0.587,-0.248) &
(-0.588,0.348,0.001)   (-0.688,0.016,-0.103)  (-1.107,0.258,0.097)   &
(-0.745,-0.557,-0.221) (-0.924,-0.533,-0.197) (-1.312,-0.393,-0.110) &
(-1.477,-0.200,-0.027) (-1.522,0.079,0.119)   (-1.532,-0.056,0.068)  &
(-1.128,0.007,-0.028)  (-0.563,-0.097,-0.147) (-0.294,-0.114,-0.168)

volume 13.6336
```

All generated clumps and their command data are listed in the Appendix.

Four typical grain shapes (Chapter 3.3.3) have been selected to categorise and consecutively model the shape of the grains numerically by clumps. Thereafter 150 particles have been randomly chosen and investigated mesoscopically. The relative fraction of each particle is given in Figure 56. Figure 56 additionally shows photos of the real grains and the ones modelled numerically with three different resolutions.

To evaluate the numerical microscopic parameters a detailed numerical calibration has been performed (Dijak 2012). Different laboratory tests have been conducted to compare the results gained from experimental tests with the ones back calculated by utilizing the DEM Method. Large scale (∅/H = 0.3/0.1 m) oedometer tests (Chapter 3.3.3) have been conducted experimentally and numerically and the numerical stiffness parameters of the granular material have been calibrated in a first step. Large scale (L/W/H = 0.3/0.3/0.2 m) direct shear tests (Chapter 3.3.3) have been conducted to experimentally estimate the shear

properties of the granular material. The direct shear tests have been numerically modelled and the numerical shear properties have been calibrated by performing a back analysis of the experimental procedure. Finally, by dumping the granular soil from a cylinder, the angle of repose β has experimentally been evaluated and back analyzed numerically.

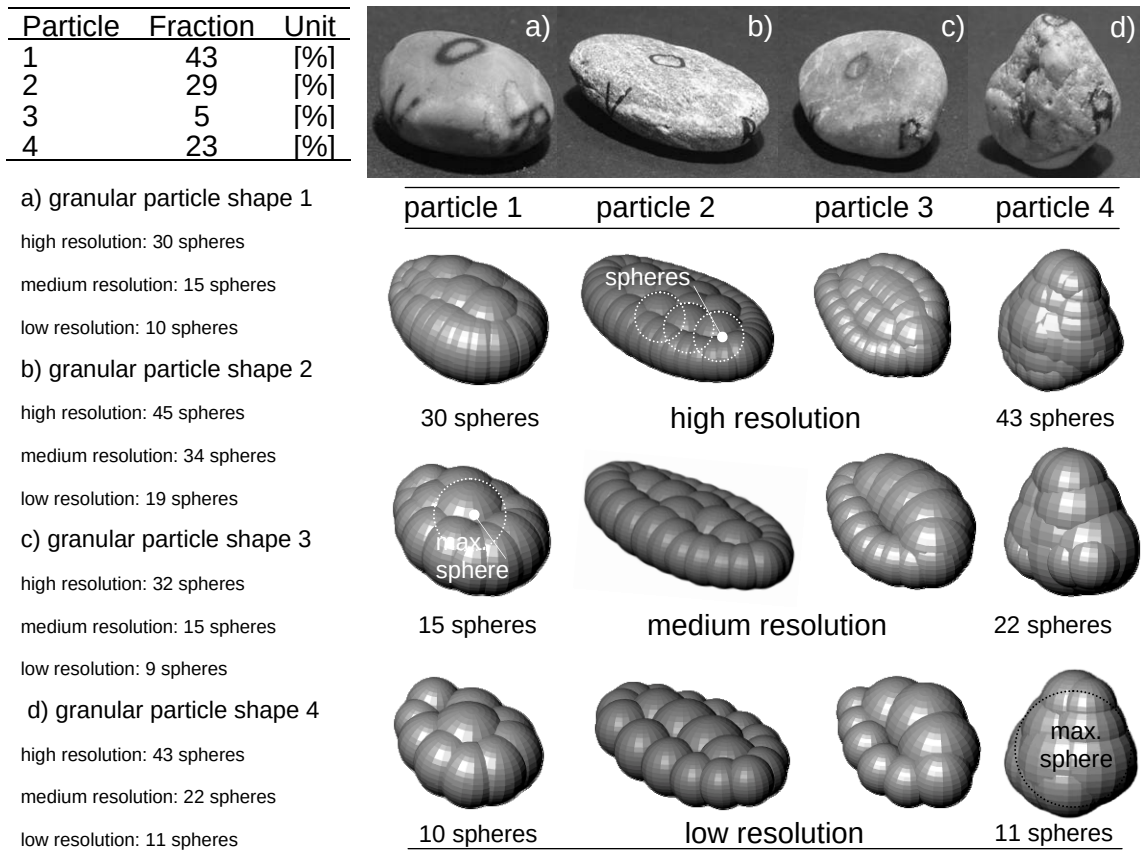

Fig. 56: Relative fraction of particles and shapes: photo of the real grains and discrete clumps of the DEM numerical model with three different resolutions (high, medium, low).

The numerical input parameters for the granular backfill material called “Murschotter” (Chapter 3.3.3) are given in Table 15.

The density of the granular material has been measured in the laboratory (Chapter 3.3.3) and amounts to 2.64 g/cm³. The Hertz Mindlin model (Itsaca Consulting Group 2005), an appropriate contact model for modelling granular particle interaction, has been implemented into the numerical simulation. The input stiffness parameters for this contact model are given in Table 15. A shear modulus G = 30 GN/m² and a Poisson ratio ν = 0.2 are applied. This value results from back analyzed large scale oedometer tests and correlates well with the values from literature as reported by Scharinger (2007).

If a clump interacts with a sphere representing the geogrid reinforcement, a linear elastic contact is assumed. The normal and shear stiffness ratios k_n and k_s are given in Table 15. In order to model interfriction processes, a microscopic roughness μ = 0.8 is applied to the Hertz Mindlin slip model. As explained, the shear properties have been calibrated by performed large scale direct shear tests.

Tab. 15 DEM soil parameters for granular backfill material

parameter	PFC	unit	value
density	*density*	[kg/m³]	2.64E+03
shear modulus	*shear*	[N]	3.00E+10
Poisson's ratio	*poiss*	[N]	0.2
normal stiffness	k_n	[N/m]	3.90E+06
shear stiffness	k_s	[N/m]	9.00E+05
friction coefficient	*friction*	[-]	0.8
local damping	*damp local*	[-]	0.90/0.00
viscous damping (normal/shear)	*damp viscous*	[-]	0.00/0.97

The local and viscous damping parameters are attached to Table 15. Local damping *damp local* is set to a value of 0.90 to accelerate quasi static analyses such as loading processes. No viscous damping is activated (damp viscous = 0.00). In the case of modelling a filling process or when dumping and dropping soil particles the viscous damping coefficient *damp viscous* is set to a value of 0.97.

A detailed soil geogrid interaction study has been performed while conducting the numerical back analysis of the experiments. The findings from the mesoscopic interaction are presented in Chapter 4.5.5.

The presented geogrid reinforcement (Chapter 3.3.3) has been numerically modelled in detail. The shape of the geogrid has been designed computer aided. The longitudinal and transverse members of the reinforcement material have been modelled in detail by bonding single spheres to each other.

Figure 57a) shows the real shape of the geogrid. The plan view and the side views on the longitudinal and transverse members of the PET woven geogrid are presented. Figure 57b) shows the numerically modelled reinforcement material. The detailed geogrid is modelled by utilizing CAD to fit the original shape of the reinforcement. The three dimensional shape of the longitudinal members is additionally modelled to gain a detailed insight in the geogrid deformation mechanism.

Additionally a standard geogrid (Fig. 57c) has been modelled. The members of the geogrid consist of single spheres bonded together next to each other. Numerical experiments, such as direct shear tests, conducted with the standard

and detailed geogrid have shown correlating macroscopic results (Dijak 2012). Still, the mesoscopic soil geogrid interaction shows a totally different behaviour.

The generated standard geogrid, the reinforcement modelled in detail and their command data are listed in the Appendix.

The material properties have been estimated by calibrating the standard and detailed geogrid with conducted laboratory tests (Dijak 2012). Table 16 provides the numerical microscopic parameters of the geogrid. The geogrid is modelled with a linear elastic soft-contact model. The density of the single spheres has been estimated by numerically back-modelling a weighing machine where a geogrid with an area of 0.1 * 0.1 m² is placed. The experimental and numerical results coincide when the detailed geogrid is generated by spheres with a density of 1.03 g/cm³.

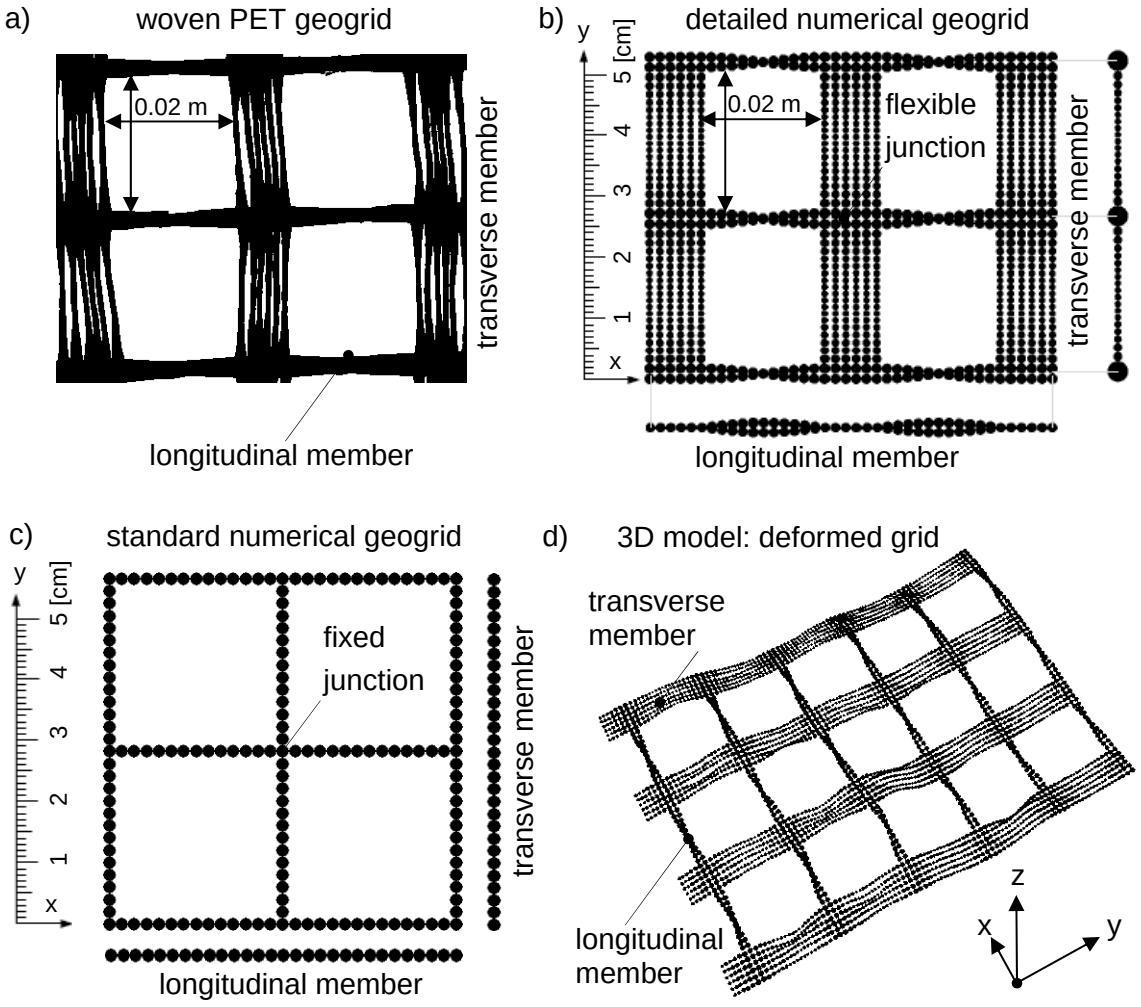

Fig. 57: Modelling of the geogrid reinforcement: a) photo of the real grid b) discrete detailed geogrid c) discrete standard geogrid d) three dimensional DEM model of deformed detailed geogrid.

The tensile strength and stiffness properties of the detailed geogrid are calibrated by experimentally (Chapter 3.3.3) performing tensile strength tests and back

analysing the experimental procedure. The experimentally and numerically investigated tensile stress-strain curves agree when the normal stiffness k_n of the numerical geogrid amounts to 4.00E+06 N/m. The shear stiffness of the reinforcement has been fixed to a value of k_s = 8.50E+05 N/m.

The tensile strength of the material is numerically defined as a contact bond normal and shear strength *n_bond* respectively *s_bond* (Itsaca Consulting Group 2005). The contact bond`s normal and shear strength *n_bond* respectively *s_bond* have been set to a value of 5.00E+05 N.

The flexural behaviour of the geogrid is calibrated by back analysing performed bending tests with the geogrid. The parallel bond normal and shear stiffness pb_k_n and pb_k_s describe the bending deformation behaviour of the material (Itsaca Consulting Group, 2005). The parallel bond`s normal stiffness pb_k_n has finally been fixed to a value of 2.80E+12 Pa/m. The parallel bond shear stiffness pb_k_s amounts to 1.80E+12 Pa/m. These values linearly correlate with the predefined radius multiplier *pb_radius*. The radius multiplier is set to 29 % of the value of the mean radius of two spheres bonded together.

Tab. 16 DEM material parameters for woven, biaxial, PET geogrid (according to Dijak 2012)

parameter geogrid	PFC	unit	value	
			detailled	standard
density	*density*	[kg/m³]	1.03E+03	2.06E+03
normal stiffness	k_n	[N/m]	4.00E+06	1.62E+07
shear stiffness	k_s	[N/m]	8.50E+05	6.00E+04
contact bond normal strength	*n_bond*	[N]	5.00E+05	5.00E+05
contact bond shear strength	*s_bond*	[N]	5.00E+05	5.00E+05
radius multiplier	*pb_radius*	[-]	0.29	0.175
parallel bond normal stiffness	pb_k_n	[Pa/m]	2.80E+12	1.25E+13
parallel bond shear stiffness	pb_k_s	[Pa/m]	1.80E+12	3.00E+11
parallel bond normal strength	$pb\_n_{strenght}$	[Pa]	8.00E+14	8.00E+14
parallel bond shear strength	$pb\_s_{strength}$	[Pa]	8.00E+14	8.00E+14
friction coefficient	*friction*	[-]	0.5	0.5

The normal and shear strength parameters $pb\_n_{strenght}$ respectively $pb\_s_{strength}$ are finally set to a value of 8.00E+14 Pa. These parameters define the strength properties of the parallel bond (Itsaca Consulting Group 2005).

The friction coefficient *friction* is finally calibrated by performing large scale direct shear tests (Dijak 2012). The tested soil element is experimentally reinforced (Chapter 3.3.3) with the geogrid. The numerical direct shear test is as well modelled with the geogrid placed in the predefined shear zone. A friction coefficient of 0.5 has been back analyzed.

It has to be stated that the back analyzed microscopic parameters for the geogrid reinforcement are numerical ones. It is possible to fit the macroscopic properties of the reinforcement with a different microscopic, numerical parameter set.

The higher the amounts of differently performed calibration tests, the more realistic the input parameters. Especially for models with high numbers of particles and large deformations, calculation times increase exponentially.

4.5.4 Numerical procedure

The reinforced soil element described in Chapter 4.5.2 is generated as described in Figure 58.

Figure 58a) shows the filling process of soil layer 1. The clumps are dumped into a box of walls by activating viscous damping until the first soil layer is generated (Fig. 58a). The input value for viscous damping *damp viscous* is set to 0.97.

The geogrid is generated just after the first soil layer has been finished (Figure 58b). A defined amount of prestress ε_{PRSi} = 2.5 % is applied to the geogrid in case of utilizing the concept of PRS_i. Therefore one end of the geogrid is fixed. A constant velocity is activated at the other end of the geogrid until the calculated (Chapter 4.4.5) tensile force F_t of the reinforcement is reached. The edges of the geogrid are finally fixed in their positions.

Figure 58c) shows the process of filling the second soil layer. Again the granular clumps are filled by active viscous damping (*damp viscous* = 0.97). During the filling process local damping (*damp local* = 0) is deactivated.

The stress boundaries calculated in Chapter 4.4.5 are applied to the servo controlled walls (Chapter 4.5.2). The walls surround the clumps and the spheres of the geogrid and load the reinforced soil element. Once the wall elements are loaded with vertical and horizontal stress conditions calculated by FEM analysis the calculation (*cycle*) process starts. The dynamic calculation is aborted when the mean contact (*mcf*) and unbalanced (*muf*) forces reach a constant value (Itsaca Consulting Group 2005).

The deformation behaviour of the reinforced soil element is finally compared to the results gained from the FEM and PIV analyses. Detailed mesoscopic investigations are additionally performed to investigate the discrete load transfer and interaction mechanism between geogrid and granular soil particles (Chapter 4.5.5). One specific load transfer and three different soil geogrid interaction mechanisms have been observed and are presented later.

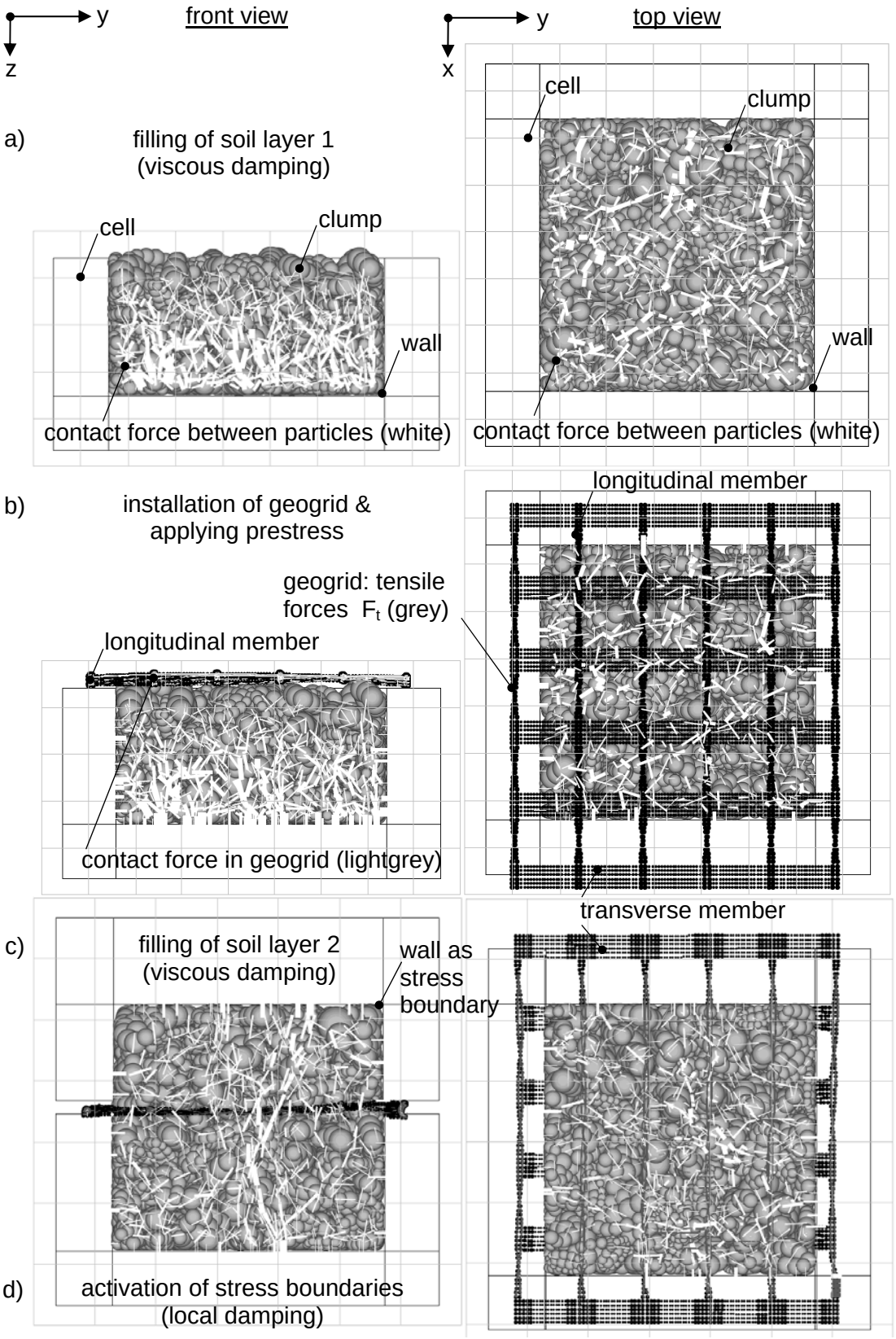

Fig. 58: Numerical procedure: a) filling soil layer 1b) installation of geogrid 1c) filling soil layer 2d) activation of stress boundaries.

4.5.5 Numerical results and discussion

As already mentioned in Chapter 4.5.3 it is essentially important to calibrate the microscopic parameters of soil and geogrid before performing numerical simulations. These numerical calibration simulations are additionally utilized to investigate the mesoscopic soil geogrid interaction mechanism.

Figure 59 presents an experimental and numerical study to evaluate the angle of repose of the granular soil. The gravel is experimentally dumped without and with reinforcing the bottom of the granular cone (Fig. 59a) and c). The angle of repose β is measured with a value of 35° in the case of testing the soil dumped on the unreinforced concrete floor. In the case of the installation of a geogrid at the bottom of the granular soil the angle of repose β increases to a value of 37° (Fig. 59c).

In other words, the granular material is numerically dumped and the macroscopic angle of repose is measured and compared with the results of the experiment. The granular soil is modelled by generating 1000 clumps consisting of 13000 spheres. 22 contacts per clump are evaluated after dumping. 2.5 contacts per clump are active contacts. Active clumps actively participate in the load transfer of the granular soil structure. The geogrid reinforcement is modelled by bonding 17352 spheres with 20250 bonds to each other. The macroscopically evaluated angle of repose shows a sound agreement with the one evaluated experimentally (Fig. 59d).

Figure 59e) shows the mesoscopic evaluation of the numerical calibration. The granular soil structure modelled by generating clumps and the discrete geogrid reinforcement are presented. The contact forces between the granular soil clumps and the discrete geogrid spheres are visualized additionally. Higher tensile forces (thick white lines) occur in the centre of the dumping cone. In the outer regions the tensile forces in the geogrid decrease. The maximum tensile force of one single string in the longitudinal member of the reinforcement is 1 N. The geogrid thereby supports the dumped granular material with an additional horizontal resistance.

Three effects are observed during the mesoscopic investigation. First, the geogrid and the soil particle interact by friction between the surface of the granular soil particles and the surface of the geogrid. Second, the granular particles interlock between the discrete members of the geogrid (Fig. 59e). The mesh expands because the clumps access the gaps between the longitudinal and transverse members of the geogrid.

The third effect is observed during the mesoscopic interaction investigation and is defined as an alignment effect. The flexible geogrid aligns well around the granular soil particles. Thereby deviation forces occur when the geogrid is

tensioned axially. This results in a higher horizontal and thereafter in a higher vertical resistance.

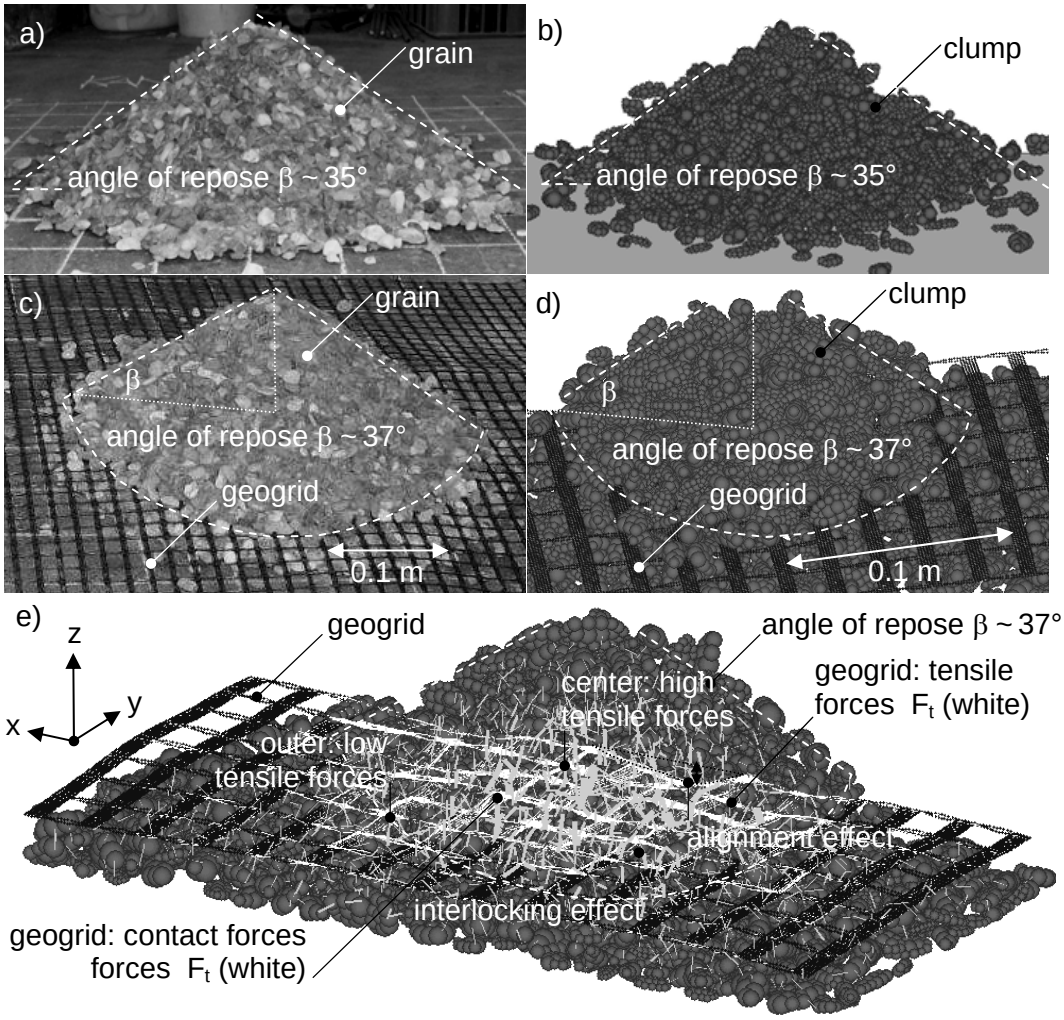

mesoscopic information
soil: 1000 clumps _13000 spheres_22 contacts/clump_2.5 active contacts
geogrid: 17352 spheres_20250 bonds

Fig. 59: DEM mesoscopic calibration results (according to Dijak 2012): a) and c) experimentally evaluating the angle of repose of the unreinforced and reinforced granular soil b) and d) modelling of an angle of repose for soil calibration e) soil and geogrid interaction mechanism. Soil: 1000 clumps, 13000 spheres, 22 contacts/clump, 2.5 active contacts. Geogrid: 17352 spheres_20250 bonds.

Figure 60 presents the DEM mesoscopic modelling of a direct shear test to evaluate the macroscopic friction angle of the granular material. The DEM simulation is additionally utilized to investigate the mesoscopic interaction mechanism between discrete geogrid and granular soil. Figure 60a) shows the plan view of the numerically modelled direct shear device. Figure 60 includes the tensile force distribution (white lines) along the geogrid reinforcement.

The higher tensile forces occur in those geogrid members that lie perpendicular to the shear direction. This is due to the interaction mechanism between soil and reinforcement. The interlocked particles translate in shear direction and thereby pull the members of the geogrid.

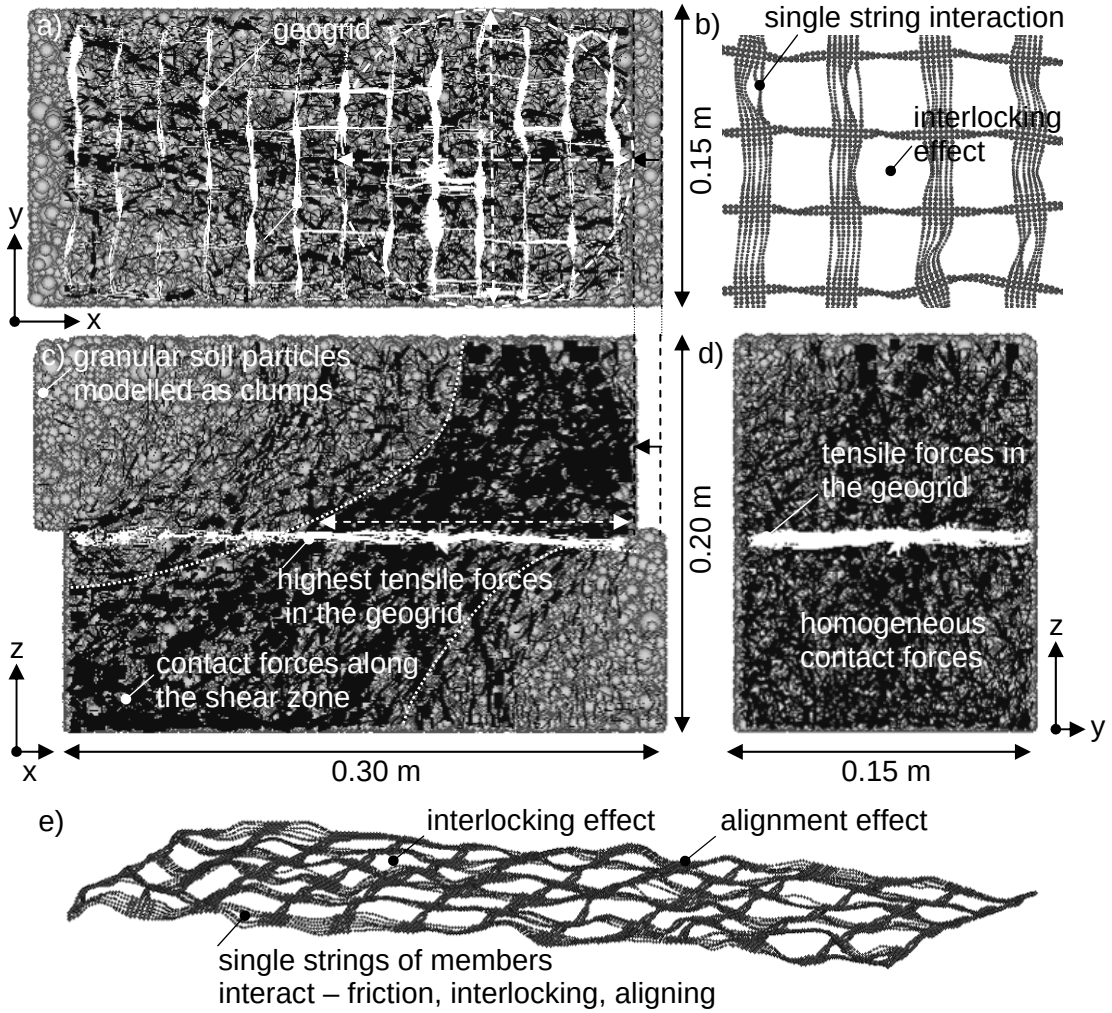

mesoscopic information
soil: 4977 clumps _63661 spheres_26.5 contacts/clump_2.5 active contacts
geogrid: 10142 spheres_11731 bonds

Fig. 60: DEM mesoscopic modelling of direct shear test to evaluate friction angle of reinforced granular soil for calibration: a) plan view including tensile force distribution along geogrid b) plan view of the deformed geogrid c) side view of the direct shear box including soil contact forces along shear zone d) front view of the direct shear box, homogeneous contact force distribution e) deformed geogrid including single string friction, interlocking and alignment effect. Soil: 4977 clumps, 63661 spheres, 26.5 contacts/clump, 2.5 active contacts. Geogrid: 10142 spheres_11731 bonds.

The highest tensile forces are activated close to the maximum particle contact forces in the shear zone. This is also shown in Figure 60c). Figure 60c) shows the

side view of the direct shear box. The black contact forces between the granular soil particles are shown along the shear zone. The tensile forces in the geogrid increase if the reinforcement layer interacts with the high contact forces between the soil particles (black lines) along the shear zone. Figure 60d) shows the front view of the direct shear box. The soil particles are translated in shear direction by the wall which results in a homogeneous contact force distribution.

Figure 60b) and e) show the deformed geogrid after the shear process. The geogrid generally interacts with the granular particles by friction. Thereafter a microscopic friction coefficient *friction* of 0.5 for the geogrid and 0.8 for the granular soil is numerically set.

Additionally, the granular particles interlock between the gaps of the longitudinal and transverse members of the reinforcement (Fig. 60b) and e). A third effect is again observed during the mesoscopic interaction investigation of the direct shear test. The flexible geogrid aligns well around the granular soil particles. Deviation forces occur and thereby the geogrid provides a higher horizontal and vertical resistance.

Once the microscopic numerical parameters are fixed (Tab. 15 and Tab. 16) the three dimensional discrete and differently reinforced soil elements are modelled according to Figure 49d). According to Figure 49e) the displacements of the soil element are analyzed and compared to the observed deformations during the PIV analysis (Chapter 3.3.5). Further, the displacement calculated by utilizing the DEM are compared to the calculated ones from the FEM study (Chapter 4.4.5).

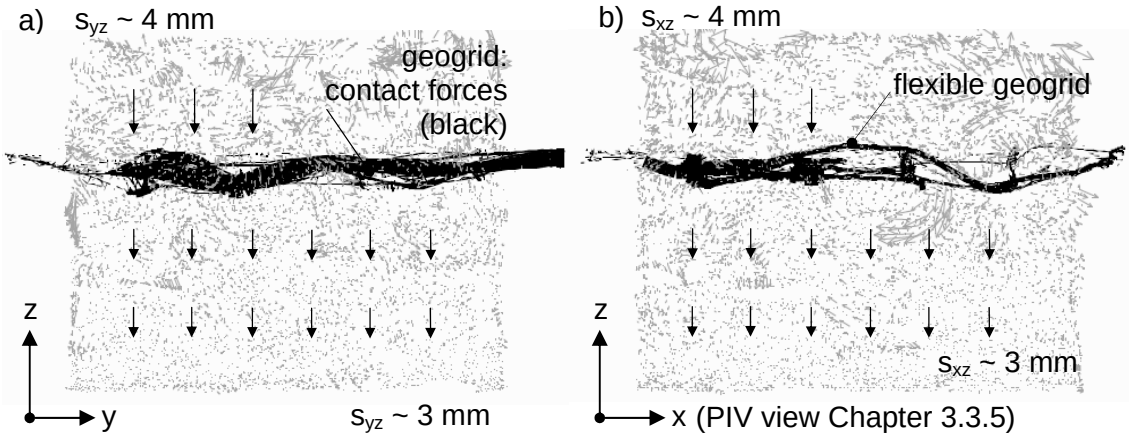

Fig. 61: DEM mesoscopic modelling of reinforced (RE) soil element to validate the mesoscopic displacement behaviour: a) side view (y-z) including displacement s_{yz} vectors of the granular material and tensile force distribution along geogrid b) front view (x-z) including displacement s_{xz} vectors of the granular material and tensile force distribution along geogrid.

Figure 61a) shows the side view (y-z) including the displacement s_{yz} vectors (grey) of the clumps above and below the geogrid layer. The soil element is

conventionally reinforced (RE). Additionally the tensile force distribution along the geogrid (black) is plotted. The average displacement s_{yz} above the geogrid layer is 4 mm. Displacement s_{yz} decreases to s_{yz} = 3 mm below the geogrid layer.

Figure 61b) shows the results gained from a front view (x-z) of the reinforced (RE) soil element. This view has also been observed by utilizing the PIV analysis. The results of DEM, FEM and PIV analysis show a sound agreement.

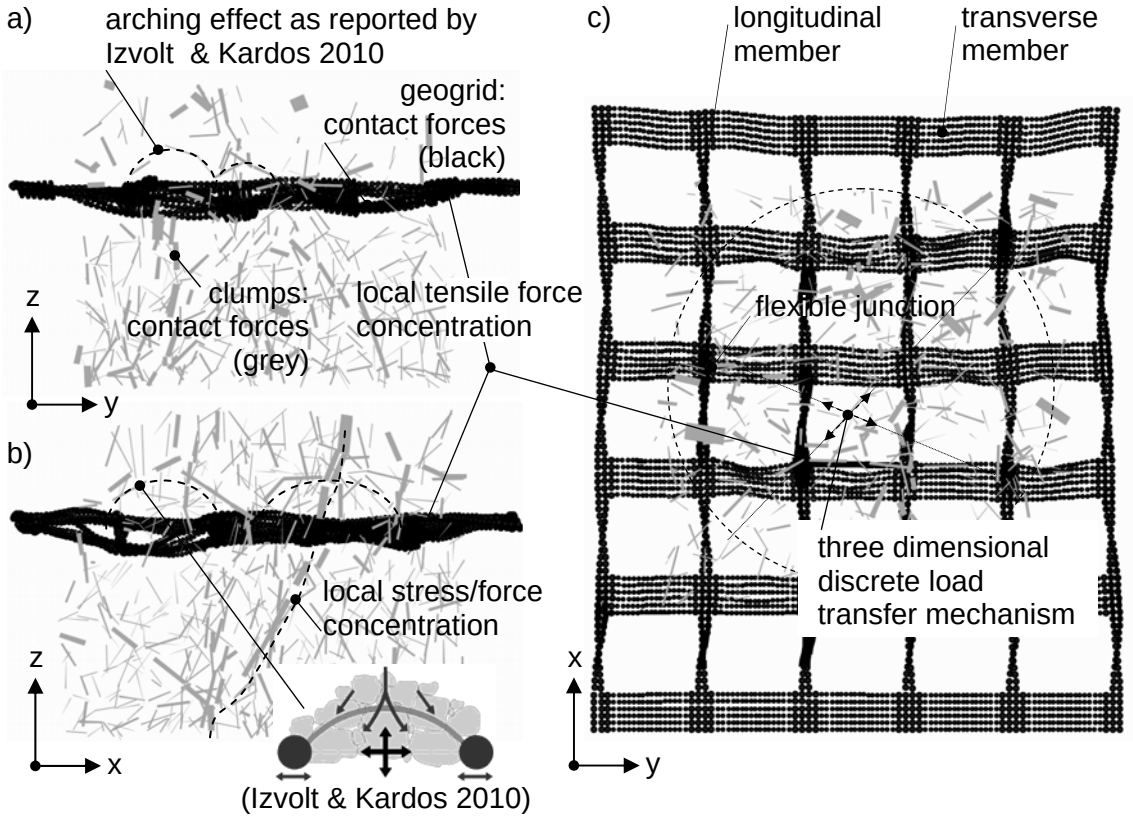

mesoscopic information
soil: 443 clumps _5478 spheres_9 contacts/clump_2 active contacts geogrid: 4333 spheres_5046 bonds

Fig. 62: DEM mesoscopic modelling of reinforced (RE) soil element to evaluate the mesoscopic load transfer mechanism: a) side view (y-z) including contact forces between the granular particles and tensile force distribution along geogrid b) front view (x-z) including contact forces between the granular particles and tensile force distribution along geogrid c) plan view including contact forces between the granular particles and tensile force distribution along geogrid.

When the deformation characteristic of the DEM results are verified, further mesoscopic investigations are performed. Figure 62 shows the DEM model of the reinforced (RE) soil element to evaluate the mesoscopic load transfer mechanism. Figure 62a) presents the side view (y-z) of the soil element. The results include the contact forces (grey) between the granular particles and tensile force distribution (black) along the geogrid.

Arching effects, as reported by Izvolt & Kardos in 2010, occur randomly between the granular soil particles and the discrete geogrid. Those arching effects lead to local stress concentrations between the particles and to high tensile forces in the geogrid at certain places. This effect is also visible in the front view (x-z) of the reinforced soil element (Fig. 62d).

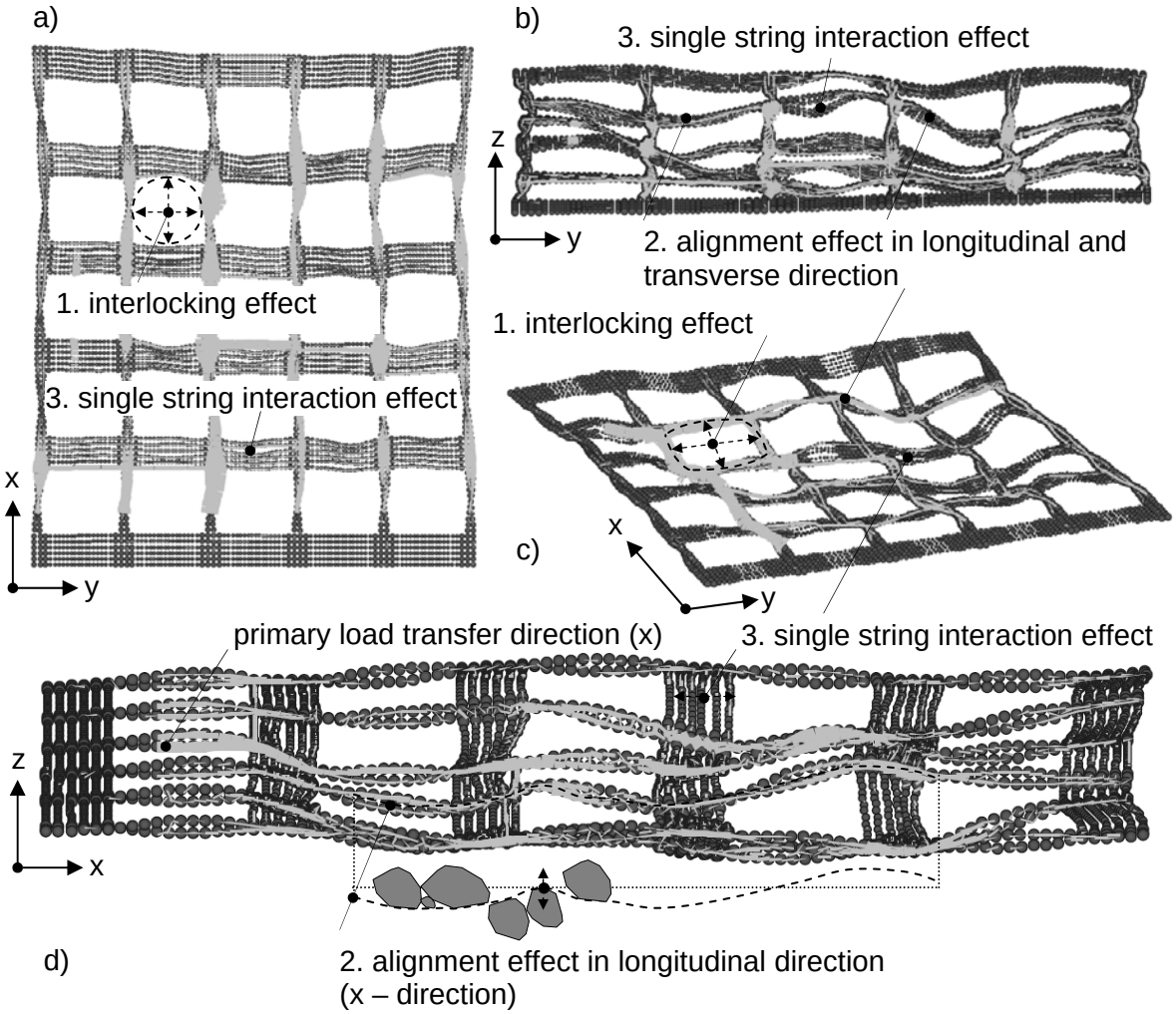

Fig. 63: DEM mesoscopic modelling of reinforced (RE) soil element to evaluate the mesoscopic deformation of the geogrid reinforcement: a) plan view of the geogrid including tensile force distribution along geogrid and interlocking effect b) side view (y-z) including tensile force distribution along geogrid and single string interaction effect c) 3D view (y-z) including tensile force distribution along geogrid d) front view (x-z) including tensile force distribution along geogrid and alignment effect.

Figure 62c) presents the plan view of the soil element. The contact forces (grey) between the clumps are plotted additionally. It is shown that the load is transferred randomly in three dimensions. The discrete mechanism may be assumed to act in two main directions. These directions are inclined with regard to the longitudinal and transverse members of the geogrid. The inclination of the load transfer direction mainly depends on the particles, their shape and their

location. Figure 62 additionally contains the mesoscopic contact information of the soil and geogrid particles included in the reinforced soil element.

Figure 63 shows the mesoscopic DEM model of the reinforced (RE) soil element to evaluate the mesoscopic deformation of the geogrid reinforcement. Three different soil geogrid interaction effects have been determined by analysing the discrete deformation behaviour of the reinforcement under loading.

Figure 63a) presents the plan view of the deformed geogrid. The tensile forces (grey) of the geogrid are plotted additionally. When the discrete clumps enter the gaps of the discrete geogrid, the longitudinal and transverse members of the reinforcement are pushed sidewards. This effect is called interlocking effect (Fig. 63a). Matis & Baslik (2004) presented a study of the interlocking effect by push tests. A cone is pushed in between the gaps of the geogrid and the pushing force is measured. Thereby, the interlocking ability of geogrids is investigated quantitatively.

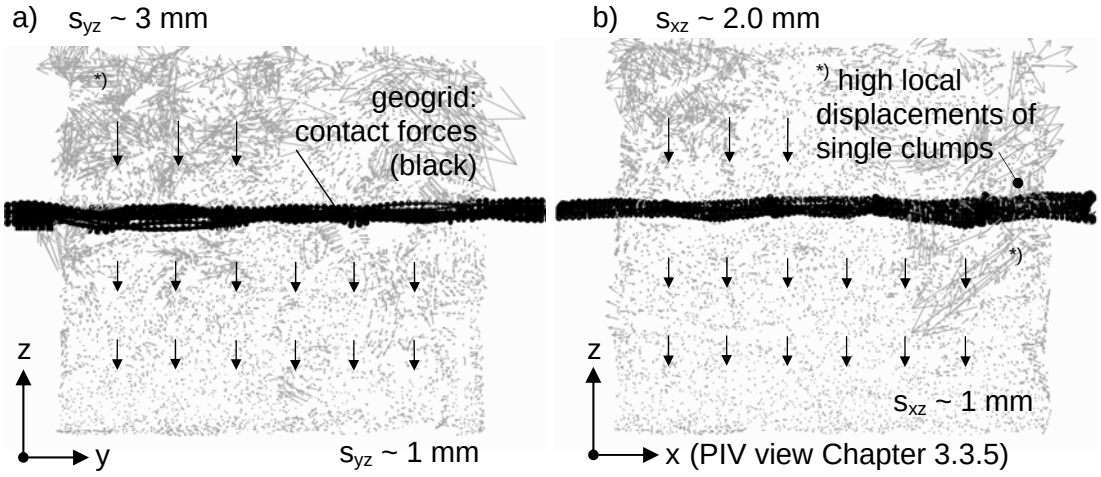

Fig. 64: DEM mesoscopic modelling of permanently prestressed reinforced (PRS_p) soil element to validate the mesoscopic displacement behaviour: a) side view (y-z) including displacement s_{yz} vectors of the granular material and tensile force distribution along geogrid b) front view (x-z) includes displacement s_{xz} vectors of the granular material and tensile force distribution along geogrid.

Figure 63b) shows the side view (y-z) of the reinforced soil element. While loading the soil element, clumps get in between the single strings of the longitudinal and transverse members of the reinforcement. This effect is defined as single string interaction effect. These two effects, interlocking and single string interaction, are well visible in the case of plotting the geogrid in three dimensions (Fig. 63c).

The front view (x-z) of the element test and the tensile force distribution along the longitudinal and transverse members of the geogrid are shown in Figure 63d). In the longitudinal and in the transverse direction the geogrid aligns to the

surrounding granular particles. This so called alignment effect results in a permanent contact between geogrid and soil particles. The more contact, the more friction can be transferred from the soil particles to the geogrid and other way round.

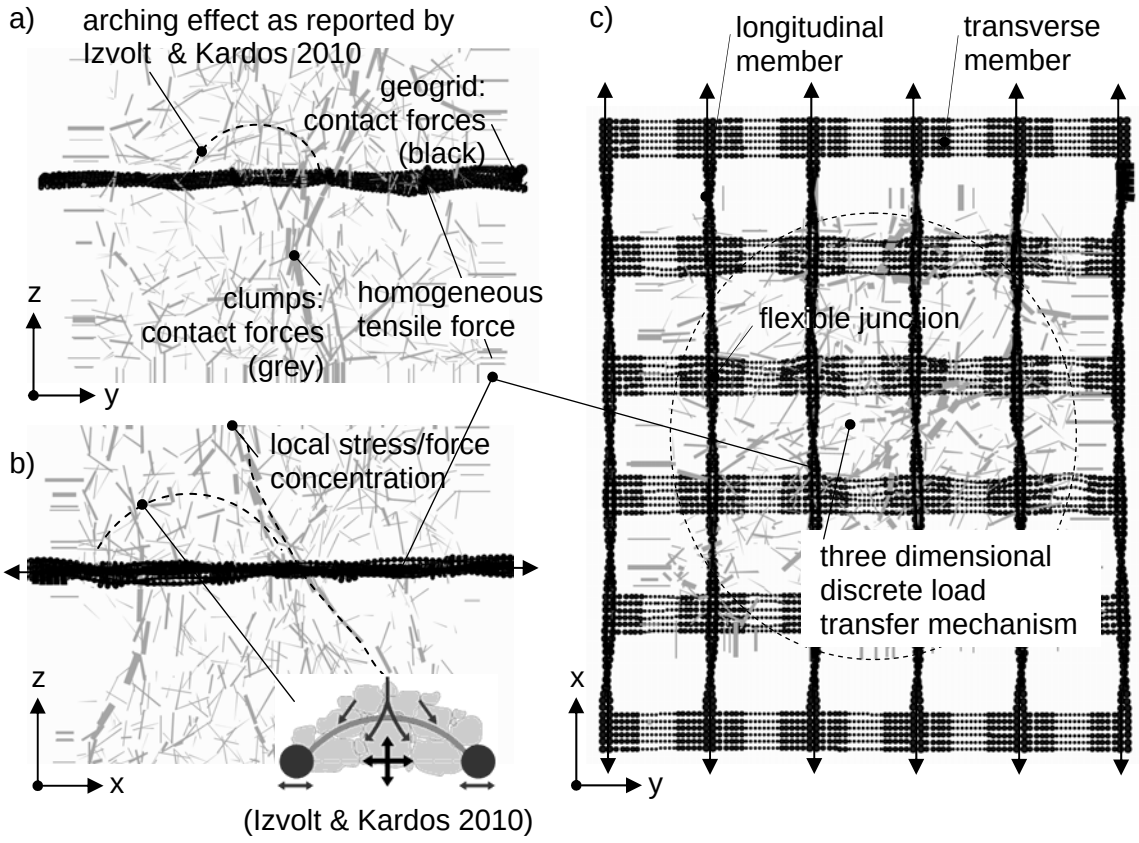

mesoscopic information
soil: 488 clumps _6037 spheres_9 contacts/clump_2 active contacts geogrid: 4332 spheres_5046 bonds

Fig. 65: DEM mesoscopic modelling of permanently prestressed reinforced (PRS_p) soil element to evaluate the mesoscopic load transfer mechanism: a) side view (y-z) including contact forces between the granular particles and tensile force distribution along geogrid b) front view (x-z) including contact forces between the granular particles and tensile force distribution along geogrid c) plan view including contact forces between the granular particles and tensile force distribution along geogrid.

In addition, the deformation behaviour of the reinforced soil element has been observed in the case of utilizing the concepts of PRS_i. Figure 64a) and b) shows the displacement vectors s_{yz} and s_{xz} of the discretely modelled permanently prestressed reinforced (PRS_p) soil element. In both directions (x-z and y-z) displacements above the geogrid layer are higher than below the geogrid. The displacements along the side view s_{yz} amount to 3 mm above the reinforcement and 1 mm below the geogrid. In the x-z directions displacements above the

geogrid are lower. They amount to 2.0 mm. This is due to the prestress of the geogrid along the longitudinal members. The results (Fig. 64b) show a sound agreement with the results gained from the FEM and PIV analyses.

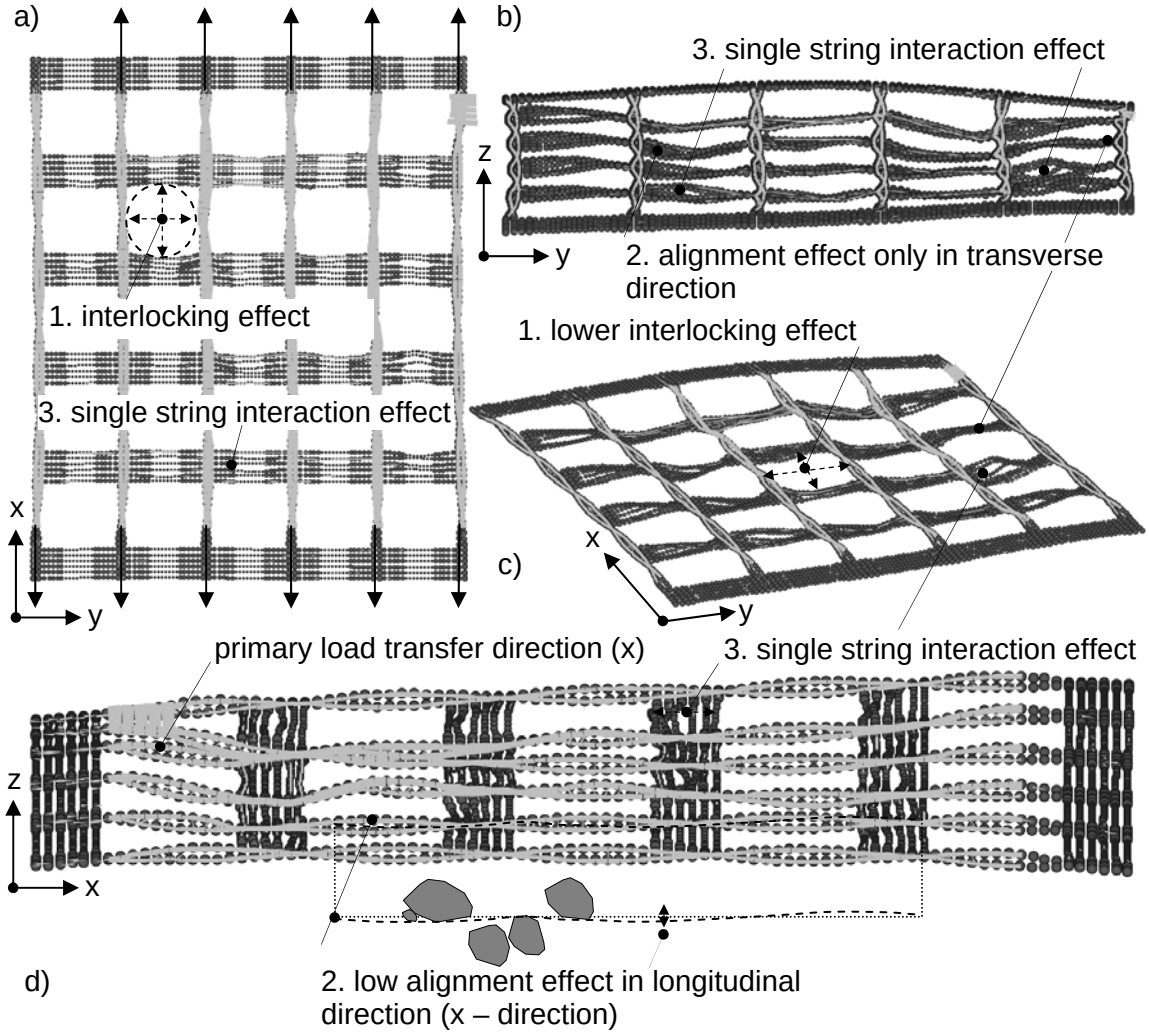

Fig. 66: DEM mesoscopic modelling of permanently prestressed reinforced (PRS_p) soil element to evaluate the mesoscopic deformation of the geogrid reinforcement: a) plan view of the geogrid including tensile force distribution along geogrid and interlocking effect b) side view (y-z) including tensile force distribution along geogrid and single string interaction effect c) 3D view (y-z) including tensile force distribution along geogrid d) front view (x-z) including tensile force distribution along geogrid and alignment effect.

Figure 65 shows the load transfer mechanism of the permanently prestressed reinforced (PRS_p) soil element. Again a so called arching effect (Izvolt & Kardos 2010) becomes visible (Fig. 65a) and b).

This effect results, as explained above, in local stress concentrations between the soil particles. The tensile force of the geogrid distributes constantly along the

reinforcement in the longitudinal (x) direction. This is due to the permanently prestress in the longitudinal direction. As opposed to the longitudinal forces in the geogrid the tensile forces in the transverse members of the reinforcement are low. Figure 65c) show the random three dimensional load transfer mechanism in the plan view.

Once, the mesoscopic deformation behaviour of the prestressed reinforcement is investigated. Figure 66 shows three effects. In the case of reinforcing the soil element conventionally (RE), interlocking effects are visible. This is also true when the geogrid is prestressed (Fig. 66a).

Figure 66b) and c) show a high quantity of single string interaction, mainly in the transverse members. This is due to the prestress of the geogrid in longitudinal direction. The transverse members are strained in x direction. Thereby, the discrete clumps can easily access between the single strings.

Figure 66d) shows the soil geogrid interaction by alignment. It is visible that the geogrid does not highly align around the particles in the longitudinal direction. This is again due to the prestress in the reinforcement. As shown in Figure 66 d) this may results in gaps between the reinforcement and the surrounding particles. Further, this results in lower interfriction between soil and reinforcement. The concept of prestressed reinforced soil usually results in an improvement of the soil structure. Although positive interaction effects such as the alignment effect, may be sometimes reduced.

It can be stated that the macroscopic results from the numerical DEM analysis show a sound agreement with the experimental investigations (Chapter 3.3.5) and the FEM simulation presented in Chapter 4.4. Additional mesoscopic analyses show the load transfer mechanism between soil and reinforcement in detail. Three effects have been observed and defined. They mesoscopically explain the positive consequences when utilizing the concept of PRS_i. As a final conclusion it can be stated that the soil geogrid interaction can be simulated well by utilizing the innovative concept of CAD clumps and geogrids for DEM simulations.

4.6 Summary and conclusions

Numerical investigations have been presented in Chapter 4. First the concept of PRS_i, presented in Chapter 2, has been generally validated. Second, results of the experimental investigations (Chapter 3.3) have been evaluated. Multiscale modelling has been utilized to investigate the macroscopic load displacement behaviour of the reinforced soil structure. Additionally, the mesoscopic soil geogrid interaction and the load transfer mechanism of the geogrid reinforced granular soil structures have been investigated. Multiscale modelling (Chapter

4.3) has combined macroscopic Finite (Chapter 4.4) Element modelling (FEM) and mesoscopic Discrete (Chapter 4.5) Element modelling (DEM).

The macroscopic results of the FEM simulation have shown a sound agreement with the results gained from experimental investigations (Chapter 3.3.3). The macroscopic results from the FEM analysis have been presented in Chapter 4.4.5. The unreinforced soil body has deformed on average by 4 mm in the vertical direction. The higher displacements (4.5 mm) have been visible in the upper right corner of the investigated region. Displacements decrease to 3 mm with respect to the depth of the unreinforced soil structure. Horizontal displacements s_h have additionally been evaluated. The soil body has moved about 3 mm in the horizontal direction. The highest horizontal movements have been observed on the surface of the slope. They amount to 4 mm. With regard to the horizontal and vertical displacements the total amount of displacements has been calculated. The total displacements s are 5 mm. The results have shown a sound agreement with the measured ones during the experimental investigations (Chapter 3.3.5). This is also recognized for the reinforced and prestressed reinforced soil structures.

In addition, the deformation boundaries of the FEM simulation have been validated and the stress boundaries for the DEM simulation have been calculated. On average, the vertical stresses level σ_v amounts to 100 kN/m². High local stresses occur close to the edges of the compaction plate. The average horizontal stresses amount to 50 kN/m². The horizontal stress and deformation distribution shows that the unreinforced soil body tends to move during the compaction (F_{comp} = 40 kN). The evaluated vertical and horizontal stresses have been used as input boundaries for the mesoscopic DEM analysis. The input values for the stress boundaries have been presented in Chapter 4.4.5.

It can finally be stated that the results from the numerical FEM analysis have shown a sound agreement with the experimental investigations (Chapter 3.3.5). Both experimental and numerical investigations have verified the concept of PRS_i.

Furthermore, a mesoscopic DEM analysis has been performed. In order to present reliable results, a detailed DEM microscopic calibration has been conducted. Once the microscopic numerical parameters are fixed (Chapter 4.5.3), three dimensional discrete and differently reinforced soil elements have been modelled. The soil elements represent the mesoscopic interaction behaviour between the reinforcement and the surrounding soil structure. First, the displacements of the soil element have been analyzed and compared to the observed deformations during the PIV analysis (Chapter 3.3.5). Second, the displacements calculated by utilizing the DEM model have been compared to the calculated ones from the FEM study (Chapter 4.4.5). The results from the DEM, FEM and PIV analyses show a sound agreement.

As soon as the deformation characteristics of the DEM results have been verified, further mesoscopic investigations are performed. The mesoscopic load transfer mechanism of the reinforced (RE) soil element has been evaluated. Arching effects as reported by Izvolt & Kardos (2010) have occurred randomly between the granular soil particles and the discrete geogrid. Those arching effects have led to local stress concentrations between the particles and to high tensile forces in the geogrid at certain places.

Moreover, three different soil geogrid interaction effects have been determined. When the discrete clumps have entered the gaps of the discrete geogrid, the longitudinal and transverse members of the reinforcement have been pushed side wards. This effect has been classified as interlocking effect. While loading the soil element, clumps have entered between the single strings of the longitudinal and transverse members of the reinforcement. This effect has been defined as single string interaction effect. In longitudinal but also in transverse direction the geogrid has aligned to the surrounding granular particles. This so called alignment effect has resulted in a permanent contact between geogrid and soil particles.

Last but not least, the deformation behaviour of the reinforced soil element has been observed in case of utilizing the concepts of PRS_i. Once again, displacements above the geogrid layer have been higher than below the geogrid. The results have shown a sound agreement with respect to the results gained from FEM and PIV analyses. So called arching effects (Izvolt & Kardos 2010) have become visible. These effects have resulted, in local stress concentrations between the soil particles. The tensile force of the geogrid has distributed constantly along the reinforcement in longitudinal direction. This has been due to the permanent prestress in the longitudinal direction. In the case of utilizing the concept of PRS_i, the transverse members have been strained in the longitudinal direction. The discrete clumps have accessed between the single strings. The geogrid has not aligned around the particles in the longitudinal direction. This has mainly been due to the prestress in the reinforcement. This may result in gaps between the reinforcement and the surrounding particles.

It can finally be stated that the macroscopic results from the numerical DEM analysis have shown a sound agreement with the experimental investigations (Chapter 3.3.5) and the FEM simulation presented in Chapter 4.4. Additional mesoscopic analyses have shown the load transfer mechanism between soil and reinforcement in detail. Three effects (interlocking, single string interaction, alignment) have been observed and defined. They have mesoscopically explained the positive consequences when utilizing the concept of PRS_i. In addition, it can be stated that the soil geogrid interaction has been simulated well by utilizing the innovative concept of CAD clumps.

The final conclusion of Chapter 4 is that the system of PRS_i has been numerically validated. As reported in Chapter 3 it may be concluded that by using the same

materials, soil and reinforcement and by prestressing the geogrid reinforcement with the presented concept (Chapter 2) the load displacement behaviour of reinforced soil structures can be increased steadily.

5 Design and construction recommendations on PRS_i by geogrids

5.1 Introduction

Chapter 5 presents design- and construction recommendations on prestressed reinforced soil (PRS_i). Design recommendations provided in literature (Lawson & Yee 2008, Chen 2007, Shukla & Kumar 2008) are validated and later enhanced. Practical construction recommendations from literature (Chew et al. 2005, Alfaro et al. 2006, Shukla & Yin 2006, NHI 2008) are discussed. Additional laboratory studies are performed and their findings are presented.

5.2 Design recommendations on prestressed reinforced soil

In the past, researchers have presented different analytical approaches to estimate the bearing capacity of strip footing (Binquet and Lee 1975a, b, Michalowski, 2004) and rectangular footing (Wayne et al. 1998, Kumar & Saran 2003) on reinforced soil foundations.

Sharma et al. (2009) reported that these analytical approaches generally assume, that all reinforcement layers either fail under tension or are pulled out. In addition, Sharma et al. (2009) stated that, the assumptions, for the analytical approaches imply that tensile forces developed in reinforcements increase with the depth of the reinforcement layer. This is in stark contrast to the tensile strain values measured along the reinforcements, installed in the experimental model footing tests conducted by Chen (2007) and Abu-Farsakh et al. (2008).

As a further example for the design of prestressed reinforced soil Lawson & Yee (2008) provide a design method for reinforced soil retaining walls where the extent of the reinforced fill zone is constrained (Fig. 67).

Due to the limited extent of the reinforced fill zone the tension forces generated in the geogrid reinforcements are fully dissipated on reaching the rigid zone at the rear of the reinforced fill. To achieve internal stability, these residual reinforcement tension forces must be dissipated. By connecting the geogrid reinforcements to anchors, respectively soil nails inserted into the rigid zone or by extending the geogrid reinforcement in the form of a wrap-around at the rear

of the reinforced backfill zone the residual tension forces of the geogrid are educed (Fig. 67).

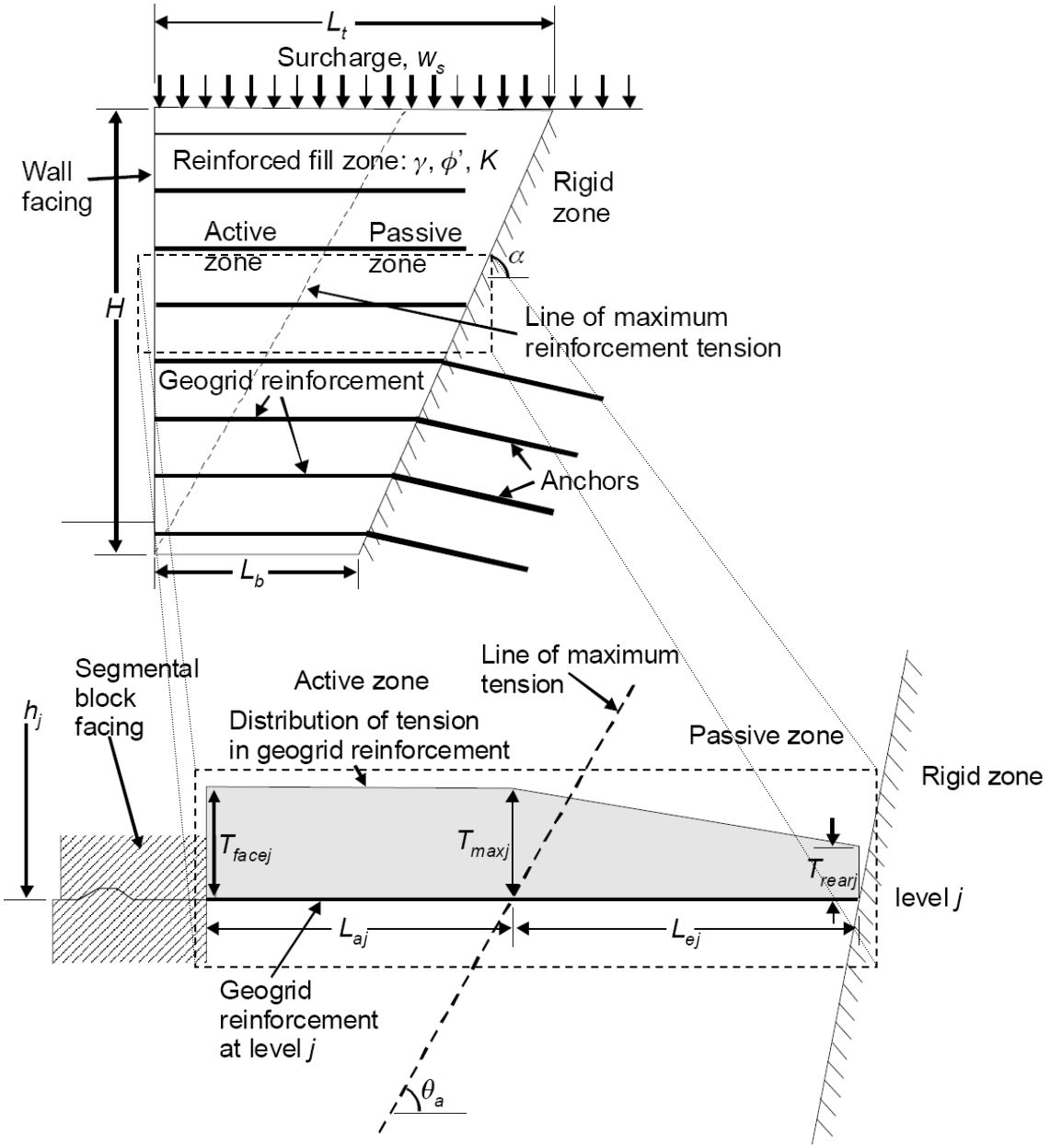

Figure 67: Reinforced soil retaining walls where the extent of the reinforced fill zone is constrained according to Lawson & Yee (2008).

5.2.1 Design recommendations for prestressed reinforced soil foundations

A new analytical approach for reinforced soil foundations has been presented by Chen (2007) based on the idea that failure is defined by a deformation criterion.

The purpose of this research has been to enhance the existing analytical approaches.

An analytical approach of reinforced soil foundations has been developed in order to gain more rational results in the case of evaluating the ultimate bearing capacity of reinforced soil foundations incorporating different soil types. Sharma et al. (2009) and Chen (2007) report that in the case of calculating the ultimate bearing capacity of reinforced soil foundations using the proposed analytical approach, it is important to find a reasonable method to estimate the tensile force in the reinforcement.

Experimental investigations conducted by Sharma et al. (2009) and Chen (2007) showed that strains developing along the reinforcement are directly related to the settlements of the footing. Sharma et al. (2009) and Chen (2007) assume that for a defined footing settlement, settlements and their distribution at a certain depth in reinforced soil foundations are assumed to be the same as the ones in unreinforced soil.

This has also been shown by the author in Chapter 4.4.5 and has further been verified by the performed macroscopic FEM simulations. The analytical approach assumes that the shape of the deformed reinforcement is compatible with the settlement distribution of the surrounding foundation soil at a certain settlement level.

The analytical approach is developed for different soil types, Sharma et al. (2009) and Chen (2007) have identified five failure modes based on a literature review (Huang & Menq 1997, Wayne et al. 1998, Huang & Tatsuoka 1990, Michalowski 2004):

- Failure above reinforcement
- Failure between reinforcement
- Failure like footing on a two layer soil system
- Failure in reinforced zone
- Partial punching shear failure in reinforced zone

The later presented failure modes are restricted to the ones, which are relevant for granular, sandy and gravely soils. The following Figure (Fig. 68) shows the two most relevant failure modes:

Failure within the reinforced zone will occur when the strength of the reinforced zone is larger than the bearing capacity of the underlying unreinforced zone. When the ratio (*d/B*) is relatively large this failure mechanism will occur. Fig. 68a) shows the

failure mechanism, where *B* presents the width of the footing and the thickness of the reinforced zone is defined by *d*. Chen (2007) defines the distance between the reinforcement layers as *h*. The distance between reinforcement and the surface is presented by *u*. The tensile forces in the reinforcement are presented by T_i.

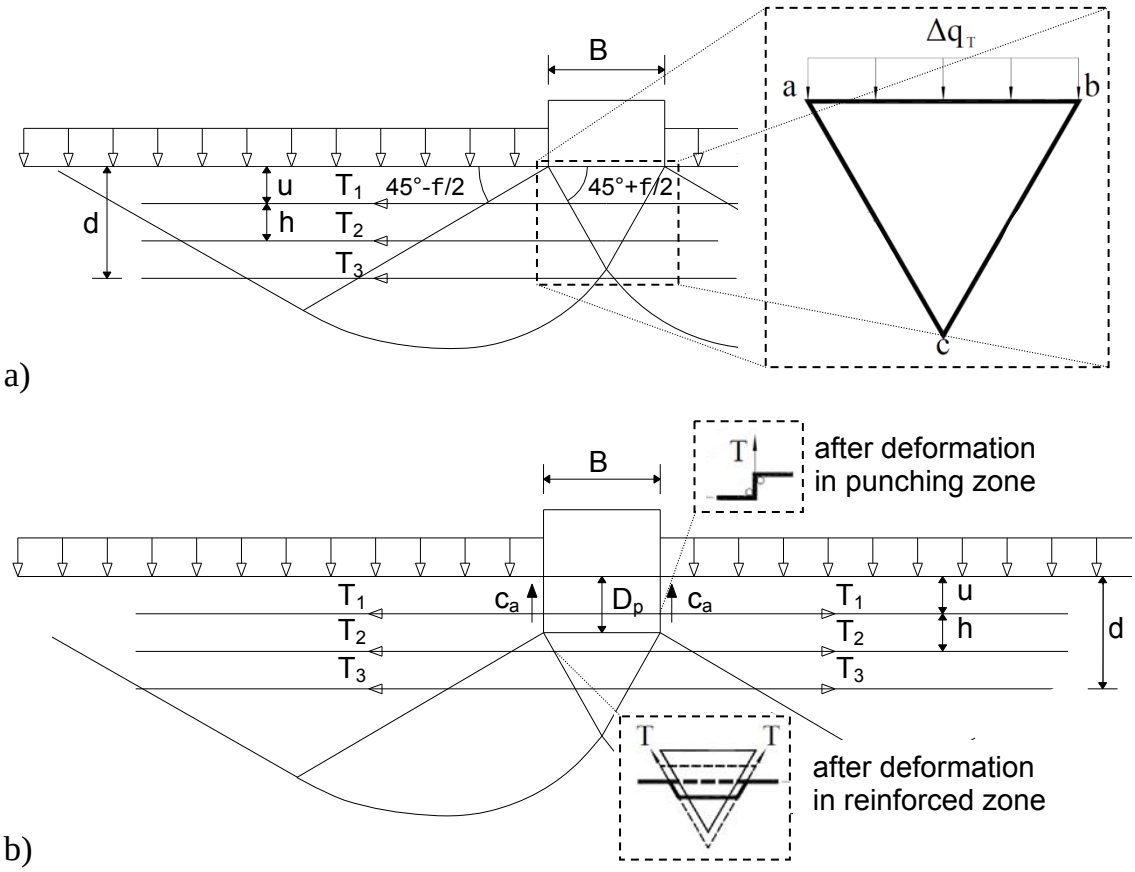

Figure 68: Failure modes relevant for granular, sandy and gravely soils according to Chen (2007): a) failure in the reinforced zone b) partial punching shear failure in the reinforced zone.

A partial punching shear failure occurs in the reinforced zone and is followed by a general shear failure shown in Figure 68b). The depth of the partial punching into the reinforcement layer is defined by d_p. When partial punching occurs in a cohesive material, an additional cohesion c_a is activated.

The analytical approach proposed by Chen (2007) has been enhanced. With the enhanced approach permanently and temporarily prestressed reinforced soil foundations can be designed.

Due to permanently prestressing, the reinforcement receives additional strains. These additional strains lead to higher tensile forces in the reinforcement. The higher tensile forces result in an increase of the ultimate bearing capacity of the reinforced soil.

In addition to the beneficial effect of higher tensile forces, a non-linear distribution of the tensile load strain behaviour of the reinforcement has been observed during laboratory tests (Chapter 3.3.3). Because of the non-linear, tensile strength behaviour of the reinforcement it is important to optimize the tensile modulus *EA* of the reinforcement if utilizing the concept of PRS_p.

These two principle effects have to be considered in the design of the permanent prestressed reinforced soil. Important input values for this design approach are the strains activated due to the prestress with respect to the stress-strain curve of the reinforcement. The tensile stress-strain curve has to be tested in the laboratory according to Chapter 3.3.3 to determine the exact tensile modulus according to the strain of the reinforcement.

The additional tensile force $T_{prs,p}$ is calculated with

$$T_{prs,p} = \varepsilon_{prs,p} \cdot EA \tag{6}$$

This additional tensile force is added to the tensile force T_i due to the settlement calculation according to Schmertmann et al. (1978).

This summation results in the total tensile force $T_{sum,i}$.

$$T_{sum,i} = T_i + T_{prs,p} \tag{7}$$

The following formulas show the increased bearing capacity due to permanent prestressing for the different combinations, which have to be added to the ultimate bearing capacity of the underlying unreinforced soil.

$$q_{u(R)} = q_b + \Delta q_{T,prs,p} \tag{8}$$

The increase of bearing capacity in the reinforced zone is calculated by the following equations according to Chen (2007):

- Horizontal confinement effect (sandy soil)

$$\Delta q_{T,prs,p} = \sum_{i=1}^{N} \frac{12 \cdot T_{sum,i} \cdot [u + (i-1) \cdot h] \cdot r_T}{B^2} \tag{9}$$

with N: number of reinforcement layers
r_T: dimensionless factor according to Chen (2007)

- Vertical membrane effect (large particle size soil)

$$\Delta q_{T,prs,p} = \sum_{i=1}^{N} \frac{4 \cdot T_{sum,i} \cdot \sin\left(\frac{\pi}{4} + \frac{\varphi}{2}\right) \cdot \left[B - 2 \cdot \left[u + (i-1) \cdot h\right] \cdot \tan\left(\frac{\pi}{4} - \frac{\varphi}{2}\right)\right]}{B^2} \quad (10)$$

with φ: effective friction angle

When partial punching shear failure occurs according to Chen (2007) the following equations have to be executed:

- Vertical membrane effect (large particle size soil)

$$\Delta q_{T,prs,p} = \frac{4 \cdot c_a \cdot D_P}{B} + 2 \cdot \gamma_t \cdot D_P^2 \cdot \left(1 + \frac{2 \cdot D_f}{D_P}\right) \cdot \frac{K_S \cdot \tan\varphi}{B} - \gamma_t \cdot D_P + \frac{4 \cdot \sum_{i=1}^{N_P} T_i}{B} + \sum_{i=N_P+1}^{N} \frac{4 \cdot T_{sum,i} \cdot \sin\left(\frac{\pi}{4} + \frac{\varphi}{2}\right) \cdot \left[B - 2 \cdot \left[u + (i-1) \cdot h - D_P\right] \cdot \tan\left(\frac{\pi}{4} - \frac{\varphi}{2}\right)\right]}{B^2} \quad (11)$$

with D_P: indentation depth
γ_t: unit weight of soil in reinforced zone
D_f: embedment depth of footing
K_S: punching shear coefficient
N_p: number of reinforcement layers located in the punching shear failure zone

In the case of prestressing the reinforcement temporarily prestressing is applied in the reinforcement during the installation process. Afterwards the soil is compacted. Due to prestressing, the reinforcement expands and the soil can access in the aperture of the reinforcement. After the compaction process the prestressing is released (Chapter 2).

The soil reinforcement interaction totally avoids the whole reduction of the applied prestress. The release of prestress in the geogrid leads to horizontal stresses in the soil and as a result to an increase of the ultimate bearing capacity. This is due to the fact that additional horizontal stresses in the soil lead to an increase of resisting vertical stresses. In addition, the tensile forces in the reinforcement increase due to the applied prestress.

The horizontal stresses due to the residual strain $\varepsilon_{prs,t}$ and the stiffness of the soil E_s can thereafter be calculated with the following formulas (12) to (14).

The factor R determines the ratio between strain due to prestressing and residual strain after releasing the prestress. This factor can take values between R = 0.0 and 1.0.

$$\Delta\sigma_{h,prs,t} = \varepsilon_{prs,t} \cdot E_S \cdot \kappa \tag{12}$$

$$\varepsilon_{prs,t} = \varepsilon_{prs,p} \cdot R \tag{13}$$

$$\kappa = \frac{id_{grain} \cdot N}{d} \tag{14}$$

The factor κ determines the thickness of the zone where horizontal stresses are transferred to the soil. The thickness may be assumed to be as thick as a shear band, progressing in the granular soil during shear failure. The author recommends setting the thickness of the zone three times the diameter of the soil grain.

These horizontal stresses can be translated in vertical stresses for a confined situation by the following equations:

$$\Delta\sigma_{v,prs,t} = \frac{\Delta\sigma_{h,prs,t}}{K_0} \tag{15}$$

$$K_0 = 1 - \sin\varphi \tag{16}$$

The vertical stresses which are calculated with equation ((15) have to be added to the ultimate bearing capacity of the reinforced soil.

The additional tensile force in the reinforcement is calculated with equations (6) and (7). In the case of temporary prestressing, $\varepsilon_{prs,p}$ has to be replaced with $\varepsilon_{prs,t}$.

Equation (17) shows the increased bearing capacity due to temporary prestressing for the different combinations, which have to be added to the ultimate bearing capacity of the underlying unreinforced soil.

$$q_{u(R)} = q_b + \Delta q_{T,prs,t} \tag{17}$$

The increase of bearing capacity in the reinforced zone is calculated by the following equations (18) to (20) according to Chen (2007).

- Horizontal confinement effect

$$\Delta q_{T,prs,t} = \Delta\sigma_{v,prs,t} + \sum_{i=1}^{N} \frac{12 \cdot T_{sum,i} \cdot [u + (i-1) \cdot h] \cdot r_T}{B^2} \tag{18}$$

- Vertical membrane effect

$$\Delta q_{T,prs,t} = \Delta\sigma_{v,prs,t} + \sum_{i=1}^{N} \frac{4 \cdot T_{sum,i} \cdot \sin\left(\frac{\pi}{4} + \frac{\varphi}{2}\right) \cdot \left[B - 2 \cdot [u + (i-1) \cdot h] \cdot \tan\left(\frac{\pi}{4} - \frac{\varphi}{2}\right)\right]}{B^2} \tag{19}$$

If partial punching shear failure occurs according to Chen the following equations have to be executed.

- Vertical membrane effect

$$\Delta q_{T,prs,t} = \frac{4 \cdot c_a \cdot D_P}{B} + 2 \cdot \gamma_t \cdot D_P^2 \cdot \left(1 + \frac{2 \cdot D_f}{D_P}\right) \cdot \frac{K_S \cdot \tan\varphi}{B} - \gamma_t \cdot D_P + \Delta\sigma_{v,prs,t} + \frac{4 \cdot \sum_{i=1}^{N_P} T_{sum,i}}{B} + \sum_{i=N_P+1}^{N} \frac{4 \cdot T_{sum,i} \cdot \sin\left(\frac{\pi}{4} + \frac{\varphi}{2}\right) \cdot \left[B - 2 \cdot [u + (i-1) \cdot h - D_P] \cdot \tan\left(\frac{\pi}{4} - \frac{\varphi}{2}\right)\right]}{B^2} \tag{20}$$

The analytical approach has been validated by back calculating the static load displacement tests presented in Chapter 3.3.

The presented results of the laboratory test (Chapter 3.3.5) are expressed by pressure-settlement curves. These curves are reliable up to a settlement of about 12 % based on the width of the foundation.

The results of the analytical approach represent the ultimate bearing capacity in case of a s/B value of 14%. Therefore it is necessary to extrapolate the pressure *p* - settlement *s* curves to the defined deformation failure criterion (s/B = 14 %).

When utilizing the concept of temporarily prestressed reinforced soil a shear band thickness of three times the maximum grain diameter has been assumed. The *R*-factor (R_{inter} = 0.8 – 1.1) has been derived from experimental studies. Table 17 shows the input parameter.

Table 18 shows the results of the calculations compared with the results of the laboratory tests.

The presented results show the analyzed bearing capacities in the case of calculating the partial punching shear failure in the reinforced zone by vertical reinforcement tension. The result from this failure mechanism shows a sound agreement with the experimental results of the tested reinforced soil foundations. The results analyzed from failure in the reinforced zone by vertical reinforcement tension fit the experimental results well in case of utilizing the concept of PRS_p and PRS_t.

Table 17: Input parameter

Parameter	Value	Unit
Width B	0.21*	[m]
Top layer spacing u	0.15	[m]
Vertical spacing h	0.15	[m]
Embedment depth of footing D_f	0	[m]
Number of reinforcement layer N	3	[-]
Unit weight of soil in reinforced zone γ_t	15.80	[kN/m³]
Friction angle φ (back analyzed)	44.30	[°]
Unit adhesion of soil c_a	0	[kN/m²]
Elastic modulus of soil E_s (back analyzed/parameter study)	3.0/8.0	MPa
Indentation depth D_P	0.035	[m]
Tensile modulus of reinforcement EA	50/400	[kN/m]
Strain due to permanent prestressing $\varepsilon_{prs,p}$	2.5	[%]
Multiple of grain diameter $i \cdot d_{grain}$	48	[mm]
Ratio prestressing strain-residual strain R_{inter}/R	0.8/1.0	[-]

Table 18: Comparison of ultimate bearing capacities for s/B = 14 % (analytical approach versus laboratory test results (Chapter 3.3.5)

	Bearing capacity $q_{u(R)}$ [kN/m²]	
	analytical approach	laboratory tests
Unreinforced	277	280
Reinforced	384 (partial punching shear failure)	390
Permanently prestressing	625 (failure in reinforced zone)	600
Temporarily prestressing	673 (failure in reinforced zone)	670

An exemplary parametric study has been carried out in order to evaluate the limits of the analytical approach. The input parameters are presented in Table 17. The elastic modulus of the soil has been set to a value of E_s = 8 MPa. The interaction coefficient R is set to 1.0. Thereafter settlement normalized by the width of the footing s/B to reach a value of 8 %.

Figure 69 shows the bearing capacity for permanently prestressed reinforced soil foundations. The maximum bearing capacity ($q_{U(R),permanent}$ = 700 kN/m²), evaluated in the case of failure according to the partial punching shear failure in

the reinforced zone by vertical reinforcement tension, changes with respect to the amount of permanent prestressing $\varepsilon_{PRS,p}$.

The highest bearing capacity is calculated with a permanent prestressing $\varepsilon_{PRS,p}$ of 3.5 %. This is due to the non-linear tensile modulus *EA* of the reinforcement (Chapter 3.3.3). Although the amount of prestress ($\varepsilon_{PRS,p}$ = 4 %) increases the tensile modulus *EA* decreases. Thereafter, the maximum bearing capacity decreases (Chapter 2).

Figure 69 additionally shows the tensile modulus *EA* with regard to the amount of permanent prestressing $\varepsilon_{PRS,p}$.

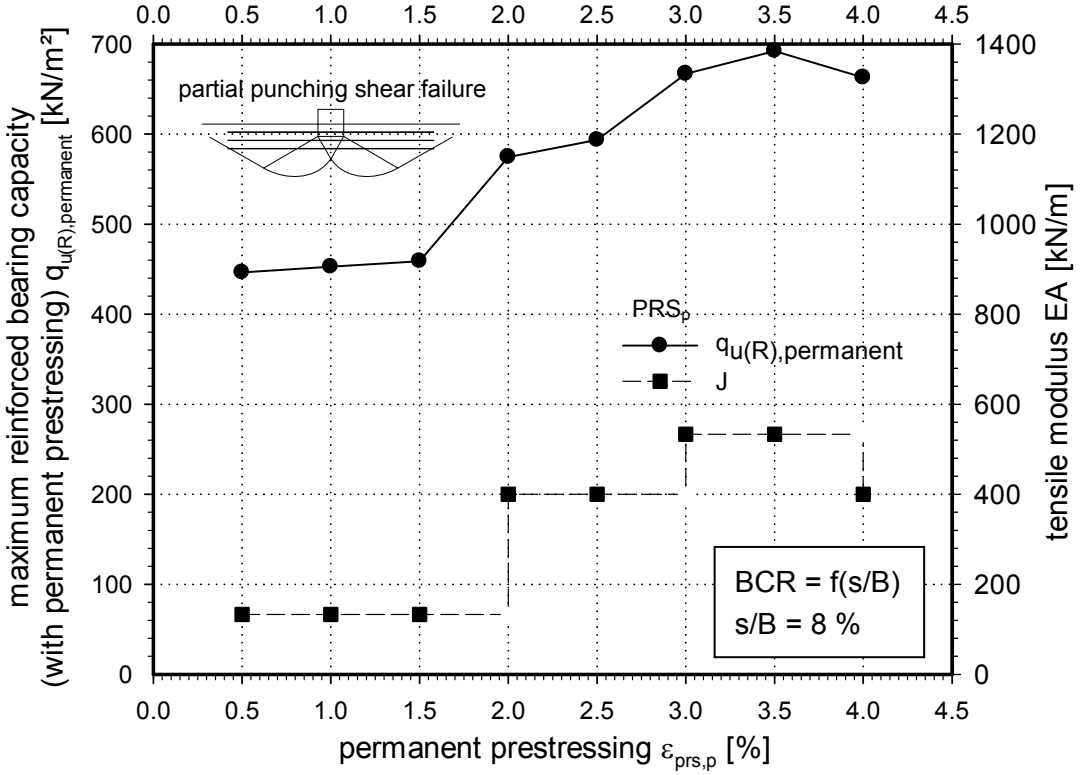

Figure 69: Permanent prestressing $\varepsilon_{PRS,p}$ versus maximum bearing capacity $q_{U(R),permanent}$ for permanently prestressed reinforced soil foundations and versus the tensile modulus *EA* of the geogrid.

The maximum bearing capacity ($q_{U(R),temporary}$ = 1000 kN/m²) for temporarily prestressed reinforced soil foundations is shown in Figure 70. The maximum bearing capacity $q_{U(R),temporary}$ increases with regard to the amount of temporarily prestressing $\varepsilon_{PRS,t}$. The highest bearing capacity is calculated with a prestressing $\varepsilon_{PRS,p}$ of 4.0 %.

Although the tensile modulus *EA* decreases at a prestress of $\varepsilon_{PRS,p}$ = 4 % the additional bedding support, by horizontal confinement, improves the temporarily prestressed reinforced soil foundation. These effects are described in Chapter 2.

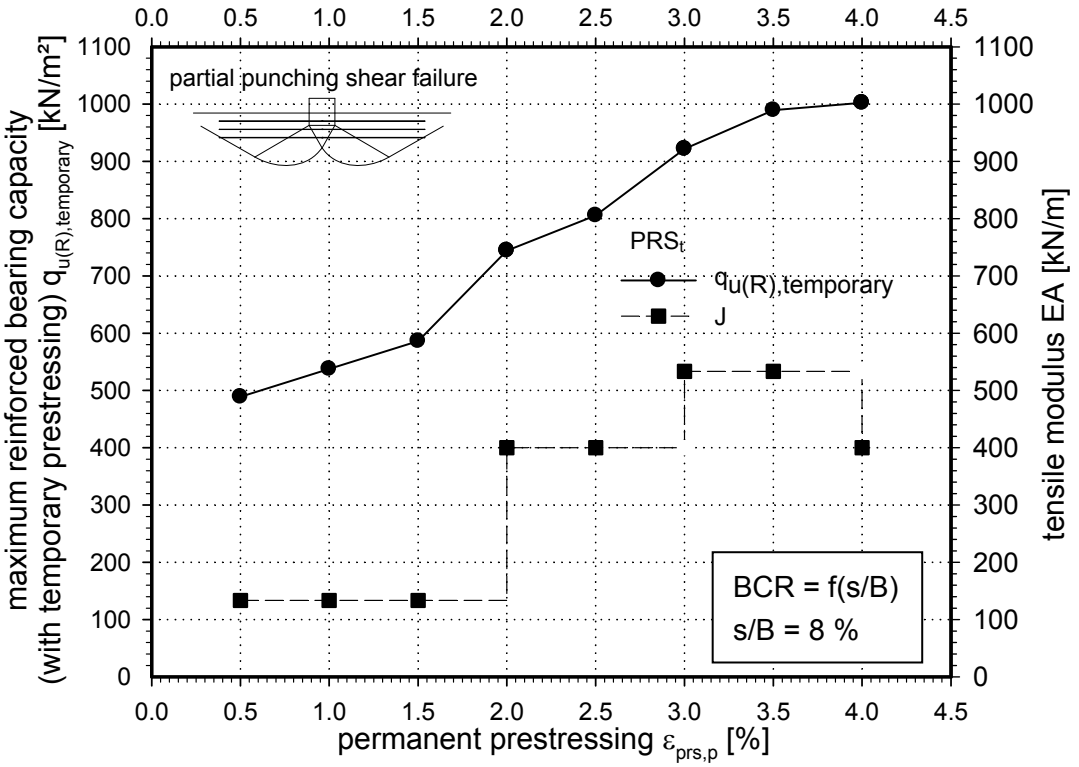

Figure 70: Permanent prestressing $\varepsilon_{prs,p}$ versus maximum bearing capacity $q_{U(R),\ temporary}$ for temporarily prestressed reinforced soil foundations and versus the tensile modulus *EA* of the geogrid.

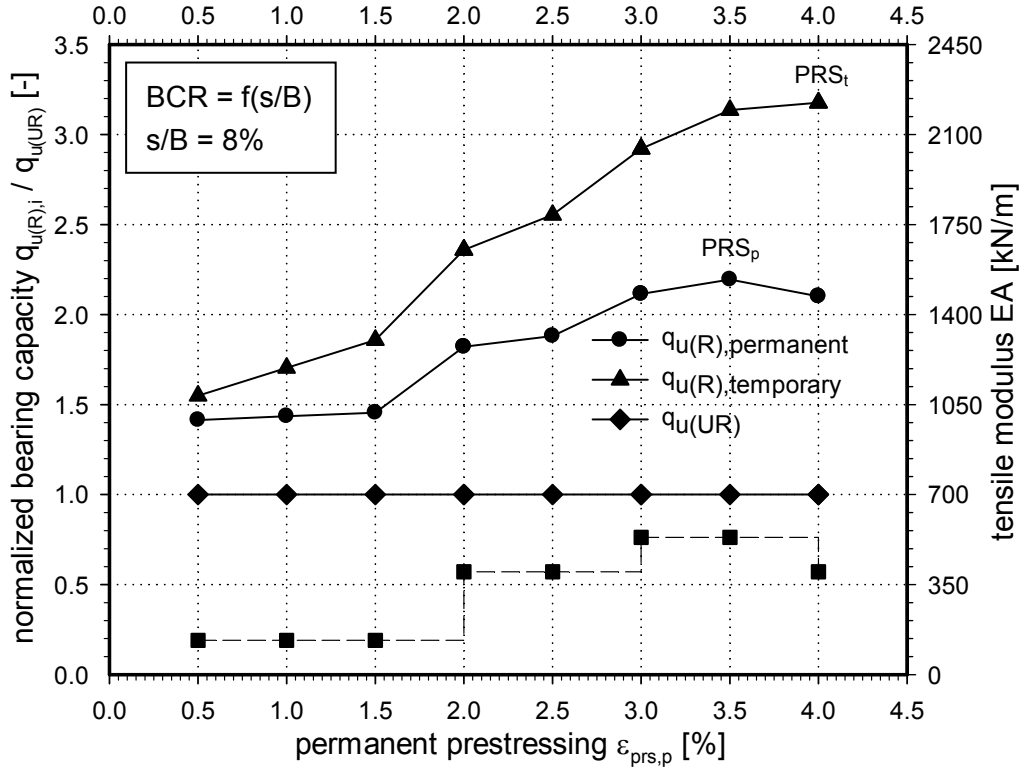

Figure 71: Permanent prestressing $\varepsilon_{PRS,p}$ versus normalized bearing capacity $q_{U(R)}/q_{U(UR)}$ for prestressed reinforced soil foundations and versus the tensile modulus *EA* of the geogrid.

Figure 71 presents the normalized bearing capacity $q_{U(R)}/q_{U(UR)}$ for reinforced soil foundation utilizing the concept of PRS_i versus amount of prestressing.

Additionally, the tensile modulus *EA* with respect to the amount of prestressing $\varepsilon_{PRS,p}$ is presented in Figure 71.

Figure 72 shows the bearing capacity $q_{U(R)}$ for reinforced (RE) soil foundations versus the spacing $u = h$. The maximum bearing capacity ($q_{U(R)}$ = 480) is analyzed in case of installing five reinforcement layers (N = 5) with a spacing ($u = h$) of 0.05 m.

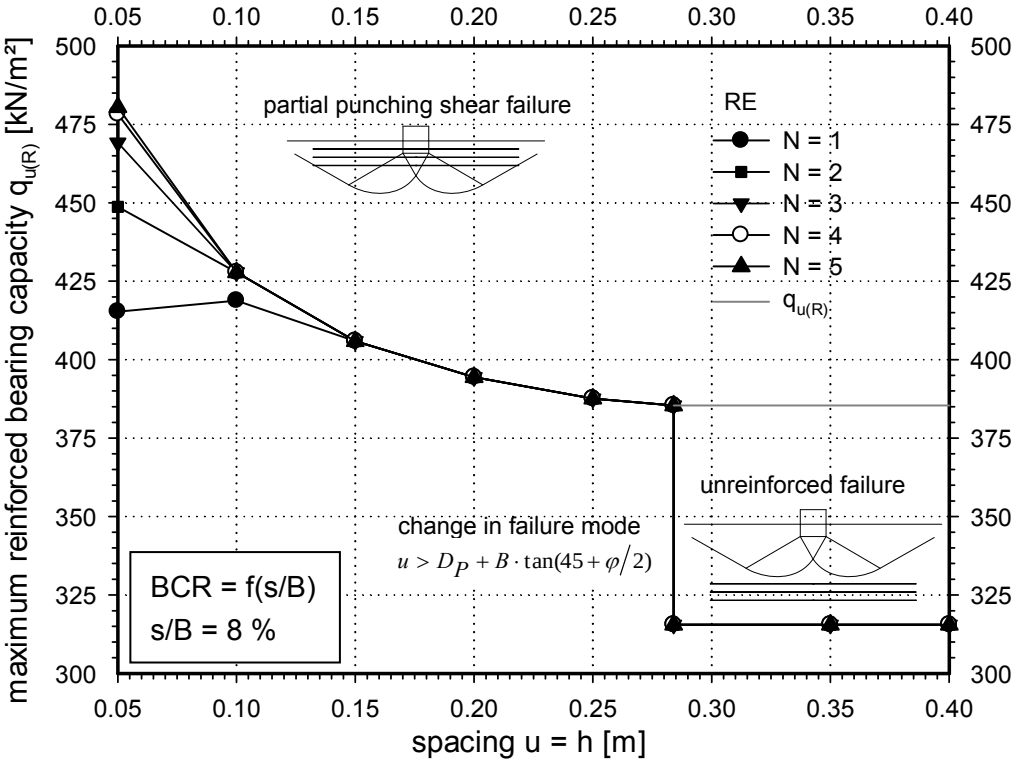

Figure 72: Spacing $u = h$ versus maximum bearing capacity $q_{U(R)}$ for reinforced soil foundations: partial punching shear failure changes into unreinforced failure if $u > D_P + B * tan(45+\varphi/2)$.

It can be stated that the tighter the spacing between the reinforcement layers, the higher the maximum bearing capacities $q_{U(R)}$ analyzed with the presented analytical approach. This is due to the fact that, when the spacing $u = h$ decreases, the number of reinforcement layers N increases.

When the ultimate bearing capacity (s/B = 8 %) of the footing is reached, the structure fails according to the partial punching shear failure mechanism presented in Figure 72.

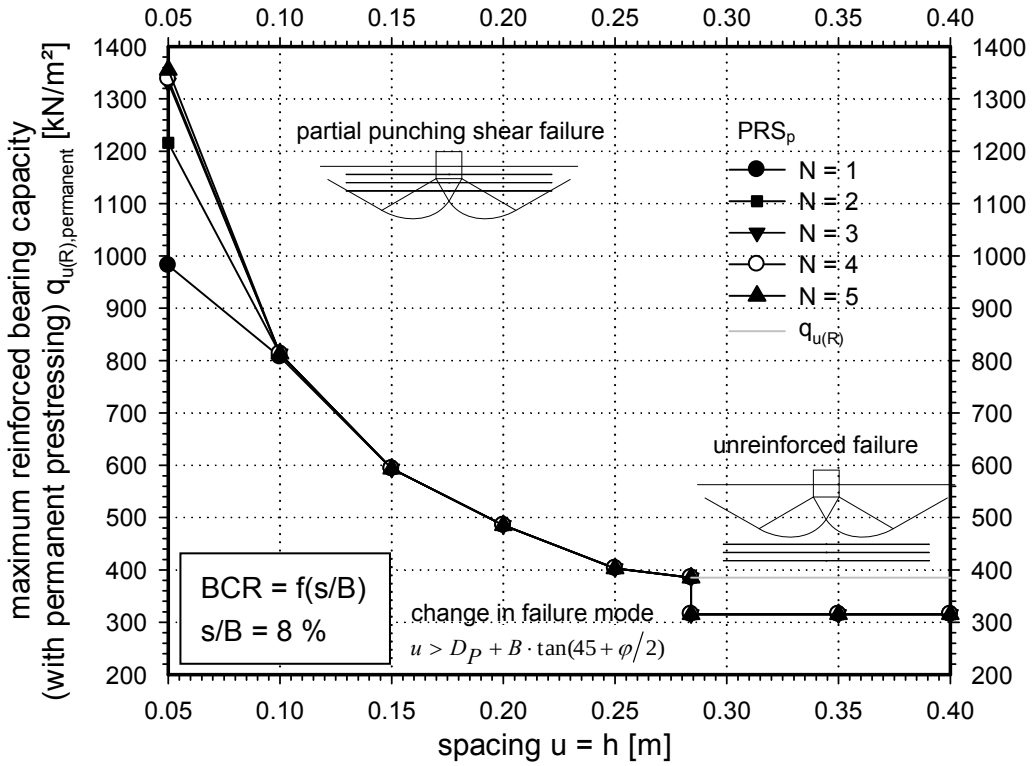

Figure 73: Spacing $u = h$ versus maximum bearing capacity $q_{U(R),permanent}$ for permanently prestressed reinforced soil foundations: partial punching shear failure changes into unreinforced failure if $u > D_P + B*tan(45+\varphi/2)$.

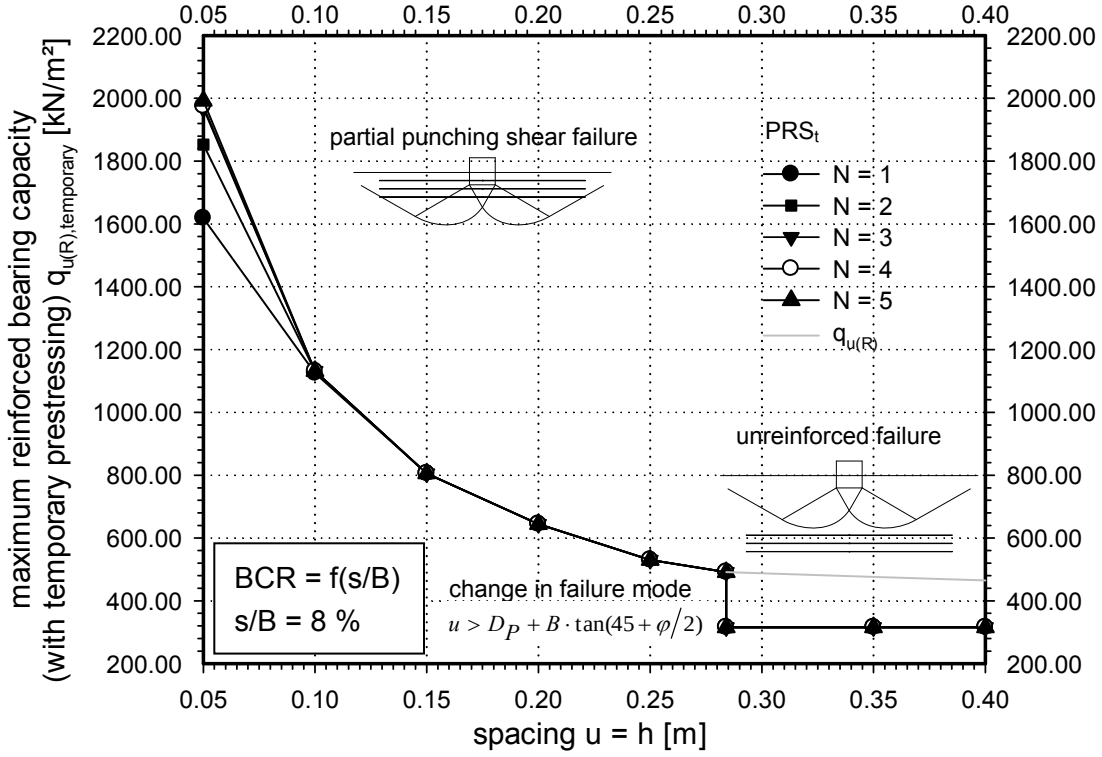

Figure 74: Spacing $u = h$ versus maximum bearing capacity $q_{U(R),temporary}$ for temporarily prestressed reinforced soil foundations: partial punching shear failure changes into unreinforced failure if $u > D_P + B*tan(45+\varphi/2)$.

When the spacing is as such,

$$u \geq D_p + B \cdot \tan(45 + \frac{\varphi}{2}) \tag{21}$$

the failure mode changes to the unreinforced failure (Fig. 72) mechanism.

With respect to the input parameters presented in Table 17, the change of the failure mode occurs at a spacing ($u = h$) equal to 0.28 m.

When the spacing reaches a distance of 0.28 m, a failure above the reinforced zone progresses. In other words, two reinforcement layers are only sufficient when the spacing $u = h$ is smaller than 0.5 times u according to Equation 21.

Figure 73 shows the bearing capacity $q_{U(R)}$ for permanently prestressed reinforced (PRS_p) soil foundations versus the spacing $u = h$. The maximum bearing capacity ($q_{U(R),permanent}$ = 1350) increases in contrast to the reinforced ultimate bearing capacity. This is due to the non linear tensile modulus EA of the reinforcement (Chapter 3.3.3). In case of utilizing the concept of PRS_p, the tensile modulus EA of the prestressed geogrid increases to 400 kN/m.

The maximum bearing capacity ($q_{U(R),temporary}$ = 1350) further increases in contrast to the reinforced ultimate bearing capacity when utilizing the concept of PRS_t (Fig. 74). This is due to the additional horizontal confinement effect. After releasing the geogrid additional pressure forces are activated between the grains of the gravelly backfill material (Equations 12 to 16).

Figure 75 shows the normalized spacing h/B in the range of 0.05 and 1, versus the normalized bearing capacity $q_{U(R)}/q_{U(UR)}$ for reinforced and prestressed reinforced soil foundation structures. The bearing capacities drastically improve in the case of utilizing the concept of PRS_i. Figure 75 includes an area of recommended installation depth. The recommended installation depths are partly based on literature (Chen 2007) and extended with the findings from the performed experimental investigations.

The experimental results verifying the analytical approach are presented in Figure 75.

It has to be stated that future research works but also real field tests should enhance the experimental investigations (Chapter 3) to further validate the presented analytical approach.

Finally, it has to be stated that this analytical approach includes its limitations. The settlements s of the footing are calculated according to Schmertmann et al. (1978).

The settlements are calculated assuming unreinforced soil. According to Chen (2007) the settlement distribution is assumed to be similar for reinforced and thereafter also for prestressed reinforced soils.

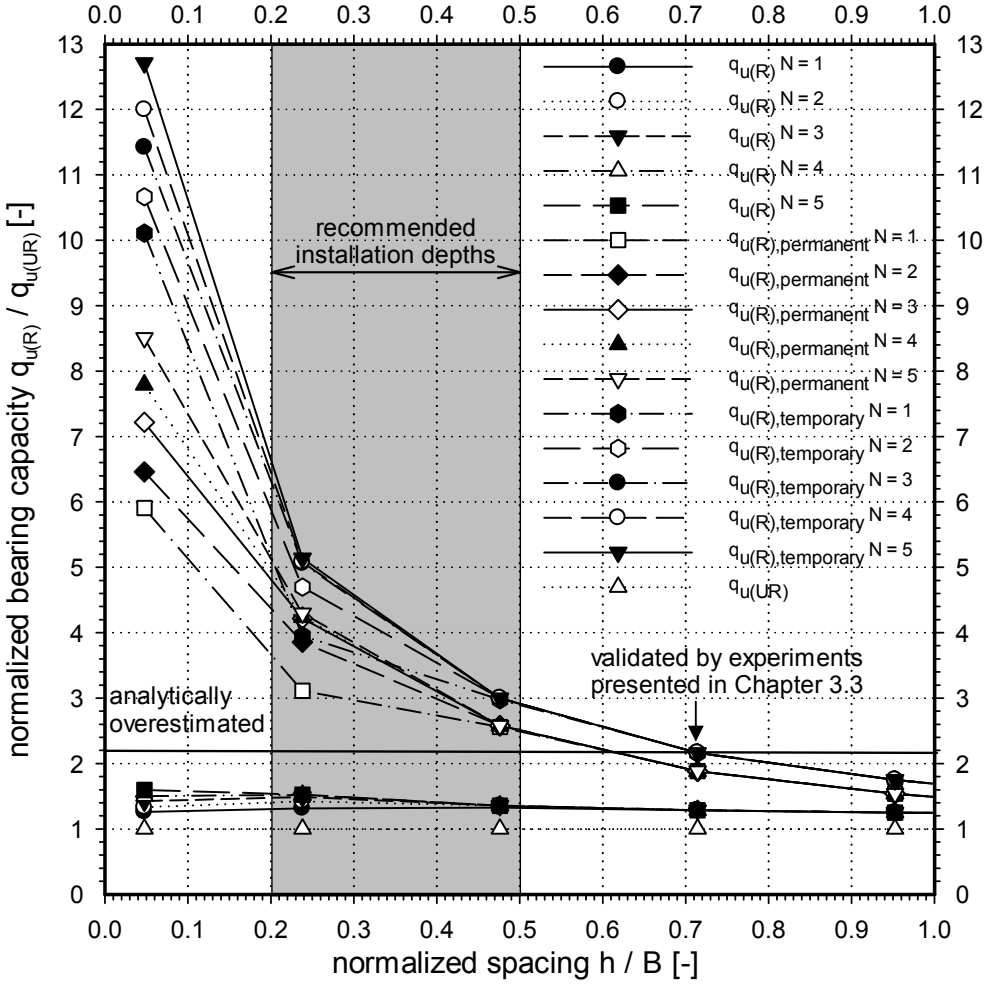

Figure 75: Normailzed spacing *h/B* versus normalized bearing capacity $q_{U(R)}/q_{U(UR)}$ for reinforced and prestressed reinforced soil foundations: recommended installation depths and experimental validation.

This may not correspond to reality. Future research should adapt the analytical approach according to Chen (2007).

5.2.2 Design recommendations for prestressed reinforced soil slopes

Shukla & Kumar (2008) have presented an analytical approach for prestressed geosynthetic reinforced embankments on soft ground based on the idea that failure is defined through a deformation criterion.

The approach presents the derivation of an expression for the factor of safety with respect to the overall slope stability of a prestressed geosynthetic reinforced embankment resting on soft ground.

The development of a mobilised tensile force in the geosynthetic layer up to the desired level requires significant settlements of the embankment which may not occur during the construction period because the settlement of an embankment over soft ground continues over a long period of time. To overcome this difficulty, the geosynthetic layer can be prestressed to achieve the desired level of tensile force.

Figure 76 shows an embankment of height *H* and slope angle *β* with a prestressed geosynthetic layer resting on soft ground. An embankment constructed on soft ground expectedly has a potential failure mode in the form of an approximately circular slip surface which extends into the foundation soil.

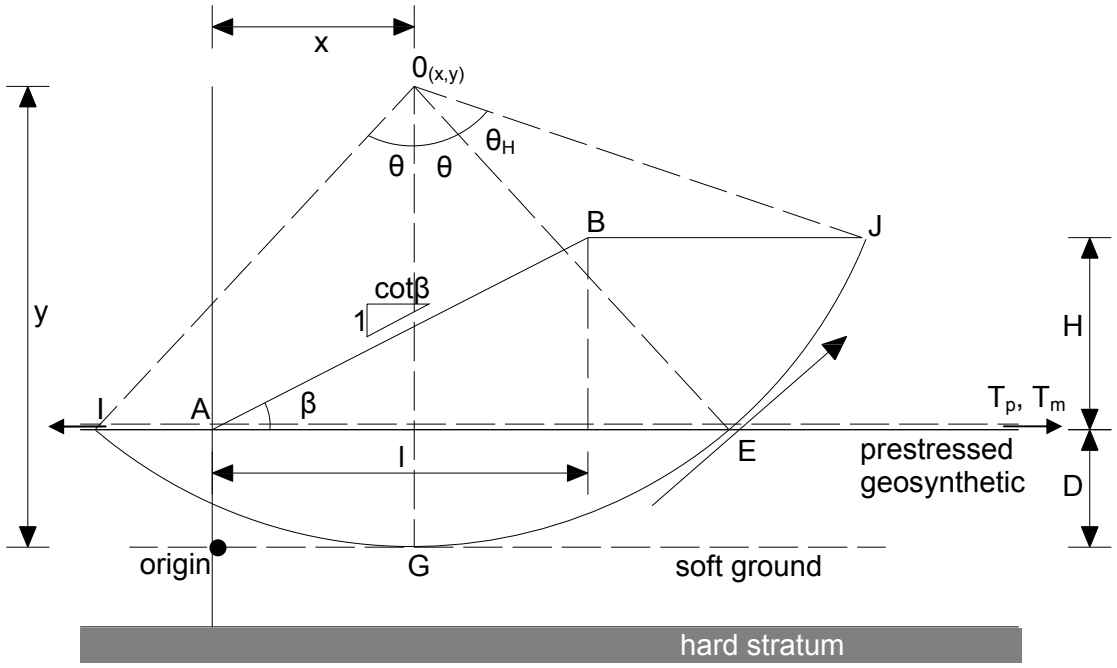

Figure 76: Embankment with prestressed geosynthetic layer resting on soft ground according to Shukla & Kumar (2008).

The lowest factor of safety corresponding to a trial limiting tangent can be computed using the expression proposed by Low (1989) and Low et al. (1990).

The origin of the axes is assumed to be at the level of the trial limiting tangent, on a vertical line passing through the toe A of the embankment.

The factor of safety *FS* is defined as based on the moment equilibrium of the slip block IGEJBA, as

$$FS = \frac{M_R}{M_0} \tag{22}$$

where M_0 is the overturning moment due to the embankment soil block ABJE, and M_R is the resisting moment along IGEJ. The resisting moment M_R caused by the prestressed geosynthetic layer, the foundation soil and the embankment soil.

From the expressions for M_0 and M_R the factor of safety FS can be expressed as a function of x and y.

The location of the critical slip surface is obtained by performing partial differentiation of FS with regard to x and y and equating them to zero.

$$\frac{\delta}{\delta_x}\left(\frac{M_R}{M_0}\right) = 0 \tag{23}$$

$$\frac{\delta}{\delta_y}\left(\frac{M_R}{M_0}\right) = 0 \tag{24}$$

The partial differentiation results in

$$y_c^* = \frac{3.13\left[0.5\left(D^* + 0.5\right)^2 + 0.0417(1+\cot^2\beta)\right].}{(D^* + 0.5)} \left\{1 + \frac{0.68\left[\frac{T_m^*}{y_c^{*0.47}} + \frac{T_p^*}{y_c^{*0.47}}\right]}{3.06 S_u^* D^{*0.53} + 1.53(c_m^* + \lambda \tan\varphi_m)[(D^*+1)^{0.53}]}\right\} \tag{25}$$

Where y_c* is the non-dimensional value of y for the critical slip circle. It is calculated according to Low (1989) with an averaging coefficient for frictional stress in the embankment λ:

$$\lambda \approx 0.19 + \frac{0.02\cot\beta}{D/H} \; for \; D/H \geq 0.5 \tag{26}$$

According to Shukla & Kumar (2008), the factor of safety can now be calculated considering the critical slip circle in non-dimensional form as:

$$FS = \frac{y_c^{*1.47}\left\{\left[\frac{T_m}{y_c^{*0.47}}\right] + \left[\frac{T_m}{y_c^{*0.47}}\right] + 3.06 S_u^* D^{*0.53} + 1.53\left(c_m^* + \lambda \tan\varphi_m\right)\left[\left(D^*+1\right)^{0.53} - D^{*0.53}\right]\right\}}{y_c^*\left(D^* + \frac{1}{2}\right) - \frac{1}{2}\left(D^* + \frac{1}{2}\right)^2 - \frac{1}{24}\left(1 + \cot^2\beta\right)} \tag{27}$$

The effect of prestressing the geosynthetic layer on the factor of safety is studied by considering a recommended range of parameters in their non-dimensional form as given below (Kumar 2007).

- Prestressing force in the geosynthetic reinforcement, T_p*: 0 – 0.1
- Undrained shear strength of foundation soil, S_u*: 0.05 – 0.25
- Cohesion of embankment soil, c_m*: 0 – 0.25
- Depth of limiting tangent in foundation soil, D*: 0.2 – 1.0
- Mobilised tensile force in geosynthetic reinforcement, T_m*: 0.02 – 0.1

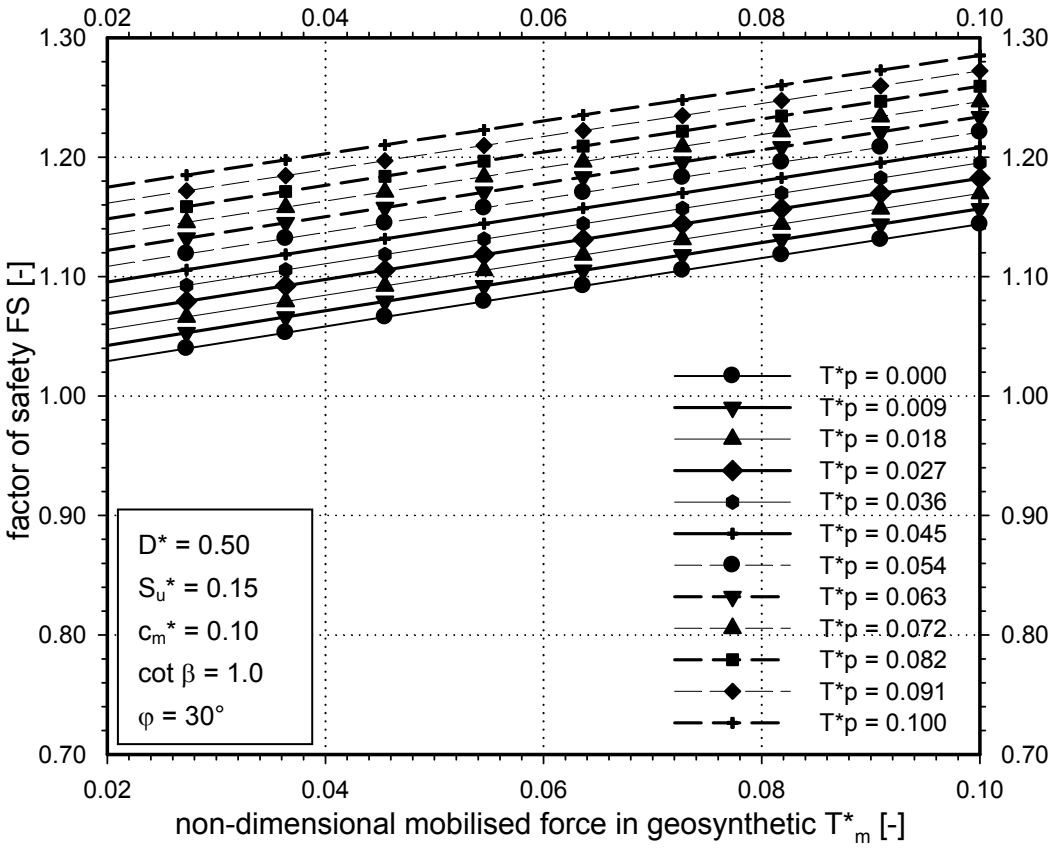

Figure 77: Non-dimensional mobilized force in the geosynthetic T^*_m versus the factor of safety FS with respect to different non-dimensional prestress forces T^*_p in the reinforcement according to Shukla & Kumar (2008).

A detailed parametric study has been performed in order to evaluate the limits of the analytical approach.

Figure 77 shows the non-dimensional mobilized force in the geosynthetic T^*_m versus the factor of safety *FS* with regard to different non-dimensional prestress

forces T^*_p in the reinforcement. The factor of safety *FS* increases linearly as soon as the prestress in the reinforcement T^*_p increases coevally.

The mobilised tensile force in the geosynthetic layer is due to the interaction between soil and reinforcement and should be limited by the pull out force of the geosynthetic layer and by the allowable tensile strength T_a of the geosynthetic reinforcement. The allowable tensile strength T_a of the geosynthetic reinforcement is limited to

$$T_m + T_p \leq T_a \tag{27}$$

Figure 78 shows the slope angle of the embankment β versus the factor of safety *FS* with regard to different non-dimensional prestress forces in the reinforcement.

The factor of safety increases nonlinearily, if the slope angle β decreases coevally.

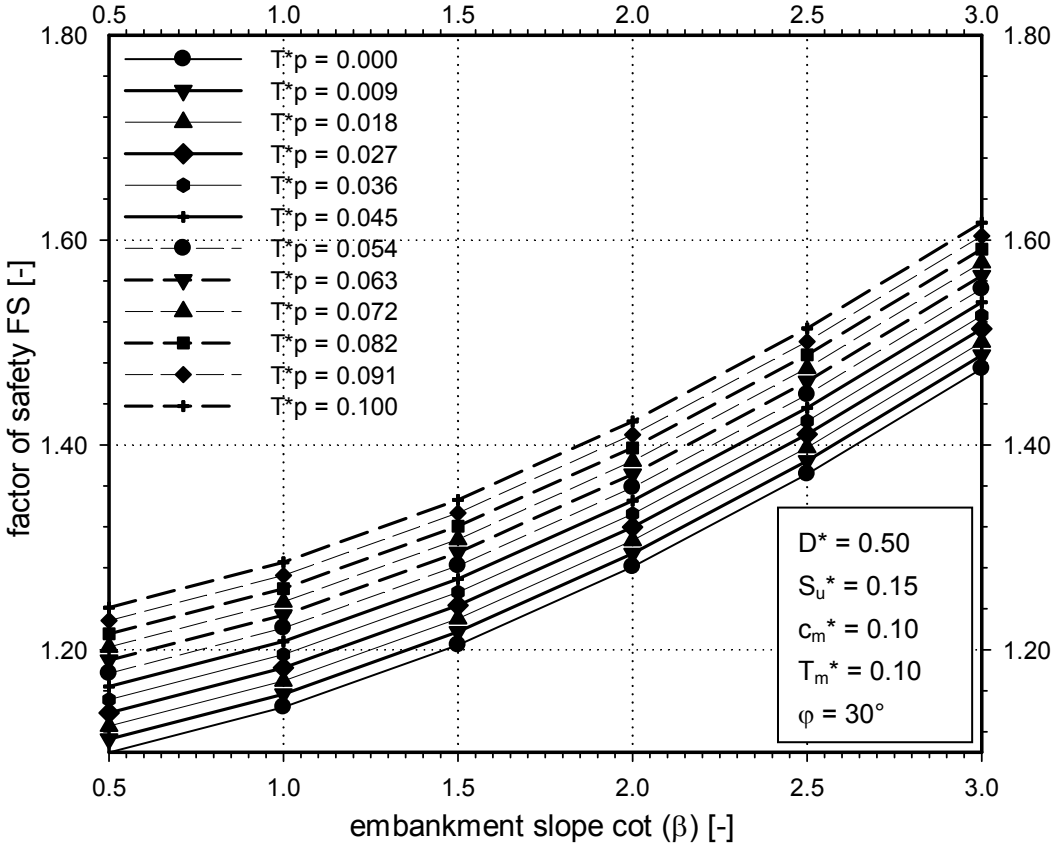

Figure 78: Slope angle of the embankment β versus the factor of safety *FS* with regard to different non-dimensional prestress forces T^*_p in the reinforcement according to Shukla & Kumar (2008).

The higher the reinforcement is prestressed (T^*_p = 0.1) the higher the factor of safety *FS*.

This aproach is well applicable to prestressed geosynthetic reinforced embankments built up on soft ground. It has to be stated that this approach is based on the idea to design a structure with respect to its deformation behaviour.

5.3 Construction recommendations on prestressed reinforced soil

In this chapter practical construction recommendations for prestressed reinforced soil structures are made. Some of the recommendations enhance building site activities from the past years (Detert et al. 2004, HÜSKER Synthetic GmbH 2006). Some recommendations have been tested experimentally in laboratory studies (Havinga 2012) and some need to be evaluated in situ, in the near future.

Chew et al. (2005) demonstrated a method of implementing field prestressing to geosynthetic reinforcement used for road construction. Figure 79 shows the completion of prestressing work on a geosynthetic reinforced road construction.

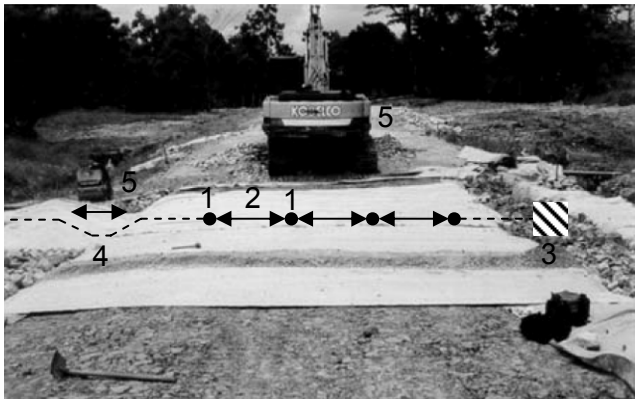

1…marks to evaluate prestress
2…amount of prestress
3…anchorage by overfilling
4…trench drain to provide anchoring and to induce prestressing
5…excavator or compactor to induce the prestressing in the trench

Figure 79: Completion of prestressing work on geosynthetic reinforcement according to Chew et al. (2005) as reported by Alfaro et al. (2006).

The first step is to anchor the geosynthetics in one side of the road next to the trench drain (4).

On the other side of the road, heaps of embankment fill or trench drain materials can be used as overburden to provide anchoring (3).

Enough slackness of the geosynthetics is provided in the trench, tapered to eliminate sharp corners in the trench. The amount of slackness in the geosynthetics in the drain is determined by estimating the amount of reinforcement strain required to achieve the desired prestressing force.

To induce the prestressing force in the geosynthetics, an excavator (5) can be used to compact the gravelly material placed on the geosynthetics in the trench.

To measure the strain (2) across the reinforcement length, selected points (1) can be marked on the geosynthetics prior to their installation. Measurements of relative displacements of the marked points are taken before and after prestressing to determine the amount of reinforcement strain and thus the prestressing force due to prestressing.

Chew et al. (2005) have found that this procedure is practical to achieve an average of 3.5 % prestressing strain across the geotextiles.

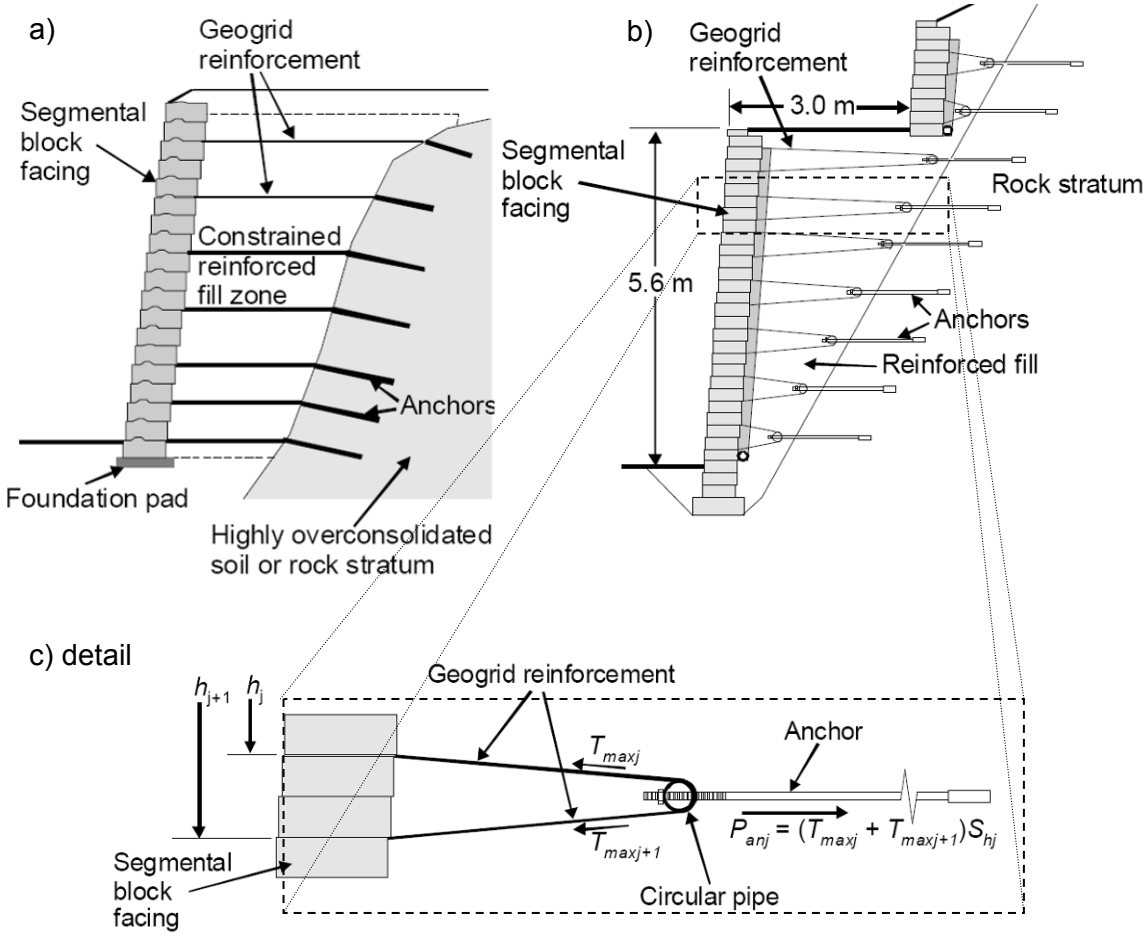

Figure 80: Reinforced soil retaining walls where the extent of the reinforced fill zone is constrained according to Lawson & Yee (2008).

In addition, Lawson & Yee (2008) provide a construction recommendation for reinforced soil retaining walls where the extent of the reinforced fill zone is constrained (Fig. 80a). The wall are planned to economize on the number of anchors by utilizing one row of anchors for every two layers of geogrid reinforcement (Fig. 80b).

The detailed layout of the reinforced segmental block wall is shown in Figure 80c. The connection between the anchors and the geogrid reinforcement has been executed by the use of a 75 mm diameter galvanized steel pipe (Fig. 80c).

Flexible polyester geogrids have been used as geogrid reinforcement. The geogrids have had the required level of bending flexibility which enabled them to align easily around the galvanized steel pipe without attracting additional tensile stress.

Tatsuoka et. al (1996a, b, 1997), Uchimura et. al (1996, 1997) and Shinoda et. al (2002) have presented the preloading and prestressing (PLPS) method (Fig. 81a).

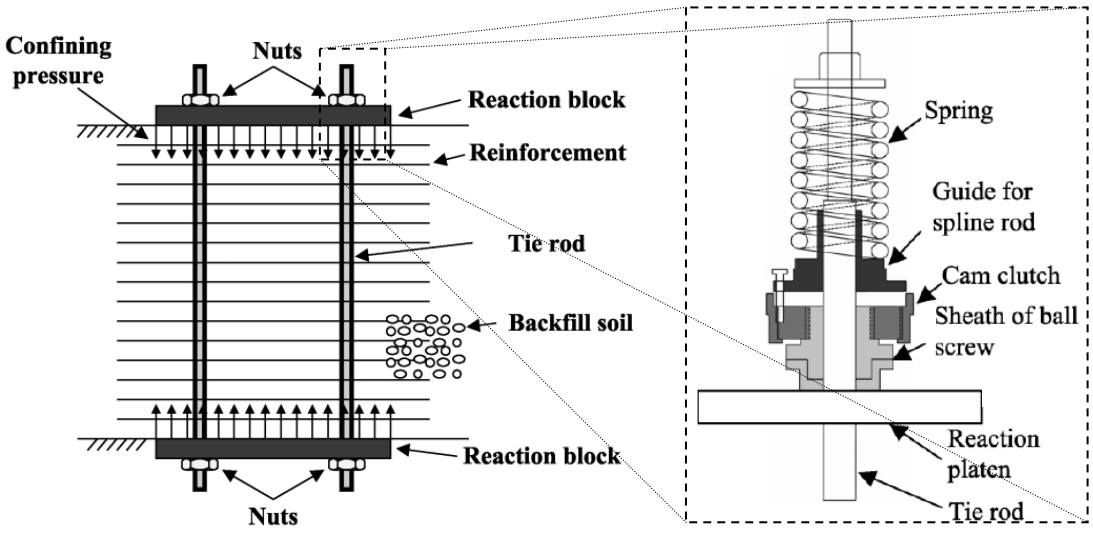

Figure 81: Preloading and prestressing (PLPS) method according to Tatsuoka et. al (1996a,b, 1997), Uchimura et.al (1996, 1997) and Shinoda et. al (2002): typical cross-section of preloaded and prestressed reinforced soil structure and restraining of bending deformation of PLPS soil structure by using ratchet connections and hydraulic jacks for preloading.

A sufficiently large preload is applied by using hydraulic jacks (Fig. 81b) that are mounted at the top ends of the tie rods.

A relatively large preload can be applied without causing failure of the backfill because the backfill soil is reinforced. Since preloading and subsequent unloading improves the stiffness of the backfill material, the wall deforms fairly elastically when the external vertical load is applied on top of the reaction block.

5.3.1 Construction recommendations for prestressing the geogrid by compaction (PRS_c)

Figure 82 shows the recommended construction principle for prestressing the geogrid by compaction (PRS_c).

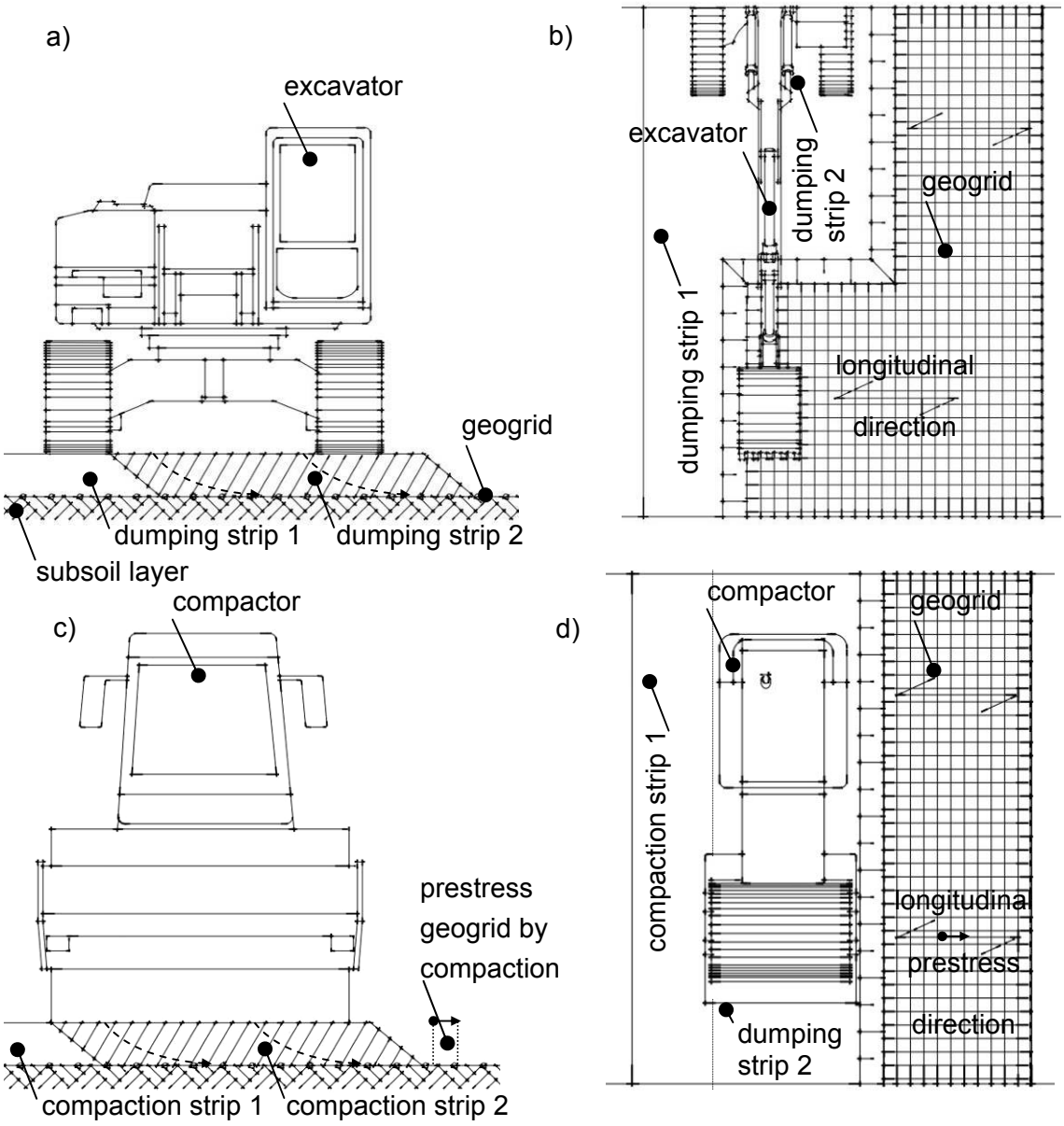

Figure 82: Geogrid prestressing as a result of compaction: a) side view of the dumping procedure b) top view of the dumping procedure a) side view of the compaction - prestressing procedure b) top view of the compaction - prestressing procedure (modified to Havinga 2012).

First, the geogrid is placed on the subsoil layer. The geogrid is laid tight onto the subsoil to avoid wrinkles in the reinforcement. Once the geogrid is installed, the first soil layer is dumped on the geogrid with an excavator (Fig. 82a). The

excavator must not operate directly on the reinforcement material. Figure 82b) presents the dumping procedure of the excavator from a top view.

The dumping strip is then compacted with a compaction roller (Fig. 82c). Thereby spreading stresses (Chapter 2) lead to a prestress in the geogrid by compaction in the longitudinal direction of the reinforcement. The top view of the compaction process is presented in Figure 82d).

During the dumping and the compaction, process workers need to ensure the tight laying of the reinforcement above the subsoil layer. The more prestress in the geogrid is activated the higher the positive effect of PRS_c. By observing the elongation of the geogrid, strains and stresses in the geogrid can be back analyzed. In situ, the designer can decide whether additional prestress shall be applied to the reinforcement in order to further decrease deformations during and after the construction.

5.3.2 Construction recommendations for prestressing the geogrid with the shovel of an excavator ($PRS_{p,t}$)

Prestressing the geogrid with the shovel of an excavator is a fast and effective construction method for rather small projects.

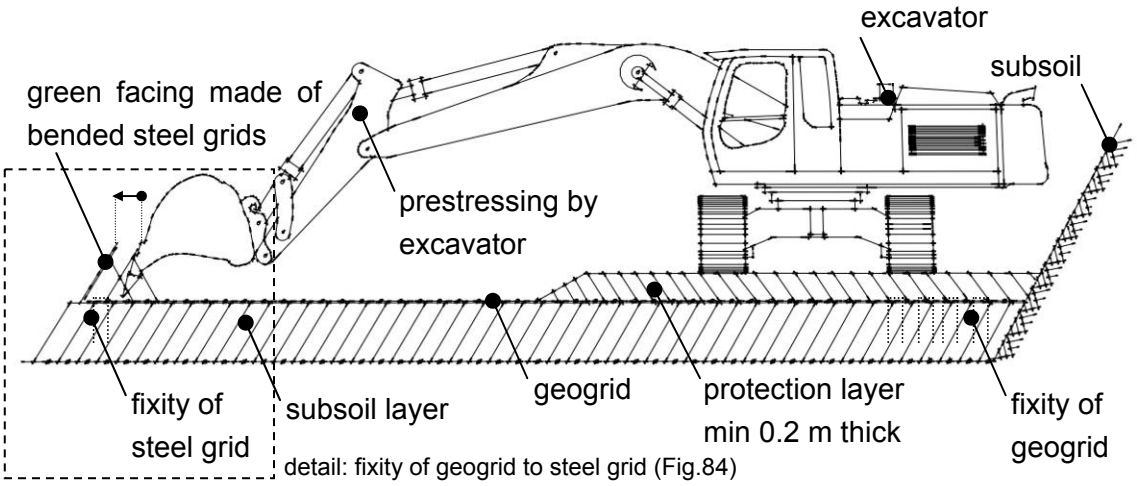

Figure 83: Geogrid prestressing with shovel of an excavator: side view of the prestressing procedure (modified according to Havinga 2012).

Figure 83 shows the side view of the construction method. First, a geogrid is laid on the subsoil layer. It is important to avoid wrinkles and bulges in the geogrid.

Second, the geogrid is fixed by either dumping it with backfill material or by driving steel binder profiles through the mesh of the geogrid into the subsoil

layer (Fig. 83). At the green facing the geogrid is connceted to the bended steel grids.

Figure 84 shows the installation of the green facing in detail. Figure 84a) presents the bending of the steel grids and their fixing into the subsoil. Once the bended steel grids are installed the geogrid is connected to the green facing (Fig. 84b). As a possible solution, steel binder profiles are driven in the subsoil.

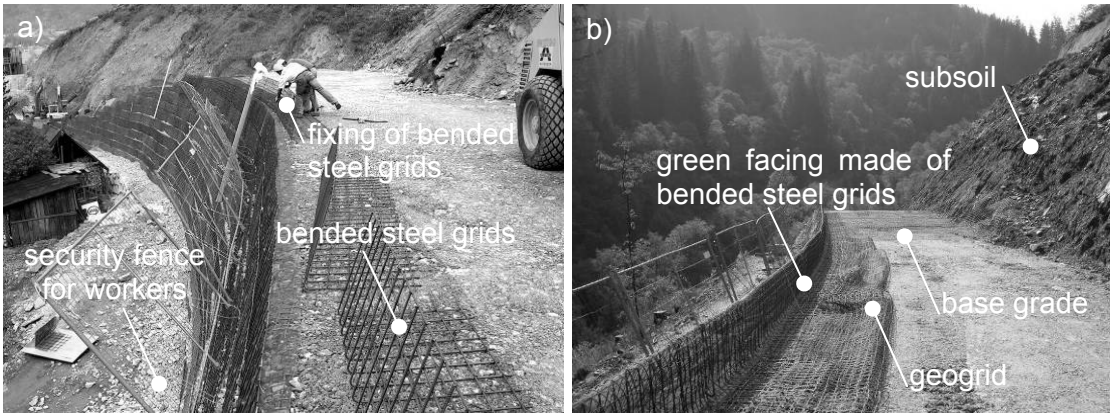

Figure 84: Detail of geogrid fixity at green facing: a) bending the green facing steel grids b) fixing geogrid to green facing (B114 Trieben-Sunk).

Detert et al. (2004) present another solution to prestress the geogrid fixed on a sheet pile wall with the shovel of an excavator (Fig. 85).

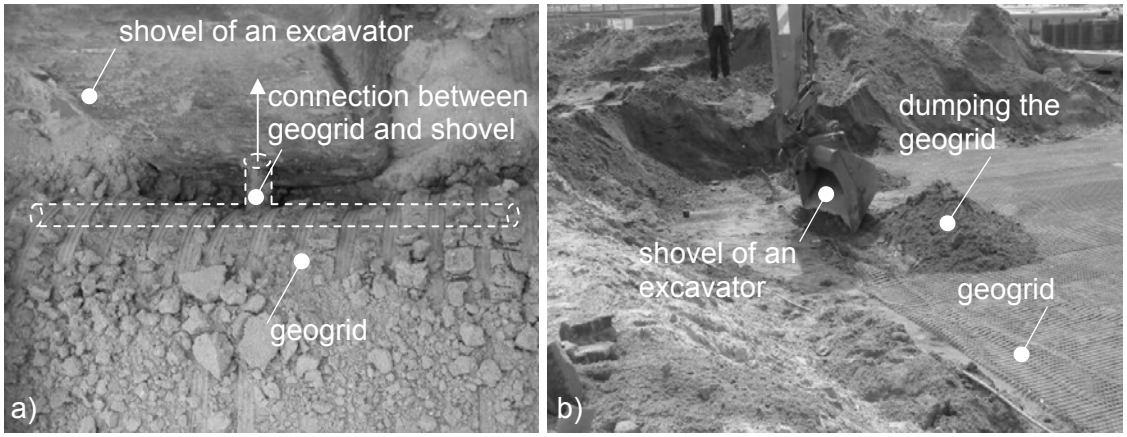

Figure 85: Geogrid prestressing with shovel of an excavator: a) connection detail between geogrid and shovel of the excavator b) backfilling the prestressed geogrid just after prestressing (according to Detert et al. 2004).

To minimise horizontal movements of a sheet pile wall, the strong and stiff geogrid (T_{max} = 600 kN/m) made out of polyvinyl alcohol (PVA) has been prestressed and afterwards dumped with backfill material. An undefined

permanent prestress has been applied to the reinforcement, simply to avoid wrinkles in the reinforcement.

5.3.3 Construction recommendations for prestressing the geogrid with a trench (PRS_p)

In the case of utilizing the concept of PRS_p, a prestress trench is well applicable to tighten the geogrid. Figure 86 presents the side view of the construction recommendation. First, the reinforcement is placed tightly on the subsoil layer and the pre-constructed prestress trench (Fig. 86a). Then, the geogrid is fixed at both ends, either by dumping the geogrid with backfill material or by using steel benders, according to Figure 86 a).

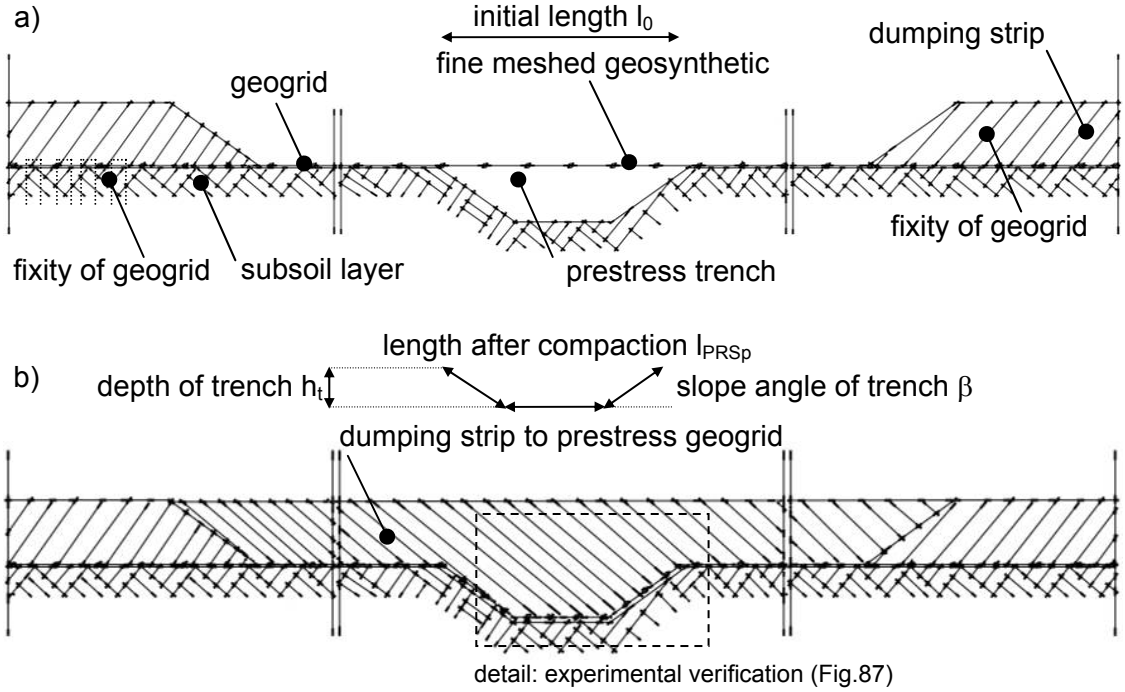

Figure 86: Geogrid prestressing with prestressing trench: a) side view of the prestressing procedure before dumping the prestressing strip b) side view of the prestressing procedure after dumping the prestressing strip (modified according to Havinga 2012).

Finally, the actual soil layer is dumped and compacted (Fig. 86b). Thereby the geogrid aligns along the prestress trench and a permanent prestress is activated.

In order to apply the required prestress to the geogrid, the geometry of the prestress trench has to be calculated. Table 19 presents the depth h_t of the prestressing trench exemplarily for a 10 m long geogrid necessary to activate prestress strains of ε_{PRSp} = 1.0 to 3.0 %. The depth of the prestress trench changes

with respect to the slope angle β of the trapezoidal trench. The smaller the slope angle β, the deeper the prestress trench.

Figure 87 shows the depth h_t of the prestress trench with respect to the slope angle β.

Table 19: Depth h_t of prestressing trench: Length of geogrid before compaction the trench: e.g.: $l_{geogrid}$ = 10 m

Prestress strain of geogrid ε_{PRSp}	1.0	1.5	2..0	2.5	3.0	Unit [%]
Slope angle of prestress trench β						[°]
30	18,7	28,0	37,3	46,7	56,0	[cm]
35	15,9	23,8	31,7	39,6	47,6	[cm]
40	13,7	20,6	27,5	34,3	41,2	[cm]
50	10,7	16,1	21,4	26,8	32,2	[cm]
60	8,7	13,0	17,3	21,7	26,0	[cm]

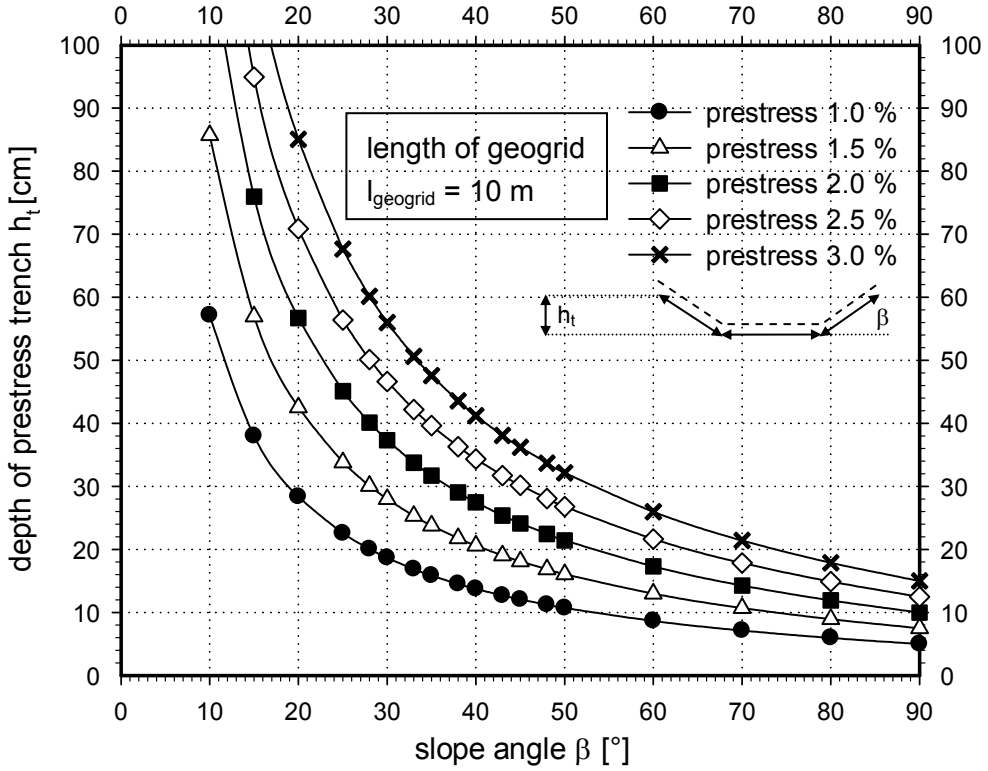

Figure 87: Geometry of prestress trench: depth h_t of the prestress trench with respect to the slope angle β.

It is visible that the depth of the prestress trench increases rapidly if the slope angle β decreases. In order to verify the presented Table 19 and Figure 87 laboratory studies have been performed (Fig. 88).

Figure 88 shows the side view of the aligned geogrid in a pre-constructed prestress trench. The Figure shows that the geogrid aligns well to the tapered, trapezoidal trench during compaction. The geogrid has been tensioned over a length of 3.6 m with a prestress ε_{PRSp} = 1.0 %.

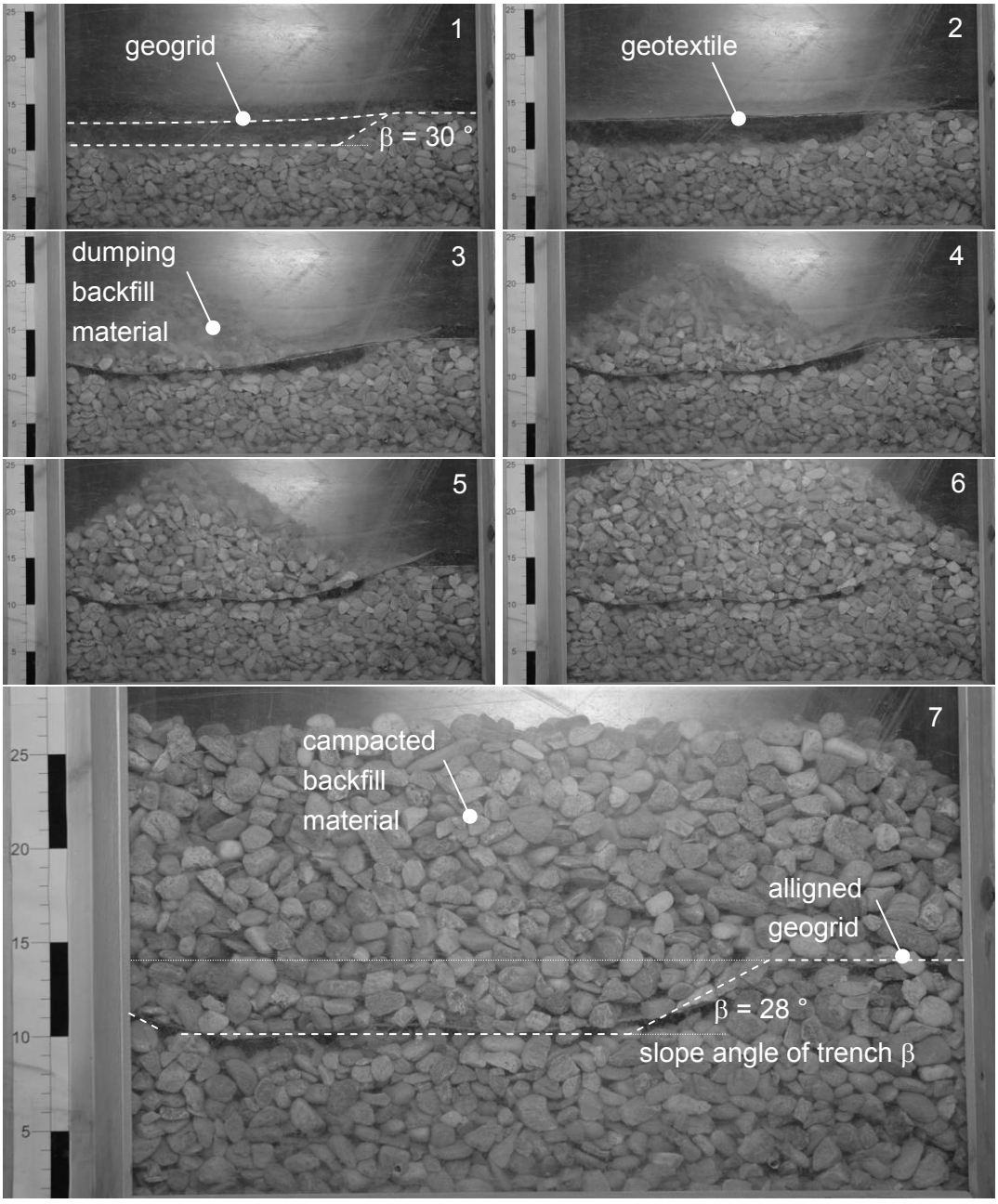

Figure 88: Verification of prestress trench: placing the geogrid and geotextile (1 and 2), dumping the backfill material (3-6) and compacting the backfill (7).

As described above the geogrid is placed on the subsoil (1) and its ends are fixed. Then a geotextile is laid on the geogrid in order to avoid particles falling through the gaps of the geogrid (2). The backfill material is dumped on the geotextile and finally compacted (3-7).

Figure 88(7) shows the aligned geogrid after the compaction of the backfill material. The final slope angle of the trapezoidal trench amounts to 28°. The initial slope angle has been measured with 30°. In other words, by dumping and compacting the backfill material the slopes of the trench become exiguously more flat.

As reported it is recommended to fix the geogrid by simply dumping backfill material on to the reinforcement. The anchorage length L_A to fix the geogrid properly is calculated by employing the following equation.

$$L_A = \frac{T_{PRSi}}{\sigma_v \cdot \tan\varphi \cdot R_{inter} \cdot n} \tag{28}$$

T_{PRSi} represents the tensile force in the prestressed reinforcement. In order to calculate shear stresses along the interaction zone, the vertical stresses σ_v have to be multiplied with the tangent of the friction angle φ and the soil geogrid interaction coefficient R_{inter}. The shear stresses generally occur on both sides of the geogrid (n = 2) in the case of the geogrid is pulled out. Equation 29 has been verified by experimental studies performed by Havinga (2012) with R_{inter} = 0.9.

5.3.4 Construction recommendations for prestressing the geogrid with tensioning equipment ($PRS_{p,t}$)

HÜSKER Sysnthetic GmbH (2006) published some project information about a bridging system for sinkholes.

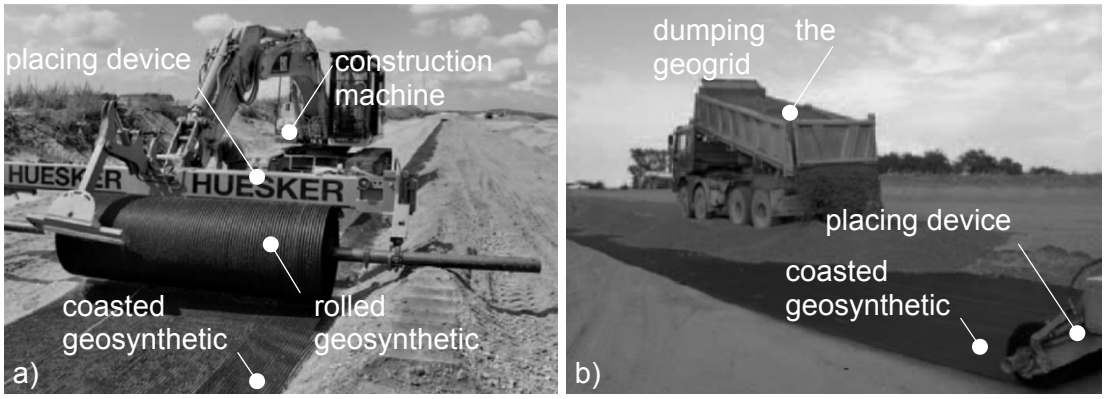

Figure 89: Geogrid installation with special tensioning equipment: a) placing the geogrid with special tensioning beam (half role width) b) backfilling sand and gravel (0-32 mm) over tensioned geogrid (according to HÜSKER Synthetic GmbH 2006).

Stiff geogrids produced of aramid have been utilized to ensure the safety of the traffic on the A143 motorway, Germany, after a sinkhole had formed.

The geogrid was placed in one layer and afterwards dumped with 0.5 m of sand and gravel (Figure 89 a, b). The grain size of the backfill material amounted from 0 to 32 mm. In order to mobilize the geogrid as fast as possible and thereby to avoid high settlements, the geogrid was prestressed with a certain amount.

HÜSKER Synthetic GmbH designed a special placing beam (Figure 90a, b, c). The placing beam was managed to add a defined prestress to the geogrid by setting the unrolling resistance of the placing device. Finally, the geogrid was fixed in its prestressed condition.

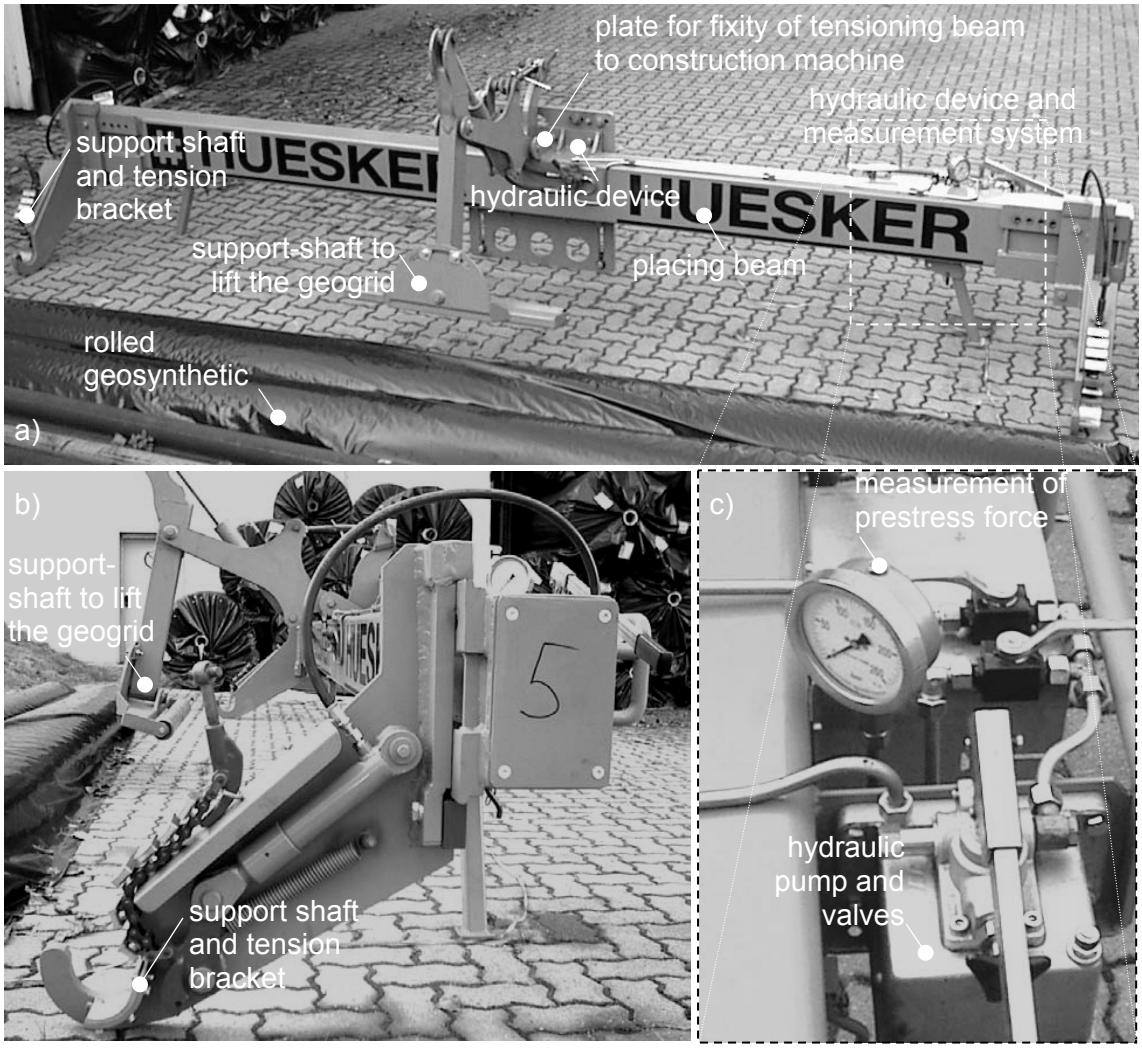

Figure 90: Special tensioning equipment: a) front view of tensioning beam b) side view of tensioning beam c) top view of hydraulic tensioning equipment according to HÜSKER Synthetic GmbH (2001).

The 6 m long placing device is later described in detail. Figure 90a) shows the front view of the tensioning and placing beam. To fix the placing beam on the construction machine a specially tuned plate has been designed. A support shaft including hydraulic tension brackets is installed at both edges of the beam. A hydraulic device sets the strength of the brackets and thereby the amount of

tension in the geosynthetic. The hydraulic pressures and the tension force in the geogrid is measured with a specially tuned measurement equipement.

The equipement and the pumps including the valves are presented in detail in Figure 90c). Figure 90b) presents the side view of the tensioning beam. The support-shaft to lift up the geogrid and to avoid a bending of the rolled geogrid is shown in Figure 90b. The presented tensioning and placing equipment is perfectly applicable, for the concept of permanently PRS_p and for temporarily PRS_t prestressed reinforced soil structures.

5.4 Summary and conclusions

In Chapter 5 design and construction recommendations for prestressed reinforced soil (PRS_i) have been presented. Design recommendations provided in literature have been validated and later enhanced. Practical design recommendations on prestressed reinforced soil foundation and prestressed reinforced soil slopes have been presented in detail.

An analytical approach to design reinforced soil foundations has been enhanced. This approach is based on the idea that failure is defined by a pre-defined deformation criterion. By utilizing the enhanced approach, permanently and temporarily prestressed reinforced soil foundations can be designed. The analytical approach has been verified by back calculating the experimental results from static load displacement tests. The results from the analytical approach have shown a sound agreement with the experimentally gained results. An exemplarily parametric study has been performed in order to evaluate the limits of the analytical approach. The amount of prestress and number of reinforcement layers have been varied.

The higher the geogrid reinforcement has been prestressed, the higher the bearing capacity of the reinforced soil foundation has been. This has been due to the increase of the tensile stiffness of the geogrid with respect to its prestress. The more prestress has been applied to the geogrid the higher have been its tensile forces supporting the reinforced soil foundation. The parametric study has further shown that, the tighter the spacing between the reinforcement layers has been the higher the maximum bearing capacities analyzed with the presented analytical approach have been. This has been due to the fact that, when the spacing between the geogrid layers has reduced, the number of reinforcement layers automatically has increased.

Finally, it has to be stated that this analytical approach includes some limitations. The settlements of the footing have been calculated according to Schmertmann et al. (1978). The settlements are calculated assuming unreinforced soil. According

to Chen (2007) the settlement distribution is assumed to be similar for reinforced and thereafter also for prestressed reinforced soils. This may not correspond to reality and should be investigated in the near future.

An analytical approach for prestressed geosynthetic reinforced embankments on soft ground based on the idea that failure is defined by a deformation criterion has been discussed in detail. The approach has presented the derivation of an expression for the factor of safety with respect to the overall slope stability of a prestressed geosynthetic reinforced embankment constructed on soft ground.
The development of a mobilised tensile force in the geosynthetic layer requires a significant settlement of the embankment. To overcome these high, time depending settlements, the geosynthetic layer has been prestressed to achieve the desired level of tensile force. The conclusion of this analytical approach is that, the factor of safety *FS* increases as soon as the prestress in the reinforcement increases coevally.

Practical construction recommendations from literature have been summarized. Additional laboratory studies have been performed and their findings have been presented. The presented construction recommendations comprehend construction methods for PRS_c, PRS_p and PRS_t.

A practical construction recommendation has been presented in order to prestress the geogrid during compaction. The granular material is backfilled in single strips and is compacted one by one.

Prestressing the geogrid with the shovel of an excavator has been presented as a fast and effective construction method for small projects where the concepts of PRS_p and PRS_t have been utilized. For larger projects a special placing beam has been presented. This placing beam may easily be adapted in order to prestress the geogrid reinforcement on the building site.

When the concept of PRS_p is employed, a prestressing trench has been validated as perfectly applicable. Experimental studies verify the analytical recommendation for the geometry of the trench.

Finally it can be stated that this chapter presented practical recommendations for the design and construction of PRS_i. In the near future it is assumed that design projects will verify the concept and will improve the practical recommendations as stated here.

6 Conclusions and further research

6.1 Conclusions

In this thesis the concept of prestressed reinforced soil (PRS_i) to improve the load displacement behaviour of reinforced soil structures has been introduced. The concept of PRS_i has been validated by large scale experimental test results produced at the Institute of Soil Mechanics and Foundation Engineering at Graz University of Technology, Austria. More than 60 path-controlled static load displacement tests have been performed. The following conclusions can be stated:

- The results have shown an improvement of the macroscopic load displacement behaviour of granular soil structures after installing geogrid reinforcement.

- In the case of utilizing the concept of PRS_i, the load displacement behaviour of the reinforced soil structures further improves considerably with respect to the unreinforced and reinforced soil structures.

- The static test results have shown that the macroscopic maximum bearing capacity doubles when prestressing the geogrid reinforcement permanently (PRS_p). The highest increase of the bearing capacity has been observed when utilizing the concept of PRS_t. This is due to the ideal interaction between coarse, granular backfill material and the geogrid reinforcement.

- Furthermore, the macroscopic load transfer mechanism has been investigated by utilizing the mesoscopic PIV analysis which demonstrates, that by prestressing the geogrid an additional bedding support has been activated.

- The macroscopic analysis has shown that, the overall displacements decrease in case of utilizing the concept of PRS_i. Additionally the total displacements below the geogrid reinforcement layer reduce. This is due to the bedding support of the prestressed geogrid.

In addition, the test results from 87 cyclic load displacement tests conducted in Weimar, Germany, have validated the concept of PRS_i under cyclic loading conditions:

- Research work on the macroscopic behaviour of the reinforced soil has shown that displacements have reached 70 % of unreinforced displacements after the installation of a geogrid. In other words, a 30 %

reduction of settlements has been observed in the case of installing a geogrid reinforcement.

- By further prestressing the geogrid and releasing the prestress after compaction (PRS_t), the soil layer displacements have decreased further. Displacements have reached about 40 % of the unreinforced displacements (60 % reduction).

- The maximum effect in reducing both vertical and horizontal displacements has been reached by prestressing the geogrid permanently (PRS_p). The settlements occurring under cyclic loading have decreased to 20 % of the displacements measured in the case of testing an unreinforced soil structure (80 % reduction). Larger displacements have been visualized above the reinforcement layer by employing the PIV method. The vertical and horizontal displacements under the geogrid layer, occurring under cyclic loading, have decreased.

- In addition, it can finally be stated that the tensile stiffness of the reinforcement has been of high importance related to the load displacement behaviour of the reinforced soil structures. The stiffer welded PP geogrid has supported the PRS_i better than the woven PET reinforcement because of its higher tensile stiffness. The better the geogrid soil interaction the better the overall load displacement behaviour of the reinforced soil structure has been.

- Summing up, it can be stated that the system of prestressed reinforced soil (PRS_i) has been experimentally, statically and cyclically validated. By using the same materials, soil and reinforcement, and by prestressing the geogrid reinforcement with the explained concepts, the load displacement behaviour of reinforced soil structures has improved tremendously.

In addition, numerical investigations have been presented in this thesis. The concept of PRS_i has been validated and results of the static experimental investigations have been evaluated. Multiscale modelling has been utilized to investigate the macroscopic load displacement behaviour of the reinforced soil structure. Additionally, the mesoscopic soil geogrid interaction and the load transfer mechanism of the geogrid reinforced granular soil structures have been investigated. Multiscale modelling has combined the macroscopic Finite Element modelling (FEM) and the mesoscopic Discrete Element modelling (DEM).

The following conclusions from the macroscopic FEM simulation of the static load displacement experiment presented in Chapter 3.3.5 are stated:

- The macroscopic results of the FEM simulation have shown a sound agreement with the results gained from experimental investigations.

- The unreinforced soil body has deformed 4 mm on average in the vertical direction. Higher displacements (4.5 mm) have been visible in the upper right hand corner of the investigated region. Displacements have decreased (3 mm) with respect to the depth of the unreinforced soil structure. Horizontal displacements have additionally been evaluated. The soil body has moved about 3 mm in horizontal direction. The highest horizontal movements have been observed on the surface of the slope. The total displacements have been 5 mm. The results have shown a sound agreement with the measured ones during the experimental investigations. This is true for the reinforced and prestressed reinforced soil structures.

- The vertical stress level σ_v has been 100 kN/m². High local stresses have expectedly occurred close to the edges of the compaction plate. The average horizontal stresses have amounted to 50 kN/m².

- It can finally be stated that the results from the numerical FEM analysis have shown a sound agreement with the experimental investigations. Both experimental and numerical investigations have verified the concept of PRS_i.

Further, mesoscopic DEM analyses have been performed. Once the microscopic parameters have been calibrated, three dimensional discrete and differently reinforced soil elements are modelled. It can be concluded:

- The reinforced soil elements have represented well the mesoscopic interaction behaviour between the reinforcement and the surrounding soil structure. First, the displacements of the soil element have been analyzed and then compared to the observed deformations during the PIV and FEM analysis. The results from DEM, FEM and PIV analyses show a sound agreement.

The mesoscopic load transfer mechanism of the reinforced soil element has been evaluated:

- Arching effects have occurred randomly between the granular soil particles and the discrete geogrid. Those arching effects have led to local stress concentrations between the particles and to high tensile forces in the geogrid at certain places.

Three different soil geogrid interaction effects have been determined:

- Once the discrete CAD clumps have entered the gaps of the discrete geogrid, the longitudinal and transverse members of the reinforcement have been pushed apart from each other. This effect has been classified as interlocking effect.

- While loading the soil element, CAD clumps have entered between the single strings of the longitudinal and transverse members of the reinforcement. This effect has been defined as single string interaction effect.

- The geogrid has aligned onto the surrounding granular particles in the longitudinal and in transverse direction. This so called alignment effect has resulted in a permanent contact between geogrid and soil particles.

- In the case of utilizing the concept of PRS_i, the longitudinal members have been strained in their direction. The discrete clumps have accessed between the single strings. The geogrid has not aligned in longitudinal direction around the particles. This has mainly been due to the prestress in the reinforcement. This may result in gaps between the reinforcement and the surrounding particles.

In addition, the deformation and load transfer behaviour of the reinforced soil element has been observed in the case of utilizing the concepts of PRS_i:

- Displacements above the geogrid layer have been higher than below the geogrid. The results have shown a sound agreement with respect to the results gained from the FEM and PIV analyses.

- Arching effects have become visible. These effects have resulted, in local stress concentrations between the soil particles.

It can finally be stated that the macroscopic results from the numerical DEM analysis have shown a sound agreement with the experimental investigations and the FEM simulations.

Further, it can be stated that the soil geogrid interaction has been simulated well by utilizing the innovative concept of CAD clumps.

The final conclusion from the numerical investigations is that the system of PRS_p has been numerically validated. It can be concluded that by using the same materials, soil and reinforcement and by prestressing the geogrid reinforcement with the presented concept, the load displacement behaviour of reinforced soil structures can be improved drastically.

Finally, design and construction recommendations for prestressed reinforced soil (PRS_i) have been presented. Practical design recommendations on prestressed reinforced soil foundation and prestressed reinforced soil slopes have been presented in detail.

An analytical approach to design reinforced soil foundations has been enhanced. This approach is based on the idea that failure is defined by a pre-defined

deformation criterion. By utilizing the enhanced approach permanently and temporarily, prestressed reinforced soil foundations can be designed:

- The results from the analytical approach show a sound agreement with the experimentally gained results.

A sample parametric study has been performed in order to evaluate the limits of the analytical approach:

- The higher the prestressing of the geogrid reinforcement the higher the bearing capacity of the reinforced soil foundation has been. This has been due to the increase of the tensile stiffness of the geogrid with respect to its prestress. The more prestress applied to the geogrid the higher its tensile forces, supporting the reinforced soil foundation.

- The tighter the spacing between the reinforcement layers the higher have been the maximum bearing capacities analyzed with the presented analytical approach. This has been due to the fact that when the spacing between the geogrid layers has reduced, the number of reinforcement layers has increased automatically.

An analytical approach for prestressed geosynthetic reinforced embankments on soft ground based on the idea that failure is defined by a deformation criterion has been discussed in detail. In can be concluded:

- The development of a mobilised tensile force in the geosynthetic layer has required significant settlements of the embankment. To overcome these high, time depending settlements, the geosynthetic layer has to be prestressed to achieve the desired level of tensile force. The factor of safety *FS* has increased when the prestress in the reinforcement has increased coevally.

Practical construction recommendations from literature have been summarized. Additional laboratory studies have been performed and their findings have presented. The presented construction recommendations comprehend construction methods for PRS_i:

- A practical construction recommendation has been presented in order to prestress the geogrid during compaction. The granular material is backfilled in single dumping strips and compacted strip by strip later on.

- Prestressing the geogrid with the shovel of an excavator has been presented as a fast and effective construction method for small projects where the concepts of PRS_p and PRS_t have been utilized. For larger projects a special placing beam has been introduceded. This placing beam may easily be adapted in order to prestress the geogrid reinforcement on the building site.

- When the concept of PRS_p is employed a prestressing trench has been analyzed as perfectly applicable. Experimental studies verify the analytical recommendation for the geometry of the trench.

- Finally it can be stated that practical recommendations for the design and construction of PRS_i have been presented. In the near future, design projects will verify the concept and will improve the practical recommendations as stated.

6.2 Further research

This thesis presents a first, fundamental research work on the concept of prestressed reinforced soil (PRS_i). More research is necessary to further enhance the fundamental understanding of the presented concept. Besides developing new research tasks, the performed investigations should further be enhanced.

It has to be stated that the presented large scale static load displacement experiment has naturally exhibited limitations:

- Although the experiment has been conducted under constant compaction conditions the compaction pressures have been low. This was due to the limited pressure force of the hydraulic cylinder.

- No doubt, the experiment has been of large scale, but in situ experiments of the presented concept will further improve the fundamental understanding of PRS_i.

- The presented conclusions have resulted from tests conducted with gravelly coarse grain materials. The backfill material has a major influence on the load displacement behaviour of the reinforced soil structure. Tests with different backfill but also reinforcement materials should be performed in the future to enhance the knowledge of PRS_i.

One major limitation of the cyclic experimental device has been its size.

- To investigate multiple reinforcement layers in the future, the biaxial testing device should be enlarged. It has to be stated that the applied loads lead to an inhomogeneous stress distribution along the stiff side walls. In order to perform “real” element tests, constant stresses can be applied by utilizing air bags.

The presented numerical investigations employ a multiscale uncoupled approach.

- In order to investigate the soil geogrid interaction and load transfer mechanisms in the future, coupled hybrid (Finite and Discrete) modelling should be performed.

- This approach is meant to combine the positive effects of a macroscopic fast and effective calculation time and detailed mesoscopic soil geogrid interaction analysis.

It also has to be stated that, the presented analytical approaches include some limitations and simplifications.

- For instance, the settlements of the footing, loading a reinforced soil foundation have been calculated according to Schmertmann et al. (1978). The settlements are calculated assuming unreinforced soil. According to Chen (2007), the settlement distribution is assumed to be similar for reinforced and thereafter also for prestressed reinforced soils. This may not correspond to reality.

Finally it has to be stated that this thesis presents the concept of PRS_i for granular soil structures reinforced with geogrids. In the future research work the concept of PRS_i should be validated as well for fine grained soil reinforced with geogrids. The variation of the reinforcement material should be extended to a higher number of reinforcement types of geosynthetics.

In situ projects should verify the experimental and numerical investigations and should point out the practical limitations of PRS_i on the building site. The behaviour of the constructed soil structures, reinforced by the concept of PRS_i should be observed accurately in the long run to guarantee the safety of the presented concept to our society.

7 Literature

Abu-Farsakh, M.; Chen, Q.; Yoon, S. (2008)
Use of Reinforced Soil Foundation (RSF) to Support Shallow Foundation, Final Report. Louisiana Transportation Research Center (LTRC), Louisiana Department of Transportation and Development (LADOTD), Baton Rouge, LA, Report No. FHWA/LA.07/424, 195.

Adams, M.T. (2000)
Reinforced soil technology at FHWA – Making old technology new. Geotechnical Fabrics Report, August 2000, 34-37.

Adams, M.T.; Collin, J.G. (1997)
Large model spread footing load tests on geosynthetic reinforced soil foundations. Journal of Geotechnical Engineering, ASCE 123 (1), 66-72.

Alexiev, D.; Lackner, K.; Detert, O.; Brokemper, D.; Lackner, C. (2010)
Twenty eight meters high geogrid reinforced embankments as flexible solutions in problematic hillsides: Project Trieben-Sunk, Austria. Proceeding of the 9th International Conference on Geosynthetics. 1681-1684.

Allen, T.M.; Bathurst, R.J. (2002)
Soil Reinforcement Loads in Geosynthetic Walls at Working Stress Conditions. Geosynthetics International, Vol. 9, No. 5-6, 525-566.

Alfaro, M. C.; Blatz J. A.; Graham J. (2006)
Lowland Technology International Vol. 8, No. 1, 47-54, International Association of Lowland Technology (IALT), ISSN 1344-9656.

Aschenbrenner, B.C. (1956)
A new method of expressing particle sphericity. Journal of Sediment Petrol. 26, 15–31.

Aydogmus, T. (2006)
Beitrag zum Interaktionsverhalten von Geokunststoff und Lockergestein. PhD thesis, Fakultät für Geowissenschaften, Geotechnik und Bergbau der Technischen Universität Bergakademie Freiberg (in German).

Bathurst, R.J.; Allen, T.M.; Walters, D.L. (2005)
Reinforcement loads in geosynthetic walls and the case for a new working stress design method. Geotextiles and Geomembranes, 23, 287–322.

Bauer, A. (1989)
Beitrag zur Analyse des Tragverhaltens von einfach bewehrten Zweischichtensystemen. PhD thesis, Technische Universität München (in German).

Bauer, E; Tantono, S (2006)
Numerical investigation of the interface behaviour between granular soil and a geogrid reinforcement. Proceedings of the First Euromediterranean Symposium on Advances in Geomaterials and Structures. 767 – 772.

Benz, T. (2007)
Small-Strain Stiffness of Soils and its Numerical Consequences. PhD thesis, Mitteilungsheft Nr. 55, Institute for Geotechnical Engineering, University of Stuttgart.

Beyer, W. (1964)
On the determination of hydraulic conductivity of gravels and sands from grain-size distributions. Wasserwirtschaft-Wassertechnik Vol. 14, 165–169 (in German).

Bergado, D. T. (1996)
Soft Ground Improvement: In Lowland and Other Environments. New York, American Society of Civil Engineers Press, 427.

Bergado, D.T.; Chai, J.C. (1994)
Pullout force–displacement relationship of extensible grid reinforcement. Geotextiles and Geomembranes Vol. 13, No. 5, 295–316.

Bergado, D.T.; Lo, K.H., Chai, J.-C.; Shivashankar, R.; Alfaro, M.C.; Anderson, L.R. (1992)
Pullout tests using steel grid reinforcements with low-quality backfill. Journal of Geotechnical Engineering, ASCE USA Vol. 118, No.7, 1047–1063.

Bergado, D.T.; Shivashankar, R.; Alfaro, M.C.; Chai, J.-C.; Balasubramanian, A.S. (1993)
Interaction behaviour of steel grid reinforcements in a clayey sand. Geotechnique Vol. 43, No. 4, 589–603.

Bhandari, A.; Han, J. (2010)
Investigation of geotextile-soil interaction under a cyclic vertical load using the discrete element method. Geotextiles and Geomembranes, Vol. 28, 33 - 43.

Binquet, J.; Lee, K.L. (1975a) b)
Bearing capacity tests on reinforced earth slabs. Journal of Geotechnical Engineering Division, ASCE 101 (GT12), 1241–1255 and 1257–1276.

Brandl, H. (1987)
Retaining walls and other restraining structures. Ground Engineer's Reference Book, F.G. Bell (ed.), Butterworths, London.

Brinkgreve, R.B.J.; Swolfs, W.M.; Engin, E. (2010)
PLAXIS 2D Reference manual. Delft University of Technology and PLAXIS b.v., The Netherlands.

Brkic, S. (2011)
Last- Verformungsverhlten an im Labor hergestellten Schüttkörpern. Master thesis, Graz University of Technology, Institute of Soil Mechanics and Foundation Engineering (in German).

British Standard Institution (BSI) (2010)
Code of practice for strengthened/reinforced soils and other fills. British Standard Institution, 258.

Burgstaller, M. (2011)
Dynamische Laborversuche an geogitterbewehrter Erde. Master thesis, Graz University of Technology, Institute of Soil Mechanics and Foundation Engineering (in German).

Bussert, F. (2006)
Verformunsgverhalten geokunststoffbewehrter Erdstützkörper. PhD thesis. Technische Universität Clausthal, 145.

Chen, Q. (2007)
An Experimental Study on Characteristics and Behaviour of Reinforced Soil Foundation. PhD thesis, Louisiana State University.

Chew, S.H.; Tan, S.A.; Leong, K.W. (2005)
Performance of geotextile stabilized unpaved road systems subjected to pretensioning. Geo-Frontiers Conference, Austin, Texas, 1-13.

Cox, E. P. (1927)
A method of assigning numerical and percentage values to the degree of roundness. Journal of Paleontology, Vol.1, 179-183.

Cundall, P. A.; Strack, O.D.L. (1979)
A Discrete Numerical Model for Granular Assemblies. Géotechnique, Vol. 29, 47-65.

Detert, O.; Wehrli, E.; Cejka, A. (2004)
Innovative applications of geogrids as tie-back anchors for vertical walls. Proceedings of EuroGeo4, Paper No. 260.

Dijak, M. (2012)
Dreidimensionale numerische Modellierung von Laborversuchen mit Geokunststoffen unter Verwendung der Diskreten Elemente Methode. Master thesis, Graz University of Technology, Institute of Soil Mechanics and Foundation Engineering (in German).

Deutsche Gesellschaft für Geotechnik (DGGT) (2010)
Recommendations for Design and Analysis of Earth Structures using Geosynthetic Reinforcements (EBGEO). Wilhelm Ernst & Sohn Verlag für Architektur und technische Wissenschaften GmbH & Co. KG, 316.

Dyer, M.R. (1985)
Observation of the Stress Distribution in Crushed Glass with Applications to Soil Reinforcement. PhD thesis, University of Oxford, UK.

Feiertag, S. (2009)
Visualisierung und Interpretation der geotechnischen Messergebnisse beim Projekt B114 Trieben - Sunk. Master thesis, Graz University of Technology, Institute of Soil Mechanics and Foundation Engineering (in German).

Fröhlich, O. K. (1934)
Druckverteilung im Baugrund. Julius Springer Verlag, Wien (in German).

Galvanetto, U.; Aliabadi, M. H. F. (2010)
Multiscale modeling in solid mechanics. Computational and Experimental Methods in Structures - Vol. 3, Imperial College Press, 352.

Gotschol, A. (2002)
Veränderlich elastisches und plastisches Verhalten nichtbindiger Böden und Schotter unter zyklisch-dynamischer Beanspruchung. PhD Thesis, Schriftenreihe Geotechnik Universität Kassel, Germany, Heft 12 (in German).

Guido, V.A.; Biesiadecki, G.L.; Sullivan, M.J. (1985)
Bearing capacity of a geotextile reinforced foundation. Proceedings of 11th International Conference on Soil Mechanics and Foundation Engineering, San Francisco, USA, 1777–1780.

Halsegger, W. (2004)
Experimentelle und numerische Untersuchungen zur geführten Senkkastenbauweise unter besonderer Berücksichtigung des Eindringvorganges der Schneide und der Risiken des Verfahrens. PhD thesis, Graz University of Technology, Gruppe Geotechnik Graz, No. 23 (in German).

Havinga, M. (2012)
Erarbeiten von Einbauempfehlungen für Geokunststoffe zur Bewehrung von Schüttkörpern. Master thesis, Graz University of Technology, Institute of Soil Mechanics and Foundation Engineering (in German).

Hazen, A. (1893)
Some physical properties of sand and gravels. Massachusetts State Board of Health, 24th annual Report.

Hippacher, W.; Lackner, C.; Köberl, J.; Steidl, A. (2009)
Neuerrichtung der B114 im Abschnitt Trieben-Sunk – Hangsicherungsmaßnahmen unter schwierigen geologischen Randbedingungen und Geländeverhältnissen. Beiträge zum 24. Christian Veder Kolloquium, Gruppe Geotechnik Graz, No. 23, 165-180 (in German).

National Higway Institute, USA. (NHI) (2008)
Geosynthetics Design and Construction Guidelines, U.S. Department of Transportation, Federal Highway Administration, Washington, D.C., FHWA-NHI-07-092, 592

Huang, C.C.; Menq, F.Y. (1997)
Deep-footing and wide-slab effects in reinforced sandy ground. Journal of Geotechnical and Geoenviromental Engineering, ASCE, Vol. 123, No.1, 30-36.

Huang, C.C.; Tatsuoka, F. (1990)
Bearing capacity reinforced horizontal sandy ground. Geotextiles and Geomembranes, Vol. 9, 51-82.

HÜSKER Synthetic GmbH (2001)
Bedienungsanleitung Abroll- und Spannvorrichtung (unpublished).

HÜSKER Synthetic GmbH (2006)
Fortrac Geogitter aus Aramid sichern BAB 143 Westumfahrung Halle/Saale gegen Erdfälle (unpublished).

Ingold, T.S. (1982)
Reinforced Earth. Thomas Telford Ltd., London, United Kingdom, 141.

Itasca Consulting Group (2005)
Particle Flow Code in 3 Dimensions. Itasca Consulting Group, Inc., Minneapolis.

Ismail, I.; Raymond, G.P. (1995)
Geosynthetic reinforcement of granular layered soil. Proceedings of Geosynthetics ’95 Conference, Nashville, TN, Industrial Fabrics Association International, Roseville, MN, USA, Vol. 1, 317–330.

Izvolt, L.; Kardos, J. (2010)
Parameter von Geogittern und ihr Einfluss auf deren Wirksamkeit im Eisenbahnunterbau. ETR Eisenbahntechnische Rundschau, No.4, 176-186 (in German).

Jewell, R.A. (1981)
Some Effects of Reinforcement on Soils. Ph.D. thesis, University of Cambridge, UK.

Kawamura, T.; Umezaki, T.; Ochiai, H.; Yasufuku, N.; Hirai, T. (2000)
Confining effect of geogrid reinforced soil. Introduction into design method, 2nd EGC, Bologna, Vol. 1.

Ketchart, K.; Wu, J.T.H. (1996)
Long-Term Performance Tests of Soil-Geosynthetic Composites. Technical Publication No. CDOT-CTI-96-1, Colorado Department of Transportation, 156.

Khing, K.H.; Das, B.M.; Puri, V.K.; Cook, E.E.; Yen, S.C. (1993)
The bearing capacity of a strip foundation on geogrid-reinforced sand. Geotextiles and Geomembranes Vol. 12 (4), 351–361.

Koerner, R. M. (1998)
Designing with Geosynthetics, Fourth Edition, Prentice Hall, Englewood Cliffs, USA.

Konietzky, H.; te Kamp, L.; Jenner, C. (2004)
Use of DEM to model the interlocking effect of geogrids under static and cyclic loading. Numerical Modeling in Micromechanics via Particle Methods, A.A. Balkema, S. 3-11.

Konietzky, H. (2006)
Neue Erkenntnisse zur Wirkungsweise von Geogittern. Proceedings of Symposium Bauen in Boden und Fels, 559-566 (in German).

Krumbein, W. C.; Sloss, L. L. (1963)
Stratigraphy and Sedimentation. 2nd edition, Freeman, San Francisco. 660.

Kumar, A.; Saran, S. (2003)
Bearing capacity of rectangular footing on reinforced soil. Geotechnical and Geological Engineering 21, 201–224.

Kumar, R. (2007)
Overall Slope Stability Analysis of Prestressed Geosynthetic-Reinforced Embankment on Soft Ground. Master thesis, Institute of Technology, Banaras Hindu University, Varanasi, India.

Lackner, C. (2008)
Numerical Simulation of Geosynthetic Reinforced Embankments. Proceedings of the 19th European Young Geotechnical Engineers` Conference, 207 – 215.

Lackner, C.; Semprich S. (2009)
A contribution to pre-stressed reinforced soil. Proceedings of the 4th International Young Geotechnical Engineers Conference ISSMGE, 79 - 82.

Lackner, C.; Semprich S. (2010)
Prestressed geosynthetic reinforced soil by compaction. Proceedings of the 9th International Conference on Geosynthetics IGS Brasil, 717 - 720.

Lackner, C.; Bergado, D.T.; Semprich S. (2012)
Prestressed reinforced soil by geogrids - Theorie, experimental and numerical investigations. Proceedings of the Geoamericas 2012 Conference (CD – Rom).

Lawson, C. R.; Yee, T. W. (2008)
Reinforced Soil Retaining Walls with Constrained Reinforced Fill Zones. Proceedings of the Sessions of the Geo-Frontiers 2005 Congress, 1-14.

Lee, J. R. J.; Smith, L. N.; Smith M. L. (2007)
A New Approach to the Three Dimensional Quantification of Angularity Using Image Analysis of the Size and Form of Coarse Aggregates. Engineering Geology, 254-264.

Lee, J.; Smith, M.; Smith, L.; Midha, P. (2005)
A mathematical morphology approach to image based 3D particle shape analysis. Machine Vision and Applications, Springer Berlin/Heidelberg, Vol. 16, 5, 282-288.

Lee, W. F. (2000)
Internal Stability Analysis of Geosynthetic Reinforced Retaining Walls. Ph.D. thesis, University of Washington, 355.

Leclercq, B.; Schaeffner, M.; Delmas, Ph., Blivet, J.C.; Matichard, Y. (1990)
Durability of Geotextiles: Pragmatic Approach Used in France. Proceedings of Fourth International Conference on Geotextiles, Geomembranes and Related Products, Balkema, Vol. 2, The Hague, Netherlands, May 1990, 679-684.

Leflaive, E. (1988)
Durability of Geotextiles: The French Experience. Geotextiles and Geomembranes, Vol. 7, Nos. 1-2, 23-31.

Lenzi, M. (2009)
Untersuchungen von mit Pfählen gesicherten Rutschhängen mit der Diskreten Elementemethode. PhD thesis, Graz University of Technology, Gruppe Geotechnik Graz, No. 37 (in German).

Liu, C.N.; Ho Y-H.; Huang J.W. (2008)
Large scale direct shear tests of soil/PET-yarn geogrid interfaces. Geotextiles and Geomembranes 27, 19–30.

Lovisa, J.; Shukla, S.K.; Sivakugan, N. (2009)
Behaviour of prestressed geotextile-reinforced sand bed supporting a loaded circular footing. Geotextiles and Geomembranes 28, 23–32.

Low, B. K. (1989)
Stability analysis of embankments on soft ground. Journal of Geotechnical Engineering, ASCE, 115, No. 2, 211–227.

Low, B. K.; Wong, K. S.; Lim, C.; Broms, B. B. (1990)
Slip circle analysis of reinforced embankments on soft ground. Geotextiles and Geomembranes, 9, 165–181.

McDowell, G.R.; Herireche, O.; Konietzky, H.; Brown, S.F. (2006)
Discrete element modelling of geogrids-reinforced aggregates. Geotechnical Engineering – ICE 159 (GE1), 35–48.

Michalowski, R.L. (2004)
Limit loads on reinforced foundation soils. Journal of Geotechnical and Geoenviromental Engineering, ASCE, Vol. 130, No.4, 381-390.

Müller-Rochholz, J. (2004)
Gutachterliche Stellungnahme MRG 05-04, Abminderungsfaktoren für das Langzeitverhalten (Zeitstandfestigkeit und Kriechen) für FORTRAC T (unpublished).

Nimmesgern, M. (1998)
Untersuchungen über das Spannungs-Verformungs-Verhalten von mehrlagigen Kunststoffbewehrungen in Sand. PhD thesis, Technische Universität München (in German).

Omar, M.T.; Das, B.M.; Puri, V.K.; Yen, S.C. (1993)
Ultimate bearing capacity of shallow foundations on sand with geogrid reinforcement. Canadian Geotechnical Journal Vol. 30, 545–549.

ÖNORM EN 933-4 (2008)
Tests for geometrical properties of aggregates - Part 4: Determination of particle shape - Shape index. Austrian Standard Institute (in German).

ÖNORM EN ISO 10319 (2008)
Geosynthetics - Wide-width tensile test. Austrian Standard Institute (in German).

Palmeira, E.M. (2009)
Soil–geosynthetic interaction: Modelling and analysis. Geotextiles and Geomembranes Vol. 27, 368–390.

Palmeira, E.M.; Milligan, G.W.E. (1989)
Scale and other factors affecting the results of pull-out tests of grids buried in sand. Geotechnique Vol. 39, 511–524.

Patra, C.R.; Das, B.M.; Atalar, C. (2005)
Bearing capacity of embedded strip foundation on geogrid-reinforced sand. Geotextiles and Geomembranes Vol. 23, 454–462.

Raffel, M.; Willert, C. E.; Kompenhans, J. (2007)
Particle ImageVelocimetry, A Practical Guide. Springer Verlag.

Rendulic, L. (1938)
Der Erddruck im Straßen- und Brückenbau. Volks- und Reichsverlag, Berlin (in German).

Rittenhouse, G. (1943)
A visual method of estimating two-dimensional sphericity. Journal of Sediment Petrol, 13 (2), 79-81.

Rüegger, R.; Hufenus, R. (2003)
Bauen mit Geokunststoffen. Schweizer Verband für Geokunststoffe SVG.

Ruiken, A.; Ziegler, M. (2009)
Large Scale Laboratory Element Testing of Geogrid Reinforced Soil. GIGSA GeoAfrica 2009 Conference, Cape Town, South Africa, 2.-5.

Sarsby, R. W. (1985)
The influence of aperture size/particle size on efficiency of grid reinforcement. Proceedings of 2nd Canadian Symposium on Geotextiles and Geomembranes, Edmonton, Alta., Canada, 7–12.

Sarsby, R. W. (2007)
Geosynthetics in Civil Engineering. Crc Pr Inc, 295.

Schmertmann, J.H.; Hartmann, J.P.; Brown, P.R. (1978)
Improved strain influence factor diagrams. ASCE Journal of the Geotechnical Engineering Division, 104 (GT8), 1131-1135.

Sharma, R.; Chen, Q.; Abu-Farsakh, M.; Yoon, S. (2009)
Analytical modeling of geogrid reinforced soil foundation. Geotextiles and Geomembranes, Vol. 27, 63–72.

Shin, E.C.; Das, B.M. (2000)
Experimental study of bearing capacity of a strip foundation on geogrid-reinforced sand. Geosynthetic International 7 (1), 59–71.

Shinoda, M.; Uchimura, T.; Maruyama, N.; Tatsuoka, F. (1999)
Effects of preloading and prestressing on the vertical stiffness of GRS structure. Proceedings of 11th Asian Regional Conference on SMGE, Seoul, Vol.1., 419-422.

Shinoda, M.; Uchimura T.; Tatsuoka F.; Tateyama M.; Natsuki T. (2002)
A new simple method to substantially increase the seismic stability of reinforced soil structures. Soil Dynamics and Earthquake Engineering Vol. 22, 1115–1123.

Shukla, S.K.; Chandra S. (1994)
The effect of prestressing on the settlement characteristics of geosynthetic-reinforced soil. Geotextiles and Geomembranes, Vol. 13, 531-543.

Shukla, S. K.; Kumar, R. (2008)
Overall slope stability of prestressed geosynthetic-reinforced embankments on soft ground. Geosynthetics International, Vol. 15, No. 2, 165–171.

Shukla, S. K.; Yin, J.-H. (2006)
Fundamentals of Geosynthetic Engineering. Taylor and Francis, London, USA, 410.

Scharinger, F. (2007)
A Multilaminate Model for Soil incorporating Small Strain Stiffness. PhD thesis, Graz University of Technology, Gruppe Geotechnik Graz, No. 31.

Sitharam, T.G.; Sireesh, S. (2004)
Model studies of embedded circular footing on geogrid-reinforced sand beds. Ground Improvement Vol. 8, No. 2, 69–75.

Stahl, M.; Konietzky, H. (2011)
Discrete element simulation of ballast and gravel under special consideration of grain-shape, grain-size and relative density. Granular Matter, 13, 417 - 428.

Tatsuoka, F.; Tateyama, M.; Koseki, J. (1996a)
Performance of Soil Retaining Walls for Railway Embankments. Soils and Foundations, Special Issue for the 1995 Hyogoken-Nambu Earthquake, 311-324.

Tatsuoka, F.; Uchimura, T.; Tateyama, M.; Muramoto, K. (1996b)
Creep Deformation and Stress Relaxation in Preloaded/Prestressed Geosynthetic-Reinforced Soil Retaining Walls. Proceedings of the Session Measuring and Modeling Time-Dependent Soil Behavior, ASCE Geotechnical Special Publication No. 6, Sheahan and Kaliakin, Editors, ASCE Washington Convention, 258-272.

Tatsuoka, F.; Uchimura, T.; Tateyama, M. (1997)
Preloaded and Prestressed Reinforced Soil. Soils and Foundations, Vol. 3, No. 2.

Tutumluer, E.; Huang, H.; Bian, X. (2009)
Research on the behaviour of geogrids in stabilisation applications. Jubilee Symposium on Polymer Geogrid Reinforcement, London (unpublished).

Uchimura, T.; Tatsuoka, F.; Maruyama, D.; Nakamura, H.; Tateyama, M.; Koga, T. (1997)
Construction of a Prototype Preloaded and Prestressed Reinforced Soil Bridge Pier. Proceedings of Thirty-Second Japan National Conference on Geotechnical Engineering, Kumamoto, Japan (in Japanese).

Uchimura, T.; Tatsuoka, F.; Nakarai, K. (2003)
Seismic stability of preloaded and prestressed reinforced soil abutments. Proceedings of the 12th Asian Regional Conference on Soil Mechanics and Geotechnical Engineering, Singapore, Vol.1, 339-342.

Uchimura, T.; Tatsuoka, F.; Sato, T.; Tateyama, M.; Tamura, Y. (1996)
Performance of Preloaded and Prestressed Geosynthetic-Reinforced Soil, Earth Reinforcement, Ochiai, H., Yasufuku, N. and Omine, K., Editors, Proceedings of the International Symposium on Earth Reinforcement, IS Kyushu ’96, Vol. 1, Japan. 537-542.

von Soos, P.; Bohac, J. (2002)
Properties of soils and rocks and their laboratory determination. Geotechnical Engineering Handbook, Ernst & Sohn Berlin, Vol. 1, 119-206.

Wayne, M.H.; Han, J.; Akins, K. (1998)
The design of geosynthetic reinforced foundations. Proceedings of ASCE’s 1998 Annual Convention & Exposition, ASCE Geotechnical Special Publication, Vol. 76, 1-18.

Wieser, P. (2011)
Design of a Large Oedometer for the Determination of Stress Dependent Moduli on Fault Rocks. Master thesis, Graz University of Technology. Institute of Rock Mechanics and Tunnelling.

Yetimoglu, T.; Wu, J.T.H.; Saglamer, A. (1994)
Bearing capacity of rectangular footingson geogrid-reinforced sand. Journal of Geotechnical Engineering, ASCE 120 (12), 2083–2099.

Zhang, J.; Yasufuku, N.; Ochiai, H. (2007)
A few considerations of pullout test characteristics of geogrid reinforced sand using DEM analysis. Geosynthetics Engineering Journal, 22, 103 – 110.

Zöhrer, A. (2006)

Laboratory Experiments and Numerical Modelling of Cone Penetration Tests into various Martian Soil Analoque Materials. PhD thesis, Graz University of Technology, Gruppe Geotechnik Graz, No. 29.

Appendix

In the following, the fish code of the generated clumps 1 to 4 (Chapter 4.5.3), implemented in the three dimensional Discrete Element Method simulation, is presented. It is prepared to be implemented in future research works, regarding to granular particle interaction.

```
clump template make RK1_HQ 30 &

     radii 0.8075 0.835 0.809 0.8485 0.985 0.867 0.8425 0.85 0.8435 0.9040 &
     0.8415 0.9635 0.8415 1.0025 1.004 0.837 0.921 0.771 0.8965 0.827 0.633 &
     0.6195 0.5365 0.407 0.374 0.402 0.3845 0.622 & 0.847 0.9155

     pos (1.336,0.086,-0.268) (1.191,0.446,-0.251) (1.281,-0.229,-0.264) &
     (1.012,0.666,-0.282) (0.780,0.081,-0.140) (0.891,0.777,-0.282) &
     (1.060,-0.442,-0.277) (0.683,0.884,-0.300) (0.870,-0.561,-0.272) &
     (0.488,0.822,-0.277) (0.612,-0.634,-0.272) (0.148,0.694,-0.224) &
     (0.331,-0.640,-0.255) (0.162,0.061,-0.139) (-0.002,0.575,-0.159) &
     (0.072,-0.614,-0.266) (-0.244,0.538,-0.118) (-0.306,-0.587,-0.248) &
     (-0.588,0.348,0.001) (-0.688,0.016,-0.103) (-1.107,0.258,0.097) &
     (-0.745,-0.557,-0.221) (-0.924,-0.533,-0.197) (-1.312,-0.393,-0.110) &
     (-1.477,-0.200,-0.027) (-1.522,0.079,0.119) (-1.532,-0.056,0.068) &
     (-1.128,0.007,-0.028) (-0.563,-0.097,-0.147) (-0.294,-0.114,-0.168)

     volume 13.6336

clump template make RK1_MQ 15 &

     radii 0.868 0.8295 0.780 0.829 0.796 0.717 0.8795 0.586 0.5745 & 0.6195
     & 0.934 0.909 0.8735 0.8325 1.0215

     pos (1.208,0.230,-0.206)(1.243,-0.187,-0.222) (1.046,-0.512,-0.228) &
     (0.543,-0.627,-0.237) (-0.089,-0.620,-0.257) (-0.600,-0.461,-0.229) &
     (-0.514,-0.085,-0.153) (-1.051,-0.269,-0.129) (-1.227,-0.042,-0.031) &
     (-1.140,0.179,0.090) (-0.380,0.429,-0.047) (0.118,0.745,-0.218) &
     (0.723,0.836,-0.273) (1,095,0.578,-0.244) (0.036,0.180,-0.116)

     volume 12.6379

clump template make RK1_LQ 10 &

      radii 0.841 0.810 0.810 0.755 0.614 0.673 0.673 0.839 0.887 0.887
      1.018

      pos (1.268,0.022,-0.212) (1.079,-0.473,-0.265) (0.447,-0.675,-0.254) &
      (-0.335,-0.596,-0.241) (-0.942,-0.415,-0.142) (-1.149,0.163,0.036) &
      (-0.290,0.626,-0.099) (0.547,0.835,-0.249) (1.045,0.612,-0.222) &
      (0.286,0.069,-0.140)

      volume 12.1966


clump template make RK2_HQ 45 &

     radii 0.689 0.659 0.658 0.657 0.675 0.743 0.768 0.794 0.834 0.816 0.803 &
     0.791 0.766 0.767 0.723 0.688 0.673 0.659 0.588 0.548 0.535 0.532 0.514 &
     0.535 0.553 0.603 0.608 0.599 0.599 0.568 0.577 0.589 0.602 0.662 0.678 &
     0.894 0.913 0.949 0.914 0.966 0.974 0.919 0.958 0.898
```

```
     pos (3.062,-0.086,0.066) (2.942,-0.384,0.007) (2.686,-0.609,-0.028) &
     (2.354,-0.823,-0.060) (1.997,-0.946,-0.067) (1.619,-1.066,-0.063) &
     (1.252,-1.077,-0.049) (0.797,-1.104,-0.038) (0.373,-1.094,-0.021) &
     (-0.100,-1.049,0.009) (-0.645,-1.039,0.036) (-1.183,-0.966,0.077) &
     (-1.582,-0.890,0.117) (-1.991,-0.766,0.167) (-2.278,-0.583,0.189) &
     (-2.520,-0.416,0.215) (-2.668,-0.314,0.240) (-2.871,0.044,0.230) &
     (-2.679,0.400,0.193) (-2.465,0.799,0.136) (-2.235,1.034,0.095) &
     (-1.962,1.207,0.073) (-1.641,1.345,0.055) (-1.283,1.469,0.038) &
     (-0.920,1.525,0.038) (-0.505,1.562,0.038) (-0.078,1.527,0.041) &
     (0.325,1.519,0.040) (0.737,1.492,0.037) (1.087,1.454,0.026) &
     (1.459,1.367,0.022) (1.791,1.264,0.012) (2.107,1.110,0.007) &
     (2.440,0.893,0.002) (2.734,0.559,0.017) (2.940,0.247,0.034) &
     (1.996,-0.004,0.052) (1.168,0.565,0.025) (1.133,-0.381,0.031) &
     (0.123,0.676,0.032) (0.112,-0.514,0.044) (0.096,0.137,0.032) &
     (-0.831,0.523,0.072) (-0.907,-0.340,0.077) (-1.725,0.151,0.109) &

     volume 29.7879

clump template make RK2_HQ 34 &

     radii 0.689 0.663 0.662 0.735 0.714 0.809 0.870 0.834 0.803 0.777 0.767 &
     0.723 0.688 0.673 0.659 0.588 0.568 0.539 0.565 0.545 0.571 0.633 0.619 &
     0.599 0.605 0.607 0.662 0.678 0.894 0.949 0.941 0.956 0.944 0.898

     pos (3.062,-0.086,0.066) (2.859,-0.462,0.012) (2.416,-0.770,-0.044) &
     (1.851,-0.946,-0.057) (1.352,-1.098,-0.057) (0.723,-1.053,-0.023) &
     (0.124,-0.997,0.009) (-0.551,-1.023,0.036) (-1.245,-0.950,0.088) &
     (-1.858,-0.808,0.137) (-2.278,-0.583,0.189) (-2.520,-0.416,0.215) &
     (-2.668,-0.314,0.240) (-2.871,0.044,0.230) (-2.679,0.400,0.193) &
     (-2.465,0.799,0.136) (-2.163,1.047,0.095) (-1.868,1.242,0.066) &
     (-1.410,1.370,0.047) (-0.908,1.516,0.049) (-0.355,1.558,0.041) &
     (0.284,1.500,0.027) (0.803,1.468,0.029) (1.273,1.412,0.026) &
     (1.706,1.276,0.026) (2.182,1.043,0.022) (2.626,0.643,0.017) &
     (2.940,0.247,0.034) (1.996,-0.004,0.052) (1.092,0.143,0.031) &
     (0.096,0.441,0.032) (0.106,-0.293,0.044) (-0.825,0.226,0.072) &
     (-1.725,0.151,0.109)

     volume 28.5859

clump template make RK2_MQ 19 &

     radii 0.689 0.698 0.735 0.797 0.834 0.792 0.723 0.699 0.614 0.598 0.624 &
     0.649 0.652 0.678 0.700 0.894 1.015 1.009 0.935

     pos (3.062,-0.086,0.066) (2.601,-0.608,-0.018) (1.851,-0.946,-0.057) &
     (0.751,-1.064,-0.023) (-0.551,-1.023,0.036) (-1.858,-0.808,0.150) &
     (-2.520,-0.416,0.215) (-2.742,0.070,0.230) (-2.526,0.701,0.157) &
     (-1.812,1.185,0.079) (-0.850,1.455,0.055) (0.284,1.500,0.019) &
     (1.320,1.354,0.027) (2.107,1.033,0.022) (2.722,0.514,0.017) &
     (1.996,-0.004,0.052) (0.798,0.202,0.044) (-0.521,0.265,0.072) &
     (-1.657,0.190,0.109)

     volume 26.9970


clump template make RK3_HQ 32 &

     radii 0.913 0.761 0.726 0.672 0.626 0.651 0.656 0.687 0.674 0.637 0.628 &
     0.612 0.750 1.082 0.720 1.158 0.729 0.729 1.209 0.729 1.222 0.729 1.227 &
     0.690 1.191 0.690 1.082 1.023 1.010 0.992 0.991
```

```
      pos (1.699,-0.138,-0.409) (1.403,-0.611,-0.549) (1.069,-0.870,-0.626) &
      (0.798,-1.065,-0.640) (0.479,-1.166,-0.638) (0.170,-1.143,-0.607) &
      (-0.185,-1.054,-0.569) (-0.512,-0.897,-0.473) (-0.884,-0.747,-0.400) &
      (-1.282,-0.594,-0.331) (-1.636,-0.373,-0.289) (-1.870,-0.183,-0.280) &
      (-1.991,0.022,-0.280) (-1.664,0.353,-0.269) (-0.998,0.521,-0.153) &
      (-0.847,0.936,0.389) (-0.428,0.629,-0.119) (-0.565,1.047,0.442) &
      (-0.133,1.118,0.482) (-0.050,0.615,-0.111) (0.287,1.089,0.482) &
      (0.285,0.570,-0.123) (0.837,0.942,0.436) (0.661,0.468,-0.158) &
      (1.146,0.804,0.406) (1.054,0.312,-0.200) (1.424,0.551,0.282) &
      (1.455,0.039,-0.279) (0.758,-0.258,-0.345) (0.134,-0.206,-0.332) &
      (-0.339,-0.108,-0.303) (-0.913,0.123,-0.249)

      volume 23.2505

clump template make RK3_MQ 15 &

      radii 0.913 0.761 0.745 0.709 0.700 0.730 0.726 0.677 0.660 0.750 1.091 &
      1.196 1.243 1.191 1.082

      pos (1.673,-0.151,-0.409) (1.469,-0.571,-0.549) (1.021,-0.857,-0.595)
      (0.670,-1.017,-0.598) (0.200,-1.051,-0.586) (-0.309,-0.913,-0.516) &
      (-0.839,-0.716,-0.421) (-1.344,-0.492,-0.323) (-1.746,-0.218,-0.280) &
      (-1.814,0.102,-0.269) (-0.998,0.521,-0.144) (-0.403,0.609,-0.119) &
      (0.285,0.570,-0.126) (0.998,0.383,-0.154) (1.455,0.039,-0.279)

      volume 21.6728

clump template make RK3_LQ 9 &

      radii 0.921 0.778 0.747 0.752 0.677 1.091 0.688 1.229 1.191

      pos (1.673,-0.131,-0.368) (1.055,-0.796,-0.578) (0.228,-1.010,-0.564) &
      (-0.697,-0.757,-0.432) (-1.344,-0.492,-0.323) (-0.998,0.521,-0.144) &
      (-1.896,-0.048,-0.269) (0.012,0.726,-0.026) (0.998,0.383,-0.154)

      volume 20.9102


clump template make RK4_HQ 43 &

      radii 0.837 0.754 0.634 0.695 0.975 0.529 1.053 0.772 0.698 0.759 0.666 &
      1.265 1.114 1.209 0.770 1.105 0.880 1.118 1.000 0.954 1.033 1.130 1.013 &
      1.013 0.933 0.814 0.585 0.585 0.656 0.535 0.966 0.536 0.585 0.542 0.571 &
      0.571 0.546 0.536 0.844 0.844 0.676 0.747 0.716

      pos (0.068,0.243,0.820) (0.394,0.191,0.882) (0.606,0.141,0.903) &
      (-0.175,0.412,0.698) (0.284,0.156,0.366) (0.830,0.156,0.755) &
      (-0.058,0.168,0.240) (-0.295,0.393,0.367) (0.133,-0.172,0.464) &
      (0.792,0.059,0.293) (0.554,0.430,0.402) (0.078,0.022,-0.330) &
      (-0.296,0.126,-0.194) (0.341,-0.005,-0.399) (0.365,-0.497,-0.290) &
      (0.680,0.117,-0.430) (0.806,0.031,-0.044) (-0.538,0.075,-0.529) &
      (-0.531,0.213,-0.362) (-0.746,0.072,-0.623) (0.300,0.265,-0.742) &
      (0.072,0.170,-0.688) (0.320,-0.269,-0.793) (-0.009,-0.223,-0.826) &
      (-0.565,-0.168,-0.722) (0.725,-0.196,-0.793) (1.226,0.063,-0.584) &
      (1.194,0.252,-0.583) (1.069,0.382,-0.577) (0.976,0.722,-0.702) &
      (0.278,0.113,-0.870) (0.791,0.780,-0.869) (0.640,0.707,-0.918) &
      (0.696,-0.575,-1.121) (0.471,-0.674,-1.169) (0.127,-0.681,-1.183) &
      (-0.284,-0.629,-1.162) (-0.549,-0.551,-1.112) (-0.324,0.341,-0.813) &
      (-0.203,0.461,-0.783) (-0.481,0.627,-0.780) (-0.741,0.512,-0.725) &
      (-0.943,0.485,-0.703)

      volume 15.8790
```

```
clump template make RK4_MQ 22 &

     radii 0.837 0.754 0.691 1.053 0.916 1.265 1.181 1.112 1.130 0.585 0.491
     0.535 0.604 1.013 0.933 0.716 0.676 0.536 0.546 0.571 0.571

     pos (0.068,0.243,0.820) (0.397,0.191,0.882) (0.614,0.133,0.773) &
     (-0.058,0.168,0.240) (0.634,0.127,0.240) (0.078,0.022,-0.330) &
     (0.601,0.095,-0.425) (-0.538,0.075,-0.548) (0.072,0.170,-0.700) &
     (0.640,0.707,-0.918) & (0.870,0.818,-0.851) (0.976,0.722,-0.702) &
     (1.092,0.418,-0.615) (0.320,-0.269,-0.812) (-0.128,-0.234,-0.800) &
     (-0.565,-0.168,-0.722) (-0.943,0.485,-0.703) (-0.481,0.627,-0.780) &
     (-0.549,-0.551,-1.112) (-0.284,-0.629,-1.162) (0.127,-0.681,-1.183) &
     (0.471,-0.674,-1.169)

     volume 15.5772

clump template make RK4_LQ 11 &

     radii 0.859 0.720 0.961 1.103 1.181 1.317 1.061 1.013 0.728 1.013 0.933

     pos (0.068,0.227,0.777) (0.501,0.168,0.861) (0.537,0.127,0.240) &
     (-0.087,0.139,0.071) (0.567,0.114,-0.434) (0.122,0.006,-0.553) &
     (-0.582,0.191,-0.528) (0.320,-0.292,-0.829) (0.778,0.594,-0.745) &
     (-0.128,-0.234,-0.800) (-0.565,-0.168,-0.722)

     volume 15.1244
```

Further, the fish code of the generated detailed geogrid (Chapter 4.5.3) is presented. It is prepared to be implemented in future research tasks, regarding to geosynthetic investigations.

```
new
;FORTRAC T 50/50-20T
; Number of meshes in x and y direction
def _nxny
       nx=2
       ny=3
end
_nxny

;Definitions
def _LaufBallID
       nextbid=max_bid+1
end

;Definieren of variables
def _variable
       xstart=-0.02332
       ystart=0
       zstart=0
       xsym=0.02332
       ysym=0.0263598478
end
;Coordinates of group Zentrum
def _koordZentrum
       x1=xstart
       y1=ystart
       z1=zstart
       x2=xstart
       y2=ystart+0.00156
       z2=zstart
       x3=xstart
       y3=ystart+0.00312
       z3=zstart
       x4=xstart
```

```
       y4=ystart+0.00468
       z4=zstart
       x5=xstart
       y5=ystart+0.00624
       z5=zstart
       x6=xstart
       y6=ystart+0.0078
       z6=zstart
       x7=xstart+0.00156
       y7=ystart
       z7=zstart
       x8=xstart+0.00156
       y8=ystart+0.00156
       z8=zstart
       x9=xstart+0.00156
       y9=ystart+0.00312
       z9=zstart
       x10=xstart+0.00156
       y10=ystart+0.00468
       z10=zstart
       x11=xstart+0.00156
       y11=ystart+0.00624
       z11=zstart
       x12=xstart+0.00156
       y12=ystart+0.0078
       z12=zstart
end
_koordZentrum
_variable

; Coordinates of group Vertikal
def _koordVertikal
       x13=xstart+0.00002657786
       y13=ystart+0.00934665398
       z13=zstart-0.00020187886
       x14=xstart+0.00153342214
       y14=ystart+0.00934665398
       z14=zstart+0.00020187886
       x15=xstart+0.00010450019
       y15=ystart+0.01089330797
       z15=zstart-0.00039
       x16=xstart+0.00145549981
       y16=ystart+0.01089330797
       z16=zstart+0.00039
       x17=xstart+0.00022845672
       y17=ystart+0.01243996195
       z17=zstart-0.00055154329
       x18=xstart+0.00133154328
       y18=ystart+0.01243996195
       z18=zstart+0.00055154329
       x19=xstart+0.00039000001
       y19=ystart+0.01398661593
       z19=zstart-0.00067549982
       x20=xstart+0.00116999999
       y20=ystart+0.01398661593
       z20=zstart+0.00067549982
       x21=xstart+0.00057812115
       y21=ystart+0.01553326992
       z21=zstart-0.00075342215
       x22=xstart+0.00098187885
       y22=ystart+0.01553326992
       z22=zstart+0.00075342215
       x23=xstart+0.00078
       y23=ystart+0.01707992390
       z23=zstart+0.00078
       x24=xstart+0.00078
       y24=ystart+0.01707992390
       z24=zstart-0.00078
       x25=xstart+0.00057812115
       y25=ystart+0.01862657788
```

```
       z25=zstart+0.00075342215
       x26=xstart+0.00098187885
       y26=ystart+0.01862657788
       z26=zstart-0.00075342215
       x27=xstart+0.00039000001
       y27=ystart+0.02017323187
       z27=zstart+0.00067549982
       x28=xstart+0.00116999999
       y28=ystart+0.02017323187
       z28=zstart-0.00067549982
       x29=xstart+0.00022845672
       y29=ystart+0.02171988585
       z29=zstart+0.00055154329
       x30=xstart+0.00133154328
       y30=ystart+0.02171988585
       z30=zstart-0.00055154329
       x31=xstart+0.00010450019
       y31=ystart+0.02326653984
       z31=zstart+0.00039
       x32=xstart+0.00145549981
       y32=ystart+0.02326653984
       z32=zstart-0.00039
       x33=xstart+0.00002657786
       y33=ystart+0.02481319382
       z33=zstart+0.00020187886
       x34=xstart+0.00153342214
       y34=ystart+0.02481319382
       z34=zstart-0.00020187886
end
_koordVertikal
_variable

; Coordinates of group Horizontal
def _koordHorizontal
       x35=xstart+0.00304
       y35=ystart
       z35=zstart
       x36=xstart+0.00439
       y36=ystart
       z36=zstart
       x37=xstart+0.00564
       y37=ystart
       z37=zstart
       x38=xstart+0.00679
       y38=ystart
       z38=zstart
       x39=xstart+0.00789
       y39=ystart
       z39=zstart
       x40=xstart+0.00894
       y40=ystart
       z40=zstart
       x41=xstart+0.00994
       y41=ystart
       z41=zstart
       x42=xstart+0.01094
       y42=ystart
       z42=zstart
       x43=xstart+0.01194
       y43=ystart
       z43=zstart
       x44=xstart+0.00304
       y44=ystart+0.00156
       z44=zstart
       x45=xstart+0.00439
       y45=ystart+0.00156
       z45=zstart
       x46=xstart+0.00564
       y46=ystart+0.00156
       z46=zstart
```

```
x47=xstart+0.00679
y47=ystart+0.00156
z47=zstart
x48=xstart+0.00789
y48=ystart+0.00156
z48=zstart
x49=xstart+0.00894
y49=ystart+0.00156
z49=zstart
x50=xstart+0.00994
y50=ystart+0.00156
z50=zstart
x51=xstart+0.01094
y51=ystart+0.00156
z51=zstart
x52=xstart+0.01194
y52=ystart+0.00156
z52=zstart
x53=xstart+0.00304
y53=ystart+0.00312
z53=zstart
x54=xstart+0.00439
y54=ystart+0.00312
z54=zstart
x55=xstart+0.00564
y55=ystart+0.00312
z55=zstart
x56=xstart+0.00679
y56=ystart+0.00312
z56=zstart
x57=xstart+0.00789
y57=ystart+0.00312
z57=zstart
x58=xstart+0.00894
y58=ystart+0.00312
z58=zstart
x59=xstart+0.00994
y59=ystart+0.00312
z59=zstart
x60=xstart+0.01094
y60=ystart+0.00312
z60=zstart
x61=xstart+0.01194
y61=ystart+0.00312
z61=zstart
x62=xstart+0.00304
y62=ystart+0.00468
z62=zstart
x63=xstart+0.00439
y63=ystart+0.00468
z63=zstart
x64=xstart+0.00564
y64=ystart+0.00468
z64=zstart
x65=xstart+0.00679
y65=ystart+0.00468
z65=zstart
x66=xstart+0.00789
y66=ystart+0.00468
z66=zstart
x67=xstart+0.00894
y67=ystart+0.00468
z67=zstart
x68=xstart+0.00994
y68=ystart+0.00468
z68=zstart
x69=xstart+0.01094
y69=ystart+0.00468
z69=zstart
x70=xstart+0.01194
```

```
y70=ystart+0.00468
z70=zstart
x71=xstart+0.00304
y71=ystart+0.00624
z71=zstart
x72=xstart+0.00439
y72=ystart+0.00624
z72=zstart
x73=xstart+0.00564
y73=ystart+0.00624
z73=zstart
x74=xstart+0.00679
y74=ystart+0.00624
z74=zstart
x75=xstart+0.00789
y75=ystart+0.00624
z75=zstart
x76=xstart+0.00894
y76=ystart+0.00624
z76=zstart
x77=xstart+0.00994
y77=ystart+0.00624
z77=zstart
x78=xstart+0.01094
y78=ystart+0.00624
z78=zstart
x79=xstart+0.01194
y79=ystart+0.00624
z79=zstart
x80=xstart+0.00304
y80=ystart+0.0078
z80=zstart
x81=xstart+0.00439
y81=ystart+0.0078
z81=zstart
x82=xstart+0.00564
y82=ystart+0.0078
z82=zstart
x83=xstart+0.00679
y83=ystart+0.0078
z83=zstart
x84=xstart+0.00789
y84=ystart+0.0078
z84=zstart
x85=xstart+0.00894
y85=ystart+0.0078
z85=zstart
x86=xstart+0.00994
y86=ystart+0.0078
z86=zstart
x87=xstart+0.01094
y87=ystart+0.0078
z87=zstart
x88=xstart+0.01194
y88=ystart+0.0078
z88=zstart
x89=xstart+0.01294
y89=ystart
z89=zstart
x90=xstart+0.01394
y90=ystart
z90=zstart
x91=xstart+0.01494
y91=ystart
z91=zstart
x92=xstart+0.01594
y92=ystart
z92=zstart
x93=xstart+0.01699
y93=ystart
```

```
z93=zstart
x94=xstart+0.01809
y94=ystart
z94=zstart
x95=xstart+0.01924
y95=ystart
z95=zstart
x96=xstart+0.02049
y96=ystart
z96=zstart
x97=xstart+0.02184
y97=ystart
z97=zstart
x98=xstart+0.01294
y98=ystart+0.00156
z98=zstart
x99=xstart+0.01394
y99=ystart+0.00156
z99=zstart
x100=xstart+0.01494
y100=ystart+0.00156
z100=zstart
x101=xstart+0.01594
y101=ystart+0.00156
z101=zstart
x102=xstart+0.01699
y102=ystart+0.00156
z102=zstart
x103=xstart+0.01809
y103=ystart+0.00156
z103=zstart
x104=xstart+0.01924
y104=ystart+0.00156
z104=zstart
x105=xstart+0.02049
y105=ystart+0.00156
z105=zstart
x106=xstart+0.02184
y106=ystart+0.00156
z106=zstart
x107=xstart+0.01294
y107=ystart+0.00312
z107=zstart
x108=xstart+0.01394
y108=ystart+0.00312
z108=zstart
x109=xstart+0.01494
y109=ystart+0.00312
z109=zstart
x110=xstart+0.01594
y110=ystart+0.00312
z110=zstart
x111=xstart+0.01699
y111=ystart+0.00312
z111=zstart
x112=xstart+0.01809
y112=ystart+0.00312
z112=zstart
x113=xstart+0.01924
y113=ystart+0.00312
z113=zstart
x114=xstart+0.02049
y114=ystart+0.00312
z114=zstart
x115=xstart+0.02184
y115=ystart+0.00312
z115=zstart
x116=xstart+0.01294
y116=ystart+0.00468
z116=zstart
```

```
x117=xstart+0.01394
y117=ystart+0.00468
z117=zstart
x118=xstart+0.01494
y118=ystart+0.00468
z118=zstart
x119=xstart+0.01594
y119=ystart+0.00468
z119=zstart
x120=xstart+0.01699
y120=ystart+0.00468
z120=zstart
x121=xstart+0.01809
y121=ystart+0.00468
z121=zstart
x122=xstart+0.01924
y122=ystart+0.00468
z122=zstart
x123=xstart+0.02049
y123=ystart+0.00468
z123=zstart
x124=xstart+0.02184
y124=ystart+0.00468
z124=zstart
x125=xstart+0.01294
y125=ystart+0.00624
z125=zstart
x126=xstart+0.01394
y126=ystart+0.00624
z126=zstart
x127=xstart+0.01494
y127=ystart+0.00624
z127=zstart
x128=xstart+0.01594
y128=ystart+0.00624
z128=zstart
x129=xstart+0.01699
y129=ystart+0.00624
z129=zstart
x130=xstart+0.01809
y130=ystart+0.00624
z130=zstart
x131=xstart+0.01924
y131=ystart+0.00624
z131=zstart
x132=xstart+0.02049
y132=ystart+0.00624
z132=zstart
x133=xstart+0.02184
y133=ystart+0.00624
z133=zstart
x134=xstart+0.01294
y134=ystart+0.0078
z134=zstart
x135=xstart+0.01394
y135=ystart+0.0078
z135=zstart
x136=xstart+0.01494
y136=ystart+0.0078
z136=zstart
x137=xstart+0.01594
y137=ystart+0.0078
z137=zstart
x138=xstart+0.01699
y138=ystart+0.0078
z138=zstart
x139=xstart+0.01809
y139=ystart+0.0078
z139=zstart
x140=xstart+0.01924
```

```
        y140=ystart+0.0078
        z140=zstart
        x141=xstart+0.02049
        y141=ystart+0.0078
        z141=zstart
        x142=xstart+0.02184
        y142=ystart+0.0078
        z142=zstart
end
_koordHorizontal
_variable

;Generating spheres group Zentrum in x
def _XRichtungZ
loop _XRZ (1,nx)
xstart=xstart+xsym
command
       _koordZentrum
        ball id=nextbid x=x1 y=y1 z=z1 rad 0.00078
        ball id=nextbid x=x2 y=y2 z=z2 rad 0.00078
        ball id=nextbid x=x3 y=y3 z=z3 rad 0.00078
        ball id=nextbid x=x4 y=y4 z=z4 rad 0.00078
        ball id=nextbid x=x5 y=y5 z=z5 rad 0.00078
        ball id=nextbid x=x6 y=y6 z=z6 rad 0.00078
        ball id=nextbid x=x7 y=y7 z=z7 rad 0.00078
        ball id=nextbid x=x8 y=y8 z=z8 rad 0.00078
        ball id=nextbid x=x9 y=y9 z=z9 rad 0.00078
        ball id=nextbid x=x10 y=y10 z=z10 rad 0.00078
        ball id=nextbid x=x11 y=y11 z=z11 rad 0.00078
        ball id=nextbid x=x12 y=y12 z=z12 rad 0.00078
end_command
end_loop
end
_XRichtungZ
_variable

; Generating spheres group Vertikal in x
def _XRichtungV
loop _XRV (1,nx)
xstart=xstart+xsym
command
_koordVertikal
        ball id=nextbid x=x13 y=y13 z=z13 rad 0.00078
        ball id=nextbid x=x14 y=y14 z=z14 rad 0.00078
        ball id=nextbid x=x15 y=y15 z=z15 rad 0.00078
        ball id=nextbid x=x16 y=y16 z=z16 rad 0.00078
        ball id=nextbid x=x17 y=y17 z=z17 rad 0.00078
        ball id=nextbid x=x18 y=y18 z=z18 rad 0.00078
        ball id=nextbid x=x19 y=y19 z=z19 rad 0.00078
        ball id=nextbid x=x20 y=y20 z=z20 rad 0.00078
        ball id=nextbid x=x21 y=y21 z=z21 rad 0.00078
        ball id=nextbid x=x22 y=y22 z=z22 rad 0.00078
        ball id=nextbid x=x23 y=y23 z=z23 rad 0.00078
        ball id=nextbid x=x24 y=y24 z=z24 rad 0.00078
        ball id=nextbid x=x25 y=y25 z=z25 rad 0.00078
        ball id=nextbid x=x26 y=y26 z=z26 rad 0.00078
        ball id=nextbid x=x27 y=y27 z=z27 rad 0.00078
        ball id=nextbid x=x28 y=y28 z=z28 rad 0.00078
        ball id=nextbid x=x29 y=y29 z=z29 rad 0.00078
        ball id=nextbid x=x30 y=y30 z=z30 rad 0.00078
        ball id=nextbid x=x31 y=y31 z=z31 rad 0.00078
        ball id=nextbid x=x32 y=y32 z=z32 rad 0.00078
        ball id=nextbid x=x33 y=y33 z=z33 rad 0.00078
        ball id=nextbid x=x34 y=y34 z=z34 rad 0.00078
end_command
end_loop
end
_XRichtungV
_variable
```

```
; Generating spheres group Horizontal in x
def _XRichtungH
loop _XRH (1,nx)
xstart=xstart+xsym
command
_koordHorizontal
        ball id=nextbid x=x35 y=y35 z=z35 rad 0.0007
        ball id=nextbid x=x36 y=y36 z=z36 rad 0.00065
        ball id=nextbid x=x37 y=y37 z=z37 rad 0.0006
        ball id=nextbid x=x38 y=y38 z=z38 rad 0.00055
        ball id=nextbid x=x39 y=y39 z=z39 rad 0.00055
        ball id=nextbid x=x40 y=y40 z=z40 rad 0.0005
        ball id=nextbid x=x41 y=y41 z=z41 rad 0.0005
        ball id=nextbid x=x42 y=y42 z=z42 rad 0.0005
        ball id=nextbid x=x43 y=y43 z=z43 rad 0.0005
        ball id=nextbid x=x44 y=y44 z=z44 rad 0.0007
        ball id=nextbid x=x45 y=y45 z=z45 rad 0.00065
        ball id=nextbid x=x46 y=y46 z=z46 rad 0.0006
        ball id=nextbid x=x47 y=y47 z=z47 rad 0.00055
        ball id=nextbid x=x48 y=y48 z=z48 rad 0.00055
        ball id=nextbid x=x49 y=y49 z=z49 rad 0.0005
        ball id=nextbid x=x50 y=y50 z=z50 rad 0.0005
        ball id=nextbid x=x51 y=y51 z=z51 rad 0.0005
        ball id=nextbid x=x52 y=y52 z=z52 rad 0.0005
        ball id=nextbid x=x53 y=y53 z=z53 rad 0.0007
        ball id=nextbid x=x54 y=y54 z=z54 rad 0.00065
        ball id=nextbid x=x55 y=y55 z=z55 rad 0.0006
        ball id=nextbid x=x56 y=y56 z=z56 rad 0.00055
        ball id=nextbid x=x57 y=y57 z=z57 rad 0.00055
        ball id=nextbid x=x58 y=y58 z=z58 rad 0.0005
        ball id=nextbid x=x59 y=y59 z=z59 rad 0.0005
        ball id=nextbid x=x60 y=y60 z=z60 rad 0.0005
        ball id=nextbid x=x61 y=y61 z=z61 rad 0.0005
        ball id=nextbid x=x62 y=y62 z=z62 rad 0.0007
        ball id=nextbid x=x63 y=y63 z=z63 rad 0.00065
        ball id=nextbid x=x64 y=y64 z=z64 rad 0.0006
        ball id=nextbid x=x65 y=y65 z=z65 rad 0.00055
        ball id=nextbid x=x66 y=y66 z=z66 rad 0.00055
        ball id=nextbid x=x67 y=y67 z=z67 rad 0.0005
        ball id=nextbid x=x68 y=y68 z=z68 rad 0.0005
        ball id=nextbid x=x69 y=y69 z=z69 rad 0.0005
        ball id=nextbid x=x70 y=y70 z=z70 rad 0.0005
        ball id=nextbid x=x71 y=y71 z=z71 rad 0.0007
        ball id=nextbid x=x72 y=y72 z=z72 rad 0.00065
        ball id=nextbid x=x73 y=y73 z=z73 rad 0.0006
        ball id=nextbid x=x74 y=y74 z=z74 rad 0.00055
        ball id=nextbid x=x75 y=y75 z=z75 rad 0.00055
        ball id=nextbid x=x76 y=y76 z=z76 rad 0.0005
        ball id=nextbid x=x77 y=y77 z=z77 rad 0.0005
        ball id=nextbid x=x78 y=y78 z=z78 rad 0.0005
        ball id=nextbid x=x79 y=y79 z=z79 rad 0.0005
        ball id=nextbid x=x80 y=y80 z=z80 rad 0.0007
        ball id=nextbid x=x81 y=y81 z=z81 rad 0.00065
        ball id=nextbid x=x82 y=y82 z=z82 rad 0.0006
        ball id=nextbid x=x83 y=y83 z=z83 rad 0.00055
        ball id=nextbid x=x84 y=y84 z=z84 rad 0.00055
        ball id=nextbid x=x85 y=y85 z=z85 rad 0.0005
        ball id=nextbid x=x86 y=y86 z=z86 rad 0.0005
        ball id=nextbid x=x87 y=y87 z=z87 rad 0.0005
        ball id=nextbid x=x88 y=y88 z=z88 rad 0.0005
        ball id=nextbid x=x89 y=y89 z=z89 rad 0.0005
        ball id=nextbid x=x90 y=y90 z=z90 rad 0.0005
        ball id=nextbid x=x91 y=y91 z=z91 rad 0.0005
        ball id=nextbid x=x92 y=y92 z=z92 rad 0.0005
        ball id=nextbid x=x93 y=y93 z=z93 rad 0.00055
        ball id=nextbid x=x94 y=y94 z=z94 rad 0.00055
        ball id=nextbid x=x95 y=y95 z=z95 rad 0.0006
        ball id=nextbid x=x96 y=y96 z=z96 rad 0.00065
        ball id=nextbid x=x97 y=y97 z=z97 rad 0.0007
        ball id=nextbid x=x98 y=y98 z=z98 rad 0.0005
```

```
        ball id=nextbid x=x99 y=y99 z=z99 rad 0.0005
        ball id=nextbid x=x100 y=y100 z=z100 rad 0.0005
        ball id=nextbid x=x101 y=y101 z=z101 rad 0.0005
        ball id=nextbid x=x102 y=y102 z=z102 rad 0.00055
        ball id=nextbid x=x103 y=y103 z=z103 rad 0.00055
        ball id=nextbid x=x104 y=y104 z=z104 rad 0.0006
        ball id=nextbid x=x105 y=y105 z=z105 rad 0.00065
        ball id=nextbid x=x106 y=y106 z=z106 rad 0.0007
        ball id=nextbid x=x107 y=y107 z=z107 rad 0.0005
        ball id=nextbid x=x108 y=y108 z=z108 rad 0.0005
        ball id=nextbid x=x109 y=y109 z=z109 rad 0.0005
        ball id=nextbid x=x110 y=y110 z=z110 rad 0.0005
        ball id=nextbid x=x111 y=y111 z=z111 rad 0.00055
        ball id=nextbid x=x112 y=y112 z=z112 rad 0.00055
        ball id=nextbid x=x113 y=y113 z=z113 rad 0.0006
        ball id=nextbid x=x114 y=y114 z=z114 rad 0.00065
        ball id=nextbid x=x115 y=y115 z=z115 rad 0.0007
        ball id=nextbid x=x116 y=y116 z=z116 rad 0.0005
        ball id=nextbid x=x117 y=y117 z=z117 rad 0.0005
        ball id=nextbid x=x118 y=y118 z=z118 rad 0.0005
        ball id=nextbid x=x119 y=y119 z=z119 rad 0.0005
        ball id=nextbid x=x120 y=y120 z=z120 rad 0.00055
        ball id=nextbid x=x121 y=y121 z=z121 rad 0.00055
        ball id=nextbid x=x122 y=y122 z=z122 rad 0.0006
        ball id=nextbid x=x123 y=y123 z=z123 rad 0.00065
        ball id=nextbid x=x124 y=y124 z=z124 rad 0.0007
        ball id=nextbid x=x125 y=y125 z=z125 rad 0.0005
        ball id=nextbid x=x126 y=y126 z=z126 rad 0.0005
        ball id=nextbid x=x127 y=y127 z=z127 rad 0.0005
        ball id=nextbid x=x128 y=y128 z=z128 rad 0.0005
        ball id=nextbid x=x129 y=y129 z=z129 rad 0.00055
        ball id=nextbid x=x130 y=y130 z=z130 rad 0.00055
        ball id=nextbid x=x131 y=y131 z=z131 rad 0.0006
        ball id=nextbid x=x132 y=y132 z=z132 rad 0.00065
        ball id=nextbid x=x133 y=y133 z=z133 rad 0.0007
        ball id=nextbid x=x134 y=y134 z=z134 rad 0.0005
        ball id=nextbid x=x135 y=y135 z=z135 rad 0.0005
        ball id=nextbid x=x136 y=y136 z=z136 rad 0.0005
        ball id=nextbid x=x137 y=y137 z=z137 rad 0.0005
        ball id=nextbid x=x138 y=y138 z=z138 rad 0.00055
        ball id=nextbid x=x139 y=y139 z=z139 rad 0.00055
        ball id=nextbid x=x140 y=y140 z=z140 rad 0.0006
        ball id=nextbid x=x141 y=y141 z=z141 rad 0.00065
        ball id=nextbid x=x142 y=y142 z=z142 rad 0.0007
end_command
end_loop
end
_XRichtungH
_variable

; Generating spheres group Zentrum and Vertikal in x
def _AbXR
xstart=(xsym*nx)
command
_koordZentrum
_koordVertikal
        ball id=nextbid x=x1 y=y1 z=z1 rad 0.00078
        ball id=nextbid x=x2 y=y2 z=z2 rad 0.00078
        ball id=nextbid x=x3 y=y3 z=z3 rad 0.00078
        ball id=nextbid x=x4 y=y4 z=z4 rad 0.00078
        ball id=nextbid x=x5 y=y5 z=z5 rad 0.00078
        ball id=nextbid x=x6 y=y6 z=z6 rad 0.00078
        ball id=nextbid x=x7 y=y7 z=z7 rad 0.00078
        ball id=nextbid x=x8 y=y8 z=z8 rad 0.00078
        ball id=nextbid x=x9 y=y9 z=z9 rad 0.00078
        ball id=nextbid x=x10 y=y10 z=z10 rad 0.00078
        ball id=nextbid x=x11 y=y11 z=z11 rad 0.00078
        ball id=nextbid x=x12 y=y12 z=z12 rad 0.00078
        ball id=nextbid x=x13 y=y13 z=z13 rad 0.00078
        ball id=nextbid x=x14 y=y14 z=z14 rad 0.00078
```

```
        ball id=nextbid x=x15 y=y15 z=z15 rad 0.00078
        ball id=nextbid x=x16 y=y16 z=z16 rad 0.00078
        ball id=nextbid x=x17 y=y17 z=z17 rad 0.00078
        ball id=nextbid x=x18 y=y18 z=z18 rad 0.00078
        ball id=nextbid x=x19 y=y19 z=z19 rad 0.00078
        ball id=nextbid x=x20 y=y20 z=z20 rad 0.00078
        ball id=nextbid x=x21 y=y21 z=z21 rad 0.00078
        ball id=nextbid x=x22 y=y22 z=z22 rad 0.00078
        ball id=nextbid x=x23 y=y23 z=z23 rad 0.00078
        ball id=nextbid x=x24 y=y24 z=z24 rad 0.00078
        ball id=nextbid x=x25 y=y25 z=z25 rad 0.00078
        ball id=nextbid x=x26 y=y26 z=z26 rad 0.00078
        ball id=nextbid x=x27 y=y27 z=z27 rad 0.00078
        ball id=nextbid x=x28 y=y28 z=z28 rad 0.00078
        ball id=nextbid x=x29 y=y29 z=z29 rad 0.00078
        ball id=nextbid x=x30 y=y30 z=z30 rad 0.00078
        ball id=nextbid x=x31 y=y31 z=z31 rad 0.00078
        ball id=nextbid x=x32 y=y32 z=z32 rad 0.00078
        ball id=nextbid x=x33 y=y33 z=z33 rad 0.00078
        ball id=nextbid x=x34 y=y34 z=z34 rad 0.00078
end_command
end
_AbXR
_variable

; Generating spheres x, in y direction
def _yRichtung
       loop _yR (1,(ny-1))
       ystart=ystart+ysym
       xstart=-0.02332
       command
       _XRichtungZ
       end_command
       xstart=-0.02332
       command
       _XRichtungV
       end_command
       xstart=-0.02332
       command
       _XRichtungH
       end_command
       xstart=-0.02332
       command
       _AbXR
       end_command
       end_loop
end
_yRichtung
_variable

; Generating spheres group Zentrum and Horizontal in y
def _yRichtungAb
       ystart=(ysym*(ny-1))+ysym
       xstart=-0.02332
       command
       _XRichtungH
       end_command
       xstart=-0.02332
       command
       _XRichtungZ
       end_command
end
_yRichtungAb
_variable

; Generating spheres group Zentrum
def _EckAb
ystart=(ysym*(ny-1))+ysym
xstart=(xsym*nx)
command
```

```
_koordZentrum
        bal id=nextbid x=x1 y=y1 z=z1 rad 0.00078
        ball id=nextbid x=x2 y=y2 z=z2 rad 0.00078
        ball id=nextbid x=x3 y=y3 z=z3 rad 0.00078
        ball id=nextbid x=x4 y=y4 z=z4 rad 0.00078
        ball id=nextbid x=x5 y=y5 z=z5 rad 0.00078
        ball id=nextbid x=x6 y=y6 z=z6 rad 0.00078
        ball id=nextbid x=x7 y=y7 z=z7 rad 0.00078
        ball id=nextbid x=x8 y=y8 z=z8 rad 0.00078
        ball id=nextbid x=x9 y=y9 z=z9 rad 0.00078
        ball id=nextbid x=x10 y=y10 z=z10 rad 0.00078
        ball id=nextbid x=x11 y=y11 z=z11 rad 0.00078
        ball id=nextbid x=x12 y=y12 z=z12 rad 0.00078
end_command
end
_EckAb
_variable

; Grouping of spheres
def _GroupGitter
       command
       group _Gitter
       end_command
end
_GroupGitter

;density / unit weight
def _dichteberechnung
        lx=0.00078+xsym*nx+3*0.00078
        ly=0.00078+ysym*(ny-1)+ysym+0.00078+10*0.00078
        _flaeche = lx * ly
        bp=ball_head
        volumen=0.0
        loop while bp # null
        volumen = volumen + 4.0/3.0 * b_rad(bp)^3.0 * pi
        bp=b_next(bp)
        end_loop
        _Gewicht_pro_EH = 0.316*_flaeche ;[kg/m2]/m²= kg
        _dichte = _Gewicht_pro_EH / volumen
        end
        _dichteberechnung
        def _massenberechnung
        masse = _dichte * volumen
        end
        _massenberechnung

;Properties of geogrid
def _EigensGi
command
        prop dens _dichte ra gr _Gitter ; [kg/m^3]
        prop kn=3.9e6 ra gr _Gitter ; [N/m]
        prop ks=9e5 ra gr _Gitter ; [N/m]
        prop n_bond 5e5 ra gr _Gitter ; [N]
        prop s_bond 5e5 ra gr _Gitter ; [N]
        prop pb_rad 0.3 ra gr _Gitter ; [-]
        prop pb_kn 2e12 ra gr _Gitter ; [Pa/m]
        prop pb_ks 2e12 ra gr _Gitter ; [Pa/m]
        prop pb_nstrength 8e14 ra gr _Gitter ; [Pa]
        prop pb_sstrength 8e14 ra gr _Gitter ; [Pa]
        prop fric 1.0 ra gr _Gitter ; [-]
end_command
end
_EigensGi
```